



Institut de Física Interdisciplinària i Sistemes Complexos

TESI DOCTORAL

**HORIZONTAL TRANSPORT AND
MIXING AND THEIR CONNECTION
WITH DYNAMICAL AND BIOLOGICAL
PROCESSES IN THE OCEAN**

Ismael Hernández Carrasco

Directors:

Dr. Cristóbal López

Prof. Emilio Hernández García

Universitat Illes Balears

2013

HORIZONTAL TRANSPORT AND MIXING AND THEIR CONNECTION WITH DYNAMICAL AND BIOLOGICAL PROCESSES IN THE OCEAN

Ismael Hernández Carrasco
Instituto de Física Interdisciplinar y Sistemas Complejos (IFISC)
Universitat de les Illes Balears (UIB)
Consejo Superior de Investigaciones Científicas (CSIC)

PhD Thesis

Directores: Dr. Cristóbal López y Dr. Emilio Hernández García

Copyright 2013, Ismael Hernández Carrasco
Universitat de les Illes Balears
Palma

This document was typeset with $\text{\LaTeX} 2_{\epsilon}$

Cristóbal López, Profesor titular de la Universitat de les Illes Balears, y Emilio Hernández García, Profesor de Investigación del Consejo Superior de Investigaciones Científicas

FAN CONSTAR

que aquesta tesi doctoral ha estat realitzada pel Sr. *Ismael Hernández Carrasco* sota la seva direcció al Instituto de Física Interdisciplinar y Sistemas Complejos (UIB-CSIC) i, per a donar-ne constància, firmen la mateixa.

Palma, 22 de Març del 2013

Cristóbal López
Director

Emilio Hernández García
Director

Ismael Hernández Carrasco
Doctorando

Resum

Els processos de mescla i transport horitzontal són centrals per a l'estudi de la dinàmica física, química, i biològica de l'oceà. Una correcta comprensió i un precís modelatge d'aquests processos són rellevants des del punt de vista teòric, i són crucials per a una varietat de problemes pràctics, tals com la dinàmica del plàncton o el control d'abocaments contaminants. En aquest sentit, els darrers anys han vist brollar nous i interessants desenvolupaments en la descripció Lagrangiana de fenòmens de transport i mescla, molts d'ells provinents de l'àrea de la dinàmica no-lineal. Aquestes aproximacions no tenen com a objectiu predir trajectòries individuals de traçadores, sinó localitzar estructures espacials que són conegudes dins la teoria de sistemes dinàmics com a estructures que actuen com a esquelet organitzador del flux sencer (Leong and Ottino, 1989; Wiggins, 1992). Això es deu principalment a la capacitat dels diagnòstics Lagrangians d'explorar la variabilitat espai-temporal del camp de velocitats mitjançant el seguiment de trajectòries de partícules de fluid, a diferència de les Eulerianes les quals analitzen mapes instantanis de dades. Entre aquestes tècniques Lagrangianes, una classe amb molt de potencial consisteix en el càlcul dels exponents de Lyapunov locals (LLE), els quals mesuren la dispersió relativa de partícules transportades. En particular, estan els anomenats exponents de Lyapunov de mida finita (FSLEs) on un calcula el temps que tarden dues trajectòries, inicialment separades per un distància finita, el separar-se una distància finita final més llarga.

Els LLEs estan captant l'atenció de la comunitat oceanogràfica. Les principals raons d'aquest interès són les següents: a) identifiquen i mostren les estructures dinàmiques del flux que fortament organitzen el moviment del fluid (Estructures Coherents Lagrangianes (LCSs)) com a vòrtex, barreres de transport, fronts, etc; b) són relativament fàcils de calcular; c) proporcionen informació extra sobre les

escales de temps característiques de la dinàmica del flux oceànic; d) són capaces de revelar estructures oceàniques per sota de la resolució nominal del camp de velocitats que és analitzat; i e) Els FSLEs, a més, és especialment apropiat per analitzar transport en àrees tancades.

Malgrat el creixent nombre d'aplicacions dels FSLEs, un anàlisi sistemàtic de moltes de les seves propietats i de la seva eficàcia per diagnosticar propietats de transport oceànic a diferents escales està encara pendent. L'objectiu general d'aquesta tesi s'ha orientat cap a l'estudi dels processos físics i biològics de l'oceà relacionats amb el transport i mescla des del punt de vista Lagrangian. L'estudi ha estat realitzat amb la idea de caracteritzar propietats de transport i estructures coherents a diferents escales, des d'escales costaneres a la planetària.

Després d'una breu introducció i una descripció de la metodologia en els primers capítols, en el Capítol 3 abordem les següents preguntes: Com es propaguen els errors del camp de velocitat en els FSLEs? És vàlida la informació que proporcionen els FSLEs per sota de la resolució espacial del camp de velocitats, o és només un artifici? Com es transformen baix canvis d'escala? Per fer això, calculem els FSLEs a diferents resolucions espacials i analitzem les seves propietats d'escala i la seva resposta a dues fonts d'error diferents, en les dades de velocitat i en la manera en la qual les trajectòries de les partícules són calculades. Per seguir en la línia de les aplicacions oceanogràfiques usem dades numèriques de velocitats de superfície marina de la Mar Mediterrània.

Una vegada que la fiabilitat dels diagnòstics de FSLEs en fluxos oceànics ha estat estudiat centrem la recerca en l'aplicació d'aquesta eina per analitzar propietats de transport marí, des d'una particular àrea costanera fins a l'oceà global. En el Capítol 4, el camp de velocitats d'una capa propera a la superfície obtinguda d'un model oceànic de circulació general ha estat analitzat usant els FSLEs per abordar les següents qüestions: Podem classificar l'oceà en regions amb diferents propietats de transport usant FSLEs? Com és la relació entre descriptores Lagrangians i Eulerians? Podem obtenir la mateixa informació sobre el transport des d'ambdues perspectives? Comencem aquest estudi amb una caracterització de les propietats d'agitació i mescla dels hemisferis Nord i Sud, i després de les principals conques i corrents oceàniques. Després estudiem la relació entre les mitjanes de FSLEs i alguns descriptores Eulerians com l'energia cinètica de remolí i la vorticitat relativa en diferents regions. Aquestes relacions són molt útils a l'hora de caracteritzar la dinàmica de diferents àrees de l'oceà.

El Capítol 5 està dedicat a l'estudi d'estructures turbulentes i al transport en l'entorn costaner de la Badia de Palma, Mallorca, en termes de FSLEs i temps de residència. Podem detectar LCSs de petita escala en fluxos costaners? Són aquestes estructures rellevants per a la dinàmica del fluid en una regió costan-

era? Com podem caracteritzar el transport entre la costa i l'oceà? Per contestar aquestes preguntes investiguem el caràcter de les semi-persistentes LCSs obtingudes dels càlculs. Estudiem l'intercanvi de partícules de fluid entre la Badia de Palma i l'oceà calculant trajectòries de partícules i temps de residència en diferents mesos. Examinem la connexió entre les LCSs i les regions costaneres amb diferents propietats de transport en termes d'escales de temps donats pels temps de residència.

Finalment, en el Capítol 6 ens centrem en la influència que tenen els processos de transport sobre els ecosistemes marins a les zones d'aflorament dels límits orientals de les conques oceàniques. En particular, analitzem els factors físics relacionats amb la productivitat de plàncton en el sistema d'aflorament de Benguela. Estudis recents, basats en dades de teledetecció i en models acoblats, han mostrat que a les zones d'aflorament hi ha una reducció de l'activitat biològica dins de les àrees on hi ha una intensa agitació horitzontal. Per entendre millor aquest fenomen, hem considerat un sistema de fluid oceànic a la zona de Benguela acoblat a un simple model biogeoquímic de tipus Nutrients-Fito-Zooplancton (NPZ). El nostre model aproximat confirma que en el sud de Benguela hi ha una reducció de la producció biològica quan l'activitat de mesoescala augmenta. La advecció horitzontal cap a l'oceà i diferències nord-sud en la taxa de creixement biològic semblen ser els processos dominants implicats.

Resumen

Los procesos de mezcla y transporte horizontal son esenciales para el estudio de la dinámica física, química, y biológica del océano. Una correcta comprensión y un modelaje preciso de estos procesos son relevantes desde el punto de vista teórico, y son cruciales para una variedad de problemas prácticos, como la dinámica del plancton o el control de vertidos contaminantes. En este sentido, los últimos años han visto brotar nuevos e interesantes desarrollos en lo que a la descripción Lagrangiana de fenómenos de transporte y mezcla se refiere, muchos de ellos provenientes del área de la dinámica no-lineal. Estas aproximaciones no tienen como objetivo predecir trayectorias individuales de trazadores, sino localizar estructuras espaciales que son conocidas en la teoría de sistemas dinámicos como estructuras que actúan de esqueleto organizador del flujo en su totalidad (Leong and Ottino, 1989; Wiggins, 1992). Esto se debe principalmente a la capacidad de los diagnósticos Lagrangianos de explorar la variabilidad espacio-temporal del campo de velocidades mediante el seguimiento de trayectorias de partículas de fluido, a diferencia de las Eulerianas las cuales analizan mapas instantáneos de datos. Entre estas técnicas Lagrangianas, una clase con mucho potencial consiste en el cálculo de los exponentes de Lyapunov locales (LLE), los cuales miden la dispersión relativa de partículas transportadas. En particular, están los llamados exponentes de Lyapunov de tamaño finito (FSLEs) donde uno calcula el tiempo que tardan dos trayectorias, inicialmente separadas por un distancia finita, el separarse una distancia finita final más larga.

Los LLEs están atrayendo la atención de la comunidad oceanográfica. Las principales razones de este interés son las siguientes: a) identifican y muestran las estructuras dinámicas del flujo que fuertemente organizan el movimiento del fluido (Estructuras Coherentes Lagrangianas (LCSs)) como vórtices, barreras de transporte, frentes, etc; b) son relativamente fáciles de calcular; c) proporcionan

información extra sobre las escalas de tiempo característicos de la dinámica del flujo oceánico; d) son capaces de revelar estructuras oceánicas por debajo de la resolución nominal del campo de velocidades que es analizado; y e) Los FSLEs son especialmente apropiados para analizar transporte en áreas cerradas.

A pesar del creciente número de aplicaciones de los FSLEs, sigue faltando un análisis sistemático de muchas de sus propiedades y de su eficacia para diagnosticar propiedades de transporte oceánico a diferentes escalas. El objetivo general de esta tesis se ha orientado hacia el estudio de los procesos físicos y biológicos del océano relacionados con el transporte y mezcla desde el punto de vista Lagrangiano. El estudio ha sido realizado con la idea de caracterizar propiedades de transporte y estructuras coherentes en diferentes escalas, desde escalas costeras a la planetaria.

Tras una breve introducción y una descripción de la metodología en los primeros capítulos, en el Capítulo 3 abordamos las siguientes preguntas: ¿Cómo se propagan los errores del campo de velocidad en los FSLEs? ¿Es válida la información que proporcionan los FSLEs por debajo de la resolución espacial del campo de velocidades, o solo un artificio? ¿Cómo se transforman bajo cambios de escala? Para estudiar esto, calculamos los FSLEs a diferentes resoluciones espaciales y analizamos sus propiedades de escala y su respuesta a dos fuentes de error diferentes, en los datos de velocidad y en la manera en la que las trayectorias de las partículas son calculadas. Para seguir en la línea de las aplicaciones oceanográficas utilizamos datos numéricos de velocidades de superficie marina del Mar Mediterráneo.

Una vez que la fiabilidad de los diagnósticos de FSLEs en flujos oceánicos ha sido estudiado, centramos la investigación en la aplicación de esta herramienta para analizar propiedades de transporte marino, desde una particular área costera hasta el océano global. En el Capítulo 4, el campo de velocidades de una capa cercana a la superficie obtenido de un modelo oceánico de circulación general ha sido analizado usando los FSLEs para abordar las siguientes cuestiones: ¿Podemos clasificar el océano en regiones con diferentes propiedades de transporte usando FSLEs? ¿Cómo es la relación entre descriptores Lagrangianos y Eulerianos? ¿Podemos obtener la misma información sobre transporte desde ambas perspectivas? Comenzamos este estudio con una caracterización de las propiedades de agitación y mezcla de los hemisferios Norte y Sur, y después de las principales cuencas y corrientes oceánicas. Después estudiamos la relación entre los promedios de FSLEs y algunos descriptores Eulerianos como la energía cinética de remolino y la vorticidad relativa en diferentes regiones. Estas relaciones son muy útiles a la hora de caracterizar la dinámica de diferentes áreas del océano.

El Capítulo 5 está dedicado al estudio de estructuras turbulentas y al transporte en el área costera de la Bahía de Palma, Isla de Mallorca, en términos de FSLEs y tiempos de residencia. ¿Podemos detectar LCSs de pequeña escala en flujos costeros? ¿Son estas estructuras relevantes para la dinámica del fluido en una región costera? ¿Cómo podemos caracterizar el transporte entre la costa y el océano? Para contestar estas preguntas investigamos el carácter de las semi-persistentes LCSs obtenidas de los cálculos. Estudiamos el intercambio de partículas de fluido entre la Bahía de Palma y el océano calculando trayectorias de partículas y tiempos de residencia en diferentes meses. Examinamos la conexión entre las LCSs y las regiones costeras con diferentes propiedades de transporte en términos de escalas de tiempo dados por los tiempos de residencia.

Finalmente, en el Capítulo 6 nos centramos en la influencia que tienen los procesos de transporte sobre los ecosistemas marinos en las zonas de afloramiento de los límites orientales de las cuencas oceánicas. En particular, analizamos los factores físicos relacionados con la productividad de plancton en el sistema de afloramiento de Benguela. Estudios recientes, basados en datos de teledetección y en modelos acoplados, han mostrado que en las zonas de afloramiento hay una reducción de la actividad biológica en las áreas donde hay más agitación horizontal. Para entender mejor este fenómeno, hemos considerado un sistema de un fluido oceánico en la zona de Benguela acoplado a un simple modelo biogeoquímico de tipo Nutrientes-Fito-Zooplancton (NPZ). Nuestro modelo aproximado confirma que en el sur de Benguela hay una reducción de la producción biológica cuando la actividad de mesoescala aumenta. La advección horizontal hacia el océano y diferencias norte-sur en la tasa de crecimiento biológico parecen ser los procesos dominantes implicados.

Summary

Horizontal transport and mixing processes are central to the study of the physical, chemical, and biological dynamics of the ocean. Correct understanding and precise modelling of them are relevant from a theoretical viewpoint and crucial for a range of practical issues, such as plankton dynamics or the fate of pollutant spills. In this regard, the last few years have seen the appearance of interesting new developments on the Lagrangian description of transport and mixing phenomena, many of them coming from the area of nonlinear dynamics. Such approaches do not aim at predicting individual tracer trajectories, but at locating spatial structures that are known from dynamical systems theory to act as templates for the whole flow (Leong and Ottino, 1989; Wiggins, 1992). This is mainly due to the capacity of the Lagrangian diagnostics to exploit the spatiotemporal variability of the velocity field by following fluid particle trajectories, at difference of Eulerian ones which analyze frozen snapshots of data. Among these Lagrangian techniques, a powerful class consists in the computation of local Lyapunov exponents (LLE) which measure the relative dispersion of transported particles. In particular, there are the so called finite-size Lyapunov exponents (FSLEs) where one computes the time taken by two trajectories, initially separated by a finite distance, to reach a larger final finite distance.

LLEs are attracting the attention of the oceanographic community. The main reasons for this interest are the following: a) they identify and display the dynamical structures in the flow that strongly organizes fluid motion (Lagrangian Coherent Structures (LCSs)) like vortices, barriers to transport, fronts, etc ; b) they are relatively easy to compute; c) they provide extra information on characteristics time-scales for the ocean flow dynamics; d) they are able to reveal oceanic structures below the nominal resolution of the velocity field being analyzed; and e) the FSLEs are specially suited to analyze transport in closed areas.

Despite the growing number of applications of Lyapunov exponents, a systematic analysis of many of their properties and their efficiency in diagnosing ocean transport properties at different scales is still lacking. The objective of this thesis have been centered in the study of physical and biological processes in the ocean related to transport and mixing from the Lagrangian point of view. The study has been made with the idea of characterizing transport properties and coherent structures at different scales, from coastal to planetary scales.

After some introduction and background in the two first chapters, in Chapter 3 we address the following questions: How do errors in the velocity field propagate onto the FSLE? Is the sub-grid information that they provide valid or just an artifact? How do they transform under changes in scale? To do this, we compute the FSLEs at different spatial resolutions and analyze their scaling properties and their response to different sources of error both in the velocity data and in the way that particle trajectories are computed. In order to keep close to the oceanographic applications we use numerical data of the marine surface velocity of the Mediterranean Sea.

Once the reliability of FSLE diagnostics in ocean flows has been studied, we focus in applying this tool to analyze marine transport properties, from a particular coastal area to the global ocean. In Chapter 4, the near-surface velocity field obtained from an ocean general circulation model has been analyzed using FSLEs in order to address the following questions: Can we classify the ocean in regions of different stirring by means of FSLEs? How is the relationship between Lagrangian and Eulerian descriptors? Can we obtain the same transport information from both perspectives? We characterize the stirring properties of Northern and Southern Hemispheres, then the main oceanic basins and currents. We study the relation between averages of FSLE and some Eulerian descriptors such as Eddy Kinetic Energy and vorticity over different regions. These relations are useful to characterize the dynamics of different ocean areas.

Chapter 5 is dedicated to study flow structures and transport in the coastal area of the Bay of Palma, Spain, in terms of FSLE and residence times. Can we detect small coastal LCSs? Are these structures relevant in the flow dynamics of a coastal region? How can we characterize the transport between the coast and the open ocean? We investigate the character of the semi-persistent detected LCSs. Fluid interchange between the Bay of Palma and the open ocean is studied by computing particle trajectories and residence times for different months. We examine the connection between LCSs and regions of different residence times.

Finally, in Chapter 6 we focus on the influence of transport processes on marine ecosystems in prominent Eastern Boundary Upwelling zones. Particularly, we analyze the physical factors which drive the planktonic productivity in the

Benguela upwelling system. Recent studies, both based on remote sensed data and coupled models, showed a reduction of biological productivity due to vigorous horizontal stirring in upwelling areas. In order to better understand this phenomenon, we have considered a system of oceanic flow in the Benguela area coupled with a simple biogeochemical model of Nutrient-Phyto-Zooplankton (NPZ) type. Our modelling approach confirms that in the south Benguela there is a reduction of biological activity when stirring is increased. Two-dimensional offshore advection and north-south differences in the growth rate of phytoplankton seem to be the dominant processes involved.

Contents

Titlepage	i
Contents	xvii
1 Introduction	1
1.1 Scales in the ocean	1
1.2 The turbulent nature of the ocean	3
1.3 Advection, diffusion and mixing	4
1.4 Turbulent coherent structures	6
1.5 Biological response to ocean transport processes	10
1.5.1 Effect of stirring on plankton ecosystems	11
1.5.2 The impact of coherent structures on marine ecosystems	12
1.6 Effect of mesoscale transport in upwelling areas	15
1.7 Plan of the thesis	17
2 Concepts and Tools	19
2.1 Eulerian and Lagrangian descriptions	19
2.2 Limits on the assessment of particle trajectories	20
2.3 Dynamical systems approach	21
2.4 The Non-asymptotic Lyapunov Exponents	25
2.4.1 Finite-Time Lyapunov Exponents (FTLEs)	27
2.4.2 Finite-Size Lyapunov Exponents (FSLEs)	28
2.5 Scale dependence of FSLE	29
2.6 Lagrangian Coherent Structures (LCS) as ridges in the FSLE field	31
2.6.1 LCS properties	32

2.7	Computation of FSLE	33
2.8	Eulerian and Lagrangian diagnosis	34
2.9	Comparison between Eulerian diagnosis and Lagrangian diagnosis from FSLEs	37
2.10	Turbulence and multifractality	38
2.11	Langevin equation and eddy-diffusivity	40
2.12	Velocity Data	42
	2.12.1 Hydrodynamical models	42
	2.12.2 Ocean altimetry	42
2.13	Ocean color	43
3	Reliability of Finite-Size Lyapunov Exponents for the assessment of ocean dynamics	45
3.1	Introduction	45
3.2	Description of the data	47
3.3	Definition and implementation of FSLEs	49
3.4	Effect of sampling scale on FSLEs	49
3.5	Effect of noise on FSLEs	55
3.6	Conclusions	62
3.7	Appendix: Change of resolution of the velocity grid	64
4	Characterization of horizontal transport in the global ocean	67
4.1	Introduction	68
4.2	Data and Methods	69
4.3	Results	73
	4.3.1 Global horizontal stirring from FSLE	73
	4.3.2 Geographical characterization of horizontal stirring	73
	4.3.3 Seasonal characterization of horizontal stirring	78
	4.3.4 Lagrangian-Eulerian relations	80
4.4	Conclusions	85
5	Lagrangian transport in a microtidal coastal area: the Bay of Palma, Spain	87
5.1	Introduction	88
5.2	Data and characteristics of the study region	89
	5.2.1 Area of study	89
	5.2.2 Data	90
5.3	Methodology	91
	5.3.1 LCSs and particle dispersion from FSLE	91
	5.3.2 Escape and residence times	93

5.4	Preliminary Eulerian description	93
5.5	Results	95
5.5.1	Average characterization of stirring	95
5.5.2	Coastal LCSs	96
5.5.3	Transport between the Bay of Palma and the open sea	97
5.5.4	Relation between LCSs and RTs	101
5.5.5	Variability of RT and FSLE	101
5.5.6	Transport at the bottom layer	103
5.6	Conclusions	105
5.7	Appendix: Mixing rise in coastal areas induced by waves	106
6	Effect of transport on plankton dynamics in the Benguela upwelling region	115
6.1	Introduction	116
6.2	Satellite and simulated data	118
6.2.1	Surface velocity fields derived from regional simulations	118
6.2.2	Surface velocity field derived from satellite	118
6.2.3	Ocean color as a proxy for phytoplankton biomass	118
6.3	Methodology	119
6.3.1	Finite-Size Lyapunov Exponents (FSLEs)	119
6.3.2	The Biological model	120
6.3.3	Coupling hydrodynamical and biological models in Benguela	122
6.4	Results and discussion	123
6.4.1	Validation of our simple 2D idealized setting using satellite data	124
6.4.2	Relationship between phytoplankton and horizontal stirring	129
6.4.3	Spatial analysis. What causes the variable biological responses within regions of distinct dynamical properties?	135
6.4.4	Seasonal variability of the bio-physical coupled system	138
6.5	Sensitivity analysis	141
6.5.1	Sensitivity with respect to different spatial resolution of the velocity field	141
6.5.2	Sensitivity with respect to different parameterization of the coastal upwelling of nutrients	144
6.6	Conclusions	146
7	General Conclusions	149
A	Numerical algorithms	153
A.1	Fourth-order Runge-Kutta method	153
A.2	Bilinear interpolation	154

A.3 Heun's algorithm	155
A.4 Semi-Lagrangian numerical algorithm	156
List of publications	159
List of Tables	161
List of Figures	163

Introduction

In a moving fluid, as is the ocean, the flow modifies the spatial distributions of physical, chemical or biological properties (temperature, pollutants, plankton) by transporting and mixing together fluid masses of different properties. Transport and mixing processes affect the evolution of the main currents, which are the responsible of the heat flux of the Earth and thus the global climate. Therefore, these processes are of great importance for understanding the ocean dynamics and thus be able to avoid possible human disasters. This thesis is a contribution to better understanding the oceanic transport and dispersion at a wide range of scales, from a particular coastal basin to the global ocean, and to study how affect these physical features on marine planktonic ecosystems.

The purpose of this introduction is to put into context the thesis. After presenting general characteristics of ocean transport we will explain some particular physical processes of the ocean dynamics occurring at different scales. Then, we will give an overview of the interaction between physical and biochemical processes, followed by the detailed objectives and plan of the thesis.

Scales in the ocean

The ocean can be thought of as complex system in which a large number of different processes (physical, chemical, biological, atmosphere-ocean interactions, etc.) at different spatial and temporal scales interact with each other. A clear schematic representation of the variety of scales associated to ocean processes can be found in the study by Dickey (2003) (see Fig. 1.1). These scales extend

CHAPTER 1. INTRODUCTION

from millimeters to thousands of kilometers and from seconds to century. Due to this variety one of the main difficulties is to deal with the correct spatial and temporal scales associated with the process under study.

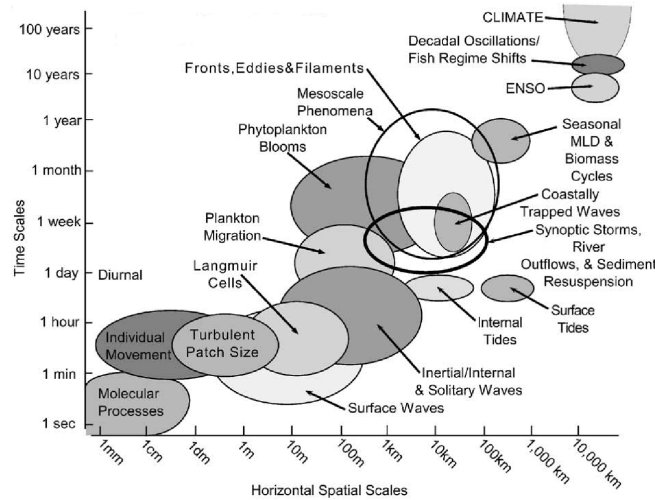


Figure 1.1: Spatial and temporal scales in the ocean and associated processes (from Dickey (2003)).

Approximately, the term large scale (basin scale, planetary scale) is used for scales of the order of 1000 km or larger. The mesoscale covers the range 10-100 km, the submesoscale covers the range 1-10 km, and thus the (sub)-mesoscale the range 1-100 km. In this thesis we are interested in the turbulent transport associated to processes of spatial scales from submesoscale to large scale and time scales from hours to 1 year. We can observe the scales heterogeneity from satellite images of surface temperature over an ocean region (Fig. 1.2). Different structures emerge at each scale iteratively. Within the large scale structure we find mesoscale structures and within these we find submesoscale structures, and so on.

1.2. THE TURBULENT NATURE OF THE OCEAN

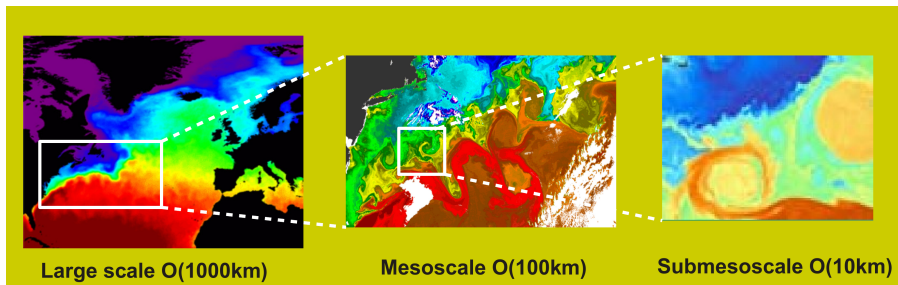


Figure 1.2: Graphical representation of the heterogeneity of ocean scales. The plots are Sea Surface Temperature (SST) images from satellite.

1.2

The turbulent nature of the ocean

The similarities between ocean and turbulent flows, such as non-linear interaction between the large number and range of length and time scales represented in Fig. 1.1 make us consider the ocean as a two-dimensional (2-D) turbulent system. The 2-D is a idealization, since the ocean flows have a 3-D aspect. Nevertheless, the strong stratification and rotation act to suppress motion in the vertical direction. Then, due to the turbulent nature of the ocean flow, ocean processes are interrelated with each other by transferring energy between different scales. Although it is obvious that large scale processes dissipate energy to the smallest scales by direct energy cascades, similar transfers of energy occur in the opposite direction, since inverse energy cascades from small to large scales exist. Thus, understanding large scale phenomena requires a comprehension of small scale processes and how mesoscale and submesoscale features coexist and interact (Klein and Lapeyre, 2009).

At large scale, atmospheric-ocean interaction and temperature and salinity latitudinal gradients induce large ocean flows characterized by their ability to transport heat, momentum and material quantities large distance. The entire climate system can be seen as a heat engine, and the solar energy absorbed at the tropics is transported, by the ocean currents and the global atmospheric circulation, toward the poles (for instance the Gulf Stream is responsible to heat up the North of Europe). Long wavelength Rossby waves (waves depending on the Coriolis force as a restoring force) propagate rapidly westwards, transmitting energy to the west. Short wavelength Rossby waves propagate very slowly eastward. This is because the Earth only spins in one direction. At a western

CHAPTER 1. INTRODUCTION

ocean boundary (continental east coast) the long Rossby waves reflect as short Rossby waves which means that energy accumulates along western boundary. This leads to the so-called western intensification of a western boundary current (Stommel, 1948). This energy goes into the main circulation and thus generates strong currents in the western sides of the ocean basins. Altimetric measurement of sea surface height (SSH) reveal that westward propagation is ubiquitous with characteristics similar to linear Rossby waves (Chelton and Schlax, 1997).

Mesoscale fronts and eddies are associated with large-scale motions from several examples. Mesoscale eddies can be produced from baroclinic instabilities. A baroclinic unstable wave can develop when horizontal density gradients are present. Meandering currents are observed in those parts of the ocean where strong density gradients are strongest. This is the case of the western boundary currents, which produce large intense fronts and eddies, producing persistent eddy circulations (see Fig. 1.2). The association between mesoscale and submesoscale processes is also evident by the formation of thin filament-like structures. The mesoscale eddies twist and fold producing smaller eddies or submesoscale filaments. This results in a cascade of energy to smaller scales. Since the ocean is considered a 2D turbulent flow, small eddies can interact and produce larger eddies, resulting in a cascade of energy to larger scales.

We have seen that processes at different scales interact with each other producing a complex network of ocean processes. Thus we think that is important to describe not only the individual processes but the ocean dynamics as a whole.

1.3

Advection, diffusion and mixing

Advection is the dominant transport mechanism in a moving fluid that consists in the transport of something from one region to another induced by the motion of the flow. Thus, this is totally associated to the velocity field (\mathbf{v}) of the flow. The particles or properties of the flow can be described by a concentration field $C(x, t)$. If we consider that the particles are passive and inert, we have that the evolution of C is determined by the conservation equation,

$$\frac{\partial C}{\partial t} + \nabla \cdot \mathbf{J} = S(x, t), \quad (1.1)$$

1.3. ADVECTION, DIFFUSION AND MIXING

where $S(x,y)$ is the spatial distribution of source-sinks term and J the flux. In this case the flux is given by the advection, then $J=\mathbf{v}C$, and Eq. 1.1 can be written as follows,

$$\frac{\partial C}{\partial t} + \nabla \cdot \mathbf{v}C = S(\mathbf{x}, t), \quad (1.2)$$

and finally, for an incompressible flow ($\nabla \cdot \mathbf{v} = 0$) and in the absence of source and sinks in the system, we obtain the equation:

$$\frac{\partial C}{\partial t} + \mathbf{v} \cdot \nabla C = 0. \quad (1.3)$$

Diffusion is the transport associated to irregular motions, at molecular scales. Diffusion has two primary properties: it is random in nature, and transport is from regions of high concentration to low concentration, with an equilibrium state of uniform concentration. A well-known example to understand this properties is the diffusion of perfume in an empty room. In the homogenization process the regions of high concentration tend to spread into regions of low concentration under the action of diffusion. Then, if we assume that the diffusive flux is proportional to the local concentration gradient (Fick's law),

$$\mathbf{J}_D = -D\nabla C, \quad (1.4)$$

and using the conservation equation Eq. 1.1 in the absence of sinks and sources, the evolution of the concentration field $C(x, t)$ under the effect of the diffusion is given by the diffusion equation:

$$\frac{\partial C}{\partial t} = \nabla \cdot (D\nabla C), \quad (1.5)$$

where D is the diffusion coefficient, which in the simplest case is assumed to be constant, independent of the concentration and uniform in space,

$$\frac{\partial C}{\partial t} = D\nabla^2 C. \quad (1.6)$$

In this case typical diffusion coefficients of solute molecules in liquids are $D \approx 10^{-9}m^2/s$. This means that about 10 minutes are needed for the molecular diffusion to disperse concentrations over a distance of the order of one

CHAPTER 1. INTRODUCTION

millimeter and half a day to disperse to centimeter scales. Thus molecular diffusion alone is a very inefficient process at any macroscopic scale, although it plays an important role at biological cell dimensions and below, down to molecular scales.

Mixing is a transport process responsible for reducing the inhomogeneities in the properties of a fluid medium. This homogenization process in a turbulent flow can be described as the combination of advection and diffusion, in which the value of the concentration gradient averaged over the domain plays a key role.

Stirring by advection produces the stretching of the fluid producing strong gradients in the concentration field enhancing the effect of the diffusion and then mixing. Indeed, in the case of turbulent flows, with high stirring, the mixing processes are strongly related to stirring. The interplay of stirring and mixing is important in the ocean for temperature, salinity, chlorophyll and other natural tracer as well as introduced material.

1.4

Turbulent coherent structures

Coherent structures are the materialization of our desire to find order in apparent disorder of the turbulent flows. There is not a precise definition of coherent structures, but some approximations. For instance a coherent structure can be defined as a structure of some property present in the flow for a relatively long time. An example of coherent structure is the vortex. In a two-dimensional turbulent flow, there are many structures that will look like vortices but only for a very short period of time. They will have a rotational velocity and will look kind of circular, but if they do not last more than a dynamical time, then they are transient, non-coherent. In another approximation, a coherent structure is a region of flow where the two point correlations do not have the same behavior as in fully developed turbulence. The visualization of coherent structures depends on the framework used in the description of the flow, Lagrangian and Eulerian. This will be explained with more details in the next chapter. In the following we will explain the dynamical mechanisms that produce the coherent structures in the ocean and their implications to transport and mixing.

We focus the study in eddies, filaments and fronts. These structures are observed from high-resolution images of tracer and physical properties at the ocean upper layer such as sea surface temperature (SST), chlorophyll patterns, and from high-resolution ships surveys of heat and salinity (McGillicuddy et al., 1998; Abraham

1.4. TURBULENT COHERENT STRUCTURES

and Bowen, 2002; Martin et al., 2002; Lévy et al., 2012). The sea color images in Fig. 1.3 show different dynamical structures formed in the ocean.

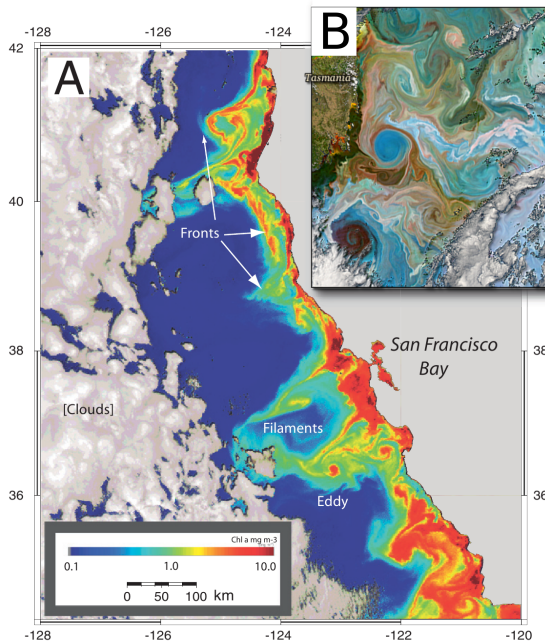


Figure 1.3: A: Ocean chlorophyll concentrations of the coastal California from SeaWiFS (Sea-viewing Wide Field-of-view Sensor) with some typical physical features annotated. This map shows the complexity of the interactions between phytoplankton and physics in the surface ocean (from Kudela (2012)). B: Ocean color image of the ocean east of Tasmanian in December, 2004.

Eddies

Coherent vortices, or eddies, are ubiquitous features of localized patches of strong vorticity that have lifetimes ranging from several weeks to more than one year and typical radius of tens/hundreds of km. These structures are generated through barotropic and baroclinic instabilities of the mean currents at mesoscale and account for a large portion of the ocean turbulent kinetic energy (Stammer, 1997; McWilliams, 1985). Coherent vortices significantly affect the dynamics and the statistical properties of ocean flows, with important consequences on

CHAPTER 1. INTRODUCTION

transport processes. Among these statistical properties one can find that when the vortices are intense and have sharp profiles the Probability Distribution Function (PDF) of the velocity field has non-Gaussian tails. These non-Gaussian distributions are related to the turbulent stirring and the exponential stretching of ocean flows. As a global characteristic of the ocean, the similarity in velocity PDFs between float data, ocean general circulation models, simplified models, suggest that the non-Gaussian nature of the velocity PDFs is due to the vortex component of ocean mesoscale turbulence (Pasquero et al., 2002; Lacasce, 2008).

The core and the periphery of these structures act in a very different way on the dispersion of fluid parcels. The core of the eddies is associated with areas of regular (non-chaotic) motion that trap particles for times comparable with the eddy lifetime (Babiano et al., 1994), and therefore that structures are characterized by a strong impermeability of particle fluxes (Provenzale, 1999). Particles can eventually move from inside to outside of an eddy or viceversa only when the eddy is dissipated, as the deformation of an eddy due to the interaction with jets, topography, with a nearby eddy, or the formation of a filament. Therefore, under some conditions eddy cores retain water parcels from possible mixing, for timescales of weeks/months, and sometimes even longer (Bracco et al., 2000; Pasquero et al., 2004; Perruche et al., 2010). At their peripheries, where strain prevails over vorticity, eddies enhance water mixing. In this case, tracer anomalies are redistributed in the eddy field in the form of filaments and become eventually mixed with the ambient waters on relatively faster timescales (days to weeks).

The topological description of eddies can be obtained from both Eulerian and Lagrangian perspectives. In the Eulerian it is used the Okubo-Weiss criteria in which the difference between the relative vorticity and the strain rate define the character of the eddy. Chelton et al. (2011) established that when the ratio of the rotational fluid speed U to the translation speed c of the feature is larger than one ($U/c > 1$), the feature is nonlinear, and the fluid is trapped within the eddy and transported along the eddy trajectory, which allows it to maintain a coherent structure as it propagates (Early et al., 2011). In the Lagrangian perspective it is used the Lyapunov exponents in which high and low values of particle dispersion define the intensity and shape of the eddy structure. This will be described in more detail in section 2.8.

Filaments

In contrast to the sea of eddies observed at the mesoscale, high resolution observations show elongated filaments as the predominant feature at the submesoscale. The size of these structures is about 1 to 50 km wide, with much longer lengths (100 km), and are extended vertically bellow the mixed layer. The time

1.4. TURBULENT COHERENT STRUCTURES

scale associated to filaments is of the order of days/weeks. The filament formation is due, mainly, to the interaction of mesoscale eddies or between fronts and eddies, that generates regions of intense stretching and small-scale instabilities (Legal et al., 2007). Thus, the spatial variability of submesoscale structures are related to the variability of the strain and rotation fields (Hua et al., 1998; Lapeyre et al., 1999).

Filaments affect different processes of the ocean dynamics. Horizontally, the elongation of water masses in thin structures intensifies local gradients, greatly enhancing the dispersion and mixing (Lapeyre and Klein, 2006; Pasquero et al., 2001). Other can act as dynamical barriers or can reinforce the coherence of mesoscale eddies (Joseph and Legras, 2002; Koh and Legras, 2002). Through lateral stirring, filaments disperse tracers like pollutants, nutrient, phytoplankton or zooplankton, affecting the plankton pattern formation (Abraham, 1998; Abraham et al., 2000; López et al., 2001; Martin, 2003; Hernández-García et al., 2003; Lehan et al., 2007), as well as the fate of contaminants (Lekien et al., 2005). They affect the low frequency variability of the ocean dynamics by redistributing heat and salinity anomalies. When they transport density anomalies, filaments are able to create intense cells of very strong vertical velocities (several tens of meters per day), exchanging material between different layers (Legal et al., 2007).

For all these reasons, filament dynamics is of great importance for understanding the ocean dynamics. Nevertheless, owing to the relative scarcity of high resolution observational data and the very high cost of submesoscale-resolving circulation models, the filamental dynamics remains still unclear. For instance, to survey only one filament in situ it is needed to sample during one month a region of 100 km at a ~ 1 km and ~ 1 day of resolution. Which is obviously impossible to achieve for global or even regional information about filaments. On the other hand, high resolution SST and ocean color images are not reliable since they are highly affected by clouds. Altimetry is not affected by clouds, but its spatial resolution is not enough.

However, some methods have been recently developed in order to overcome this limitation. These methods are based on extract filament information indirectly from both the spatial and the temporal variability of coarse velocity fields (Boffetta et al., 2001), such as geostrophic velocities derivated from altimetry or from ocean general circulations models. One of these methods is the Lyapunov exponent calculation (Aurell et al., 1997; d'Ovidio et al., 2004; Haller and Yuan, 2000), which will be explained with more details in section 2.4 and section 2.9. The technique is based on the observation that the ocean filaments are often the consequence of a tracer being stirred by a relatively larger structure of the velocity field.

CHAPTER 1. INTRODUCTION

Fronts

Fronts are narrow regions in the ocean characterized by high density gradients. A front is a interface between warm and cold masses of water or change of current direction. The surface fronts produce energetic mesoscale and submesoscale activity. These structures usually produce alternating zones of downwelling and upwelling flow. Owing to its associated intense vertical motions they play an important role in the vertical transport of nutrients or plankton, affecting strongly on the biological production. Characteristic motions have been detected on scales that range from few (tidal flow) to hundreds (western boundary currents) of kilometers laterally and 1 to 10^3 m in depth, and persist from a few hours to virtual permanence (Owen, 1981).

Such motions can be determined by the presence of topographic features such as coastlines, islands, etc. and may also be controlled by dynamic features such as atmospheric forcing and ocean current confluence, or other flow instabilities. Fronts of the dynamic type occur anywhere in the sea, whereas the topographic type occur most frequently along continental margins and in island wakes.

Submesoscale fronts arise at scales just smaller than the mesoscale: a horizontal scale of $O(1-10)$ km, a vertical scale of $O(100)$ m, and a time scale of $O(1)$ day. Submesoscale fronts are formed through advective interactions involving mesoscale currents. Submesoscale fronts are distinct from the filaments by mesoscale stirring, because they are characterized by density jumps and sharp velocity jets.

1.5

Biological response to ocean transport processes

The plankton community represents roughly half of the biological production (PP) on the planet and supports almost all marine life. It also plays a key role in the carbon cycle of the Earth. The carbon is fixed by phytoplankton through photosynthesis at the surface. Phytoplankton need nutrients and light for growth and reproduction. Thus, the oceanic layer where photosynthesis can take place is the surface sunlit layer called euphotic zone (defined by more than 1% of incoming light). When the conditions are favorable, phytoplankton population can growth rapidly. This phenomenon is referred as blooms. Most of the phytoplankton is consumed by zooplankton at the surface, and a part of its biomass is regenerated in nutrients at the euphotic layer which is used for another round of production (Regenerated Production). The fraction of primary

1.5. BIOLOGICAL RESPONSE TO OCEAN TRANSPORT PROCESSES

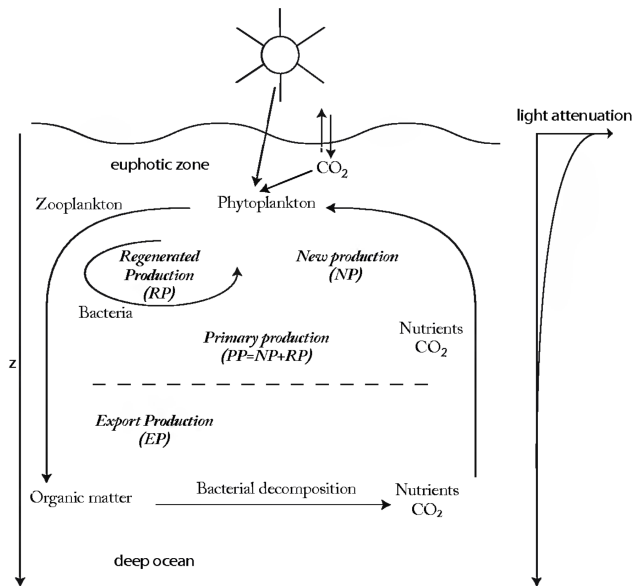


Figure 1.4: Schematic representation of the biological pump in the ocean, where the planktonic ecosystems in the upper ocean play a key role in the carbon cycle (from Lévy (2008)).

production that reaches the deep sea (below the euphotic layer) in form of dead cells and detritus or sometime by downwelling or mixing, is named Export Production. Most of the Export Production is regenerated into inorganic form (nutrients and carbon) by bacteria, and this inorganic material is upwelling to the euphotic layer that is used in the New Production. This collective action is so-called biological pump (see Fig. 1.4)

1.5.1 Effect of stirring on plankton ecosystems

Stirring effects on chemical reactions in fluid media have been well reported with consequences for reactive flows (Neufeld and Hernández-García, 2009). Owing to the similarity between chemical reactions and marine ecosystems, it is expected that stirring effects are also relevant in the distribution and production of plankton populations.

CHAPTER 1. INTRODUCTION

Using a modeled turbulent flow coupled to a plankton model, Abraham (1998) showed that the patchiness in such systems is primarily due to the interplay between advection and the local population dynamics. Indeed in the experiment by Abraham et al. (2000), the authors observed by satellite images the stretching of the patch of iron-fertilized phytoplankton into a long filament. At the same time López et al. (2001); Hernández-García et al. (2003) showed that the biological concentrations can be smoothly or filamentary distributed (multifractal distributions) depending on the strength of the stirring of the flow with respect to that of the biological reaction. The width of individual filaments is controlled by the ratio of the stirring rate to the reaction rate (Neufeld et al., 1999; Martin, 2000). The faster the stirring is, the more irregular is the pattern. Thus, the key parameter of the interplay between stirring and population dynamics is the ratio of the characteristics timescales corresponding to the biological and physical transport processes (Neufeld et al., 1999, 2000; López et al., 2001; Hernández-García et al., 2002, 2003; Martin, 2003; Neufeld, 2012).

Stirring also affects the production of plankton. In the context of excitable populations, the study by Neufeld et al. (2002); Hernández-García and López (2004) shows that strong stirring may suppress the development of plankton blooms by quickly diluting the plankton density. The particular systems studied by Sandulescu et al. (2007); McKiver et al. (2009); Neufeld (2012) show that the existence of a bloom is sensitive to the ratio of biological and hydrodynamical time scales. When the flow stirring rate is small relative to the growth rate of phytoplankton the system is within the bi-stable regime, where both high and low carrying capacity values exist, and hence there are blooms. However, beyond a certain flow stirring rate (relative to the phytoplankton growth rate) the system undergoes a transition to the single equilibrium case, with a uniform low plankton concentration. Increasing stirring reduces the effective carrying capacity of the environment.

1.5.2 The impact of coherent structures on marine ecosystems

In many cases, plankton can be considered passive particles, so ocean current advection has a strong effect on their production and spatial distribution in several ways. Primarily, the flow transports and disperse the main biological components, such as phytoplankton, zooplankton, bacteria, dissolved and particulate organic matter. Secondly, vertical movements can displace nutrient or phytoplankton within (or out) the euphotic layer and thus modulating the rates of the biological dynamics, i.e. phytoplankton growth rate. Also, depending on the encounter rate between nutrients and phytoplankton or phytoplankton and zooplankton their corresponding rate of growth can be affected. The physical

1.5. BIOLOGICAL RESPONSE TO OCEAN TRANSPORT PROCESSES

mechanisms that affect the marine ecosystems occur over a large range of spatial and temporal scales.

On the planetary scales, and for timescales beyond the year, the transport of nutrients is controlled by the thermohaline and by the wind-driven circulations. Westward propagation associated to Rossby waves is also evident in chlorophyll data derived from satellite measurements of ocean color, although this is due to nonlinear rotating mesoscale coherent structures, eddies (Chelton et al., 2011).

At basin scale the production pattern is directly related with the vertical Ekman pumping. This transport is produced by the constant wind blowing along one direction combined with the Coriolis forc. The displacement of surface water mass produce a vertical movement of water, producing the upwelling of rich-nutrients water to the euphotic layer and thereby encourages phytoplankton growth. This is confirmed by satellite observations. Fig. 1.5 shows a global image of the ocean color, related to phytoplankton, from SeaWiFS. The ocean can be classified in different biogeochemical provinces. The high concentrations of chlorophyll are located in regions of upwelling (eastern boundary currents, equator and subpolar gyres) and minimal in regions of downwelling (in the center of subtropical gyres).

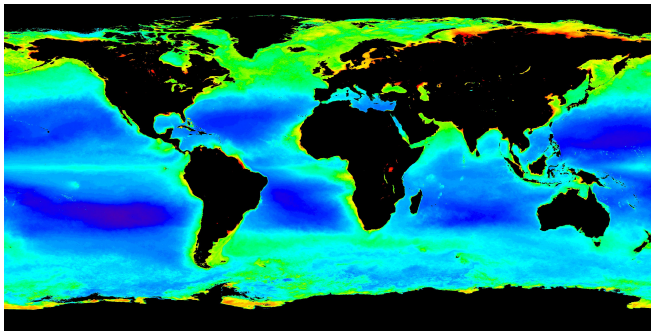


Figure 1.5: Global view of chlorophyll distribution from SeaWiFS sensor data generated by the NASA. The image corresponds to one year average. The blue color indicates poor chlorophyll concentrations (i.e. oligotrophic gyres), whereas green to red indicate high chlorophyll concentrations (i.e. eastern boundary upwelling systems, equatorial upwelling, high latitude spring bloom...).

At mesoscale, frontal and eddie circulations can occur at any depth and affect populations of organism at all trophic levels, from planktonic to top predator (Oschlies and Garçon, 1998; Mahadevan and Archer, 2000; Tew Kai et al., 2009).

CHAPTER 1. INTRODUCTION

Fig. 1.3 shows a clear association of plankton variability with mesoscale flow features such as fronts, eddies and filaments. The eddies have two different natures, can increase or reduce the biological production. On one hand, in the biological increasing by eddies there are two mechanism related with the supply of nutrients into the euphotic layer by the deflection of the isopycnal: the *eddy-pumping mechanism* associated to vertical transport (McGillicuddy et al., 1998), and the stretching of water column associated to horizontal transport (Lévy, 2008). These eddies, as cyclonic as anticyclonic, can be formed by baroclinic instabilities of a density fronts in the oligotrophic gyres, and thus can be responsible of the episodic blooms produced in such poor-nutrients regions (Oschlies and Garçon, 1998; Oschlies, 2002a,b). In this way, mesoscale eddies could be the dominant agents of nutrient transport in the open ocean.

On the other hand, the works by Rossi et al. (2008, 2009); Gruber et al. (2011) show that eddies can suppress phytoplankton productivity in the eastern boundary upwelling, and Williams (2011) propose that the reduction effect of plankton by eddies also occurs in other upwelling areas, such as the Southern Ocean. This will be explain later. Other interpretation, given by Lathuiliere et al. (2011), who used a very simple analytical model to show that the effect of mesoscale activity on plankton production depend on the strength of the large-scale upwelling. In weak upwelling conditions, phytoplankton abundance increases with the intensity of mesoscale turbulence. In contrast, when the upwelling is stronger than a critical value, phytoplankton abundance decreased due to the intensification of mesoscale turbulence. In this case, the governing process is downward export of phytoplankton below the euphotic layer.

In the last years, there are growing evidences that the upper few hundred meters of the oceans are dominated by submesoscale circulations at fronts (Klein and Lapeyre, 2009), and this circulation is important because they can regulate the exchange of properties between the euphotic layer and the ocean interior and thereby the biological production (Lévy et al., 2012). Some preliminary modeling studies to explore the vertical advection at smaller scales (Oschlies and Garçon, 1998; Mahadevan and Archer, 2000; Garçon et al., 2001) suggest that decreasing the resolution of the grid from 10km to 40km can result in errors of 30% in the estimation of PP. Furthermore, some simulations at even higher resolution (2 km) show that the incorrect representation of submesoscale can result in even larger errors, up to 50% (Lévy et al., 2001). This significant increase is mainly due to the resolution of intense vertical velocities, captured within filaments (Klein et al., 1998). In general, the regional flux of nutrients due to submesoscale vertical advection depends on how often and how strong is the vertical circulation distribution and on the rate of the exportation of nutrients in upwelling regions by horizontal advection (Martin, 2003; Pasquero et al., 2005). An important

1.6. EFFECT OF MESOSCALE TRANSPORT IN UPWELLING AREAS

difference between submesoscale motions and mesoscale eddies in the biological production lies in the time scales associated to both processes. Though the vertical velocities associated with mesoscale eddies are much smaller than the submesoscale ones, the residence time of nutrient in the euphotic layer is longer for mesoscale eddies than for submesoscale fronts, allowing phytoplankton to uptake nutrients during more time (McGillicuddy et al., 2007).

Strongly non-uniform chaotic mixing was shown to promote coexistence of competing species by distributing them along complex manifolds. Alternatively, the coherent structures characteristics to two-dimensional turbulence, like vortices, were shown to contribute to the survival of species with lower fitness. This is supported by recent analysis of satellite data indicating the formation of fluid dynamical niches producing localized transient patches of blooms of different species, which contributes to the maintenance of planktonic biodiversity (d'Ovidio et al., 2010). On another hand, the influence of structures generated by Lyapunov exponents also influence on top marine predators. Trajectories of frigatebirds on top of ridges of Lyapunov structures were found in Tew Kai et al. (2009).

1.6

Effect of mesoscale transport in upwelling areas

The Eastern Boundary Upwelling Systems (EBUS) are some of the most productive marine ecosystems of the world oceans. Despite representing less than 1% of the world ocean area, their primary production accounts for about 10% of the oceanic new production (Mackas et al., 2006). EBUSs are characterized by a high abundance of a reduced number of small pelagic fish species that support large fisheries and a number of top predator populations. EBUSs also contribute very significantly to gas exchange between the ocean and the atmosphere, particularly CO_2 and N_2O .

The four main EBUS, the Canary, California, Humboldt and Benguela Currents are narrow strips of the ocean that extend latitudinally over several thousands of kilometers and longitudinally to beyond the continental shelves whose widths range from 20 to 200 km. They are located on the western margin of the continents (eastern part of the oceans), on both hemispheres. In these regions, intense trade winds combined with the earth's rotation coastal upwelling, bring cold, nutrient-rich water from the deep ocean (of the order of 200 to 300 m) to the surface (see Fig. 1.6). These rich waters reaching the euphotic layer fuel primary production

CHAPTER 1. INTRODUCTION

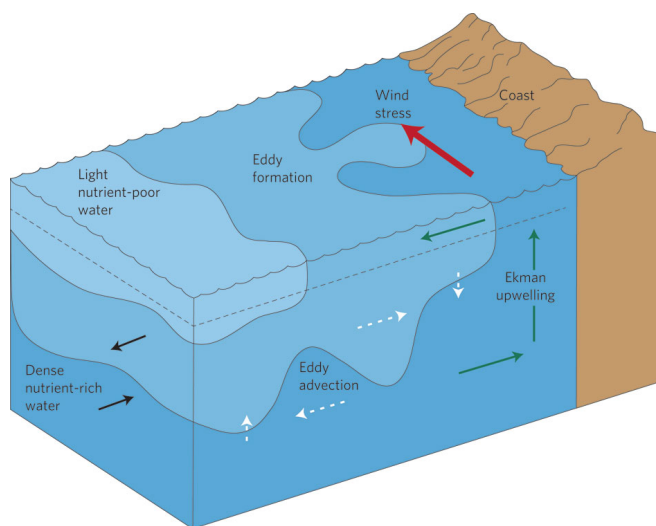


Figure 1.6: A schematic section of coastal upwelling systems and the eddy formation in the southern hemisphere. Equatorial trade winds are blowing almost all year along the coast, that create westward Ekman drift in the upper layer, and divergence in the coast, that is being compensated by upwelling of deep, cold and nutrient-rich waters. Picture from Williams (2011).

(up to two orders of magnitude higher than in other coastal or open ocean regions), which supports a highly productive food web.

In the past two decades, several multidisciplinary approaches have studied physical and biological processes in these highly dynamic boundary regions (Brink and Cowles, 1991; Barton E. et al., 1998) and more recently (Mackas et al., 2006; Correa-Ramirez et al., 2007; Rossi et al., 2009). It has been shown that (sub)-mesoscale processes are ubiquitous features of these areas, related to the complex coastal circulation and its instabilities, as well as coastline irregularities (Lévy, 2008). This strong (sub)-mesoscale variability also modulates the structure and dynamics of ecosystems. For instance Aristegui et al. (1997) studied the interaction between the Canary island archipelago and the coastal upwelling, showing that both systems present numerous mesoscale structures that strongly interact and influence the biology.

A few academic modelling studies also reported a strong bio-physical interactions in upwelling areas. Pasquero et al. (2005) studied the dependence of PP on

1.7. PLAN OF THE THESIS

the spatial and temporal variability of the nutrient flux. Sandulescu et al. (2007, 2008) studied the planktonic biological activity in the wake of an island which is close to an upwelling region. They showed that the interplay between wake structures and biological growth leads to plankton blooms inside mesoscale hydrodynamic vortices that act as incubators of PP. One of the first high resolution coupled modelling studies of an upwelling area was performed by Koné et al. (2005) over the Benguela area and one year later by Gruber et al. (2006) over the California system. Among other findings, they globally stressed out the importance of the 3-D nature of circulation and mixing in coastal upwelling systems, that strongly influence the biological modelled components.

More recently, Rossi et al. (2008, 2009) from satellite observations, studied the effect of the mesoscale turbulence on the surface phytoplankton distributions. They used the Lyapunov exponents to quantify the mesoscale turbulence of the flow derived from altimetry data, and chlorophyll-a from SeaWiFS data as a proxy of phytoplankton concentration. They observed an anti-correlation between both biological and physical quantities; more mixing less plankton production. Using satellite-based measurements of chlorophyll and eddy kinetic energy, together with model simulations, Gruber et al. (2011) showed that eddies reduce productivity in eastern boundary upwelling zones. Eddies form and provide an opposing circulation (white dashed arrows in Fig. 1.6) to that of the wind blowing along the coast. The overall effect of the winds and eddies is to provide a nutrient pathway (black arrows) along density surface from the coast to the open ocean. The nutrients transfer might support productivity in adjacent nutrient-poor environments (Williams, 2011). The findings of Gruber et al. (2011) might also be applicable to the upwelling waters off Antarctica (Williams, 2011).

1.7

Plan of the thesis

Although the importance of turbulent coherent structures on transport and mixing has been widely studied some properties and applications of this structures in ocean flows from the Lagrangian approach are still poorly understood. The aim of this thesis is to study the reliability of Lagrangian Coherent Structures given by Lyapunov exponents and the description of global and coastal properties of transport and mixing and their relation with other dynamical quantities and with plankton productivity in upwelling areas.

The manuscript is organized as follow:

CHAPTER 1. INTRODUCTION

After this general introduction **Chapter 2** presents a brief description of the methodology, including tools and relevant concepts that have been used through the thesis. Lagrangian techniques from the dynamical systems approach, comparison between Eulerian and Lagrangian diagnosis, multifractality, eddy-diffusion are introduced.

Chapter 3 aims at studying scale properties and robustness of Lagrangian diagnosis from Finite Size Lyapunov Exponents when these are computed in surface marine flows.

In **Chapter 4** regional and seasonal characterization of stirring in the surface global ocean is studied by means of FSLEs. We investigated the relationship of the eddy kinetic energy and vorticity with FSLE in order to analyze the Eulerian-Lagrangian relation of dispersion.

To complete the study of lagrangian transport at a variety of scales, we applied different Lagrangian quantities such as FSLE, residence times and escape rate to the coastal area of the Bay of Palma in **Chapter 5**. We are interested in the description of particular LCSs and its relation with residence times in semi-enclosed areas and for different seasonal months.

Chapter 6 is devoted to present the effect of stirring in the evolution of a plankton ecosystem in the Benguela upwelling region. We study possible mechanisms drive the reduction of plankton production in this region.

Through the thesis we have preserved the chapters to be self-contained. In this way the reader can understand each chapter independently of the others.

Concepts and Tools

In this chapter we introduce the concepts and tools, which will help us to understand the global geometry of fluid flows, and will allow a quantitative analysis of transport and mixing in oceanic process.

2.1

Eulerian and Lagrangian descriptions

The description of fluid motion can be addressed following two different ways. One can deal at any time with velocity, pressure and density fields at any spatial point in the fluid, or either, one deals with the trajectory of each fluid particle. The first approach is usually called *Eulerian* and the second one *Lagrangian*. In principle both are equivalent, and if we denote by $\mathbf{v}(\mathbf{x},t)$ the Eulerian velocity field, which tells us the value of the fluid velocity at any space-time point (\mathbf{x},t) , then the motion of a fluid particle with initial localization $\mathbf{x}(0)$ is given by

$$\frac{d\mathbf{x}}{dt} = \mathbf{u}(t) = \mathbf{v}(\mathbf{x}, t). \quad (2.1)$$

(2.2)

This expression establishes the physical connection between the Eulerian and Lagrangian description. It clearly reads that when a particular fluid particle is known to be at a specific space-time point, its Lagrangian velocity \mathbf{u} must be equal to the Eulerian field value at that space-time point. As a side note, through this chapter we will try to denote vector valued quantities by boldfaced letters.

Limits on the assessment of particle trajectories

The simple equation 2.1 presents difficulties in establishing the relationship between Lagrangian trajectories and the underlying flow field, when it is applied to real systems, such as ocean flows. First, it is too complicated to measure the velocity field, $v(x,t)$, with the necessary accuracy to determine all the scales involved in the ocean flow. This is because the ocean flow presents a large number of degrees of freedom and thus a large range of scales, due to its turbulent character. In the case of a 3-D turbulent flow, the degrees of freedom can be estimated by the 9/4th power of the Reynolds number, $R = \frac{lv_l}{\nu}$ (Frisch, 1995), where v_l is a characteristic velocity, l is a characteristic length describing the flow, and ν is the kinematic viscosity. For typical values in the open ocean ($v_l=0.1\text{m/s}$, $l = 10^6\text{m}$, $\nu = 10^{-6}\text{m}^2/\text{s}$) we obtain that $R = 10^{11}$ (Stewart, 2008), and the degrees of freedom is $R^{9/4} \approx O(10^{24})$. This is the minimum number of spatial sampling points per time needed to describe the ocean flow accurately. Clearly this is a very large number in the context of the present observing systems. These degrees of freedom are reduced in 2-D turbulent flows, as is the case of rotating and stratified flows. Also, in many cases, the ocean flow can be dominated by turbulent coherent structures, which contain the most kinetic energy for a long time. Although this implies a reduction in the degrees of freedom, the presence of coherent structures does not always make easier the prediction of particle trajectories since their fundamental nature remains not well understood. In particular, the time variability of these structures produces chaotic Lagrangian trajectories. In a chaotic flow trajectories with intimate initial conditions follow a completely different history, enhancing the difficulty in transport prediction (Aref, 1984)

In order to overcome this Lagrangian transport problem in ocean flows, some methods have been developed. One of them, is a statistical approach named Lagrangian Stochastic Model, in which the Lagrangian velocity is decomposed into a mean flow component and a stochastic, eddy or subgrid scale component modeled by the Langevin equation (Griffa, 1996)(see section 2.11). In this method the transport due to the sub-grid scale velocity associated with processes not contained in v is parameterized as a diffusive process.

The other method is based on dynamical system concepts, assuming that the time evolution of the Eulerian velocity ($v(x,t)$) is completely known and that transport is mostly controlled by turbulent structures. This approach used the concepts of Lagrangian Coherent Structures given by the unstable and stable manifolds of hyperbolic points.

Dynamical systems approach

A dynamical system of general form is often expressed by

$$\frac{d\mathbf{x}}{dt} = \mathbf{v}(\mathbf{x}, t), \quad (2.3)$$

$$\mathbf{x}(t_0) = \mathbf{x}_0. \quad (2.4)$$

In these equations, t represents time and it is the independent variable, $\mathbf{x}(t)$, represents the state of the system at time t and it is the dependent variable. The vector function $\mathbf{v}(\mathbf{x}, t)$ typically satisfies some level of continuity. As time evolves, solutions of Eqs. (2.3), (2.4) trace out curves, or in dynamical systems terminology, they flow along their trajectory. Numerical solutions of Eqs. (2.3), (2.4) can almost always be found, however such solutions by themselves are not very desirable for general analysis. While the exact solution of Eqs. (2.3), (2.4) would be ideal, unless $\mathbf{v}(\mathbf{x}, t)$ is a linear function of the state \mathbf{x} and independent of time t , and a few other cases, there is no general way to determine the analytic solution of Eqs. (2.3), (2.4).

When \mathbf{v} is independent of time t the system is known as time-independent, or autonomous, and there are a number of standard techniques for analyzing such systems. For instance, the global flow geometry of autonomous systems can often be understood by studying invariant manifolds of the fixed points of Eqs. (2.3), (2.4), in particular stable and unstable manifolds often play a central role. These concepts are described in the following. A fixed point of \mathbf{v} is a point \mathbf{x}^c such that $\mathbf{v}(\mathbf{x}^c) = \mathbf{0}$. The stable manifolds of a fixed point \mathbf{x}^c are all trajectories which asymptote to \mathbf{x}^c when $t \rightarrow \infty$. Similarly, the unstable manifolds of \mathbf{x}^c are all trajectories which asymptote to \mathbf{x}^c when $t \rightarrow -\infty$. The term invariant manifold is the mathematician notion of material curve. This means that the trajectory of any condition starting on the manifold, must remain on the curve. Often, stable and unstable manifolds act as separatrices, which separate distinct regions of motion, making them effective in understanding the flow geometry.

Let us consider the planar, frictionless pendulum to explain these concepts. This setup has a point mass, m , at the end of a weightless rod of length l , as shown in Fig. 2.1. The dynamics is given by the second order equation

$$\frac{d^2\theta}{dt^2} = -mg l \sin \theta(t), \quad (2.5)$$

where \mathbf{g} denotes the acceleration due to gravity. Since any n th-order system is equivalent to a set of first order equations, let us define $x = \theta$ and $y = \dot{\theta}$, which

CHAPTER 2. CONCEPTS AND TOOLS

allows us to write Eq.(2.5) as

$$\dot{y} = -mgl \sin x, \dot{x} = y, \quad (2.6)$$

which places it in the first-order vector form given by Eq.(2.3).

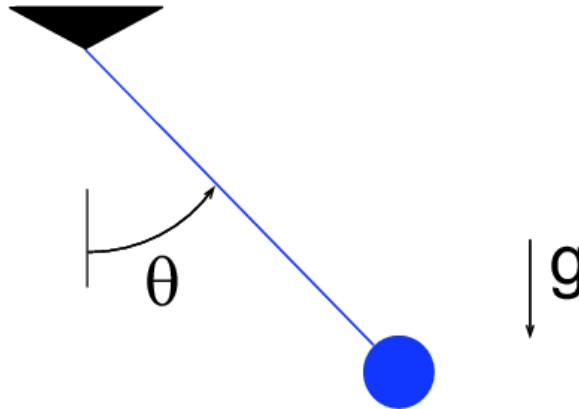


Figure 2.1: Pendulum setup

The phase portrait of the pendulum is shown in Fig. 2.2. Since all values for the positions θ are consistent for values over the interval from $-\pi$ to π , we only show the phase portrait for θ ranging over this interval. If we equate positions in this manner, then technically $\theta = \pi$ is equivalent to $\theta = -\pi$, however they appear as two separate points in the phase portrait, but one can reconcile this by mentally wrapping the phase portrait around a cylinder such that $\theta = \pi$ and $\theta = -\pi$ meet up. The pendulum has fixed points at $(\theta, \dot{\theta}) = (0, 0)$ and $(\theta, \dot{\theta}) = (\pi, 0)$. The fixed point $(\pi, 0)$ is hyperbolic. In a system of differential equations a stationary hyperbolic point is a point such that the eigenvalues of the linearized system have non-zero real part, and is the point where the stable and unstable manifolds intersect. We will see later that hyperbolicity plays an important role in transport. The stable and unstable manifolds of the fixed point $(\pi, 0)$ are shown in blue in Fig. 2.2 and form separatrices. These separatrices divide the flow into regions of distinct dynamics. Inside these separatrices, the pendulum oscillates back and forth (green lines). Outside the separatrices, the pendulum continually spins in one direction (red lines).

The pendulum example allows us to demonstrate how the stable and unstable manifolds can help uncover the global flow geometry of a dynamical system.

2.3. DYNAMICAL SYSTEMS APPROACH

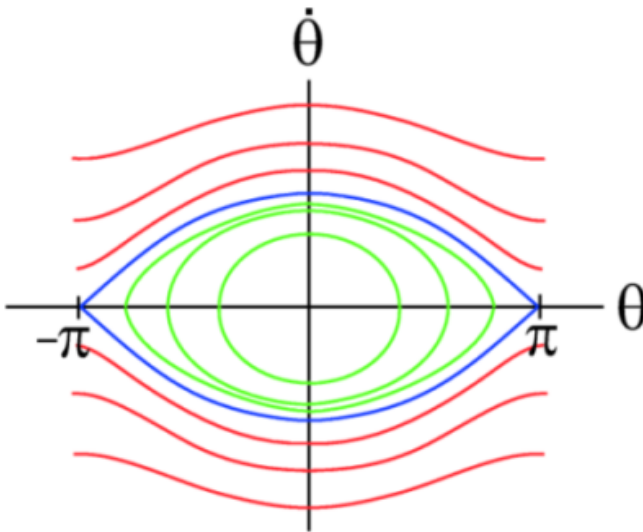


Figure 2.2: Pendulum phase portrait

This is one of the main reasons why numerous researchers have performed different methods for computing, or growing, such manifolds. Many methods are based on growing manifolds from their hyperbolic fixed points. This is possible because for autonomous systems the stable and unstable manifolds of a fixed point are locally tangent to the eigenvectors of the linearized vector field about that point.

The notion of stable and unstable manifolds becomes ambiguous for time-dependent systems, which are the most relevant for us. For example, such systems rarely even have fixed points in the traditional sense, and in addition asymptotic limits for such systems are often meaningless. While there are many academic examples of time-independent dynamical systems, many dynamical systems of practical importance are time-dependent, especially in cases where the dynamical system represents the motion of a fluid.

Time-dependent dynamical systems typically have regions of dynamically distinct behavior which can be thought of as being divided by separatrices. However, for such systems these regions change over time, and hence so do the

CHAPTER 2. CONCEPTS AND TOOLS

separatrices, and one should not read into the analogy between these separatrices and traditional definitions of stable and unstable manifolds too much. The concept of hyperbolic point in a time-independent flow can be generalized to time-dependent flows as hyperbolic fluid particle trajectory. It could be thought of as a moving hyperbolic point. Its stable and unstable manifolds are the time-dependent generalizations of the separatrices of the saddle type hyperbolic point of the steady flow (Mancho et al., 2004). We refer to these separatrices as Lagrangian Coherent Structures (LCS), a name which is common in fluid mechanics. They are material curves, which means that they cannot be crossed by other fluid particle trajectories.

To find separatrices in time-dependent systems, one might take an approach similar to above and look at fixed points of the instantaneous vector field and try to grow these manifolds by seeding near an instantaneous fixed point and advecting the points according to the time-dependent vector field. While this might seem reasonable, separatrices in time-dependent flows usually are not connected to instantaneous fixed points, although they might be located nearby. Instead of trying to directly grow these manifolds, or separatrices, let us try to indirectly obtain them. We will do this by considering the behavior of trajectories near such structures. The indirect method will avoid us the challenging task of having to locate fixed points.

To get us thinking in the right direction, consider a generic hyperbolic point and its associated stable and unstable manifolds, which is depicted in Fig. 2.3. If we integrate two points that are initially on either side of a stable manifold forward in time, then these points will eventually diverge from each other. Likewise, if we started two points on either side of an unstable manifold, then these points would quickly diverge from each other if integrated backward in time. This is why these manifolds are often called separatrices, since they separate trajectories which do qualitatively different things. Therefore we take the viewpoint that, since separatrices divide regions of qualitatively different dynamics, we can perhaps uncover or define such structures by looking at the divergence or stretching between trajectories. To find separatrices that are analogous to stable manifolds, we measure stretching forward in time and to find separatrices that are analogous to unstable manifolds, we measure stretching backward in time (Fig. 2.3). The Local Lyapunov Exponent (Finite-Time Lyapunov Exponent and Finite-Size Lyapunov Exponent) provides the best measures when trying to understand the flow geometry of general time-dependent systems. These measures allows us to deal flow inhomogeneities, revealing areas with intense or weak dispersive regions.

2.4. THE NON-ASYMPTOTIC LYAPUNOV EXPONENTS

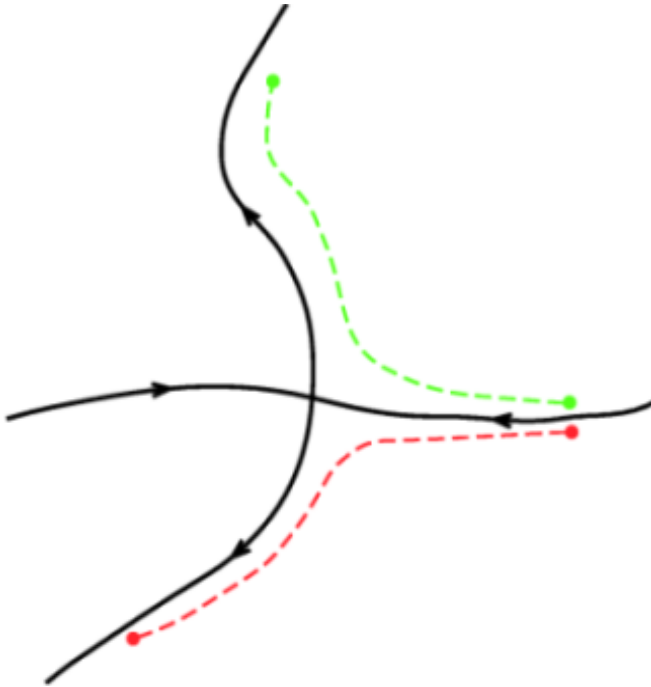


Figure 2.3: Two points on either side of a separatrix will diverge from each other

2.4

The Non-asymptotic Lyapunov Exponents

The possibility of chaotic systems was first introduced by the French mathematician Henri Poincaré in the 1890s in a paper on the stability of the Solar System. Some time later, other scientists found additional chaotic systems and they developed new mathematics and theories (Kovalevska, Hopf, Kolmogorov among others). In 1963, Edward Lorenz described the behavior related to chaotic attractors occurring in dissipative systems, and recognized the unpredictability of chaotic behavior in connection with the numerical solution of an atmospheric model. Chaos is a motion irregular in time, unpredictable in the long term and sensitive to initial conditions, and complex, but ordered, in the phase space: it is associated with a fractal structure. In present day literature a system is said

CHAPTER 2. CONCEPTS AND TOOLS

to be chaotic if small— i.e. infinitesimal— perturbations grow exponentially with time, and this is connected to a positive Lyapunov exponent.

The classical Lyapunov exponent is defined as the exponential rate of separation, averaged over infinite time, of particle trajectories initially separated infinitesimally. Consider $\mathbf{x}(t_0)$ and $\mathbf{x}(t) = \mathbf{x}(t_0) + \delta\mathbf{x}(t)$ as two particle trajectories separated initially by a distance $\delta\mathbf{x}(t_0)$. The global Lyapunov exponent is defined by

$$\lambda = \lim_{t \rightarrow \infty} \lim_{\delta\mathbf{x}(t_0) \rightarrow 0} \frac{1}{t} \ln \frac{|\delta\mathbf{x}(t)|}{|\delta\mathbf{x}(t_0)|} \quad (2.7)$$

This number, λ , is useful for distinguishing among the various types of systems. Negative Lyapunov exponents are characteristic of stable solutions of dissipative or non-conservative systems (the damped harmonic oscillator for instance). Such systems exhibit asymptotic stability (the orbit attracts to a stable fixed point or stable periodic orbit). If λ is positive, the orbit is unstable and chaotic. Nearby points will diverge to any arbitrary separation. All neighborhoods in the phase space will eventually be visited. These points are said to be unstable. For a continuous system, the phase space would be a tangled sea of wavy lines like a pot of spaghetti.

The Lyapunov exponent is quite useful in the study of time-independent dynamical systems. The seminal works of Lyapunov (1992); Oseledec (1968) were very important in laying the theory of Lyapunov exponents for time-independent systems, although the manuscript by Barreira and Pesin (2002) contains a good modern and comprehensive treatment of the subject. However, many dynamical systems of practical importance, especially in the realm of fluids, are time-dependent and only known over a finite interval of time and space. Because of its asymptotic nature, the classical Lyapunov exponent is not suited for analyzing time-dependent dynamical systems or those that are only defined on a finite time-space interval, so its value is quite limited for practical analysis. The infinite-time limit in Eq.(2.7) makes the Lyapunov exponent of limited practical use when dealing with experimental data. The second limit, $\delta\mathbf{x}(t_0) \rightarrow 0$, makes it an even more difficult quantity to evaluate either experimentally or numerically. Whereas the (global) Lyapunov exponent gives a measure for the total predictability of a system, it is sometimes interesting to estimate the local predictability around a point \mathbf{x} in phase space. In this case, a generalization of the Lyapunov exponent, called the Local Lyapunov exponent (LLE), has been proposed to study the growth of noninfinitesimal perturbations (distance between trajectories) in dynamical systems. Recently the concept of a LLE has been applied to study dispersion in turbulent flow fields.

2.4. THE NON-ASYMPTOTIC LYAPUNOV EXPONENTS

The LLE is a scalar value which characterizes the amount of stretching about the trajectory of point \mathbf{x} over time interval. For most flows of practical importance, the LLE varies as a function of space and time. The LLE is not an instantaneous separation rate, but rather measures the average, or integrated, separation between trajectories. This distinction is important because in time-dependent flows, the instantaneous velocity field often is not very revealing about actual trajectories, that is, instantaneous streamlines can quickly diverge from actual particle trajectories. However the LLE accounts for the integrated effect of the flow because it is derived from particle trajectories, and thus is more indicative of the actual transport behavior. We discuss this feature in next sections. Depending on what asymptotic character is eliminated, there are two non-asymptotic Lyapunov exponents: finite-time and finite-size Lyapunov exponents.

2.4.1 Finite-Time Lyapunov Exponents (FTLEs)

Let us derive the expression for the FTLE considering the stretching between two neighboring particles. Consider an arbitrary point \mathbf{x} in phase space at time t_0 advected by the flow a time interval T . Since the flow has a continuous dependence on initial conditions, we know that an arbitrary point near \mathbf{x} at time t_0 will behave similarly as \mathbf{x} when advected in the flow, at least locally in time. However, as time evolves, the distance $\delta\mathbf{x}(t_0)$ between this neighboring point and the point \mathbf{x} will be $\delta\mathbf{x}(t_0 + T)$. We obtain an expression for the finite-time Lyapunov exponent (FTLE) at the initial point \mathbf{x} at time t_0 with a finite integration time T :

$$\lambda_{t_0}^T(\mathbf{x}) = \frac{1}{|T - t_0|} \ln \frac{|\delta\mathbf{x}(t_0 + T)|}{|\delta\mathbf{x}(t_0)|}. \quad (2.8)$$

The FTLE is a function of the initial position \mathbf{x} at time t_0 , but if we vary t_0 , then it is also a function of time. Note that in FTLE the limit condition $T \rightarrow \infty$ is relaxed. We assume $\delta\mathbf{x}(t_0)$ is infinitesimal and the orientation is chosen so that λ is maximal. One can obtain FTLEs using the flow map $\phi_{t_0}^T$, defined as the function that take the initial position \mathbf{x}_0 at time t_0 of any fluid element advected by the flow to its final position $\phi_{t_0}^T(\mathbf{x}_0) = \mathbf{x}(t_0 + T, t_0, \mathbf{x}_0)$ after an integration time T . If we make a small perturbation, \mathbf{q} , in the initial condition and we consider the evolution of trajectory starting at the position $\mathbf{x}_0 + \mathbf{q}$ instead of \mathbf{x}_0 , the final position will be

$$\phi_{t_0}^T(\mathbf{x}_0 + \mathbf{q}) = \phi_{t_0}^T(\mathbf{x}_0) + \frac{\partial \phi_{t_0}^T}{\partial \mathbf{x}_0} \mathbf{q} + O(\|\mathbf{q}\|^2) \quad (2.9)$$

CHAPTER 2. CONCEPTS AND TOOLS

From this approximation, we have that

$$\delta\mathbf{x}(t_0 + T) = \phi_{t_0}^T(\mathbf{x}_0 + \mathbf{q}) - \phi_{t_0}^T(\mathbf{x}_0) \approx \frac{\partial \phi_{t_0}^T}{\partial \mathbf{x}_0} \mathbf{q} = \nabla \phi_{t_0}^T(\mathbf{x}_0) \quad (2.10)$$

and the Eq 2.8. can be rewritten as

$$\lambda_{t_0}^T(\mathbf{x}) = \frac{1}{|T - t_0|} \ln \sqrt{\max \frac{\|\nabla \phi_{t_0}^T(\mathbf{x}_0) \mathbf{q}\|}{\|\mathbf{q}\|}} \quad (2.11)$$

In this way the FTLE along each trajectory is calculated from the maximum eigenvalues of the finite-time version of Cauchy-Green deformation tensor defined by (see Haller (2001); Shadden et al. (2005)):

$$C_{t_0}^T(\mathbf{x}) = \left[\nabla \phi_{t_0}^T(\mathbf{x}_0) \right]^\dagger \left[\nabla \phi_{t_0}^T(\mathbf{x}_0) \right] \quad (2.12)$$

where $\nabla \phi_{t_0}^T(\mathbf{x}_0)$ is the deformation-gradient tensor given by the derivatives of the flow map with respect to variations of the initial positions, and M^\dagger denotes the transpose of M .

2.4.2 Finite-Size Lyapunov Exponents (FSLEs)

If we want to know about the predictability time in the large with respect to a finite perturbation, it should be determined by a quantity analogous to the Lyapunov exponent. The natural starting point in looking for such a quantity is the time it takes for a perturbation to grow from an initial size δ to a given but arbitrary threshold value Δ . This is called the (δ, Δ) predictability time and denoted by $T(\delta, \Delta)$. A natural definition (Aurell et al., 1997) of the finite-size Lyapunov exponent must be, therefore, an average of some function of the predictability time, such that if both δ and Δ are in the infinitesimal range, we will recover the usual Lyapunov exponent, and an obvious choice is then

$$\lambda(\delta, \Delta) = \left\langle \frac{1}{T(\delta, \Delta)} \right\rangle \log \left(\frac{\Delta}{\delta} \right), \quad (2.13)$$

where the average is over different initial conditions. In contrast to infinitesimal perturbations, for finite perturbations the threshold Δ is typically not to be taken much larger than the finite perturbation δ . In contrast with FTLE now we have relaxed the limit $\delta\mathbf{x}(t_0) \rightarrow 0$.

FSLE can be used to study dispersion of particles in flows. In this case the perturbations are distances between particles, and the given threshold of tolerance

2.5. SCALE DEPENDENCE OF FSLE

Δ can be defined to be proportional to the initial perturbation δ in the following way,

$$\lambda(\delta) = \frac{\ln(r)}{\langle \tau(\delta, r\delta) \rangle} \quad (2.14)$$

where $\langle \tau(\delta) \rangle$ is the average time (over the number of particles pairs) required to separate from a distance of δ to $r\delta$.

We can obtain different information from FSLE. On one hand, the computation of the ensemble FSLE as a function of delta ($\lambda(\delta)$) is a powerful way of exploring the relationship between the temporal and spatial scales affecting tracer dispersion. In this case r is chosen to be small. On other hand, an initially small and circular patch of tracer will be deformed into an ellipse, and λ is the rate of increase of the major axis of this ellipse (see Fig. 2.5). Therefore FSLE fields characterize regions of particle divergence or convergence in two ways: (a) existence of regions with different stirring. A large value of λ corresponds to a location where there is rapid, exponential separation of two nearby particles (chaotic stirring), whereas for small values of λ there is slow or no exponential separation of particles (weakly chaotic stirring), (b) locate Lagrangian Coherent Structures. In this case we use large values of r .

2.5

Scale dependence of FSLE

What is interesting, and what makes finite-size Lyapunov exponents different from Lyapunov exponents for infinitesimal perturbation, is the dependence on δ (see Eq 2.14). In fact, FSLE was introduced by Artale et al. (1997); Aurell et al. (1997) to characterize flows with multiple length and timescales. The explicit dependence of the FSLE on the separation scale δ allows one to isolate the contribution of dynamics at different space scales to particle separation. The scale-dependent dispersion laws in the oceanic context are schematically summarized in Fig. 2.4 a) (Özgökmen et al., 2012). For $\delta > R_d$ (radius of deformation), geophysical turbulence leads to Richardson scaling, $\delta^{-2/3}$ (Hypothesis-II), or in the presence of strong shear flows such as western boundary currents, to ballistic scaling (δ^{-1}). For $\delta \gg R_d$, on the order of the circulation scale, one can expect diffusive scaling associated with uncorrelated pair velocities. At these large separation scales the motion is uncorrelated, and the dispersion is local. In this case a power law regimen emerge, likely caused by either an energy cascade or by a mean shear (Lacorata et al., 2001; Lacasce, 2008).

CHAPTER 2. CONCEPTS AND TOOLS

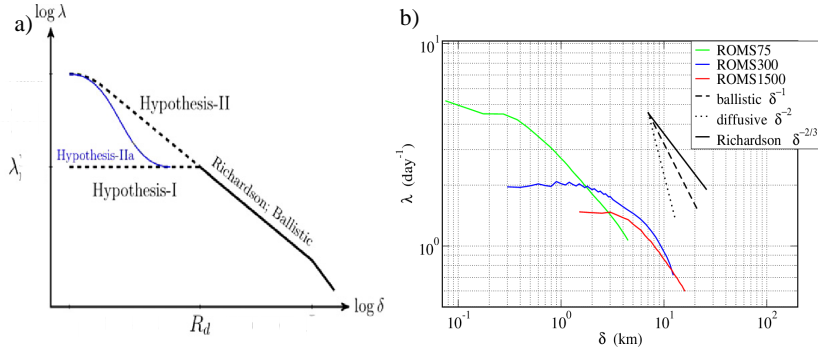


Figure 2.4: a) Schematic depiction of FSLE in the multi-scale setting of the ocean. Hypothesis-I and -II correspond to non-local and local transport, respectively. Hypothesis-IIa shows a case if there is a significant spectral gap between the submesoscale and mesoscale coherent features inducing the relative dispersion (taken from Özgökmen et al. (2012)). b) Spatial average of FSLE ($\lambda(\delta)$) at different scales δ using velocity data sets of the south of Mallorca Sea from a realistic simulation ROMS at different high spatial resolution. The slopes of different regimes of relative dispersion correspond to ballistic, diffusive and Richardson are included in the plot.

For $\delta < R_d$ (submesoscale) there are three hypothesis (2.4 Hypothesis I: When $\lambda(\delta)$ values are constant over a range of scales (scale independent), the separation between particles is exponential at a constant rate within that range of scales, and we have a exponential regime. At this separation scales the dispersion is non-local, and the dynamic is governed by larger scale. This means that the submesoscale field is weak and is controlled by the mesoscale eddy field.

Hypothesis II: If the submesoscale processes are energetically important, they exert control on relative dispersion at their own scales (exponential regime and local dispersion). This is consistent with an inverse cascade from submesoscale to mesoscale.

Hypothesis IIa. If the spectral gap between the submesoscale and mesoscale is sufficiently large, then scale-dependent dispersion metrics should show two distinct regimes of local transport properties.

In Fig. 2.4 (b) we plot the scale dependence of FSLE from numerical ROMS velocity data of the south of Mallorca Sea at three high different spatial resolution: 75m , 300m and 1500m. The results show that the model explicitly resolve the

2.6. LAGRANGIAN COHERENT STRUCTURES (LCS) AS RIDGES IN THE FSLE FIELD

submesoscale. Here there is a well defined plateau in the FSLE at the smallest scales, but overall domain size is too small to address the role of mesoscale features in transport and stirring.

2.6

Lagrangian Coherent Structures (LCS) as ridges in the FSLE field

To compute FSLE fields using velocity data of the ocean we say that the initial perturbation, δ (Eq. 2.13), is the initial spatial separation of two particles, δ_0 , (one of them placed at \mathbf{x}) and the tolerance Δ (Eq. 2.13) is the final separation of these two particles, δ_f , and τ is the time required for two particles of fluid to separate from an initial distance of δ_0 to a final one of δ_f . Thus the expression for the FSLE at time t_0 in the spatial position \mathbf{x} is given by

$$\lambda(\mathbf{x}, t_0, \delta_0, \delta_f) = \frac{1}{|\tau|} \ln \frac{\delta_f}{\delta_0}, \quad (2.15)$$

Now instead of fixing a finite integration time (FTLE), we fix a finite initial and final spatial separation between particles. As the FSLE is a function of the initial distance δ_0 but also of the final distance δ_f , we can analyze oceanic structures at different sizes (LCS) using different δ_f values. In the definition of λ in Eq. (2.15), we used $|\tau|$ instead of τ because it is often the case that we are interested in computing λ for $t > 0$ and $t < 0$, to produce LCS related to stable and unstable manifolds, as was mentioned towards the end of the Section 2.3.

The technique identifies dynamical objects that organize the transport, and relevant coherent structures. Until recently, the power of these novel Lagrangian approaches has been mainly relegated to mathematical systems or simplified workbench models, since the required detailed knowledge of the velocity field was not readily available in real geophysical situations. However, in the last decades the situation has dramatically changed, with a rapidly increasing amount of data available from Lagrangian drifters (Mariano et al., 2002), satellite measurements (Halpern, 2000), and especially from detailed computer models (Haidvogel, 1999; Dietrich, 1997)

To define a hyperbolic trajectory precisely for systems given only over a finite time-space interval one should be careful (e.g. see Haller and Poje (1998); Mancho et al. (2006b)). However, let us just think of hyperbolic trajectories as ones about which there is a direction of expansion and a direction of compression.

CHAPTER 2. CONCEPTS AND TOOLS

In dynamical systems terminology, this means that there should exist stable and unstable directions about a hyperbolic trajectory. For incompressible flows, without sources or sinks, any expansion in one direction must be balanced by compression in another direction, making such trajectories ubiquitous.

If exponential separation between trajectories occurs, and if the domain of the system is compact, which is typically the case, these trajectories must mix together. This is especially true for turbulent flows, but even for simple dynamical systems this is also true and is often termed "deterministic chaos", which refers to the phenomenon that simple vector fields can produce chaotic trajectories. The structures of strongest hyperbolicity often dictate transport in dynamical systems (Leong and Ottino, 1989), which we will come to see. However, for time-dependent systems these structures, which we refer to as LCS, are often recondite when viewing the Eulerian velocity field or even particle trajectories. For time-independent systems, separatrices are given by the stable and unstable manifolds of hyperbolic fixed points, as in the pendulum example presented before. However, for highly time-dependent systems, the FSLE fields admit analogous ridges that divide dynamically different regions, and these structures are themselves time-dependent. We study a time-dependent flow in terms of LCS as the analog of studying a time-independent flow in terms of stable and unstable manifolds. In previous works Joseph and Legras (2002); d'Ovidio et al. (2004, 2009); Lehan et al. (2007); Calil and Richards (2010) have been shown that a wide range of systems admit well-defined ridges in the FSLE fields which govern the global flow structure.

If we refer to LCS as ridges of the FSLE field, we must define a ridge. Intuitively, a ridge is a curve such that if somebody walking along a ridge, then stepping in the direction transverse to the ridge, he would be stepping down. For FTLE, it is known that LCSs represent invariant manifolds, and there is mathematical theory for that, but it is not started for FSLE. However we assume that ridges in the FSLE field track the LCS.

2.6.1 LCS properties

There are not theorems for FSLE but on the basis of the works by Joseph and Legras (2002); d'Ovidio et al. (2004, 2009); Hernández-Carrasco et al. (2011); Bettencourt et al. (2012) we assume some heuristic properties of LCS derived from FSLE:

2.7. COMPUTATION OF FSLE

- For well-defined LCS, which are obtained from FSLE field with a enough spatial difference between the inital and the final separation of particles, the flux of matter across such structures is expected to be small.
- The FSLE measures the integrated effect of the flow, so if the time is too small then this integrated effect is ignored and thus the FSLE is not very indicative of Lagrangian behavior.
- LCS can be computed below the spatial resolution of the velocity field.
- LCS are robust when errors are introduced in the velocity data and in the particle trajectory.
- LCS (at least the ones which are clearly visible in the FSLE fields) are invariant manifolds for all practical purposes.

2.7

Computation of FSLE

As already mentioned, to compute FSLE (Eq. 2.15) we need to obtain the time, τ , required for two particles of fluid (one of them placed at \mathbf{x}) to separate from an initial distance of δ_0 to a final one of δ_f (see Fig. 2.5). To compute this time we need to know the trajectories of the particles. The FSLE are computed for the points \mathbf{x} of a lattice with lattice spacing coincident with the initial separation of fluid particles δ_0 . The equations of motion that describe the horizontal evolution of particle trajectories in our velocity field are

$$\frac{d\varphi}{dt} = \frac{u(\varphi, \theta, t)}{R \cos \theta}, \quad (2.16)$$

$$\frac{d\theta}{dt} = \frac{v(\varphi, \theta, t)}{R}, \quad (2.17)$$

where u and v represent the eastwards and northwards components of the velocity field coming from simulations or from satellite derived altimetry (described in Section 2.12); R , is the radius of the Earth (6400 *km* in our computations), φ is longitude and θ latitude. Numerically we proceed integrating Eqs. (2.16) and (2.17) using a standard, fourth-order Runge-Kutta scheme, (see Appendix A.1), with an integration time step dt , which depends on the time resolution of the data. Since information is provided just in a discrete space-time grid, spatiotemporal interpolation of the velocity data is achieved by bilinear interpolation (see Appendix A.2). However we notice that bilinear interpolation requires an

CHAPTER 2. CONCEPTS AND TOOLS

equally spaced grid. If our data input is expressed in spherical coordinates, the grid is not uniformly spaced in the latitude coordinate. This occurs with the velocity field from numerical ocean model applied to the Mediterranean Sea used in Chapter 3, and from the ROMS output used in Chapter 6 to simulate the currents in the Benguela region. In order to interpolate in an uniformly spaced grid, we transform our coordinate system (φ, θ) to a new coordinate system with coordinates (φ, μ) , where the grid turns out to be uniform (Mancho et al., 2008). The latitude θ is related to the new coordinate μ by

$$\mu = \log |\sec \theta + \tan \theta|. \quad (2.18)$$

In the new variables the equations of motion are:

$$\frac{d\varphi}{dt} = \frac{u(\varphi, \mu, t)}{R \cos \theta(\mu)} \quad (2.19)$$

$$\frac{d\mu}{dt} = \frac{v(\varphi, \mu, t)}{R \cos \theta(\mu)}, \quad (2.20)$$

and one can convert the μ values back to latitudes θ by inverting Eq.(2.18):

$$\theta = \pi/2 - 2 \arctan (e^{-\mu}). \quad (2.21)$$

Once trajectories are integrated from these equations, one can convert μ values to θ by using Eq.(2.21). Once we integrate the equations of motion, Eqs.(2.19, 2.20), we compute the FSLEs with Eq. (2.15) for the points \mathbf{x} of a lattice with spacing δ_0 . Initial conditions for which the prescribed final separation δ_f has not been reached after using all the available times in the data sets are assigned a value $\lambda = 0$. The largest Lyapunov values concentrate along characteristic lines which are the LCSs (Joseph and Legras, 2002; d'Ovidio et al., 2004, 2009; Hernández-Carrasco et al., 2011).

2.8

Eulerian and Lagrangian diagnosis

In this section we briefly introduce some Lagrangian and Eulerian diagnosis that we will use in the thesis and that likely, besides Lyapunov exponents, are the most widespread used tools for analyzing the topology and transport in ocean flows.

Traditionally, transport information has been inferred with Eulerian diagnosis based on the analysis of instantaneous snapshots of tracers and velocity fields. Among the best quantities known are:

2.8. EULERIAN AND LAGRANGIAN DIAGNOSIS

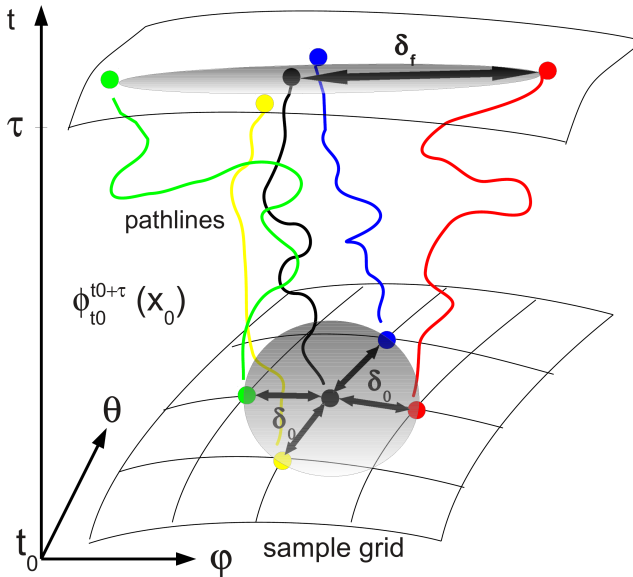


Figure 2.5: Schematic representation of the evolution of particle pair trajectories initially located on the points of a grid.

- *Strain Rate.* The initial stretching is given by the local strain rate γ , $\gamma^2 = \left(\frac{\partial u}{\partial x} - \frac{\partial v}{\partial y}\right)^2 + \left(\frac{\partial v}{\partial x} + \frac{\partial u}{\partial y}\right)^2$, where u and v are the zonal and meridional components of the velocity field, and x and y the orthogonal spatial coordinates.
- *Relative Vorticity.* It is given by $\omega = \frac{\partial v}{\partial x} - \frac{\partial u}{\partial y}$. It is related with the dispersion processes in vortex and gives information of the degree of rotation.
- *Okubo Weiss.* This parameter describes the topology of turbulent flows, by comparing the intensity of the strain to the vorticity: $OW = \gamma^2 - \omega^2$. It is a way to characterize local hyperbolicity-ellipticity, but in a purely Eulerian view (without accumulating deformation in time). Thus, regions of the flow where the strain rate dominates ($OW > 0$) the fluid parcels are stretched, and in regions of the flow where the rotation dominates ($OW < 0$) there is not exponential separation and only weak (or no) stirring, as inside of vortices.

CHAPTER 2. CONCEPTS AND TOOLS

- *Eddy Kinetic Energy (EKE)*. It is a diagnostic of the mesoscale variability in the oceans and gives information of the turbulent component of the flow. The EKE per unit of mass is given by $EKE = \frac{1}{2} \langle u'^2 + v'^2 \rangle$, where u' and v' are the instant deviations in zonal and meridional velocities from the average over the period T , and the brackets denote average over that period.

In recent years new techniques have been developed to study ocean transport from the Lagrangian point of view. Some of them are briefly presented in the following:

- *Leaking methods*. They were introduced to visualize Lagrangian structures in theoretical complex flows by Schneider et al. (2002) and later in the Mediterranean Sea from a numerical model by Schneider et al. (2005). This method is based on the evolution during a prefixed time of a set of particles initially released in a preselected open region of the system. The initial positions of trajectories remaining in the preselected region form the contracting stable manifold, and the final positions of trajectories remaining in the preselected draw the stretching unstable manifolds. This method provide time-scales in a easy way, but it has the disadvantage of depending on the orientation of the open boundary and not on the strength of the hyperbolic point.
- *Distinguished Hyperbolic Trajectories*. The unstable and stable manifolds are computed from the hyperbolic trajectories previously computed by a iterative method. The analytical solutions of hyperbolic trajectories and some numerical cases were developed by Ide et al. (2002). Mancho et al. (2004, 2006a) introduced the algorithm to compute the invariant manifolds of hyperbolic trajectories in oceanic flows. This method is very rigorous and it is suitable to compute lobe areas. On another hand the visualization of manifolds is one by one and it is computationally expensive and sensitive.
- *Function M*. This descriptor, developed by Mendoza and Mancho (2010, 2012), measures the lengths of curves traced by trajectories on the phase space, so it is expected it will change abruptly at the boundaries of regions comprising trajectories with qualitatively different evolution, and this is exactly what stable and unstable manifolds separate. The technique locates simultaneously hyperbolic and nonhyperbolic flow regions. Some of the advantages are its lower computational cost, it is defined for general vector fields, and one can obtain global dynamics maps of the flow.
- *Residence Times*. These maps are the color representation of residence times. Are based on the characterization of entry and exit residence times of

2.9. COMPARISON BETWEEN EULERIAN DIAGNOSIS AND LAGRANGIAN DIAGNOSIS FROM FSLES

particles initially released in a preselected area of the system. The sum of this two quantities gives the *residence time*, which is defined as the length of time that a fluid particle remains in an area before crossing a particular encounter zone.

- *Relative dispersion*. It is given by the evolution in time of the spatial separation of two particles. This method gives us a good idea of the dispersion of particles in a flow, but manifolds can not be obtained. The average over all particle pairs in the definition of the relative dispersion does not allow a systematic investigation of the effects of disparate scales of motion on the dispersion statistics (Lacasse and Ohlmann, 2003).

2.9

Comparison between Eulerian diagnosis and Lagrangian diagnosis from FSLEs

Focusing in the use of FSLE for detecting Lagrangian structures, Boffetta et al. (2001) compared the Eulerian diagnosis, Okubo-Weiss criterion and its generalization introduced by Hua and Klein (1998), with the Lagrangian diagnosis FTLE and FSLE applied to a meandering jet. They concluded that FSLE diagnosis shows a major skill in detecting the presence of large-barriers to the transport in the geometry studied.

On another hand, Waugh et al. (2006) studied the relation of stirring obtained from FTLE with Eulerian descriptors in the Tasman Sea. They found that low values of FTLE are located in rotation-dominated regions inside coherent vortices ($OW < 0$) while the filaments of high FSLE occur in strain-dominated regions surrounding the vortices ($OW > 0$). The same was studied by Garcia-Olivares et al. (2007) and d'Ovidio et al. (2009) in the Mediterranean Sea, and they found similarities between FSLE and OW only in persistent vortices, such as Alboran gyres, but not in dynamically active regions, like the fast evolving eddies formed in the Algerian current. In such persistent regions is possible to visualize the connection between eddies given by lines of FSLE. Comparison of climatologies of FTLE with that of EKE was studied initially by Waugh et al. (2006) in the Tasman Sea and by Waugh and Abraham (2008) in the North Atlantic, finding a compact relationship with $FTLE \propto EKE^{1/4}$. On the contrary d'Ovidio et al. (2009) showed a much looser relationship when these quantities are computed by using a finer velocity field. Climatologies of Lyapunov exponents do not show any compact relation with other Eulerian diagnostics, unveiling a different structure

CHAPTER 2. CONCEPTS AND TOOLS

even at the basin scale.

The FSLE lines are manifolds that can be computed below the spatial resolution of the velocity field, improving the visualization. In contrast with Eulerian diagnostics, Lagrangian tools like the FSLE have the advantage of exploiting both spatial and temporal variability of the velocity field and are in principle able to unveil subgrid filaments generated by chaotic stirring. This is best seen with an example. Consider a chlorophyll or surface temperature filament winding around a mesoscale eddy. This filament is not necessarily created by submesoscale velocities, but it can be the effect of a large scale chlorophyll or SST front colliding with the mesoscale eddy. In this case, the mesoscale structure of the velocity field contains all the information for reconstructing the filament. In particular, by integrating the velocity field, the advection of a numerical tracer can mimic the stirring effect of the eddy, and the tracer submesoscale filaments winding around the eddy can be estimated.

Filamentation dynamics can be detected by reprocessing available altimetric or numerical velocity data with Lagrangian tools, giving insight into (sub-)mesoscale stirring processes relevant to tracer observations and complementing traditional Eulerian diagnostics. However, in respect to these traditional diagnostics, Lagrangian methods have a much higher degree of complexity and are several orders of magnitude slower, since they involve the construction of particle trajectories.

2.10

Turbulence and multifractality

In fluid dynamics, (Frisch, 1995) turbulence or turbulent flow is a fluid regime characterized by chaotic and stochastic properties. This includes low momentum diffusion, high momentum convection, and rapid variation of pressure and velocity in space and time. Flow that is not turbulent is called laminar. At very low speeds the flow is laminar, i.e., the flow is smooth (though it may involve vortices on a large scale). As the speed increases, at some point the transition is made to turbulence. In turbulent flow, unsteady vortices appear on many scales and interact with each other. Because laminar-turbulent transition is governed by Reynolds number (that gives a measure of the ratio of inertial forces to viscous forces), the same transition occurs if the size of the object is gradually increased, or the viscosity of the fluid is decreased, or if the density of the fluid is increased.

2.10. TURBULENCE AND MULTIFRACTALITY

In the ocean the turbulence causes the formation of eddies of many different length scales. Most of the kinetic energy of the turbulent motion is contained in the large scale structures. In conventional threedimensional turbulence, the energy cascades from the large scale structures to smaller scale structures by an inertial and essentially inviscid mechanism. This process continues, creating smaller and smaller structures which produces a hierarchy of eddies. Eventually this process creates structures that are small enough that molecular diffusion becomes important and viscous dissipation of energy finally takes place. The turbulence in oceanic flow is in two dimensions and the energy cascade is in the inverse direction. There is however a cascade of vorticity towards small scales.

Moreover, the ocean is a system displaying scale invariant behavior. From complex systems theory it is known that fractal sets have an intrinsic scale-invariant nature which can be expressed by a characteristic exponent that is the fractal dimension of the set. There are many definitions of fractal dimension and none of them should be treated as the universal one. The fractal dimension (Barabasi and Stanley, 1995) is used to characterize quantitatively a self-similar system. Self-similarity is a symmetry property of the system. By self-similarity we mean invariance under an isotropic transformation, namely a simple dilation. If we consider an object S formed by a set of points $R = (x_1, x_2, x_3, \dots)$, a dilation, or similarity transformation with a scaling factor b , changes the coordinates to $bR = (bx_1, bx_2, bx_3, \dots)$. The set S formed by the particles of coordinates R is self-similar if it is invariant under this transformation. For a deterministic fractal, scale invariance means that the rescaled system bS is identical with a part of the original system S .

By embedding dimension, d_E , we understand the smallest Euclidean dimension of the space in which a given object can be embedded. The volume $V(l)$ of an arbitrary object can be measured by covering it with balls of linear size l , and volume l^{d_E} . We need $N(l)$ balls to cover it, so

$$V(l) = N(l)l^{d_E}. \quad (2.22)$$

One might at first expect that for any object, $N(l) \sim l^{-d_E}$, since the volume of standard objects does not change with the unit of measurement l . But for fractals we have in general

$$N(l) \sim l^{-D_f}. \quad (2.23)$$

Objects with $D_f < d_E$ are called fractals, with D_f is the fractal dimension. If we have a structure that is a line, the fractal dimension is $D_f=1$, if the structure is a

CHAPTER 2. CONCEPTS AND TOOLS

surface $D_f=2$, and if we have a structure between a line and a surface, we obtain a dimension equals to a fractional number between one and two.

For a homogeneous fractal, with fractal dimension D_f , many relevant scale-dependent quantities decay as a power law of the scale with exponents which are directly related to the fractal dimension D_f . The widespread occurrence of this behavior led researchers to interpret those systems in terms of fractal sets, and try to characterize universality classes in terms of possible underlying fractal attractors or fractal interfaces.

Nevertheless, a better understanding of the mechanisms that govern the evolution of some dynamical systems, turbulent flows being one of the most relevant cases, evidence that the observed intrinsic complexity could not be covered by a simple description based on the existence of a single fractal interface. As a consequence, a richer framework was required and the natural step forward was to consider multiple-fractal hierarchies which could fit better with the available evidence. Therefore a multifractal system is a generalization of a fractal system in which a single exponent (the fractal dimension) is not enough to describe its dynamics; instead, a continuous spectrum of exponents is needed.

2.11

Langevin equation and eddy-diffusivity

A stochastic differential equation (SDE) (San Miguel and Toral, 2000) is a differential equation which contains a stochastic process $\xi(t)$:

$$\frac{dx(t)}{dt} = G(x(t), t, \xi(t)). \quad (2.24)$$

As a consequence a SDE is not a single differential equation but rather a family of ordinary differential equations, a different one for each outcome u of the stochastic process:

$$\frac{dx_u(t)}{dt} = G(x_u(t), t, \xi_u(t)). \quad (2.25)$$

Therefore, the family of solutions x_u of these differential equations, for different outcomes u , constitute a stochastic process $x(t)$. We can say that to each realization $\xi_u(t)$ of the stochastic process ξ , corresponds a realization x_u of the stochastic

2.11. LANGEVIN EQUATION AND EDDY-DIFFUSIVITY

process x . The solution x becomes then a functional of the process ξ . To solve a SDE means to characterize completely the stochastic process $x(t)$, i.e. to give the m -times probability density function (pdf) $f(x_1, \dots, x_m; t_1, \dots, t_m)$. Again, this is in general a rather difficult task and sometimes one focuses only on the evolution of the moments $\langle x(t)^n \rangle$ and the correlation function $\langle x(t_1)x(t_2) \rangle$. When the stochastic process $\xi_u(t)$ appears linearly one talks about a *Langevin equation*. Its general form being:

$$\frac{dx(t)}{dt} = q(x, t) + g(x, t)\xi(t). \quad (2.26)$$

In this case, $\xi(t)$ is usually referred to as the *noise* term. A word whose origin comes from the random noise one can actually hear in electric circuits. Another notation concept: if the function $g(x, t)$ is constant, one talks about additive noise, otherwise, the noise is said to be multiplicative. Finally, $q(x, t)$ is usually referred to as the 'drift' term, whereas $g(x, t)$ is the 'diffusion' term.

We can use the Langevin equation with additive noise to simulate missing information between points of the grid of the velocity data in the computation of particle's trajectories of the marine flow. In this case x will be the coordinates, $q(x, t)$ is the velocity field and $g(x, t)$ is the Lagrangian diffusion term related to the oceanic diffusivity. Empirical relations between diffusion characteristics were investigated Okubo (1971) by the use of carefully examined data from instantaneous dye-release experiments in the upper mixed layer of the sea. In this work, among others things, the relation of the variance σ^2 of the initial distribution of patch with the diffusion time (time of diffusion during which a patch from a point source grows into the size σ) was studied. The following empirical relation was found:

$$\sigma^2 = 0.0108 t^{2.34}, \quad (2.27)$$

where σ^2 and t are expressed in terms of cm^2 and sec , respectively. The scale of diffusion represents in our case the spatial resolution of the velocity data. The relationship between the diffusivity D_a , in m^2s^{-1} , and the scale of the diffusion, l in m , is given by

$$D_a = 2.055 \cdot 10^{-4} l^{1.15}. \quad (2.28)$$

This ocean diffusivity represents the eddy diffusivity, and it depends on the spatial resolution of the FSLE field.

CHAPTER 2. CONCEPTS AND TOOLS

2.12

Velocity Data

In the thesis we have used velocity data from hydrodynamical models and from altimetry derived from satellite.

2.12.1 Hydrodynamical models

Within the field of ocean general circulation modelling, all models resolve very similar equations (primitive equations) but differ by their choice of spatial discretization (finite difference, finite element, finite volume) and vertical coordinate (geopotential, isopycnic, sigma, hybrid).

The primitive equations are based on the Navier-Stokes equations on a rotating sphere with thermodynamic terms for various energy sources (radiation, latent heat, etc...). These equations are the basis for complex computer programs commonly used for simulating the evolution of the atmosphere or the ocean. They are three-dimensional (x,y and z) models that discretize the equations for fluid motion and integrate them forward in time (time is the fourth dimension). They also contain parameterizations for processes such as convection, or turbulence, that occur on scales too small to be resolved directly. To model a region of the ocean, fluxes from the frontiers such as the atmosphere, the coast, etc.. are imposed as external forcings. Most models include a software to diagnose a wide range of output variables for comparison with observations or study of oceanic processes.

Examples of such models are ROMS (for Regional Ocean Model System, see Shchepetki and McWilliams (2005); Song and Haidvogel (1994); Haidvogel et al. (2000) and <http://www.myroms.org/>) or OFES (for global eddy-resolving model <http://www.jamstec.go.jp/esc/ofes/>).

2.12.2 Ocean altimetry

Altimetry satellites basically determine the distance from the satellite to a target surface by measuring the satellite-to-surface round-trip time of a radar pulse. However, this is not the only measurement made in the process, and a lot of other information can be extracted from altimetry. The magnitude and shape of the echoes (or waveforms) also contain information about the characteristics of the surface which caused the reflection.

2.13. OCEAN COLOR

Several different frequencies are used for radar altimeters. Each frequency band has its advantages and disadvantages : sensitivity to atmospheric perturbations, better observation of ice, rain, coastal zones, land masses, etc..

Radar altimeters permanently transmit signals to Earth, and receive the echo from the reflecting surface. The satellite orbit has to be accurately tracked and its position is determined relative to an arbitrary reference surface, an ellipsoid. The sea surface height (SSH) is the deviation from the sea surface to a reference ellipsoid or a mean sea surface. The geostrophic currents are calculated from the gradients of SSH, assuming a geostrophic balance:

$$u_g = -\frac{g}{f} \frac{\partial h}{\partial y'} \quad (2.29)$$

$$v_g = -\frac{g}{f} \frac{\partial h}{\partial x'} \quad (2.30)$$

where $f = 2\Omega\sin\theta$ is the Coriolis parameter depending on latitude, θ , g is the acceleration due to gravity and h is the height of the sea surface above a level surface (SSH).

The satellite surface currents we used are the sum of the gridded geostrophic velocities and the Ekman currents at 15 m depth (Sudre and Morrow, 2008).

2.13

Ocean color

When an incident light reaches a surface, a part is absorbed by the surface, whereas another part is reflected, which provides its color. The Ocean Color uses passive teledetection principles to estimate the ocean color: the remote sensor measures the solar reflected light by terrestrial and oceanic surfaces. In a cloud free sky, the measured signal will be constituted by the ocean reflectance, but also by the atmospheric diffusion and reflectance. The signal has to be corrected to extract only the oceanic signal.

The color of the ocean is determined by the interactions of incident light with dissolved substances or particles present in the water. The most significant constituents are free-floating photosynthetic organisms (phytoplankton) and inorganic particles. Phytoplankton contain chlorophyll-a (as well as other optically active pigments), which absorbs light at blue and red wavelengths and transmits in the green. Particulate matter as sediment load from coastal inputs, can reflect

CHAPTER 2. CONCEPTS AND TOOLS

and absorb light, which reduces the clarity (light transmission) of the water. Substances dissolved in the water, such as chemical emissions, can also affect its color. Satellite instruments measure the amount of reflected light of different wavelengths (electromagnetic signal of 400-700 nm wavelength). In true color mode, very productive waters with a high concentration of plankton appear blue-green, whereas very pure waters appear deep-blue, almost black. Semi-empirical equations can be used to estimate the concentration of chlorophyll a (and its degradation products) from satellite measurements of backscattered sunlight.

Reliability of Finite-Size Lyapunov Exponents for the assessment of ocean dynamics

Much of atmospheric and oceanic transport is associated with coherent structures. Lagrangian methods are emerging as optimal tools for their identification and analysis. An important Lagrangian technique which is starting to be widely used in oceanography is that of Finite-Size Lyapunov Exponents (FSLEs). Despite this growing relevance there are still many open questions concerning the reliability of the FSLEs in order to analyse the ocean dynamics. In particular, it is still unclear how robust they are when confronted with real data. In this Chapter we analyze the effect on this Lagrangian technique of the two most important effects when facing real data, namely noise and dynamics of unsolved scales. Our results, using as a benchmark data from a primitive numerical model of the Mediterranean Sea, show that even when some dynamics is missed the FSLEs results still give an accurate picture of the oceanic transport properties.

3.1

Introduction

In recent years mixing and transport properties of the sea surface have been widely studied from the Lagrangian viewpoint (Buffoni et al., 1997; Griffa, 1996; Iudicone et al., 2002; Mancho et al., 2006a; Molcard et al., 2006). Lagrangian diag-

CHAPTER 3. RELIABILITY OF FSLE

nostics exploit the spatio-temporal variability of the velocity field by following fluid particle trajectories, in contrast with Eulerian diagnostics, which analyze only frozen snapshots of data. Among Lagrangian techniques the most used ones involve the computation of local Lyapunov exponents (LLE) which measure the relative dispersion of transported particles (Artale et al., 1997; Aurell et al., 1997; Boffetta et al., 2001; Haller and Poje, 1998; Haller, 2000; Iudicone et al., 2002). LLEs give information on dispersion processes but also, and even more importantly, can be used to detect and visualize Lagrangian Coherent Structures (LCSs) in the flow like vortices, barriers to transport, fronts, etc (Beron-Vera et al., 2008; Haller and Yuan, 2000; Joseph and Legras, 2002; Koh and Legras, 2002; Lapeyre, 2002; Peacock and Dabiri, 2010).

The standard definition of Lyapunov exponents (Ott, 1993) involves a double limit, in which infinitely-long times and infinitesimal initial separations are taken. These limits can not be practically implemented when dealing with realistic flows of geophysical origin. Over real data, LLEs are defined by relaxing some of the limit procedures. In finite-time Lyapunov exponents (FTLE) (Lapeyre, 2002; Ott, 1993) trajectory separations are computed starting still at infinitesimal distance, but only for a finite time. In the case of finite-size Lyapunov exponents (FSLE), the key tool used in our work (Aurell et al., 1997; Boffetta et al., 2001), one computes the time which is taken for two trajectories, initially separated by a finite distance, to reach a larger final finite distance.

FSLEs are attracting the attention of the oceanographic community (Artale et al., 1997; d'Ovidio et al., 2004, 2009; Garcia-Olivares et al., 2007; Haza et al., 2008; Iudicone et al., 2002; Molcard et al., 2006; Tew Kai et al., 2009; Poje et al., 2010). Despite the growing number of applications of FSLEs, a rigorous analysis of many of their properties is still lacking. There are two main concerns before applying FSLE to real data, namely the effect of noise and the role of observation scale. Concerning noise, real data are discretized and noisy, and this can affect the reliability of FSLE-based diagnostics (related studies for FTLE can be consulted in Haller, 2002; Peacock and Dabiri, 2010). Concerning scale properties, FSLEs can be obtained over a grid finer than that of the data. This enables to study submesoscale processes under the typical mesoscales (below 10 kilometers) that nowadays provide, for example, altimetry data (d'Ovidio et al., 2009; Tew Kai et al., 2009). But then the question is if results from finer-grid LCSs are meaningful or just an artifact. On the other side, we can have access to a limited-resolution velocity field, and then ask ourselves if any refinement in the velocity grid (by improved data acquisition, for instance) is going to modify our previous assessment of LCS at the rougher scale. The main objective of this Chapter is to address these questions, in particular with reference to their potential applications into ocean dynamics. A related study of the sensitivity

3.2. DESCRIPTION OF THE DATA

of relative dispersion of particles statistics, when the spatial resolution of the velocity field changes, has appeared recently (Poje et al., 2010).

The benchmark for the study of FSLEs properties used in this work is a two-dimensional velocity field of the marine surface obtained from a numerical model of the Mediterranean Sea. The first half of the Chapter is devoted to study what we have just called scale properties of the FSLE field. As will be clarified later on, all along this Chapter we will manage two different spatial grids: the one where we compute values of the FSLEs, and the one where the velocity field is given. By changing gradually the resolution of the FSLE-grid, we will show that they have typical multifractal properties. This means, in particular, that FSLEs obtained for a finer resolution than that provided by the data provides non-artificial information. In other words, we can capture some effects of the large length-scales on scales which are smaller than the data resolution. Of course, we cannot reconstruct all the effects taking place at the smaller scales (like for example the ones originated by small mixed layer eddies), but only the ones that have been originated by the large velocity features. Subsequently, we will consider a somewhat opposite case, i.e., what happens to the FSLEs if the velocity-data grid is changed. Their robustness under data-resolution transformations will be discussed. The second half of the work will analyze the effect of noise. Again, two different scenarios are considered: a) uncertainties in the velocity data, and b) noise in the particle trajectories. FSLEs will be shown to be robust against these two sources of error, and the reasons for this will be discussed.

3.2

Description of the data

We analyze a velocity dataset generated with the DieCAST (Dietrich for Center Air Sea Technology) numerical ocean model adapted to the Mediterranean Sea (Fernández et al., 2005). The dataset has been already used in previous Lagrangian studies (d’Ovidio et al., 2004; Mancho et al., 2008; Schneider et al., 2005). DieCAST is a primitive-equation, z-level, finite difference ocean model which uses the hydrostatic, incompressible and rigid lid approximations. At each grid point, horizontal resolution is the same in both the longitudinal, ϕ , and latitudinal, λ , directions, with resolutions $\Delta\phi = 1/8^\circ$ and $\Delta\lambda = \Delta\phi \cos \lambda$. Vertical resolution is variable with 30 layers. The model has been integrated for 20 years being forced by yearly repeating monthly climatological atmospheric forcing (wind stress and heat and freshwater fluxes at the sea surface). Using such climatological forcing the model properly reproduces the general surface

CHAPTER 3. RELIABILITY OF FSLE

circulation and many of the important features of the observed annual cycle of the basin (Fernández et al., 2005). Because of this annual climatological forcing, it is enough to store model outputs as instantaneous values each model day. In Fernández et al., 2005 it is shown that the DieCAST model can reproduce the Mediterranean mesoscale activity (i.e., it is eddy-permitting). This is because it has a horizontal resolution (10 kilometers on average, with 12 kilometers the maximum grid interval) that is close to the deformation radius in the Mediterranean (10 – 20 kilometers), is enough to resolve mesoscale structures which are typically larger than about 30 km. Besides this adequate grid resolution, the DieCAST model has low values of horizontal viscosity and diffusivity that permit baroclinic instability, and presents in general a low total numerical dissipation that allows to create and maintain frontal regions and coastal jets.

We will use velocity data corresponding to the second layer, which has its center at a depth of 16 meters. This sub-surface layer is representative of the marine surface circulation and is not directly driven by wind. We have recorded daily velocities for five years (taken after the model has reached an equilibrium state for the surface circulation), and concentrate our work in the area of the Balearic Sea. In Figure 3.1 we show a snapshot of the velocity field from the DieCAST model.

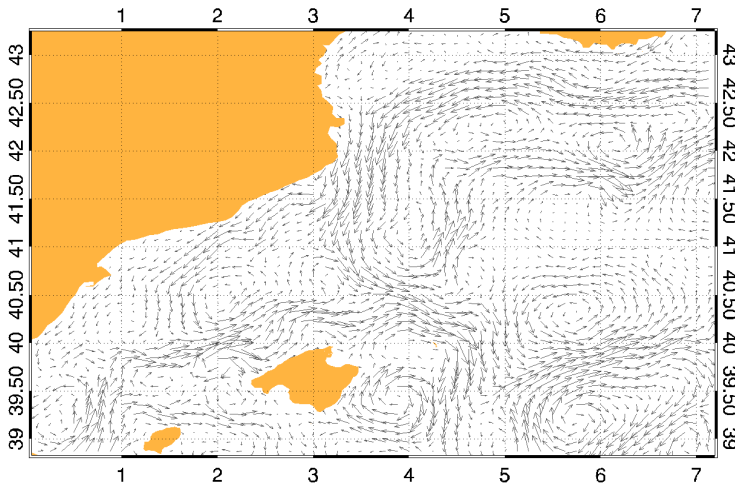


Figure 3.1: Snapshot of the surface velocity field of the Balearic Sea corresponding to day 640 in the DieCAST simulation.

Definition and implementation of FSLEs

FSLEs provide a measure of dispersion as a function of the spatial resolution, serving to isolate the different regimes corresponding to different length scales of oceanic flows, as well as identifying the LCSs present in the data. To calculate the FSLEs we have to know the trajectories of fluid particles, which are computed by integrating the equations of motion for which we need the velocity data (u, v) . FSLE are computed from τ , the time required for two particles of fluid (one of them placed at (x, y)) to separate from an initial (at time t) distance of δ_0 to a final distance of δ_f , as:

$$\Lambda(x, y, t, \delta_0, \delta_f) = \frac{1}{\tau} \log \frac{\delta_f}{\delta_0}. \quad (3.1)$$

In principle obtaining $\Lambda(x, y, t, \delta_0, \delta_f)$ would imply to consider all the trajectories starting from points at distance δ_0 from our basis point; in practice, when confronted with regular, discretized grids, only the four closest neighbors are considered. It is convenient to choose δ_0 to be the intergrid spacing among the points on which the FSLEs will be computed, i.e., it is the resolution of the "FSLE grid". More details on the calculation of the FSLEs are in Section 2.7.

Effect of sampling scale on FSLEs

Notice that we distinguish two types of grids, namely the FSLE grid (in the following "F-grid") and that where the velocity field is given (called velocity grid or "V-grid"). These two grids need not to coincide. We explore first the effect of changing the resolution of FSLE grid.

In Figure 3.2 we show an example of the FSLEs derived using four different F-grids with increasing resolutions. Visually, as the resolution of the F-grid is increased the structures already observed in the coarser version are kept, just increasing their detail level. In addition, also when resolution is increased, new less active structures are appearing in areas previously regarded as almost inactive. The North Balearic Sea is a clear example where all this happens; in 3.2a) no structures are seen and large values of FSLEs almost fill the region, but filamental structures appear resolved as the resolution improves. Taking a F-grid finer than the associated V-grid would make no sense if FSLE was an Eulerian

CHAPTER 3. RELIABILITY OF FSLE

measure obtained from single snapshots of the velocity field. But FSLE is a Lagrangian measure, i.e. they are computed using trajectories which integrate information on the *history* of the velocity field. This allows capturing the effects of the large scales on scales smaller than the V-grid. This does not mean that we reconstruct all the effects taking place at the smaller scales, but only the ones that have been originated by the relatively large velocity features which are resolved on the V-grid.

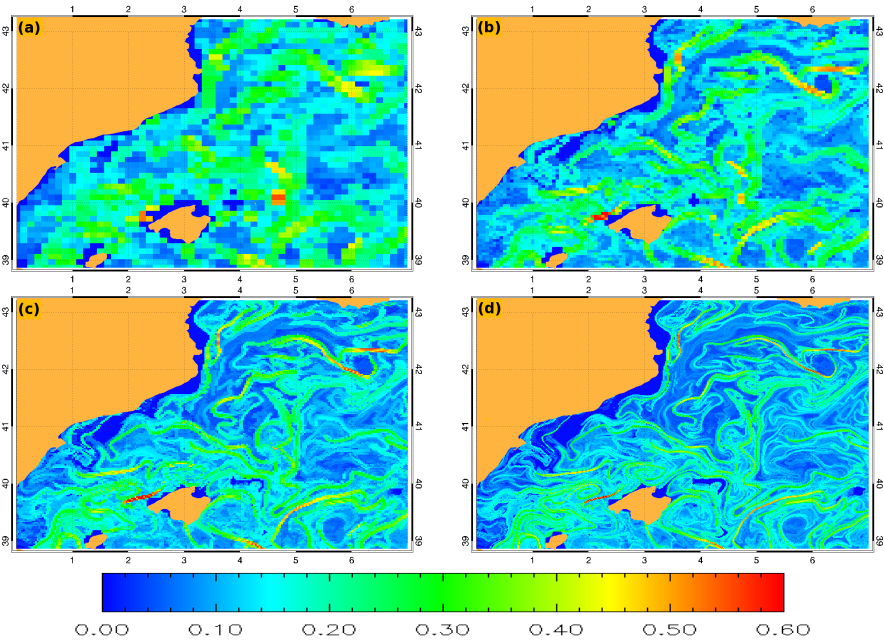


Figure 3.2: Snapshots of FSLEs backward in time starting from day 640 at different F-grid resolutions: a) $\delta_0 = 1/8^\circ$, b) $\delta_0 = 1/16^\circ$, c) $\delta_0 = 1/32^\circ$, d) $\delta_0 = 1/64^\circ$. In all of them we take $\delta_f = 1^\circ$. The values in the color bar have units of day^{-1} .

The main structures of the flow, which are essentially filaments, become finer as resolution is increased, behaving much like the geometrical persistence of a fractal interface Falconer, 1990. The question naturally rises about the possible multifractal character of FSLEs. Multifractality is a property characteristic to turbulent flows, and it is associated to the development of a complex hierarchy of eddies across which energy is transmitted and utterly dissipated (Frisch, 1995; Turiel et al., 2008). At difference of fractals, where a single exponent (the fractal

3.4. EFFECT OF SAMPLING SCALE ON FSLES

dimension) is enough to describe it, multifractal objects need of a continuous spectrum of exponents (the so-called singularity spectrum) to be completely defined. This is because they show local scale-invariance, as compared with global scale-invariance of standard fractals. 2d or quasigeostrophic turbulence have an inverse energy cascade towards large scales, but also a direct enstrophy cascade towards small scales. This is linked also to the direct cascade towards small scales of the variance of transported scalars. This last cascade is the relevant one for the FSLE structure: The ridges of FSLE, as well as other local Lyapunov measures, move as transported scalars. The reason why they are filamental is the same that for scalar or vorticity filamentation: even though large-energy vortices are the largest ones, they stretch and fold filaments of fluid and of vorticity, and it is expected that FSLE filaments will resemble the multifractal character of turbulent vorticity.

Thus, to study if FSLEs behave like multifractal fields we have computed their probability density distribution, $P(\delta_0, \Lambda)$, for different resolutions δ_0 . It must follow that for any resolution scale δ_0 of FSLE grid we should observe:

$$P(\delta_0, \Lambda) \propto \delta_0^{d-D(\Lambda)}, \quad (3.2)$$

where d is the dimension of the space embedding the FSLE-ridges curves, i.e., $d = 2$, and $D(\lambda)$ is the fractal dimension of these curves, which is a number between 1 and 2. Notice that as $d - D(\Lambda)$ is a positive quantity, $P(\delta_0, \Lambda)$ becomes smaller as δ_0 is reduced. In fact, a characteristic signature of multifractal scaling is having a scale-dependent histogram which becomes more strongly peaked as the resolution scale becomes smaller. We know that there is a FSLE for each domain point, so we can normalize the FSLE distribution by its maximum (that will be attained for a value Λ_c) and then retrieve the associated singularity spectrum (the continuous set of exponents characterizing the multifractal system) according to the following expression:

$$D(\Lambda) = d - \frac{\log \frac{P(\delta_0, \Lambda)}{P(\delta_0, \Lambda_c)}}{\log \delta_0}. \quad (3.3)$$

In Figure 3.3, top, we show the histograms (averaged over 30 snapshots distributed among 15 months) normalized to have the same unitary area. One can see that when the resolution gets finer the $P(\delta_0, \Lambda)$ narrows, and the peak height increases, in agreement with Equation (3.2). According to the definition of Microcanonical Multifractals Isern-Fontanet et al., 2007; Turiel et al., 2008, the system will be multifractal if the curves $D(\Lambda)$ estimated at different resolutions δ_0 using Equation (3.3) are all equal. This can be observed in Figure 3.3, bottom.

CHAPTER 3. RELIABILITY OF FSLE

The collapse of the four curves is not perfect due to the lost of translational invariance produced by the small size of the domain -the Balearic basin- that we analyze, but improves for smaller δ_0 . Thus, the interfaces of constant Λ values build an approximate multifractal hierarchy and generalized scale invariance is present in the FSLE field.

The above study of the scaling properties of the distribution of FSLEs at the different resolution scales reveal that they are multifractal. This implies that changes in scale are accounted for by a well-defined transformation, namely a cascade multiplicative process (Frisch, 1995; Turiel et al., 2008). It also implies that information is hierarchized Turiel and del Pozo, 2002 and so what is obtained first, at the coarsest scales, is the most relevant information. Due to multifractality, small-scale structures, as unveiled by the FSLEs, with typical sizes smaller than that of the velocity resolution, are determined by the larger ones and the multi-scale invariance properties. The origin of these small scale structures has already been discussed: the stretching and folding in between large coherent vortices. Thus, no artificiality is induced by this calculation and the robustness of FSLE analysis under changes in scale is confirmed.

A different question concerns the robustness of FSLEs when the V-grid is changed. For instance, when a diagnosis is obtained with a low-resolution velocity field, is this diagnosis compatible with a later improved observation of the velocity? The answer is yes. In Figure 3.4 we show the FSLEs obtained at a fixed F-grid resolution of $1/8^\circ$ for varying velocity resolutions (namely, $1/8^\circ$, $1/4^\circ$ and $1/2^\circ$). The change of resolution of the velocity grid is performed as indicated in Appendix 3.7. We observe that the global features observed with the coarser resolution V-grid are kept when this is refined. Obviously, as the velocity field is described with enhanced resolution new details (with short-range effect on the flow structure and so no contradicting the large-scale picture) become apparent in the FSLEs. A more quantitative way to confirm this assertion can be seen in fig. 3.5. Here we plot the instantaneous relative error

($\epsilon_{ij} = \sqrt{\frac{1}{N_U} \sum_{\mathbf{x}} |\Lambda_i(\mathbf{x}) - \Lambda_j(\mathbf{x})|^2 / |\Lambda_i(\mathbf{x})|^2}$, with the sum running over the N_U spatial points with the value of Λ larger than the threshold U) between any i and j - pair of FSLE fields of Fig. 3.4, when we change the threshold. I.e., we are comparing the snapshots of FSLEs for values larger than U . In all the plots the relative error decreases when the value of the threshold increases. Thus, in the global features (which are organized by the large Λ values) the images in Fig. 3.4 are similar. In particular, the error between Fig. 3.4b) and Fig. 3.4c) has always relatively small values.

The effect of refining the V-grid is not only introducing new small-scale structures: there is a consistent increase in the values of the FSLEs as the V-grid is

3.4. EFFECT OF SAMPLING SCALE ON FSLES

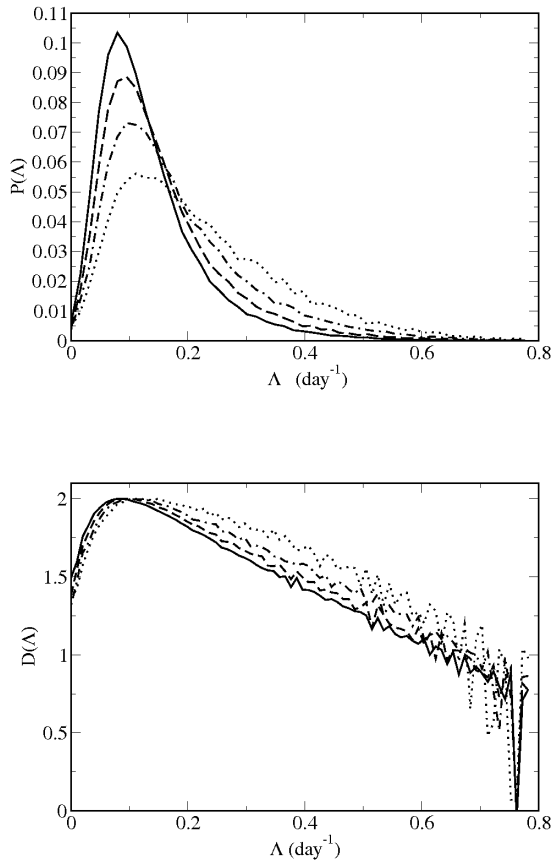


Figure 3.3: Top: Comparison of the probability density functions $P(\delta_0, \Lambda)$ for the FSLEs at different resolutions. It is obtained from the temporal average (30 snapshots) of histograms. Dotted line is for $\delta_0 = 1/8^\circ$, dashed-dotted line $\delta_0 = 1/16^\circ$, dashed $\delta_0 = 1/32^\circ$, and solid line for $\delta_0 = 1/64^\circ$. **Bottom:** $D(\Lambda)$ for different values of δ_0 . Dotted for $\delta_0 = 1/8^\circ$, dashed-dotted line $\delta_0 = 1/16^\circ$, dashed $\delta_0 = 1/32^\circ$, and solid line line for $\delta_0 = 1/64^\circ$.

refined. The histograms of the FSLEs, Λ_f , for a given velocity resolution conditioned by the FSLEs, Λ_c , obtained from a coarser velocity field are shown in Figure 3.6. The modal line (the line of maximum conditioned probability) is

CHAPTER 3. RELIABILITY OF FSLE

close to a straight line. The best linear regression fits are $\Lambda_{1/8^\circ} = 1.08\Lambda_{1/4^\circ} + 0.05$ (correlation coefficient, $\rho = 0.69$) and $\Lambda_{1/4^\circ} = 0.99\Lambda_{1/2^\circ} + 0.04$ ($\rho = 0.69$). According to these results, we can approximate the finer FSLEs Λ_f in terms of the coarser FSLEs Λ_c as:

$$\Lambda_f(\vec{x}) = \Lambda_c(\vec{x}) + \Delta\Lambda_{fc}, \quad (3.4)$$

where the quantity $\Delta\Lambda_{fc}$ determines the contribution to the FSLE by the small-scale variations in velocity not accounted for by the lower resolution version of this field. It is hence independent of Λ_c , so the intercept of the vertical axis with the linear regression equals the mean of this quantity.

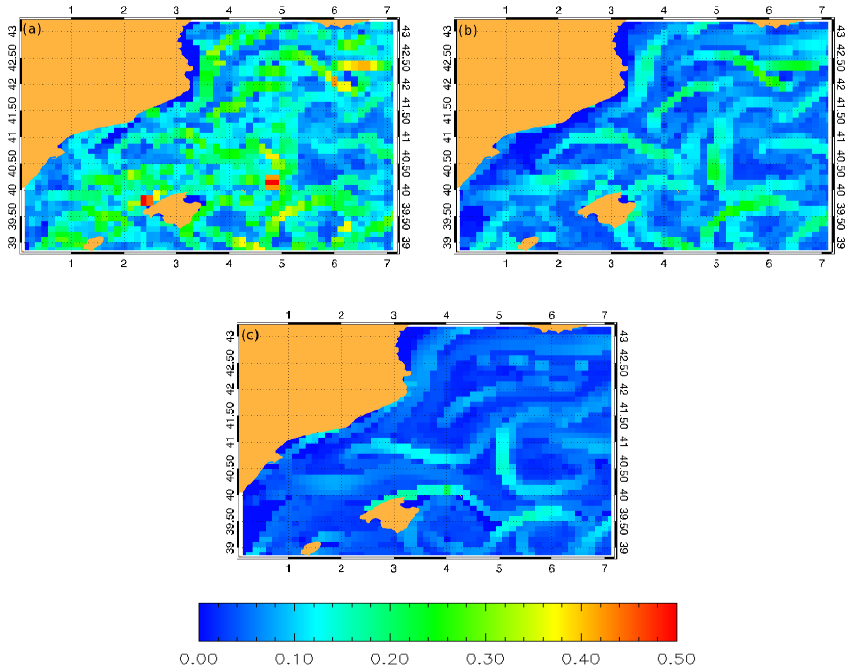


Figure 3.4: Snapshots of FSLEs backward in time starting from day 640 at different initial V-grid resolutions: a) $\Delta_0 = 1/8^\circ$, b) $\Delta_0 = 1/4^\circ$, c) $\Delta_0 = 1/2^\circ$. In all of them we take the same F-grid resolution of $\delta_0 = 1/8^\circ$, and $\delta_f = 1^\circ$. The color bar has units of day^{-1} .

3.5. EFFECT OF NOISE ON FSLES

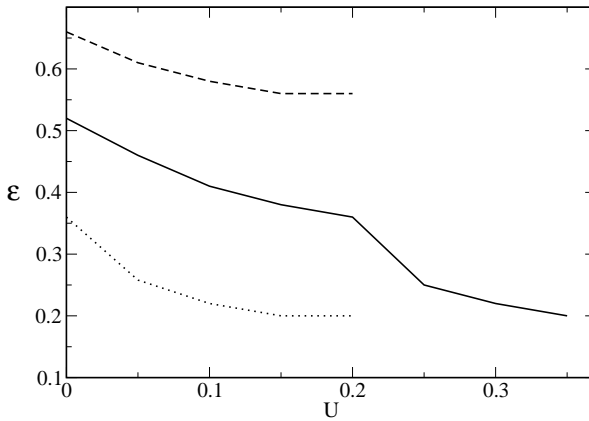


Figure 3.5: Relative error between the FSLE fields drawn in Fig. 3.4, at locations having a FSLE value larger than a threshold U . Dashed line is for ϵ between Fig. 3.4a) and Fig. 3.4c); solid line is between Fig. 3.4a) and Fig. 3.4b); and dotted line is the error between Fig. 3.4b) and Fig. 3.4c). In all of them the relative error decreases when the threshold increases.

A linear dependence of Λ_f with Λ_c when scale is changed implies that FSLEs follow a multiplicative cascade (Turiel et al., 2006, 2008), an essential ingredient in multifractal systems which gives further confirmation to our previous results. We have hence shown that a) the dependence of FSLEs on both types of scale parameters reveals a multifractal structure; b) what is diagnosed at the coarser scales is still valid when scale is refined (although as V-grid resolution is increased the reference level of FSLEs is increased by a constant).

3.5

Effect of noise on FSLEs

We compute the FSLEs after applying a random perturbation to all components of the velocity field. The velocity is changed from (u, v) to (u', v') , with $u'(x, t) = u(x, t)(1 + \alpha\eta_x(\mathbf{x}, t))$ and $v'(\mathbf{x}, t) = v(\mathbf{x}, t)(1 + \alpha\eta_y(\mathbf{x}, t))$. $\{\eta_x(\mathbf{x}, t), \eta_y(\mathbf{x}, t)\}$ are sets of Gaussian random numbers of zero mean and unit variance. α measures the

CHAPTER 3. RELIABILITY OF FSLE

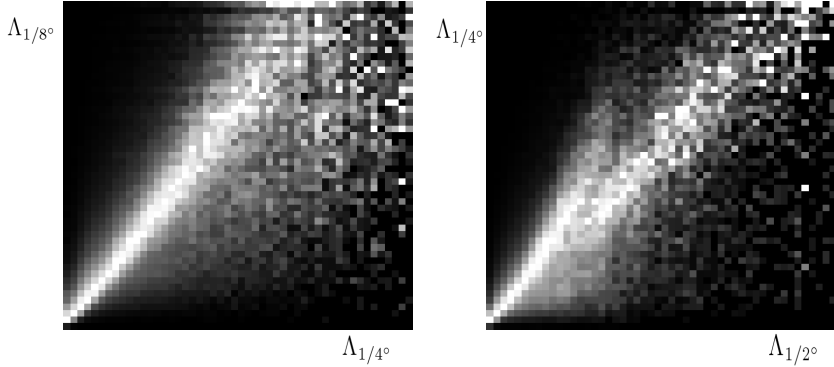


Figure 3.6: Probability distributions (coded as grey levels) of FSLEs derived at a coarse velocity resolution (Λ_c , vertical axis) conditioned by a finer velocity grid (Λ_f , horizontal axis). The range of values of both axes run linearly from 0 to 0.5 day^{-1} . To obtain a statistics large enough, we have considered 30 FSLEs snapshots, starting from $t = 640$ up to $t = 1075$ days, in steps of 15 days. The brightest color (pure white) corresponds to the maximum probability at each column; the darkest color (pure black) corresponds to zero. *Left panel:* FSLEs derived from $1/4^\circ$ velocities conditioned by FSLEs at original $1/8^\circ$ velocities. *Right panel:* FSLEs from $1/2^\circ$ velocities conditioned by FSLEs from $1/4^\circ$ velocities.

relative size of the perturbation. We introduce three different kinds of error: uncorrelated noise, i.e. different and uncorrelated values of $\{\eta_x(\mathbf{x}, t), \eta_y(\mathbf{x}, t)\}$ for each \mathbf{x} and t ; correlated in time and uncorrelated in space (uncorrelated for different \mathbf{x} but the same values at given \mathbf{x} for different t); and correlated in space and uncorrelated in time (uncorrelated values for different t , but the same values for different \mathbf{x} at fixed t). Note that the perturbation is proportional to the original velocity. Figure 3.7 shows a snapshot of FSLEs for the velocity field perturbed by uncorrelated noise of a relative size $\alpha = 10$, i.e., noise is 10 times larger than the amplitude of the initial velocity field. The computed Lagrangian structures look rather the same, despite the large size of the perturbation introduced. This is confirmed by computing the histograms of the FSLEs (not shown), which turn out to be very similar. The reason for this is again the average along trajectories made to compute the FSLEs and also the fact that the perturbation added to the velocity is proportional to the velocity itself.

In order to quantify the influence of the velocity perturbation in the FSLE calculation we compute the relative error (RE) of perturbed FSLEs with respect to unperturbed FSLEs, $\langle \epsilon(t) \rangle$, at a given instant of time, and then averaging in

3.5. EFFECT OF NOISE ON FSLES

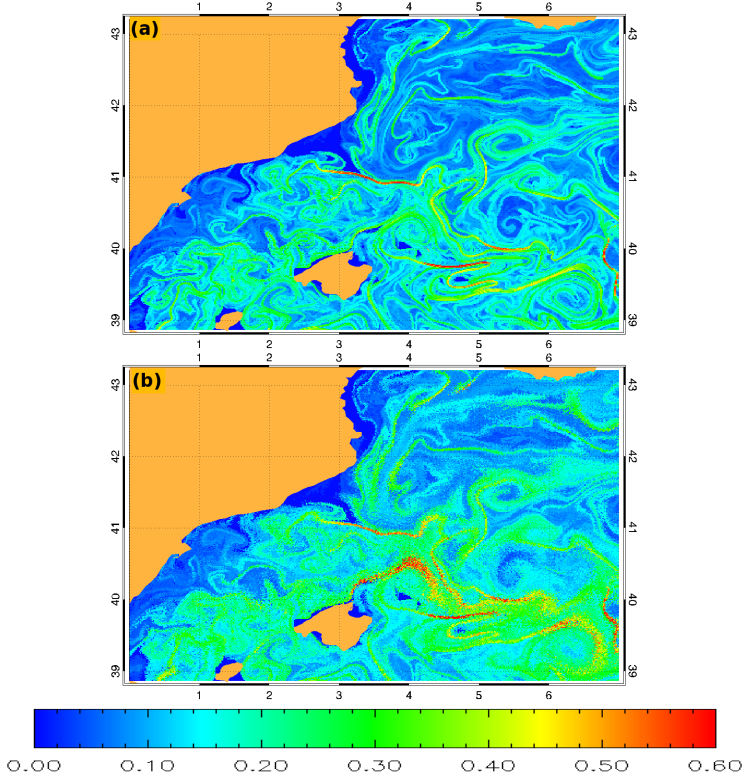


Figure 3.7: Snapshots of FSLEs calculated backwards in time starting from day 600 at fixed spatial resolution ($\delta_0 = 1/64^\circ$), and at different α : a) $\alpha = 0$, b) $\alpha = 10$. In both of them we take $\delta_f = 1^\circ$. The color bar has units of day^{-1} . Initial conditions for which the separation δ_f has not been reached after 600 days are assigned a value $\Lambda = 0$.

time (we have $M = 100$ snapshots : $t = t_1, \dots, t_M$) as:

$$\epsilon(t_i) = \sqrt{\frac{1}{N} \sum_{\mathbf{x}} \frac{|\Lambda^\alpha(\mathbf{x}, t_i) - \Lambda(\mathbf{x}, t_i)|^2}{|\Lambda(\mathbf{x}, t_i)|^2}}, \quad \langle \epsilon(t) \rangle \equiv \frac{1}{M} \sum_{i=1}^M \epsilon(t_i). \quad (3.5)$$

$\Lambda(\mathbf{x}, t_i)$ and $\Lambda^\alpha(\mathbf{x}, t_i)$ are the FSLEs fields without and with inclusion of the perturbation in the velocity data, respectively. The sum over \mathbf{x} runs over the $N = 2679$ spatial points. Figure 3.8 shows the average RE as a function of α . It must be remarked that the RE has always small values: even for $\alpha = 10$ the RE remains

CHAPTER 3. RELIABILITY OF FSLE

smaller than 0.23 for the three kinds of noise. To get an idea of how relevant these quantities are, we have computed the RE of shuffled FSLEs (permuting locations at random) with respect to the original ones, and obtained a value of 1.143. FSLEs are thus robust against noise; the reason is the averaging effect produced when computing them by integrating over trajectories which extend in time and space, that tends to cancellate random errors. The most uncorrelated the error the most effective this averaging process turns out to be.

Now we proceed by adding noise to the particle trajectories. This is a simplified way of including unresolved small scales in the Lagrangian computations (Griffa, 1996). To be precise we solve numerically the system of Equations (3.6) and (3.7), where a stochastic term with a Gaussian random number and an effective eddy-diffusion, D , has been added:

$$\frac{d\phi}{dt} = \frac{u(\phi, \lambda, t)}{R \cos(\lambda)} + \frac{\sqrt{2D}}{R \cos(\lambda)} \xi_1(t), \quad (3.6)$$

$$\frac{d\lambda}{dt} = \frac{v(\phi, \lambda, t)}{R} + \frac{\sqrt{2D} \xi_2(t)}{R}. \quad (3.7)$$

$\xi_i(t)$ $i = 1, 2$ are the components of a two-dimensional Gaussian white noise with zero mean and correlations $\langle \xi_i(t) \xi_j(t') \rangle = \delta_{ij} \delta(t - t')$. Eqs. (3.6 and 3.7) use a simple white noise added to the trajectories. A more realistic representation of small-scale Lagrangian dispersion in turbulent fields requires using other kinds of correlated noises (Griffa, 1996) but, as we are interested in examining influences of the missing scales, it is convenient to use white noise, since this would represent the extreme case of very irregular trajectories which gives an upper bound to the effects of more realistic smoother small scales. Thus the tests presented here are similar to the ones considered before (perturbation of the velocity) when adding uncorrelated perturbations to the velocity, but here the perturbation acts at arbitrarily small scales, as appropriate for a turbulent field, instead of being smooth below a cutoff scale, as appropriate for modelling observational errors.

For the diffusivity we use Okubo's empirical formula Okubo, 1971, which relates the effective eddy-diffusion, D in m^2/s , with the spatial scale, l in meters: $D(l) = 2.055 \cdot 10^{-4} l^{1.15}$. If we take $l = 12 \text{ km}$, which is the approximate length corresponding to the $1/8^\circ$ DieCAST resolution at Mediterranean latitudes, we obtain $D \sim 10 \text{ m}^2\text{s}^{-1} \equiv D_0$.

In Figure 3.9 we show particle trajectories without (top panel) and with (bottom panel) eddy diffusion. As expected diffusion introduces small scale irregularities on the trajectories, and also substantial dispersion at large scales. In Figure 3.10,

3.5. EFFECT OF NOISE ON FSLES

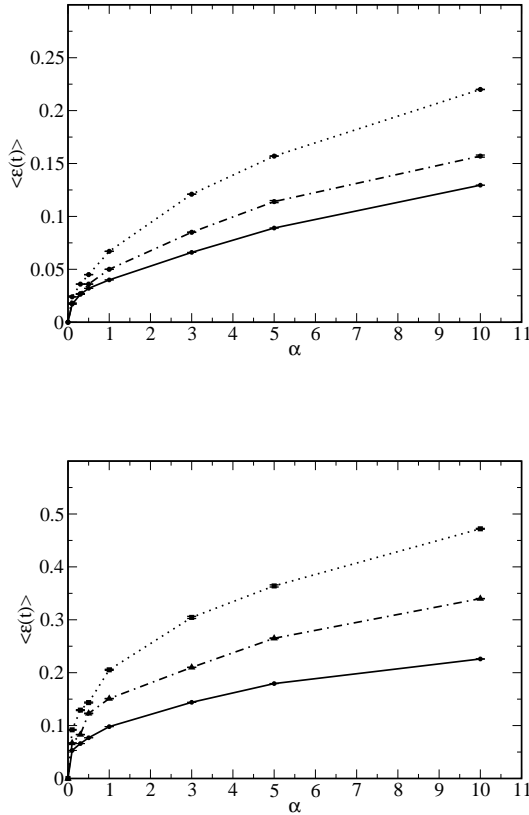


Figure 3.8: Relative error $\langle \epsilon(t) \rangle$ of the FSLE fields for different perturbation intensity α in the velocity data. Solid line is for uncorrelated noise in space and time, dashed-dotted line is for uncorrelated noise in time and correlated in space, and dotted line is for uncorrelated noise in space and correlated in time. $\langle \epsilon(t) \rangle$ is obtained by averaging the RE in 100 snapshots (see Eq. (3.5)). The error bar is the statistical error of the temporal average $\langle \epsilon(t) \rangle$. Left: spatial resolution $\delta_0 = 1/8^\circ$. Right: spatial resolution $\delta_0 = 1/64^\circ$. In all calculations we take $\delta_f = 1^\circ$

FSLEs with $\delta_0 = 1/64^\circ$ $D = 0 \text{ m}^2\text{s}^{-1}$ and $D = 0.9 \text{ m}^2\text{s}^{-1}$ (obtained for this scale by Okubo's formula for spatial resolution) are shown. We can see that the main

CHAPTER 3. RELIABILITY OF FSLE

mesoscale structures are maintained, but small-scale filamental structures are lost since filaments become blurred. This is somehow expected a priori because diffusion introduces a new length scale l_D proportional to \sqrt{D} . A pointwise comparison of noiseless and noise-affected FSLEs makes no sense, since the noise-induced blurring disperses FSLEs values specially at places with low values, see Figure 3.10. But for Lagrangian diagnostics high FSLE values are much more relevant, so we compute the error restricted to the places where $\Lambda > 0.2$ for $D = 0$. Left panel of Figure 3.11 shows the RE respect to the $D = 0$ case (applying Equation (3.5)) for different values of D . The RE monotonously increases with D , but remains smaller than 0.6 for the largest value of D considered. Again, to get an idea of how relevant these relative errors are, we have to compare them with the RE of shuffled FSLEs, of value 1.143.

As a matter of fact, diffusion introduces an effective observation scale, and one should not go beyond that limit to obtain sensible results; this is illustrated in the right panel of Figure 3.11. As shown in the figure, for fixed eddy diffusivity (in the case of the figure, $D_0 = 10m^2s^{-1}$), when δ_0 becomes greater the error diminishes. Hence, a fixed diffusion will eventually be negligible at a scale large enough, in this way determining an observation scale. A completely different situation is given when the eddy-diffusion depends on the scale according to Okubo's formula (in our case, at $\delta_0 = 1/16^\circ$ $D = 4,5m^2s^{-1}$; at $\delta_0 = 1/32^\circ$ $D = 2m^2s^{-1}$; and at $\delta_0 = 1/64^\circ$, $D = 0.9m^2s^{-1}$). Now $\langle \epsilon(t) \rangle$ takes a constant value close to 0.45, meaning that Okubo's diffusion behaves the same at all scales. This is expected since Okubo's law is based on the hypothesis that unsolved scales act as scale-dependent diffusers, like in turbulence (Frisch, 1995). Our result is consistent with the ideas behind Okubo's hypothesis.

We can characterize the effective diffusion scale from the properties of the histograms. In Figure 3.12 we present the histograms of FSLEs at different F-grid resolutions, and including or not eddy diffusion which takes always the same value $D_0 = 10m^2s^{-1}$. For $\delta_0 = 1/8^\circ$ the histograms with and without diffusion are almost coincident. This is due to the fact that the value of diffusion we are using is the one corresponding, by the Okubo's formula, to $1/8^\circ$. i.e., we are parameterizing turbulence below $1/8^\circ$, and this has no effects on the FSLE computations if the minimum scale considered is also $1/8$. However, this behavior is different for smaller δ_0 (always keeping $D_0 = 10m^2s^{-1}$). The histograms for $\delta_0 = 1/16, 1/64^\circ$, with and without diffusion, are clearly different, those including diffusion becoming closer to the histogram for $\delta_0 = 1/8^\circ$.

3.5. EFFECT OF NOISE ON FSLES

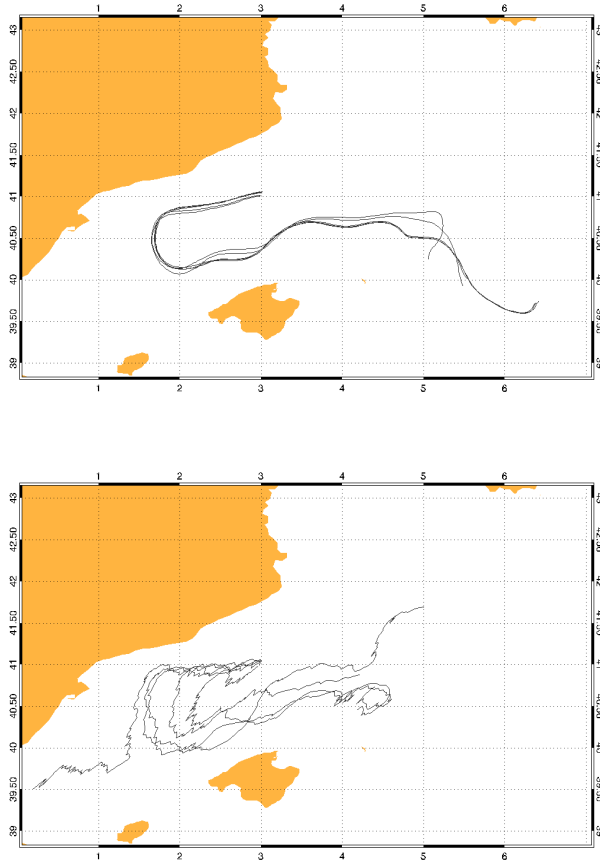


Figure 3.9: Trajectories of five particles without diffusion (top) and with diffusion (bottom). The difference in the initial positions of all five particles is about 0.06° , and we use these initial conditions in both computations. The trajectories were computed for 50 days of integration. We used the eddy-diffusion $D_0 \sim 10m^2s^{-1}$ assigned by the Okubo formula to the resolution of the DieCAST model at Mediterranean latitudes.

CHAPTER 3. RELIABILITY OF FSLE

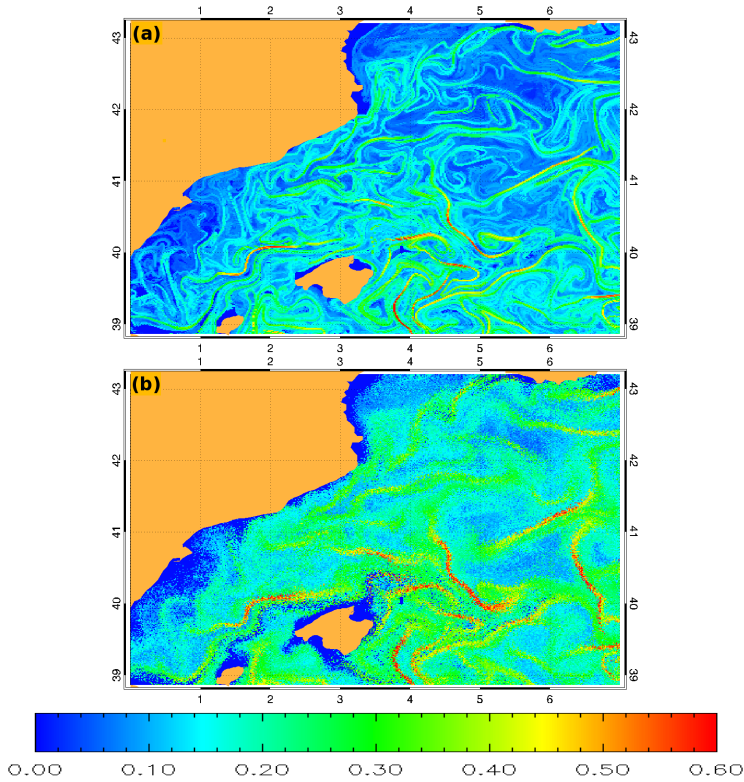


Figure 3.10: FSLEs computed backwards from day 500 at the same spatial resolution ($\delta_0 = 1/64^\circ$), and for different eddy-diffusion values: a) $D = 0 \text{ m}^2 \text{ s}^{-1}$ b) $D = 0.9 \text{ m}^2 \text{ s}^{-1}$. We take $\delta_f = 1^\circ$. The color bar has units of day^{-1} . Initial conditions for which the separation δ_f has not been reached after 500 days are assigned a value $\Lambda = 0$.

3.6

Conclusions

In this Chapter, we have analyzed the sensibility of FSLE-based analyses for the diagnostic of Lagrangian properties of the ocean (most notably, horizontal mixing and dispersion). Our sensibility tests include the two most important effects when facing real data, namely dynamics of unsolved scales and of noise. Our results show that even if some dynamics are missed (because of lack of

3.6. CONCLUSIONS

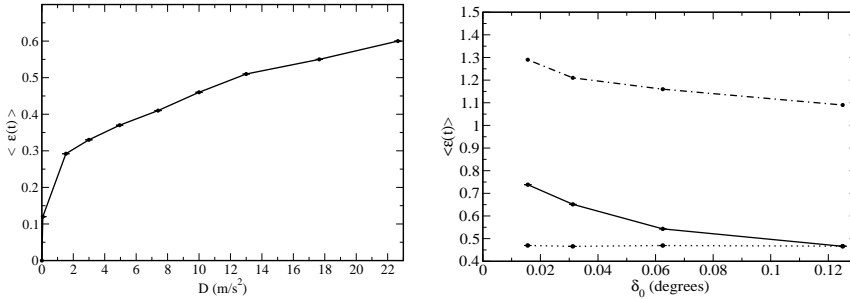


Figure 3.11: Left: Relative error $\langle \epsilon(t) \rangle$ of the FSLE at the different values of D in the particle trajectories, with respect to the $D = 0$ case. Spatial resolution is $\delta_0 = 1/8^\circ$, and $\delta_f = 1^\circ$. $\langle \epsilon(t) \rangle$ is obtained by temporally averaging the relative errors in 100 snapshots. The (small) error bars indicate the statistical error in the $\langle \epsilon(t) \rangle$ average. Right: Dotted line is the RE $\langle \epsilon(t) \rangle$ of the FSLE at different spatial resolution δ_0 and at one assigned eddy-diffusion D for every spatial resolution in the particle trajectories with respect to the $D = 0$ case. Solid line is the RE $\langle \epsilon(t) \rangle$ of the FSLE at different spatial resolution δ_0 , and at the same eddy-diffusion $D_0 = 10m^2s^{-1}$ in the particle trajectories with respect to the $D = 0$ case. Dashed-dotted line is the RE of shuffled FSLE with respect to the original case ($D = 0$) at different spatial resolution. $\langle \epsilon(t) \rangle$ by temporally averaging the RE in 100 snapshots. The (small) error bar indicates the statistical error in the $\langle \epsilon(t) \rangle$ average. In all of them we take $\delta_f = 1^\circ$.

sampling or inaccuracy of any kind in the measurements) FLSEs results would still give an accurate picture of Lagrangian properties, valid for the solved scales. This does not mean that scale and/or noise leave FSLEs unaffected, but the way in which they modify this Lagrangian diagnostics can be properly accounted.

Lagrangian methods provide answers to problems which have a deep impact on risk management (e.g. control of pollutant dispersion) as well as on ecosystem analysis (e.g. tracking nutrient mixing and transport, identifying the role of horizontal mixing in primary productivity). They utterly will give hints about energy exchanges in the upper ocean and will help in understanding processes driving global change in the oceans. The use of Lagrangian techniques for the assessment of the transport and mixing properties of the ocean has grown in importance in the latest years, with increasing efforts devoted to the implementation of appropriate techniques but few studies on the validity of the results

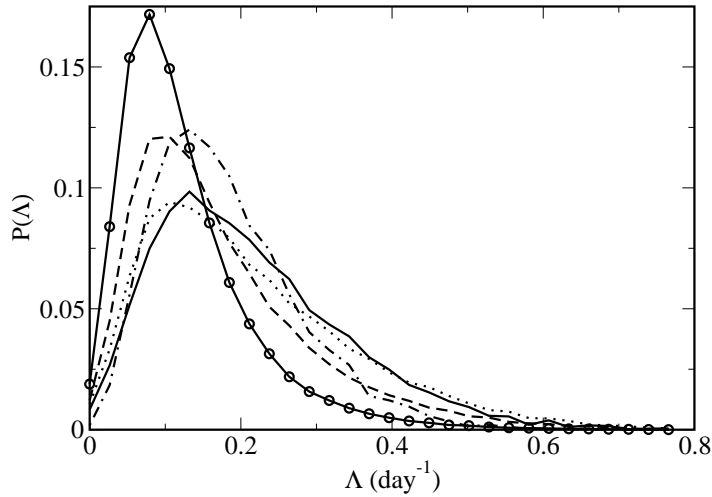


Figure 3.12: Comparison between probability density function for the FSLEs at different resolutions with different values of eddy-diffusion, and without diffusion. It is obtained from the temporal average (30 snapshots) of histograms. Solid line for $\delta_0 = 1/8^\circ$ with diffusion, dotted $\delta_0 = 1/8^\circ$ without diffusion, dashed $\delta_0 = 1/16^\circ$ without diffusion, dashed-dotted line for $\delta_0 = 1/64^\circ$ with diffusion, and circle-line for $\delta_0 = 1/64^\circ$ without diffusion.

when real data, affected by realistic constraints, are used. Our work will serve to unify and interpret the analyses provided by Lagrangian methods when real data are processed.

3.7

Appendix: Change of resolution of the velocity grid

In order to reduce the resolution of a given velocity grid, the easiest way would be by subsampling the existing grid points or by block-averaging the values of the velocity and assign the result to the central grid point. However, in the case of a complex boundary such as the Mediterranean coast such a strategy

3.7. APPENDIX: CHANGE OF RESOLUTION OF THE VELOCITY GRID

is strongly inconvenient, as the coarsening of the grid would imply to change land circulation barriers (islands, straits). The disappearance of a land barrier or the creation of a new one as a consequence of the coarsening would imply a dramatic change in the value of FSLEs at all points affected by the modified circulation; if the circulation patterns are rather complex almost every point could be affected. We have thus preferred to smooth the velocity with a convolution kernel weighted with a local normalization factor, and keeping the original resolution for the data so land barriers are equally well described than in the original data.

We define the coarsening kernel of scale factor s , κ_s , as:

$$\kappa_s(x, y) = e^{-\frac{x^2+y^2}{2s^2}} \quad (3.8)$$

We disregard the introduction of a normalization factor at this point since we will need to normalize locally later. The coarsened version of the velocity vector would hence be given by the convolution of this kernel with the velocity, denoted by $\kappa_s \star \vec{v}$. A coarsening convolution kernel turns out to be convenient with almost horizontal fields, as the derivatives commute with the convolution operator so if $\nabla \vec{v} \approx 0$ hence $\kappa_s \star \nabla \vec{v} \approx 0$. However, this coarsening scheme needs to be improved. By convention, we take the velocity \vec{v} as zero over land points. For that reason, a simple convolution does not produce a correct coarsened version of the velocity because points close to land would experience a loss of energy. The easiest way to correct this is to normalize by the weight of the sea points. Let us first define the sea mask $M(x, y)$ as 1 over the sea and 0 over the land. The normalization weight is given by $\kappa_s \star M$. For points very far from the land, this weight is just the normalization of κ_s . For points surrounded by land points the weight takes the contributions from sea points only. We thus define the coarsened version by a scale factor s of the velocity, \vec{v}_s , as:

$$\vec{v}_s = \frac{\kappa_s \star \vec{v}}{\kappa_s \star M} \quad (3.9)$$

In Figure 3.13 we show two examples of coarsened velocities. We can see that typical circulation patterns are coarsened as s increases, while land obstacles are preserved. In fact, if Δ_0 is the velocity resolution scale, the effective resolution scale of \vec{v}_s is $s\Delta_0$ (the nominal resolution, on the contrary, is the original one, Δ_0).

CHAPTER 3. RELIABILITY OF FSLE

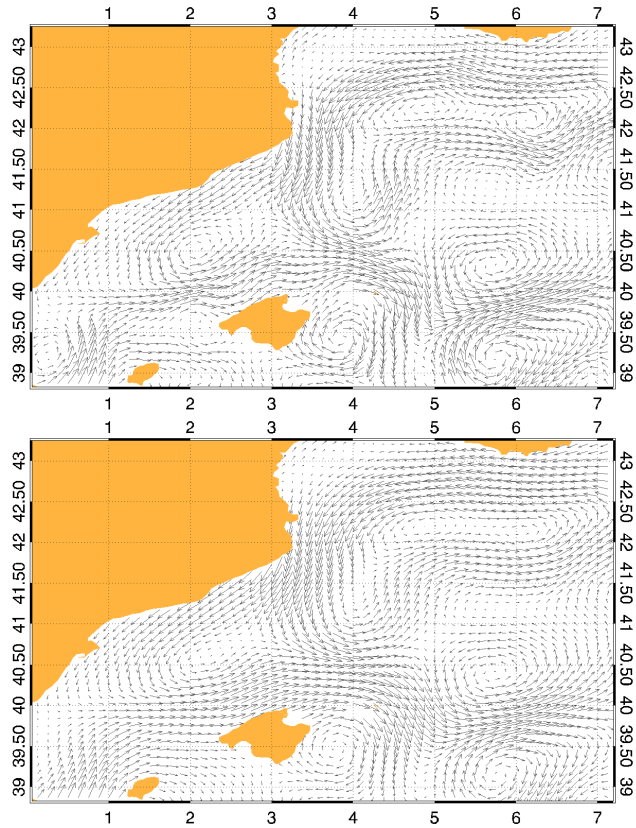


Figure 3.13: Top: Velocity field coarsened by a scale factor $s = 2$, for a equivalent resolution $\Delta_0 = 1/4^\circ$. **Bottom:** Velocity field coarsened by a scale factor $s = 4$, for a equivalent resolution $\Delta_0 = 1/2^\circ$.

Characterization of horizontal transport in the global ocean

Recent work on Lagrangian descriptors has shown that Lyapunov Exponents can be applied to observed or simulated data to characterize the horizontal stirring and transport properties of the oceanic flow. However, a more detailed analysis of regional dependence and seasonal variability was still lacking. In this paper, we analyze the near-surface velocity field obtained from the *Ocean general circulation model For the Earth Simulator* (OFES) using Finite-Size Lyapunov Exponents (FSLE). We have characterized regional and seasonal variability. Our results show that horizontal stirring, as measured by FSLEs, is seasonally-varying, with maximum values in Summer time. FSLEs also strongly vary depending on the region: we have first characterized the stirring properties of Northern and Southern Hemispheres, then the main oceanic basins and currents. We have finally studied the relation between averages of FSLE and some Eulerian descriptors such as Eddy Kinetic Energy (EKE) and vorticity (ω) over the different regions. These relations reveal the existence of dynamical and dispersion relations which characterize the dynamics of different ocean regions, which can be used for instance to explain differences in the distribution of quantities of biological interest.

Introduction

A detailed knowledge of the transport, dispersion, stirring and mixing mechanisms of water masses across the global ocean is of crucial interest to fully understand, for example, heat and tracer budgets, or the role of oceans in climate regulation. There has been a recent strong activity in the study of these processes from a Lagrangian perspective. Some works have addressed the *global* variability of them using finite-time Lyapunov exponents (FTLEs) computed from currents derived from satellite altimetry (Beron-Vera et al., 2008; Waugh and Abraham, 2008). These studies quantify stirring intensity, and identify mesoscale eddies and other Lagrangian Coherent Structures (LCSs). Furthermore, previous works (Waugh et al., 2006) pointed out relationships between Lagrangian and Eulerian quantifiers of stirring/mixing activity (FTLEs and Eddy Kinetic Energy (EKE) or mean strain rate).

Having in mind the implications for the distribution of biogeochemical tracers, our goal is to extend the previous works to provide detailed seasonal analysis and a comparative study between different ocean regions and different scales: Earth's hemispheres, ocean basins, and boundary currents. To this end we use finite-size Lyapunov exponents (FSLEs). These quantities are related to FTLEs since they also compute stretching and contraction time scales for transport, but they depend on explicit spatial scales which are simple to specify and to interpret in oceanographic contexts (d'Ovidio et al., 2004, 2009; Hernández-Carrasco et al., 2011; Tew Kai et al., 2009). In particular we will focus on the impact on transport of mesoscale processes, for which characteristic spatial scales as a function of latitude are well known. We are also interested in checking the existence of relationships between Lagrangian measures of horizontal stirring intensity, as given by averages of finite-size Lyapunov exponents (FSLE), and other dynamic, Eulerian quantities, such as EKE or vorticity. Such a functional relation does not need to hold in general, but may be present when there is a connection between the mechanisms giving rise to mesoscale turbulence (probably, baroclinic instability) and horizontal stirring.

The paper is organized as follows. In Section 4.2 we describe the data and tools used in this study. In section 4.3 we first present the geographical and seasonal characterization of the horizontal stirring, and then we investigate the relation of FSLE with EKE and vorticity. Finally, in the Conclusions we present a summary and concluding remarks.

Data and Methods

Our dataset consists of an output from the *Ocean general circulation model For the Earth Simulator* (OFES) (Masumoto et al., 2004; Masumoto, 2010). This is a near-global ocean model that has been spun up for 50 years under climatological forcing taken from monthly mean NCEP (United States National Centers for Environmental Prediction) atmospheric data. After that period the OFES is forced by the daily mean NCEP reanalysis for 48 years from 1950 to 1998. See Masumoto et al. (2004) for additional details on the forcing. The output of the model corresponds to daily data for the last 8 years. Horizontal angular resolution is the same in both the zonal, ϕ , and meridional, θ , directions, with values of $\Delta\theta = \Delta\phi = 1/10^\circ$. The output has been interpolated to 54 vertical z-layers and has a temporal resolution of one day. The velocity fields that we have used in this work correspond to the first two years, 1990 and 1991, of the output. Vertical displacements are unimportant during the time scales we consider here so that, despite horizontal layers are not true isopycnals, most fluid elements remain in their initial horizontal layer during the time of our Lagrangian computation. Thus we use in our analysis horizontal velocities in single horizontal layers. We refer to recent works (Özgökmen et al., 2011; Bettencourt et al., 2012) for Lyapunov analyses considering vertical displacements. Unless explicitly stated, our calculations are for the second output layer, at 7.56 m depth, which is representative of the surface motion but limits the effect of direct wind drag (we have also studied the layer at 97 m depth; results on this layer are briefly shown in Fig. 4.3). See Masumoto et al. (2004) and Masumoto (2010) for a thorough evaluation of the model performance.

Among Lagrangian techniques used to quantify ocean transport and mixing, local Lyapunov methods are being widely used. The idea in them is to look at the dispersion of a pair of particles as they are transported by the flow. To calculate FTLEs, pairs of particles infinitesimally close are released and their separation after a finite time is accounted; for FSLEs (Aurell et al., 1997) two finite distances are fixed, and the time taken by pairs of particles to separate from the smallest to the largest is computed. Both methods thus measure how water parcels are stretched by the flow, and they also quantify pair dispersion. The methods can also be tailored to reveal two complementary pieces of information. On the one hand they provide time-scales for dispersion and stirring process (Artale et al., 1997; Aurell et al., 1997; Buffoni et al., 1997; Lacorata et al., 2001; d’Ovidio et al., 2004; Haza et al., 2008; Poje et al., 2010). On the other, they are useful to identify Lagrangian Coherent Structures (LCSs), persistent structures that organize the fluid transport (Haller and Yuan, 2000; Haller, 2001; Boffetta et al., 2001; Joseph

CHAPTER 4. GLOBAL CHARACTERIZATION OF STIRRING

and Legras, 2002; Koh and Legras, 2002; Lapeyre, 2002; Haller, 2002; Shadden et al., 2005; Beron-Vera et al., 2008; d’Ovidio et al., 2009; Tew Kai et al., 2009; Peacock and Dabiri, 2010). This second capability arises because the largest Lyapunov values tend to concentrate in space along characteristic lines which could often be identified with the manifolds (stable and unstable) of hyperbolic trajectories (Haller and Yuan, 2000; Haller, 2001, 2002, 2011; Shadden et al., 2005). Since these manifolds are material lines that can not be crossed by fluid elements, they strongly constrain and determine fluid motion, acting then as LCSs that organize ocean transport on the horizontal. Thus, eddies, fronts, avenues and barriers to transport, etc. can be conveniently located by computing spatial Lyapunov fields. We note however that more accurate characterization of LCSs can be done beyond Lyapunov methods (Haller, 2011), that high Lyapunov values can correspond also to non-hyperbolic structures with high shear (d’Ovidio et al., 2009), and that an important class of LCSs is associated to small, and not to large values of the Lyapunov exponents (Rypina et al., 2006; Beron-Vera et al., 2010).

In the present work, however, we are more interested in obtaining the first type of information, i.e. in extracting characteristic dispersion time-scales, quantifying the intensity of stirring, for the different ocean regions and seasons. In particular we want to focus on the transport process associated to eddies and other mesoscale structures. Previous Lagrangian analyses of the global ocean (Beron-Vera et al., 2008; Waugh and Abraham, 2008) used FTLE to quantify such horizontal stirring. This quantity depends on the integration time during which the pair of particles is followed. FTLEs generally decrease as this integration time increases, approaching the asymptotic value of the infinite-time Lyapunov exponent (Waugh and Abraham, 2008). We find difficult to specify finite values of this integration time for which easy-to-interpret results would be obtained across the different ocean regions. But for the mesoscale processes on which we want to focus, characteristic spatial scales are related to the Rossby Deformation Radius (RDR), with easily defined values and latitudinal dependence (see below). Thus, we use in this paper FSLEs as a convenient way to identify characteristics of stirring by mesoscale processes. FSLE are also convenient in finite ocean basins, where relevant spatial scales are also clearly imposed (Artale et al., 1997; Boffetta et al., 2000; Lacorata et al., 2001). As a quantifier of horizontal stirring, measuring the stretching of water parcels, FSLEs give also information on the intensity of horizontal mixing between water masses, although a complete correspondence between stirring and mixing requires the consideration of diffusivity and of the stretching directions (d’Ovidio et al., 2009).

More in detail, at a given point the FSLE (denoted by λ in the following) is obtained by computing the minimal time τ at which two fluid particles, one

4.2. DATA AND METHODS

centered on the point of study and the other initially separated by a distance δ_0 , reach a final separation distance δ_f . At position \mathbf{x} and time t , the FSLE is given by: $\lambda(\mathbf{x}, t, \delta_0, \delta_f) = \tau^{-1} \ln(\delta_f/\delta_0)$. To estimate the minimal time τ we would need to integrate the trajectories of all the points around the analyzed one and select the trajectory which diverges the first. We can obtain a very good approximation of τ by just considering the four trajectories defined by the closest neighbors of the point in the regular grid of initial conditions at which we have computed the FSLE; the spacing of this grid is taken equal to δ_0 . The equations of motion that describe the horizontal evolution of particle trajectories are

$$\frac{d\phi}{dt} = \frac{u(\phi, \theta, t)}{R \cos \theta}, \quad (4.1)$$

$$\frac{d\theta}{dt} = \frac{v(\phi, \theta, t)}{R}, \quad (4.2)$$

where u and v stand for the zonal and meridional components of the surface velocity field coming from the OFES simulations; R is the radius of the Earth (6400 km), ϕ is longitude and θ latitude. Numerically we proceed by integrating Eqs. (4.1) and (4.2) using a standard, fourth-order Runge-Kutta scheme, with an integration time step $dt = 6$ hours. Since information is provided just in a discrete space-time grid, spatiotemporal interpolation of the velocity data is required, that is performed by bilinear interpolation. Initial conditions for which the prescribed final separation δ_f has not been reached after integrating all the available times in the data set are assigned a value $\lambda = 0$. A possible way to introduce small-scale features that are not resolved by our simulated velocity fields is by inclusion of noise terms in the equations of motion (4.2). We have recently shown (Hernández-Carrasco et al., 2011) that the main mesoscale features are maintained when this eddy-diffusivity is taken into account, though sub-mesoscale structures may change considerably. For global scales we expect the effects of noise to be even more negligible.

The field of FSLEs thus depends on the choice of two length scales: the initial separation δ_0 (which coincides with the lattice spacing of the FSLE grid and is fixed in our computations to the model resolution, $\delta_0=1/10^\circ$) and the final separation δ_f . As in previous works in middle latitudes (e.g. d’Ovidio et al., 2004, 2009; Hernández-Carrasco et al., 2011) we will focus on transport processes arising from the mesoscale structures. In these studies δ_f was taken about 110 km , which is of the order of, but larger than, the mesoscale size in middle latitudes. Note that δ_f should be a decreasing function of the latitude, since mesoscale structures decrease in size with Rossby Deformation Radius (RDR). We need not to exactly match RDR but to guarantee that our choice of δ_f is similar but larger

CHAPTER 4. GLOBAL CHARACTERIZATION OF STIRRING

than mesoscale lengths, and also that it is a smooth function to avoid inducing artifacts. We have then chosen δ_f as $\delta_f = 1.3|\cos \theta|$ degrees; other reasonable choices lead to similar results to those presented here.

We compute the FSLEs by *backwards* time integration. In this way we quantify the fluid deformation by *past* stirring. When computing LCSs this leads to structures easier to interpret since they can be associated with the actual shape of tracer filaments (Joseph and Legras, 2002; d’Ovidio et al., 2009). However, given that forward and backward exponents in incompressible flows are related by temporal shifts and spatial distortions (Haller and Sapsis, 2011), and that we are interested in temporal and spatial averages over relatively large scales, we do not expect significant differences when using *forward* exponents to calculate the stirring quantifiers presented below. This was explicitly checked in a similar framework in d’Ovidio et al. (2004).

Lagrangian measurements have been shown to correlate well with several Eulerian quantities at several scales (Waugh et al., 2006; Waugh and Abraham, 2008). In particular it is pertinent to correlate stirring with Eddy Kinetic Energy (EKE) since it is expected that more energetic turbulent areas would also present stronger horizontal stirring, mainly due to the spawning of eddies (see however Rossi et al. (2008, 2009)). Given an integration period T long enough (for instance $T =$ one year), the EKE (per unit of mass) is given by: $EKE = \frac{1}{2} \langle u'^2 + v'^2 \rangle$, where u' and v' are the instant deviations in zonal and meridional velocities from the average over the period T , and the brackets denote average over that period. Another Eulerian measurement used in this work is the surface relative vorticity, given by $\omega = \frac{\partial v}{\partial x} - \frac{\partial u}{\partial y}$, with positive (vs negative) ω associated to cyclonic (vs anticyclonic) motion in the Northern Hemisphere (opposite signs in the Southern Hemisphere). An additional Eulerian candidate to look for Lagrangian correspondences is the local strain rate, but it has been shown (Waugh et al., 2006; Waugh and Abraham, 2008) to scale linearly with $EKE^{1/2}$ and thus it will not be explicitly considered here.

Conditioned averages of λ as a function of another variable y (let y be $EKE^{1/2}$ or ω) introduced in Subsection 4.3.4 are obtained by discretizing the allowed values of y by binning; 100 bins were taken, each one defining a range of values (y_n, y_{n+1}) and represented by the average value $\hat{y}_n = \frac{y_n + y_{n+1}}{2}$. So, for each discretized value of \hat{y}_n the average of all the values of λ which occur coupled with a value in (y_n, y_{n+1}) is computed. The result is an estimate of the conditioned average $\tilde{\lambda}(y)$ (which is a function of y) at the points \hat{y}_n .

Results

4.3.1 Global horizontal stirring from FSLE

In Fig. 4.1 we present a map of FSLEs at a given time. Typical values are in the order of $0.1 - 0.6 \text{ days}^{-1}$, that correspond well to the horizontal stirring times expected at the mesoscale, in the range of days/weeks. Spatial structures, from filaments and mesoscale vortices to larger ones, are clearly identified; see a representative zoom of the South Atlantic Ocean (Bottom of Fig. 4.1), where the typical filamental structures originated by the horizontal motions are evident.

Instantaneous maps of FSLEs have a significant signature of short-lived fast processes and are adequate to extract LCSs, but we are more interested in slower processes at larger scales. We have hence taken time averages of FSLEs over different periods, in order to select the low-frequency, large-scale signal. In this way we can easily characterize regions in the global ocean with different horizontal stirring activity; areas with larger values of averaged FSLEs are identified as zones with more persistent horizontal stirring (d'Ovidio et al., 2004), as shown in Fig. 4.2a. As expected, we can observe that high stirring values correspond to Western Boundary Currents (WBCs) and to the Antarctic Circumpolar Current, while the rest of the ocean and the Eastern Boundary Currents (EBCs) display significantly lower values.

4.3.2 Geographical characterization of horizontal stirring

A convenient quantity used to characterize stirring in a prescribed geographical area A was introduced by d'Ovidio et al. (2004), which is simply the spatial average of the FSLEs over that area at a given time, denoted by $\langle \lambda(\mathbf{x}, t) \rangle_A$. Time series of this quantity for the whole ocean and the Northern and Southern hemispheres are shown in Fig. 4.3a. It is worth noting that the stirring intensity is typically larger in the Northern Hemisphere than in the Southern one.

Further information can be obtained by analyzing the FSLE Probability Distribution Functions (PDFs). In Fig. 4.3b we present the PDFs for both hemispheres and the whole ocean; the required histograms are built using λ values computed once every week during one year (52 snapshots) at each point of the spatial FSLE grid in the area of interest. Each one of these PDFs is broad and asymmetric, with a small mode λ_m (i.e., the value of λ at which the probability attains its maximum) and a heavy tail. Similarly to what was discussed by Waugh

CHAPTER 4. GLOBAL CHARACTERIZATION OF STIRRING

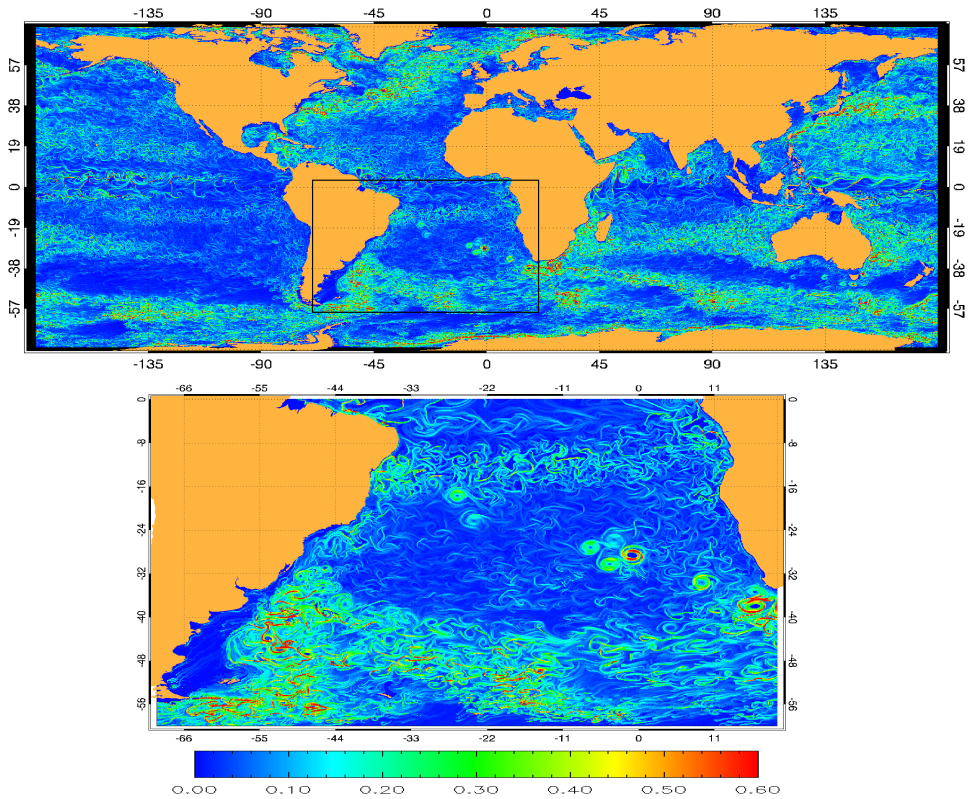


Figure 4.1: Top: Snapshot of spatial distributions of FSLEs backward in time corresponding to November 11, 1990 of the OFES output. Resolution is $\delta_0 = 1/10^\circ$. Bottom: Zoom in the area of the box inside top figure (South Atlantic Ocean). Coherent structures and vortices can be clearly seen. The colorbar has units of day^{-1} .

et al. (2006) and Waugh and Abraham (2008) for the FTLE case, these PDFs are well described by Weibull distributions with appropriate values for the defining parameters. We note that an explicit relationship between FTLE and FSLE distributions was derived by Tzella and Haynes (2010), but we have not checked if our flow is in the regime considered in that reference. The mode λ_m for the Southern Hemisphere is smaller than that of the Northern Hemisphere. Thus, Northern Hemisphere is globally more active in terms of horizontal dispersion

4.3. RESULTS

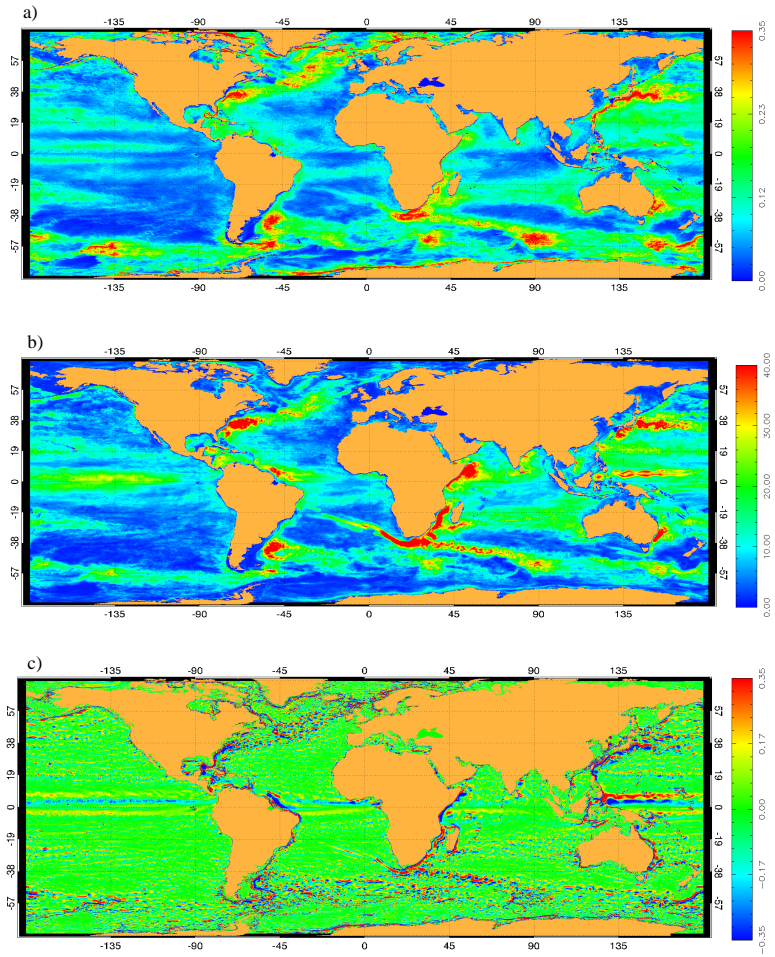


Figure 4.2: a) Time average of the FSLEs in the Global Ocean. Geographical regions of different stirring activity appear. The colorbar has units of day^{-1} . b) Spatial distribution of annual $EKE^{1/2}$ (cm/s). c) Time average of Relative Vorticity (ω) in the Global Ocean. The colorbar has units of day^{-1} . In all the plots the averages are over the 52 weekly maps computed from November 1st, 1990 to October 31th, 1991.

CHAPTER 4. GLOBAL CHARACTERIZATION OF STIRRING

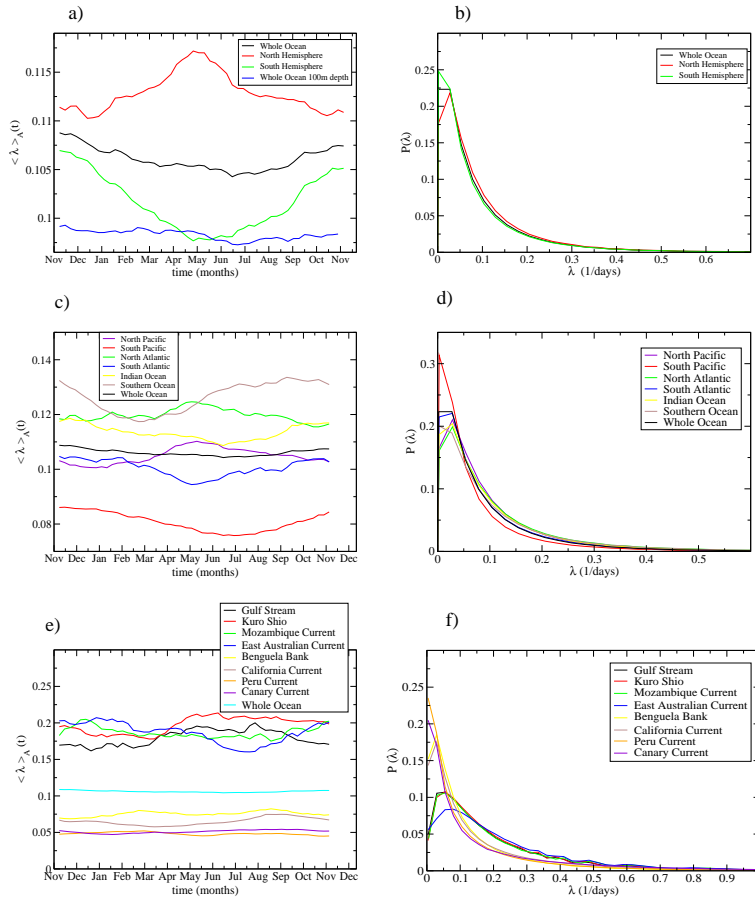


Figure 4.3: Left column: Temporal evolution (from November 1st, 1990 to October 31th, 1991) of the horizontal stirring (Spatial average of FSLEs). Right column: PDFs of the FSLEs (histograms are built from the λ values contained at all locations of the 52 weekly maps computed for the second simulation output year). Top: for both hemispheres and for the whole ocean. Middle: for different oceanic regions. Bottom: for some main currents during one simulation year. In addition to the results from the second surface layer analyzed through the paper, panel a) shows also stirring intensity in a layer close to 100m depth.

4.3. RESULTS

than the Southern one. The same conclusions hold when looking at seasonally averaged instead of annually averaged quantities (not shown).

Taking into account the observed differences between Northern and Southern Hemispheres, we have repeated the same analyses over the main ocean basins in a search for isolating the factors which could contribute to one or another observed behaviors. In Fig. 4.3c we show the time evolution of $\langle \lambda \rangle_A$ as computed over the six main ocean basins (North Atlantic, South Atlantic, North Pacific, South Pacific, Indian Ocean and Southern Ocean), compared to the one obtained over the global ocean. The Southern Ocean happens to be the most active (in terms of horizontal stirring) because of the presence of the Antarctic Circumpolar Current, followed by the Atlantic and Indian Oceans, and finally the Pacific. We have also computed (Fig. 4.3d) PDFs of FSLE for the different oceans. As before, we obtain broad, asymmetric PDFs with small modes and heavy tails. The smallest mode λ_m corresponds to the Southern Pacific, meaning that there is less horizontal stirring activity in this basin, in support of what is also visually evident in Fig. 4.3c. On the opposite regime we observe that the largest FSLE values correspond to the Southern Ocean. For the rest of oceans the PDFs are rather coincident with the whole ocean PDF.

We have gone further to a smaller scale, by repeating the same analyses for the main currents in the global ocean: Gulf Stream, Benguela, Kuroshio, Mozambique, East Australian, California, Peru and Canary currents. As evidenced by Fig. 4.3e there is a clear separation in two groups of currents in terms of their horizontal stirring properties: the most active currents (including Gulf Stream, Kuroshio, Mozambique and East Australian currents, all of them WBCs) and the least active ones (including Benguela, California, Peru and Canary Currents, which correspond to EBCs). The distinction remains in the PDF analysis: we can clearly distinguish two groups of PDFs: a) narrow PDFs highly peaked around a very small value of λ (EBCs); b) PDFs peaking at a slightly greater value of λ , but significantly broader (WBCs). Since the PDFs of the WBCs are broader, large values of FSLEs are found more frequently, i.e., more intense stirring occurs. This appears to be a reflection of the well-known mechanism of Western Intensification by Stommel (1948). Also, the asymmetry and tails of the PDFs show that the FSLE field is inhomogeneous and that there are regions with very different dispersion properties. Following Beron-Vera (2010), asymmetry and heavy tails make the PDFs quite different from the Gaussians expected under more homogeneous mixing. These characteristics are then indications that chaotic motion plays a dominant role versus turbulent, smaller scales, dynamics. That is, the large scale velocity features control the dynamics, something that is also reflected in the filamentary patterns of the LCS shown in Fig. 4.1.

CHAPTER 4. GLOBAL CHARACTERIZATION OF STIRRING

4.3.3 Seasonal characterization of horizontal stirring

Horizontal stirring in the global ocean has a strong seasonal variability, as shown in Fig. 4.3a. Maximum values of $\langle \lambda \rangle_A$ in the Northern Hemisphere are reached early in that hemisphere Summer, and minimum ones early in that hemisphere Winter. The same happens for the Southern hemisphere related to its Summer and Winter periods.

Seasonally averaged FSLEs in the whole ocean over the four seasons are shown in Fig. 4.4. The spatial pattern is rather similar in all of them, and also similar to the annually-averaged spatial distribution shown in Fig 4.2a. Higher FSLE levels are found at the Gulf Stream and Kuroshio in the Northern Hemisphere in Spring and Summer of that hemisphere. Analogously for the Eastern Australia and Mozambique Currents in the Southern Hemisphere relative to their own Spring and Summer time.

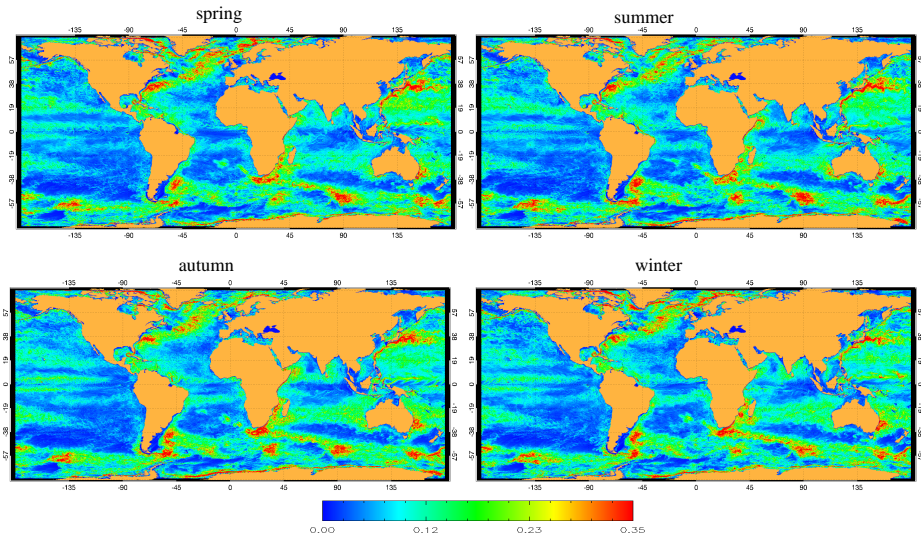


Figure 4.4: Time average of the FSLEs in the Global Ocean for the each season. Spring: from March 22 to June 22. Summer: from June 22 to September 22. Autumn: from September 22 to December 22. Winter: from December 22 to March 22. The colorbar has units of day^{-1} .

Following Zhai et al. (2008), to analyze which areas are more sensitive to seasonal changes, we computed the standard deviation of the annual time series of FSLE (see Fig. 4.5). Larger values appear to correspond to the more energetic

4.3. RESULTS

regions thus showing a higher seasonal variability. More information about seasonal variability of different oceanic regions can be obtained again from Fig. 4.3. Time evolution of stirring in the North Atlantic and North Pacific, shown in Fig. 4.3c, attains high values in Spring and Summer, and minimum ones in Winter. Concerning the main currents, we found that values of stirring in Kuroshio, Gulf Stream, East Australia, and Mozambique currents increase in Spring and Summer and decrease in Winter (see Fig. 4.3e). This seasonal variability is also present in EBCs but the amplitude of the changes is smaller than in WBCs.

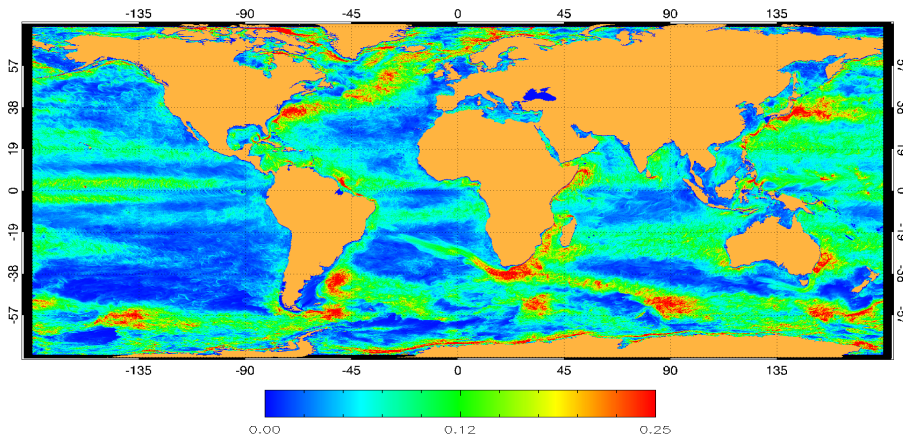


Figure 4.5: Standard deviation of weekly FSLE maps of one year. The colorbar has units of day^{-1}

The generic increase in mesoscale stirring in Summer time detected here with Lyapunov methods has also been identified in previous works and several locations (Halliwell et al., 1994; Qiu, 1999; Morrow et al., 2003; Qiu and Chen, 2004; Zhai et al., 2008) (in most of the cases from the EKE behavior extracted from altimetric data). Although no consensus on a single mechanisms seems to exist (see discussion in Zhai et al. (2008)) enhanced baroclinic instability has been proposed in particular areas (Qiu, 1999; Qiu and Chen, 2004), as well as reduced dissipation during Summer (Zhai et al., 2008).

We have also calculated longitudinal (zonal) averages of the time averages of FSLE in Figs. 4.2a and 4.4. This is shown in Fig. 4.6 (top figure for the Northern hemisphere and bottom figure for the Southern one). First of all, we see that horizontal stirring has a general tendency to increase with latitude in both

CHAPTER 4. GLOBAL CHARACTERIZATION OF STIRRING

hemispheres. One may wonder if this is a simple consequence of the decreasing value of δ_f we take when increasing latitude. We have checked that the same increasing tendency remains when the calculation is redone with a constant δ_f over the whole globe (not shown), so that this trivial effect is properly compensated by the factor $\ln(\delta_f/\delta_0)$ in the FSLE definition, and what we see in Fig. 4.6 is really a stronger stirring at higher latitudes. Note that this type of dependence is more similar to the *equivalent sea surface slope variability*, K_{sl} , calculated from altimetry in Stammer (1997) than to the raw zonal dependency of the EKE obtained in the same paper. Since K_{sl} is intended to represent Sea Surface Height variability with the large scale components filtered out, we see again that our FSLE calculation is capturing properly the mesoscale components of ocean stirring observed by other means.

It is also clearly seen that latitudinal positions of local maxima of stirring correspond to the main currents (e.g. Gulf Stream and Kuroshio around 35°N ; Mozambique, Brazil and East Australia around 25°S). The picture in Fig. 4.6 confirms that horizontal stirring is somehow higher in local Summer in mid-latitudes, where the main currents are, for both hemispheres. At low and high latitudes however the horizontal stirring is higher in local winter-time for both hemispheres, which is particularly visible in the Northern Hemisphere at high latitudes. A similar behavior was noted by Zhai et al. (2008) in the subpolar North Pacific and part of the subpolar North Atlantic for EKE derived from altimetry. Possible causes pointed there are barotropic instabilities or direct wind forcing.

4.3.4 Lagrangian-Eulerian relations

Lagrangian measures such as FSLEs provide information on the cumulative effect of flow at a given point, as it integrates the time-evolution of water parcels arriving to that point. They are not directly related to instantaneous measurements as those provided by Eulerian quantities such as EKE or vorticity, unless some kind of dynamic equilibrium or ergodicity-type property is established so that the time-integrated effect can be related to the instantaneous spatial pattern (for instance, if the spatial arrangement of eddies at a given time gives an idea about the typical time evolution of a water parcel) or their averages. EKE gives information on the turbulent component of the flow, which is associated to high eddy activity, while relative vorticity ω takes into account the shear and the rotation of the whole flow. Eventual establishment of such dynamic equilibrium would allow to substitute in some instances time averages along trajectories by spatial averages, so providing a useful tool for rapid diagnostics of sea state. Thus, we will relate the Lagrangian stirring (as measured by the FSLEs) with

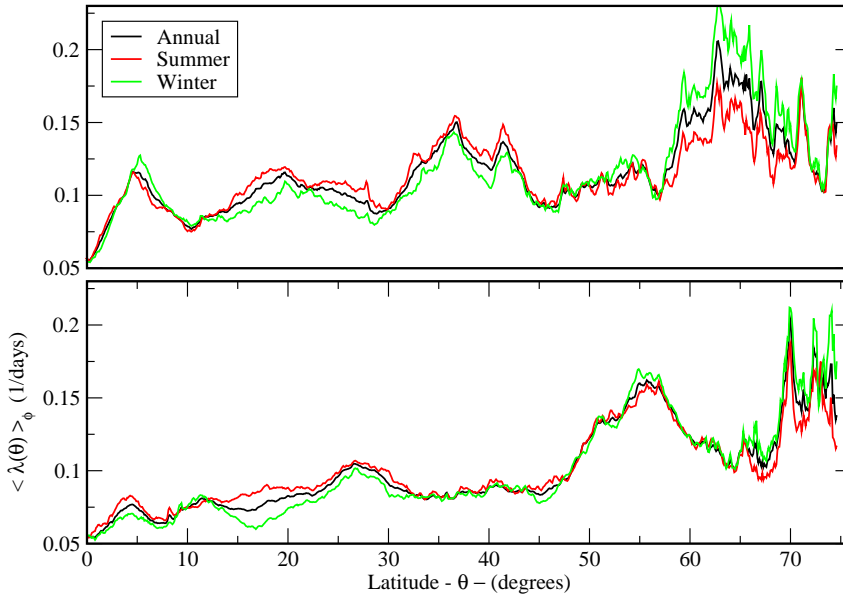


Figure 4.6: Cross-ocean zonal average of the annual, relative Summer and relative Winter time average of FSLE maps from Fig 4.2a as a function of latitude (expressed as absolute degrees from Equator to make both hemispheres comparable). Top: Northern Hemisphere; bottom: Southern Hemisphere.

an instantaneous, Eulerian, state variable. Of course, the Lagrangian-Eulerian relations will be useful only if the same, or only a few functional relationships hold in different ocean regions. If the relation should be recalculated for every study zone, the predictive power is completely lost.

We have thus explored the functional dependence of FLSEs with EKE and relative vorticity. In Fig. 4.2 the time average of these three fields is shown. Comparing FSLEs (Fig. 4.2a) and EKE (Fig. 4.2b), we see that high and low values of these two quantities are generally localized in the same regions. There are a few

CHAPTER 4. GLOBAL CHARACTERIZATION OF STIRRING

exceptions, such as the North Pacific Subtropical Countercurrent, which despite being energetic (Qiu, 1999) does not seem to produce enough pair dispersion and stretching at the scales we are considering. It was already shown by Waugh et al. (2006) and Waugh and Abraham (2008) that variations in horizontal stirring are closely related to variations in mesoscale activity as measured by EKE. Note the similarity, with also an analogous range of values, of the EKE plot in Fig. 4.2b), obtained from a numerical model, to that of Waugh and Abraham (2008) (first figure), which is obtained from altimetry data. In (Waugh et al., 2006) a proportionality between the stretching rate (as measured by FTLE) and $EKE^{1/4}$ was inferred for the Tasman Sea (a relation was found but no fit was attempted in the global data set described in Waugh and Abraham (2008)). In order to verify if a similar functional dependence between FSLE and EKE could hold for our global scale dataset, we have computed different conditioned averages (see Section 4.2), shown in Fig. 4.7: in the left panel we present the conditioned average $\bar{\lambda}(EKE)$, while in the right panel $\bar{\lambda}(\omega)$ is shown; both functions were derived from the time averaged variables shown in Figure 4.2.

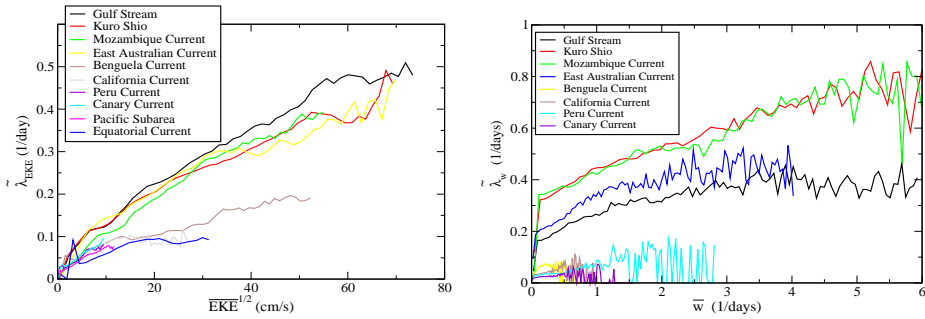


Figure 4.7: Left: Lagrangian-Eulerian relations. Left: the conditional average $\bar{\lambda}_{EKE}$ as a function of its corresponding annually averaged (second year) \overline{EKE} for different regions and currents. We clearly observe two groups of relations FSLE-EKE. Right: same plot for the conditional average $\bar{\lambda}_{\omega}$ as a function of its corresponding annually averaged (second year) $\bar{\omega}$. Although we observe also the same two two groups of FSLE- ω relations, these functions are much noisier and region-dependent.

The smooth curve depicted in Fig. 4.7, left, is an indication of a well-defined functional relationship between $\bar{\lambda}$ and \overline{EKE} , similar to the ones found by Waugh et al. (2006) and Waugh and Abraham (2008) from altimeter data. Notice how-

4.3. RESULTS

ever that the plot just gives conditioned averages, but the conditioned standard deviation -which is a measure of randomness and fluctuations- is not negligible. An idea of the scatter is given for selected areas in Fig. 4.8. Considerably less compact relationships were obtained in the Mediterranean sea (d'Ovidio et al., 2009). Fig. 4.8 shows that very different dynamical regimes identified by different values of λ may correspond to the same level of EKE. As a Lagrangian diagnostic, we believe that FSLE is more suitable to link turbulence properties to tracer dynamics than Eulerian quantifiers such as EKE. FSLEs provide complementary information since very energetic areas, with large typical velocities, do not necessarily correspond to high stretching regions. A paradigmatic example is a jet, or a shear flow, where small dispersions may be found because of the absence of chaotic trajectories. A functional relation between $\bar{\lambda}$ and $\bar{\omega}$ is also obtained (Fig. 4.7, right), although it is much noisier and probably worse-behaved. When particularizing for the different regions, we see that for EKE the WBCs are all roughly associated with one particular functional relation for the conditioned average $\bar{\lambda}$ while EBCs gather around a different one. None of the two prototype Lagrangian-Eulerian relations fits well to the relation $\lambda \propto EKE^{1/4}$ proposed for FTLE by Waugh et al. (2006) from altimeter data in the Tasman sea. Data are too scarce to make a reliable fitting for the conditioned average, in particular for the EBC. In Fig. 4.8 we see that relations of the form $\lambda \propto EKE^\alpha$ could be reasonably fitted to scatter plots of the data, with α larger than the 0.25 obtained in Waugh et al. (2006), specially for WBC were α is in the range (0.34, 0.40). This quantitative difference of our results with Waugh et al. (2006) may rest upon the fact that they considered just the Tasman Sea and we consider the different oceans. Other sources for the difference could be that we are using FSLE of velocity data from a numerical model, instead of FTLE from altimetry, or that they use a grid of relatively low resolution $0.5^\circ \times 0.5^\circ$, while ours is $0.1^\circ \times 0.1^\circ$. Maybe their coarser resolution is not enough to resolve filaments which are the most relevant structures in our FSLE calculations. Despite this the qualitative shape of the Lagrangian-Eulerian relations is similar to the previous works (Waugh et al., 2006; Waugh and Abraham, 2008).

In order to analyze the ocean regions beyond boundary currents, we have also computed the conditioned averages for the Equatorial Current and for a 40° longitude by 20° latitude sub-region centered at 245° longitude and -30° latitude in the middle of the sub-tropical gyre in the Pacific Ocean (and hence an area of scarce horizontal stirring activity). We see (Fig. 4.7, left) that the EBC Lagrangian-Eulerian relation is valid for these two areas. We have also verified that the relations derived from annually-averaged quantities remain the same for seasonal averages (not shown). The important point here is the occurrence of just two different shapes for the EKE-FSLE relations across very different ocean

CHAPTER 4. GLOBAL CHARACTERIZATION OF STIRRING

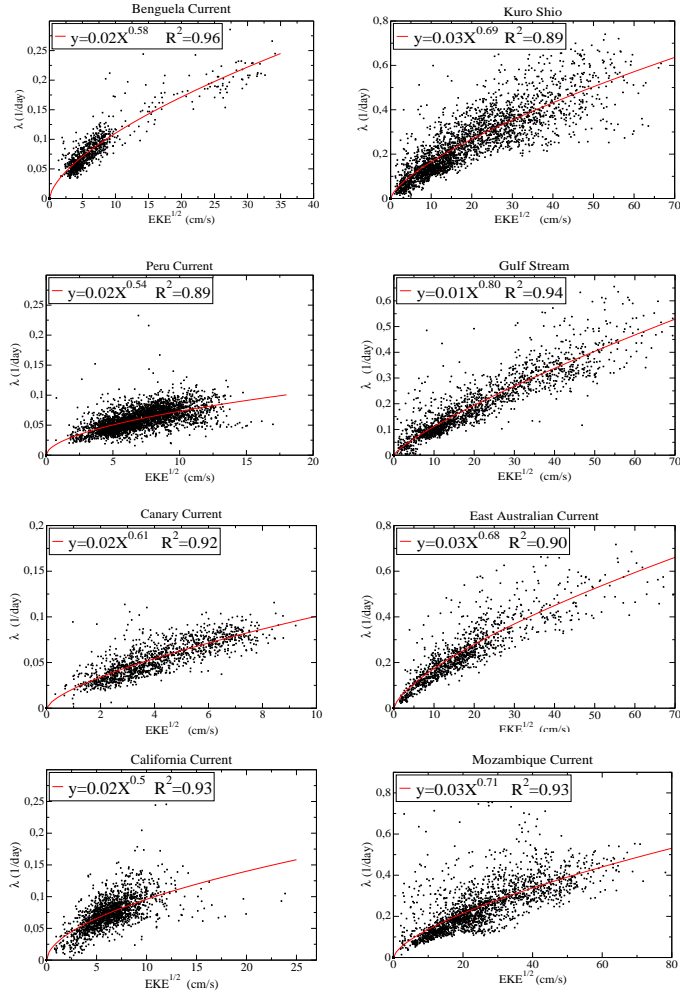


Figure 4.8: Scatter plots showing temporally averaged FSLE values at different spatial points in regions of Fig. 4.2a, and EKE values (as displayed in Fig. 4.2b) at the same points. The regions displayed here are eight of the main currents. Fittings of the type $y = cX^b$ are also displayed, where y is the temporal mean of FSLE and X is $EKE^{1/2}$. Note that this implies $\langle FSLE \rangle = c EKE^\alpha$ with $\alpha = b/2$.

4.4. CONCLUSIONS

regions, which may make useful this type of parametrization of a Lagrangian quantity in terms of an Eulerian one. For the relations of FSLE in terms of relative vorticity, a distinction between WBC and EBC still exists but the results are less clear and class separation is not as sharp as in the case of EKE (see Fig. 4.7, right). For instance, Gulf Stream and Kuroshio, despite being both WBC, do not seem to share the same Lagrangian-Eulerian relation, which limits its usefulness.

4.4

Conclusions

In this paper we have studied the space and time variability of horizontal stirring in the global ocean by means of FSLE analysis of the outputs of a numerical model. Similarly to what has been done in previous works, FSLEs can be taken as indicators of horizontal stirring. Being Lagrangian variables, they integrate the evolution of water parcels and thus they are not completely local quantities. We have taken averages to analyze two main time scales (annual and seasonal) and three space scales (planetary scale, ocean scale and horizontal boundary scale). Our velocity data were obtained by using atmospheric forcing from NCEP. Structures and dynamics at small scales will be probably more realistic if forcing with higher resolution observed winds, as in Sasaki et al. (2006). But since we have not studied the first model layer which is directly driven by wind, and we have focused on averages at relatively large time and spatial scales, we do not expect much differences if using more detailed forcing.

Horizontal stirring intensity tends to increase with latitude, probably as a result of having higher planetary vorticity and stronger wind action at high latitudes, or rather, as argued in Zhai et al. (2008) because of barotropic instabilities. Certainly, new studies are required to evaluate these hypothesis. At a planetary scale we observe a significantly different behavior in the Northern hemisphere with respect to the Southern Hemisphere, the first being on average more active in terms of horizontal stirring than the second one. This difference can probably be explained by the greater relative areas of subtropical gyres in the Southern Hemisphere with small stirring activity inside them, which compensates in the averages the great activity of the Antarctic Circumpolar Current. At an ocean scale, we observe that the level of stirring activity tends to decay as the size of subtropical gyres increases, what is an indication that the most intense horizontal stirring takes place at the geographical boundaries of ocean basins. For that reason, we have finally analyzed the behavior of stirring at boundary scale, which is mainly related to WBCs and EBCs. EBCs behave in a similar way to ocean interior in terms of all the quantities we have computed, including the

CHAPTER 4. GLOBAL CHARACTERIZATION OF STIRRING

Lagrangian-Eulerian relations. Thus, the main hot spots of horizontal stirring in the ocean are WBC. The observed small mode in the global FSLE PDFs also indicates that horizontal stirring is not very intense for the vast majority of the ocean, but the heavy tails indicate the existence of large excursions at some specific, stretched locations (e.g., inside the WBCs and other smaller scale currents active enough to generate stirring). This type of uneven distribution is characteristic of multifractal systems arising from large scale chaotic advection, something that was discussed for oceanic FSLEs in Hernández-Carrasco et al. (2011).

Regarding seasonal variability, generally we observe stronger stirring during each hemisphere's Summer time. Medium and high latitudes behave however in the opposite way: stirring is more active during the hemisphere Summer for medium latitudes and during the hemisphere Winter for high latitudes. Medium latitudes are strongly affected by the behavior of WBC, which experience intensification of horizontal stirring during Summer (Halliwell et al., 1994; Qiu, 1999; Morrow et al., 2003; Qiu and Chen, 2004; Zhai et al., 2008). As commented before, high latitude Winter intense stirring could be the result of a stronger action of wind during that period or of barotropic instabilities (Zhai et al., 2008), and dedicated studies are required to evaluate these hypothesis.

Finally, we have studied the connection between time-extended Lagrangian FSLEs and instant Eulerian quantities such as EKE and relative vorticity. For the case of EKE, the different ocean regions give rise to just two different Lagrangian-Eulerian relations, associated to an intense or a weak stirring regimes. The existence of these two regimes implies that pair dispersion and stretching strength are larger in a class of ocean areas (represented by WBC) than in another (e.g. EBC) at mesoscales, even when having the same EKE.

Lagrangian transport in a microtidal coastal area: the Bay of Palma, Spain

Coastal transport in the Bay of Palma, a small region in the Balearic Islands, Spain, is characterized in terms of Lagrangian descriptors. The data sets used for this study are the output for two months of a high resolution realistic numerical model, ROMS, forced atmospherically and with a spatial resolution of 300 m. Semi-persistent Lagrangian coherent structures (LCS) are found during both months. We study the fluid interchange between the Bay of Palma and the open ocean by computing particle trajectories and residence times. We found clear differences between autumn and summer. Stirring is smaller in autumn (October) than in summer (July), presenting diurnal variability at both months, probably induced by the effect of the wind. The escape rate of particles out of the Bay is qualitatively different, with more particles escaping to the ocean in October than in July. We show that LCSs separate regions with different transport properties, and display spatial distributions of residence times on synoptic Lagrangian maps. Finally, we compare the transport at the bottom layer, strongly influenced by the bottom drag, with surface transport strongly forced by the wind.

Introduction

The study of transport and mixing in coastal flows is of major interest because of their economic and ecological importance. Due to the particularities that they present, like influence of complex topography, coastline shape and the direct driving at the surface by highly variable wind forcing, coastal flow dynamics remains still poorly understood.

Recently, coastal observations and modeling efforts in different regions have been addressed from the Lagrangian point of view: Lekien et al. (2005) showed that Lagrangian Coherent Structures (LCSs) computed from velocity fields obtained from HF Radar measurements can be used to predict pollutant dispersion in the coast of Florida; Gildor et al. (2009) detected LCSs with HF Radar data in the Gulf of Eliat, Israel, and Haza et al. (2010) studied small-scale properties of dispersion measurements obtained from HF Radar data in the Gulf of La Spezia, Italy. Besides Radar measurements, velocity data from high resolution numerical models have been used to analyze the effect of the waves on LCS in the Bay of Palma de Mallorca, Spain (Galan et al., 2012), and to study the transport in the tidal flow of Ria de Vigo, Spain (Huhn et al., 2012). Fiorentino et al. (2012) showed how LCS can be used to study the water quality of a very small coastal region, the Hobie Beach, USA, from a numerical model. Also, data from drifters released in the Santa Barbara Channel were used by Ohlmann et al. (2012) to characterize relative dispersion, very useful to improve Lagrangian stochastic models. The application of Lagrangian techniques to study the dynamics in a shallow lake (small closed basin) has been performed in Pattantyús-Ábrahám et al. (2008).

In this work we study some transport properties in the Bay of Palma using Lagrangian techniques. The Bay is a semi-enclosed basin located in the southwest of the island of Mallorca (western Mediterranean sea), whose coastal flow is strongly induced by the wind, particularly characterized by the presence of persistent sea breeze during the summer months. The Lagrangian diagnosis will be obtained from velocity data of a realistic numerical model at high resolution, which resolves spatial scales of a few hundred of meters. We investigate the horizontal transport during two months corresponding to different seasons (autumn and summer) at the sea surface and at the deepest layer, in order to highlight the effect of the wind on transport. We compute the barriers and avenues to transport (LCS). We also present calculations of residence times and show synoptic Lagrangian maps (SLM) of these times (Lipphardt et al., 2006), which will allow us a detailed visualization of the interchange of fluid particles between the Bay

5.2. DATA AND CHARACTERISTICS OF THE STUDY REGION

and the open sea. As a central point in our study, the relationship between LCSs and areas of different residence times will be also analyzed.

The organization of this Chapter is as follows. The data set used in the computations and the area of study is described in Section 5.2. Section 5.3 presents a brief overview of the Lagrangian tools that are used in this study. Before presenting the Lagrangian results, we show in Section 5.4 a short list of Eulerian results by studying the velocities in the Bay. We show in Section 5.5 a coastal characterization of stirring of the Bay of Palma in terms of FSLE and residence times. Using the definition of LCS given in Section 5.3, Lagrangian barriers are identified in the domain of interest. We compute escape rates and residence times of fluid particles to describe the transport relation between the Bay and the open ocean. We provide possible mechanisms to explain differences in the residence times and FSLE between different seasonal months. Finally we summarize the main results in Section 5.6.

5.2

Data and characteristics of the study region

5.2.1 Area of study

The island of Mallorca (Fig. 5.1) is part of the Balearic Islands Archipelago and is located in the center of the western Mediterranean (between 39° and 40°N and 2.50° and 3.50°E). The Bay of Palma is a nearly semi-circular and semi-enclosed basin located in the southwest coast of Mallorca and it can reach depths of more than 60 m . The area of the Bay of Palma is defined as the water mass inside the square in Fig.5.1, consisting of a northern limit at $39^\circ34'\text{N}$, a southern limit at $39^\circ24'\text{N}$, and $2^\circ30'\text{E}$ and $2^\circ45'\text{E}$ as the eastern and western limits, respectively. The open boundary to the sea is in the southern part and it is 20 km wide.

The size of the Bay of Palma is smaller than the Rossby radius of deformation at these latitudes, and the circulation is determined by the submarine topography in the bottom layer and by the wind and sea breeze at the surface layer. During summer there are persistent sea breeze conditions. In July and August, the weather is often almost identical from one day to the next. In the vicinity of the Bay and along the southern coast of Mallorca the breeze blows from the south-west. Several studies (Ramis and Alonso, 1988; Ramis and Romero, 1995), have pointed out that the meteorological conditions of Mallorca (intense solar radiation, clear skies, soil water deficit, dryness, weak surface pressure

CHAPTER 5. COASTAL LAGRANGIAN TRANSPORT

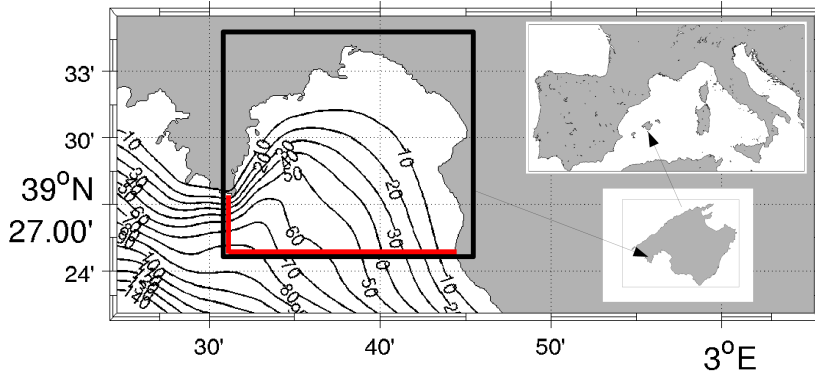


Figure 5.1: Bathymetry contours (in meters) of the model domain. The black box indicates the Palma Bay and the inset graphics give the geographical location of Mallorca Island in the western Mediterranean Sea.

gradients,..) favors the development of sea breeze, often from April to October, and almost every day during July and August.

5.2.2 Data

The velocity data sets were obtained from the numerical model ROMS (Regional Ocean Model System). ROMS is a free surface, hydrostatic, primitive equation ocean model, and the run used here was eddy resolving and atmospherically forced. The model uses a stretched, generalized nonlinear coordinate system to follow bottom topography in the vertical, and orthogonal curvilinear coordinates in the horizontal (Song and Haidvogel, 1994; Haidvogel et al., 2000). At each grid point, linear horizontal resolution Δ_0 is the same in both the longitudinal, ϕ , and latitudinal, θ , directions.

We run the simulation with a resolution of $\Delta_0 = 0.0027^\circ$ (300m, ROMS300), which is itself nested into a larger and coarser grid with $\Delta_0 = 1/74^\circ$ (1500m). The ROMS300 domain covers $39.2014^\circ\text{N} - 39.5987^\circ\text{N}$ (latitude), and $2.4013^\circ\text{E} - 3.0987^\circ\text{E}$ (longitude). The total number of grid nodes is 260×148 . Vertical resolution is variable with 10 layers in total. All domains were forced using realistic winds provided by the PSU/NCAR mesoscale model MM5. The initial vertical structure of temperature and salinity was obtained from the Levitus database.

5.3. METHODOLOGY

We will analyze velocity data from the surface layer and the bottom layer for the grid of $\Delta_0 = 300m$. This domain allows us to analyze the fluid interchange between the Bay and the open ocean, using a high resolution velocity field. Vertical displacements between layers are neglected, which is justified by the small integration times we will use. Nevertheless, close to the coast they can have an impact that will be the subject of future work. We will study two different intervals of time: one starting on October 5th, 2008 and finishing on October 29th, 2008; and the other extends from July 1st, 2009 until July 26th, 2009. Temporal resolution is 15 minutes and 10 minutes for October and July, respectively, resulting in a total of 2375 snapshots of the velocity field for October, and 3744 for July. The work by Galan et al. (2012) in the same Bay used a different month of the output from the numerical simulation, and a finer resolution (75m).

5.3

Methodology

5.3.1 LCSs and particle dispersion from FSLE

Our methodology is based on the Lagrangian analysis of coastal flows. In the Lagrangian view, particles are advected by the flow and their horizontal motion (neglecting motions between model layers) is governed by the differential equations

$$\frac{dx}{dt} = v_x(x, y, t), \quad (5.1)$$

$$\frac{dy}{dt} = v_y(x, y, t), \quad (5.2)$$

where $(x(t), y(t))$ are the west-east and the south-north coordinates of the trajectories and (v_x, v_y) are the eastwards and northwards components of the velocity. Note that it is not necessary to consider curvilinear coordinates because of the small size of the Bay.

LCSs (Haller and Yuan, 2000; d'Ovidio et al., 2004; Shadden et al., 2005), are roughly defined as the material lines organizing the transport in the flow. They are the analogs, for time-dependent flows, of the unstable and stable manifolds of hyperbolic fixed points. Among other approaches (Mancho et al., 2006b; Mendoza and Mancho, 2010; Haller and Beron-Vera, 2012), ridges of the local Lyapunov Exponents provide a convenient tool to locate them. In our case, we use the so-called Finite-Size Lyapunov Exponents (FSLEs) which are the

CHAPTER 5. COASTAL LAGRANGIAN TRANSPORT

adaptation of the asymptotic classical Lyapunov Exponent to finite spatial scales (Aurell et al., 1997; Boffetta et al., 2001). Thus, they are specially suited for closed or semi-closed basins. FSLEs are a local measure of particle dispersion and thus of stirring and mixing, as a function of the spatial resolution, serving to isolate the different regimes corresponding to different length scales of the oceanic flows, very useful in coastal systems (Cencini et al., 2010).

For any pair of fluid particles, one of them located at \mathbf{x} , the FSLE at time t_0 and at the spatial point \mathbf{x} is given by the formula:

$$\lambda(\mathbf{x}, t_0, \delta_0, \delta_f) = \frac{1}{|\tau|} \ln \frac{\delta_f}{\delta_0}, \quad (5.3)$$

where δ_0 is the initial distance of the two given particles, and δ_f is their final distance. Thus, to compute the FSLEs we need to calculate the time, τ , needed for the two particles initially separated δ_0 , to get a final distance δ_f . (In this way the FSLE represents the inverse time scale for mixing up fluid parcels between length scales δ_0 and δ_f). To obtain this time we need to know the trajectories of the particles (from Eqs. (5.1) and (5.2)) which gives the Lagrangian character to this quantity. The FSLEs are computed for the points \mathbf{x} of a lattice with lattice spacing coincident with the initial separation of fluid particles δ_0 . Numerically we integrate the equations of motion using a standard, fourth-order Runge-Kutta scheme, with an integration time step of $dt = 15$ minutes in October and $dt = 10$ minutes in July. Since information is provided just in a discrete space-time grid, spatiotemporal interpolation of the velocity data is achieved by bilinear interpolation. For the spatial scales that define FSLEs, we take $\delta_f = 0.1^\circ$, i.e., final separations of about 10 km , because of the size of the Bay. On the other side, we take δ_0 equals to 75 m , four times smaller than the resolution of the velocity field, $\Delta_0 = 300 \text{ m}$. Since we are interested only in fast time scales, our integrations are restricted to 5 days. Locations for which the final separation at the end of this period has not reached the prescribed $\delta_f = 10 \text{ km}$ (or for which particles have been trapped by land) are assigned a value $\lambda = 0$.

FSLEs can be computed from trajectory integration *backwards* and *forwards* in time. Their highest values organize in filamental structures approximating relevant manifolds: ridges in the spatial distribution of backward (forward) FSLEs identify regions of locally maximum compression (separation), approximating attracting (repelling) material lines or unstable (stable) manifolds of hyperbolic trajectories, which can be identified with the LCSs (Haller and Yuan, 2000; d'Ovidio et al., 2004; Shadden et al., 2005; Tew Kai et al., 2009; Hernández-Carrasco et al., 2011), and characterize the flow from the Lagrangian point of view (Joseph and Legras, 2002; Koh and Legras, 2002). Attracting LCSs associated to backward integration (the unstable manifolds) have a direct physical

5.4. PRELIMINARY EULERIAN DESCRIPTION

interpretation (Joseph and Legras, 2002; d'Ovidio et al., 2004, 2009). Tracers (chlorophyll, temperature, ...) spread along these attracting LCSs, thus creating their typical filamental structure (Tel and Gruiz, 2006; Lehan et al., 2007; Tew Kai et al., 2009; Calil and Richards, 2010).

5.3.2 Escape and residence times

Another characteristic time-scale for transport processes in open flows is the so-called escape rate (Lai and Tel, 2011). This quantity measures how quickly particles trajectories escape from a domain. If we initiate $N(0)$ particles in a flow, we can measure how the trajectories escape the pre-selected region. In the case in which the decay in the number of particles remaining in the region up to time t , $N(t)$, decays exponentially with time, $N(t)/N(0) \sim e^{-\kappa t}$, there is a well defined escape time defined as the inverse of the escape rate κ : $\tau_e = 1/\kappa$. For the range of times explored in our work, we will see that the particle escape is close to exponential and then we can estimate the value of τ_e .

τ_e is a global quantity associated to the whole basin. A more detailed description of the transport processes can be obtained by other suitable Lagrangian quantities such as residence times (Buffoni et al., 1996, 1997; Falco et al., 2000). The particle residence time (RT) is defined as the interval of time that a fluid particle remains in a region before crossing a particular boundary. For each fluid particle inside the Bay at an initial time, we need to compute two times: the forward exit time, t_f , computed as the time needed for a particle to cross the line delimiting the Bay, taking the forward-in-time dynamics; and the backward exit time, t_b , the same but in the backward-in-time dynamics. The residence time is defined as $RT = t_f + t_b$. RTs can be displayed in plots named Lagrangian Synoptic Maps (Lipphardt et al., 2006), in which the residence time of each fluid particle is referenced to its initial position on the grid.

5.4

Preliminary Eulerian description

A first approach to the transport process in the Bay can be a description from the Eulerian point of view, by studying averages of the velocity field. To do this we consider separately the meridional v_y and zonal v_x components of the surface flow, and we analyze the time evolution of their spatial averages.

CHAPTER 5. COASTAL LAGRANGIAN TRANSPORT

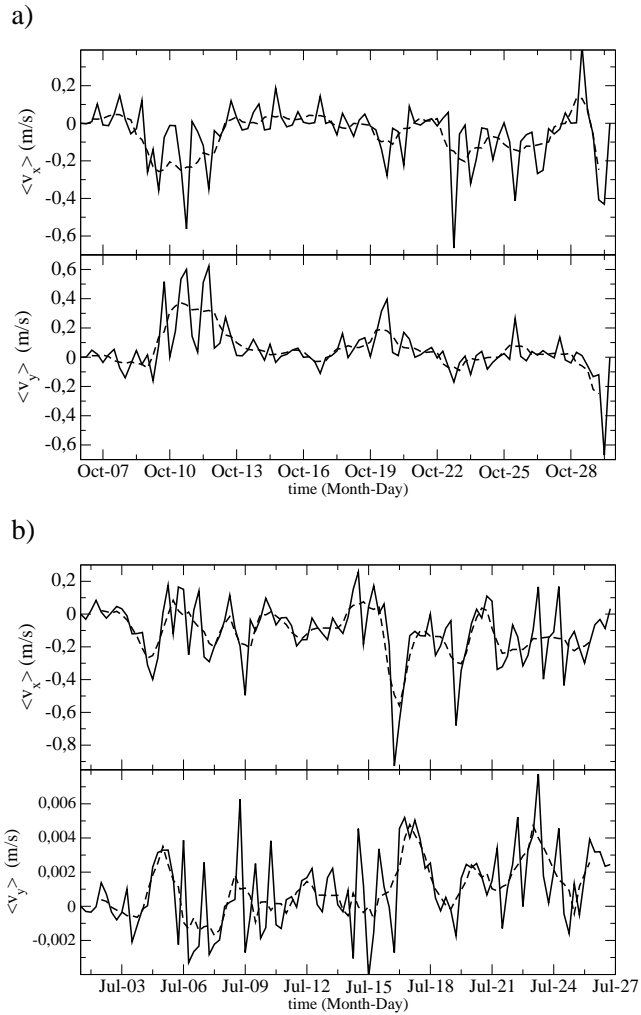


Figure 5.2: a) Time series throughout October of the zonal (top) and meridional (bottom) components of the velocity field every 6 hours (dashed-line) and daily averaged (solid line); b) the same that a) but for July.

Figures 5.2 a) and b) show the time series of data taken every 6 hours (solid line), and daily average time series (dashed-line) of v_x and v_y for October and July, respectively. During the two months both components of the flow present daily

variability probably related to the presence of land and sea breezes. In July the meridional fluctuations are more noticeable, being $\langle v_y \rangle$ very small. In October there are some large fluctuations of low frequency, probably induced when the large-scale winds are variable.

Comparing the velocity components of both months we observe qualitative differences. The values of v_y in the case of October range from -0.6 to 0.6 m/s (bottom panel of Fig. 5.2 a), while in the case of July, v_y is two orders of magnitude smaller, ranging from -0.004 to 0.008 m/s (bottom panel of Fig. 5.2 b). On other hand, v_x are similar during October and July. In the case of October, v_x ranges from -0.6 to 0.3 m/s (top panel of Fig. 5.2 a), the same order of magnitude than the meridional velocity, resulting in circular motions (clockwise along the Bay). In July the situation is significantly different. The zonal velocity ranges from -0.8 to 0.2 m/s (top panel of Fig. 5.2 b), much larger than the meridional velocity, resulting in a flow dominated by the zonal component.

5.5

Results

5.5.1 Average characterization of stirring

We now describe the Lagrangian results. First we compute the temporal average (over the months of October and July) of the FSLEs for the surface layer, and for July in the bottom layer. This calculation helps us to unveil areas of different stirring and the differences between layers and months.

The surface computations for the different seasonal months, October and July (Fig. 5.3 a, b) show different values and spatial distributions of stirring. The Bay of Palma appears to be an area with important activity. FSLE field looks more homogeneous in July than in October. During October filamental structures of high values of FSLE are accumulated over the northeast side of the Bay, forming a linear structure running from north to south-east which can act as a barrier, and therefore dividing the Bay in two flow regions of qualitatively different dynamics. The response of the surface currents to forcing by the wind could be an explanation of the difference between seasons. The effect of the terrain topography on stirring is clear in Fig. 5.3 c), where FSLEs are computed at the deepest layer for July. The high values of time-averaged FSLEs are located close to a region of high bathymetry gradient. This feature is likely owing to the presence of a region of compression of the flow induced by the bathymetry.

CHAPTER 5. COASTAL LAGRANGIAN TRANSPORT

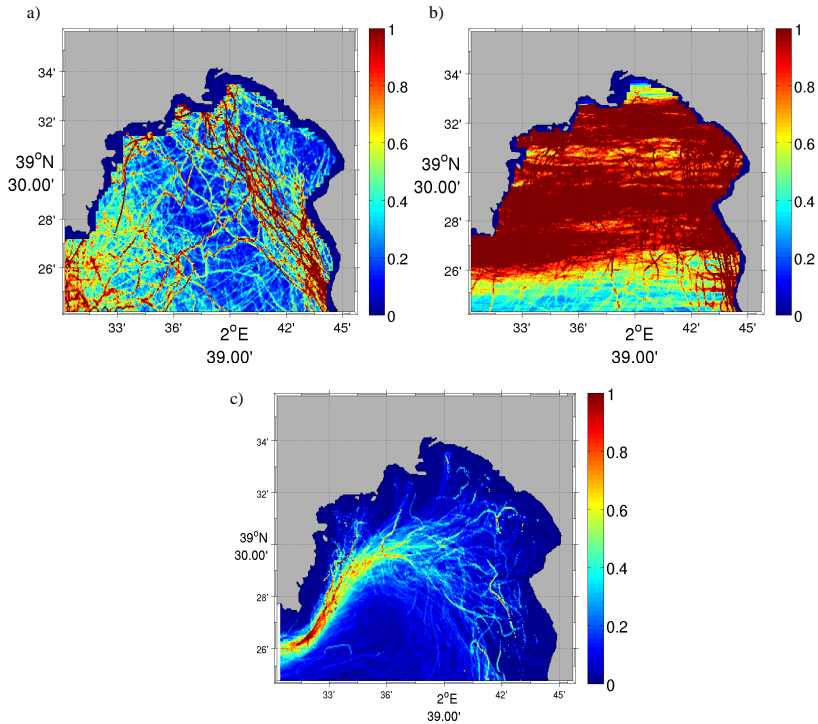


Figure 5.3: Spatial distribution of the time average of 6-hourly FSLEs maps over different months and at different layers: a) October at surface layer, b) July at surface layer, c) July at bottom layer.

5.5.2 Coastal LCSs

The temporal averages computed in Sec. 5.5.1 give us a rough idea of stirring in the Bay. More detailed information is obtained by looking at non-averaged quantities, that may reveal the existence of barriers to transport. Figure 5.4 shows the location of the high backward FSLE values, appearing as a network of lines, computed at successive instants of time in October. These temporary structures can remain for one or more days, as happens in October, or they can appear in the same location periodically (not shown). We stress here the appearance of a clear barrier, from north to south-east, that divides the Bay in two areas that correlates with the temporal average in Fig. 5.3 a). This barrier appears in almost the same position in different days, remaining without displacing too much. To

5.5. RESULTS

effectively see that it acts as a barrier we have considered the evolution of virtual particles released at both sides of the barrier. Red and black particles do not mix and they tend to spread along the barrier (confirming that, as expected, it is an attracting line).

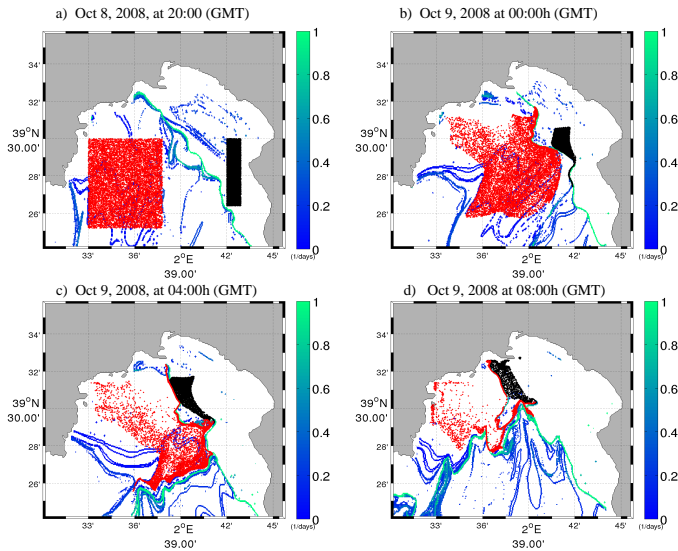


Figure 5.4: Evolution of the locations of two sets of particles in the Palma Bay during a night of October, superimposed on the spatial distributions of high values of backward FSLEs. The colorbars specify FSLE values in days^{-1} . Zero FSLE values, displayed as white, are assigned to locations for which the particles do not attain the prescribed $\delta_f = 10\text{km}$ separation after 5-days integration. Note the highest values of FSLEs (green lines) act as a barrier practically dividing the Bay in two parts. The two sets of particles are deployed from both sides of the barrier. (a) Initial conditions of the particles on October 8 at 20:00 GMT, 2008.; (b) October 9 at 00:00 GMT, 2008 ; (c) October 9 at 04:00 GMT, 2008 ; (d) October 9 at 08:00 GMT, 2008. Particles marked by black dots were released in the right side (northeast) of the barrier while the particles marked with red were released on the left side of the barrier.

5.5.3 Transport between the Bay of Palma and the open sea

In this section we study the surface transport of particles in and out of the Bay. To have an idea of the time scales involved in this interchange we proceed

CHAPTER 5. COASTAL LAGRANGIAN TRANSPORT

by computing the number of particles remaining in the Bay, $N(t)$, starting at different times (separated by 18 hours in order to collect the information of diurnal and nocturnal signal; this gives us 15 different simulations) as a function of the integration time t . A particle is considered to leave the Bay when crossing the red open-sea boundary in Fig. 5.1, so that particles landing on the coast are considered not escaped. Fig. 5.5 shows the different decays (averaged over the 15 different starting times at each month) for October and July. In both cases $N(t)$ is reasonably fitted by an exponential in the considered time-range, thus identifying the escape rates $\kappa = 0.62$ and 0.47 days^{-1} , respectively. The corresponding escape times, given by the inverse of the escape rate, are, respectively, $\tau_e = 1.61$ and 2.12 days . The exchange of fluid particles between the open ocean and the Bay is then less active in summer than in autumn.

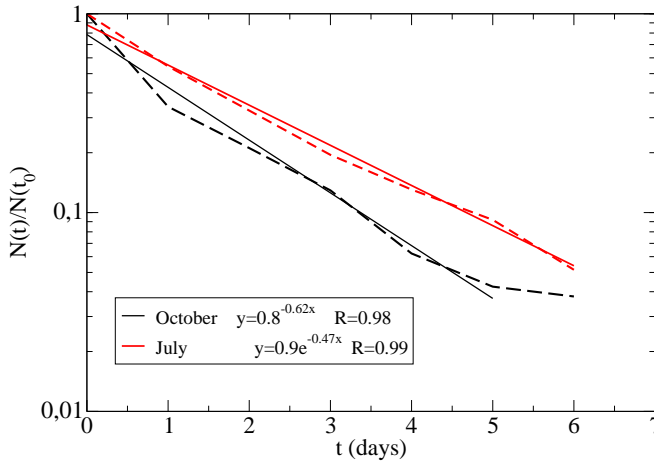


Figure 5.5: Average of 15 different subsequent estimations of $N(t)$, started at t_0 values separated 18 hours. $N(t)/N(t_0)$ is the proportion of particles remaining in Palma Bay at least for a lapse of time t after release at t_0 . Black and red lines are for surface layer in October and July respectively.

Next we compute synoptic maps of the residence times. As was indicated in Sec. 5.3.2 the residence time of the particles throughout the study area is considered as the sum of the entry time (t_b) and the escape time (t_f). To compute t_f and t_b particles are initialized every 6 hours in a regular grid of $75m$ spacing and they

5.5. RESULTS

are integrated forward and backward in time during 5 days. We consider that 5 days is a proper integration time according with the time scales associated with the coastal processes of this small Bay, and also owing to the short period of the available data. In these computations we assign the maximum possible value of t_f and t_b (5 days) to the fluid particles that remain in the pre-selected area after the 5 days of integration.

In Fig. 5.6 we color the initial positions of particles in the Bay attending to the time they transit through the Bay ($RT = t_f + t_b$) for different days. Initial positions of particles with short residence times are indicated in blue in Fig. 5.6. Regions from where particles have longer residence time (i.e. take more time to enter and escape) are marked in red.

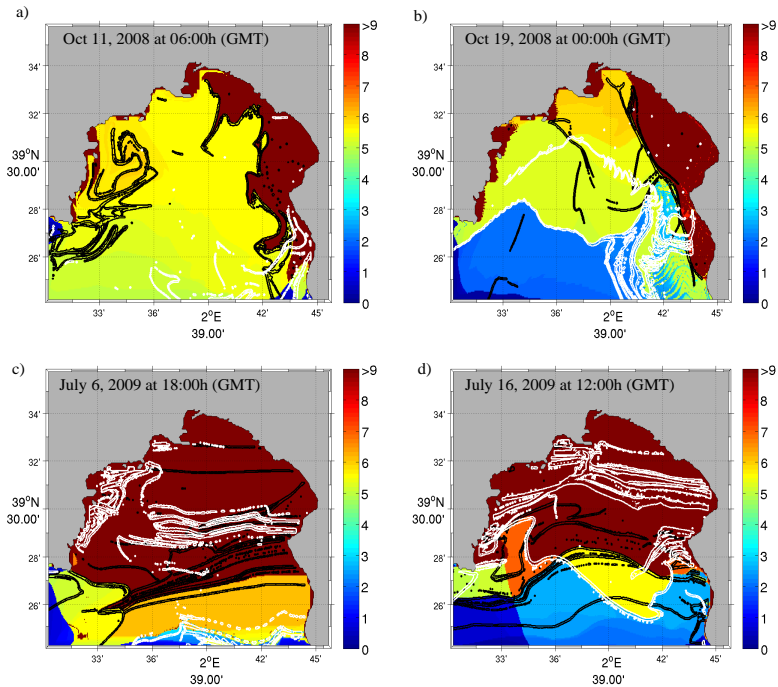


Figure 5.6: Lines are the locations of top values of FSLE (greater than 0.5 in October and greater 1.5 in July). Backward FSLE lines are colored in black and forward FSLEs in white. They are superimposed on spatial distributions of residence times in Palma Bay for different months. The colorbars give the residence times in days. a) and b) correspond to two different days in October, and c) and d) in July.

CHAPTER 5. COASTAL LAGRANGIAN TRANSPORT

These maps show that the spatial distribution of residence times of particles can be complex and time depending, presenting different patterns at different times. A number of small structures can be observed, including thin filaments or small lobes. Comparing both months, one can see differences in the RT distributions. The most noticeable is the approximate east-west alignment of the zones of similar RT in July, which is not seen in October. Also, in October the values of residence times of the particles are smaller, in agreement with the global rate estimations showed before. A common feature is the southwest region with low values of residence times, because in this region there are not coastal boundaries and it is totally open to the ocean.

In order to reveal regions with different persistent transport properties we compute time averages of the spatial distributions of residence times. We average 6-hourly snapshots of RT during 15 days (i.e. 60 snapshots) for each month. The results, plotted in Fig. 5.7 a) and b), show the common features that, in general, the low values of RT are for particles initiated close to the open ocean, specially in the southwest part, and high values are for particles started near the coast, as expected. However, on average, the residence time is larger in July than in October (3.25 days in July and 1.51 days in October) consistent with the behavior of the corresponding values of τ_e . Also, in July there is a clear boundary between the interior of the Bay to the north, with large average residence times and the open sea to the south, whereas the boundary between high and low residence times in October is well inside the Bay, aligned with the Lagrangian structure identified from the FSLE analysis, as will be discussed in the next section.

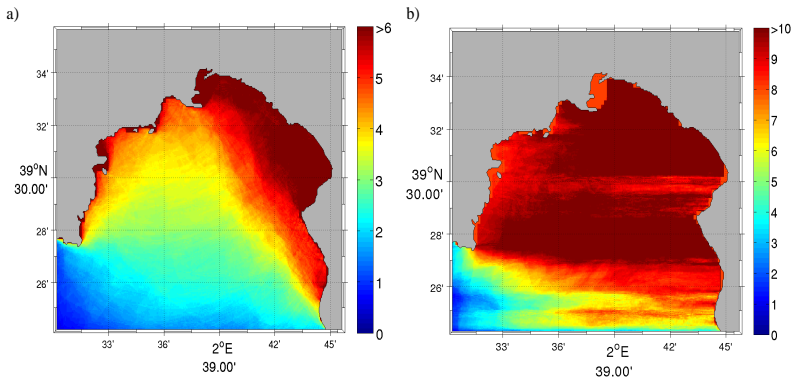


Figure 5.7: Spatial distributions of time averages of 60 snapshots of 6-hourly RT values collected over 15 days in Palma Bay for a) October and b) July. The colorbar units are *days*.

5.5.4 Relation between LCSs and RTs

We now examine the connection between regions of different residence times with LCSs. To compare RT and FSLE we have superimposed in Fig. 5.6 the filaments of high values of forward (white) and backward FSLE (black) values on the spatial distribution of residence times. This Figure shows a clear correspondence between structures of RT and FSLE. The LCSs given by high values of FSLE clearly separate regions with different values of residence times, confirming the value of the FSLE technique to identify boundaries between different flow regions and barriers to transport. Pattantyús-Ábrahám et al. (2008) studied the relation between residence time and FSLE for a wind-forced hydrodynamical model of a shallow lake. They found that areas with long residence time visualize the stable manifolds of the so-called chaotic saddle, a structure controlling the escape properties at long times. In our case, our integrations are restricted to times too short to characterize long-time chaotic behavior, but still there is a good correspondence between the FSLE structures characterizing divergent or convergent trajectories, and escape or residence times.

Fig. 5.7 a) shows a time average over October of the spatial distribution of RT, to be compared with the corresponding average figure (Fig. 5.3 a) for FSLE. It is evident that the region in the north and east side of the Bay with high values of RT is separated from the rest by a region of high values of FSLE. This can be explained by the presence of persistent barriers which do not allow particles to escape from the northeast side of the Bay, and thus separating the Bay in regions with different residence times. In July the situation is different, because the spatial distribution of FSLE (Fig.5.3 b) and RT (Fig. 5.7 b) is almost homogeneous, with higher values over the whole area of the Bay, and lower values in the small region bordering the open ocean. Nevertheless, the instantaneous configurations of high FSLE lines (Fig. 5.6) reveal their general east-west alignment, consistent with the orientation of the boundaries between areas of different RTs.

5.5.5 Variability of RT and FSLE

The differences of residence times and FSLEs in the two considered months indicate that the dynamics of the flow is qualitatively different. Now we analyze the time evolution of their spatial averages.

Figures 5.8 a) and b) show the time series of the spatial mean of residence times (top panel) and FSLE (bottom panel) for October and July, respectively.

Comparison between time evolution of spatial average of the RT for the different months confirms, again, that particles tend to stay longer times in the Bay during

CHAPTER 5. COASTAL LAGRANGIAN TRANSPORT

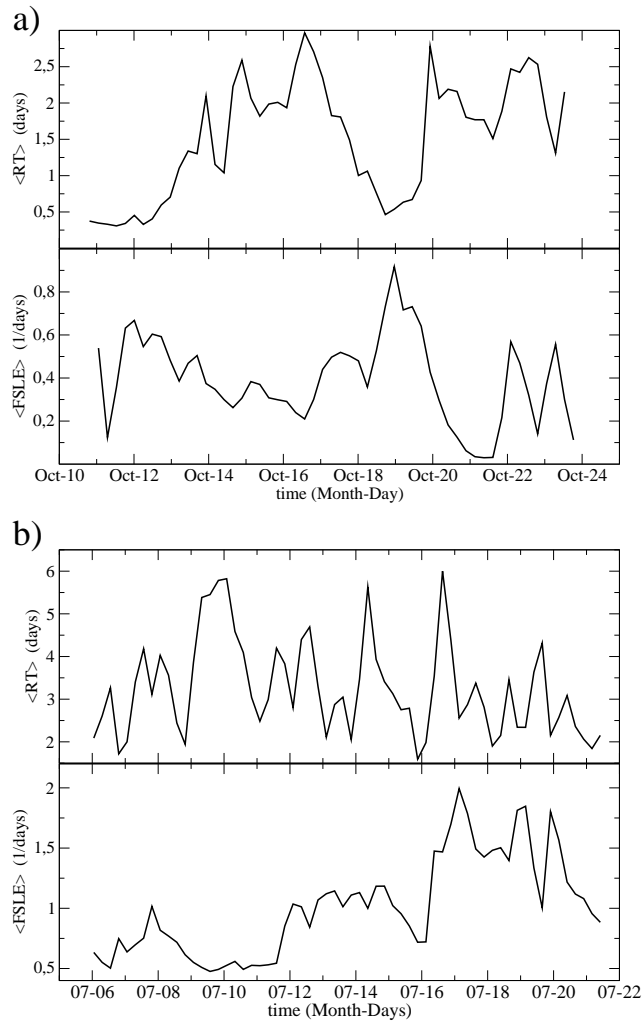


Figure 5.8: a) Time series throughout October of the spatial average of residence times (top) and spatial average of FSLE (bottom) for the surface layer of Palma Bay. b) the same that a) but for July.

July than in October. The values of RT varie approximately from 0.25 days to 3 days in October (Fig. 5.8 a, top), and from 2 days to 6 days in July (Fig. 5.8 b, top). The same happens with FSLE, higher values correspond to July and

5.5. RESULTS

lower ones to October. Diurnal fluctuations, likely related to the effect of the sea breeze, are evident in RT and FSLE for both months. In October there are some large fluctuations of low frequency in RT, probably induced by the variability of large-scale winds. On the other hand, during October, minima of RT correspond to maxima of FSLE, and maxima of RT correspond to minima of FSLE. In July, the relationship between FSLE and RT is only observed in the high frequency fluctuations.

We have observed in movies of particles trajectories (not shown) that in October the particles follow mostly a clockwise circulation, while in July the particles oscillate practically in the zonal direction (as discussed in Section 5.4). This difference is likely to be the main responsible for the different escape behavior between both months.

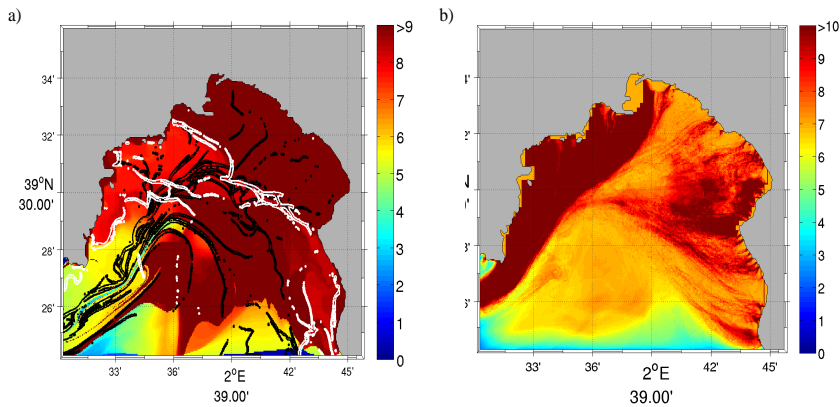


Figure 5.9: a) Snapshot of spatial distributions of residence times at the bottom layer in Palma Bay corresponding to July 17, 2009 at 18:00h (GMT). b) spatial distribution of time average of 60 snapshots of 6-hourly maps of RT collected over 15 days in July at the bottom layer.

5.5.6 Transport at the bottom layer

In this subsection we compare the main Lagrangian characteristics at the bottom layer, not driven directly by wind, with those at the surface. In Fig. 5.9 a) we show an instantaneous map of the residence times in the bottom layer one day of July, overlaid with lines of high FSLE values. Again, the spatial distribution is inhomogeneous, and we find high values of RT over all the Bay except very

CHAPTER 5. COASTAL LAGRANGIAN TRANSPORT

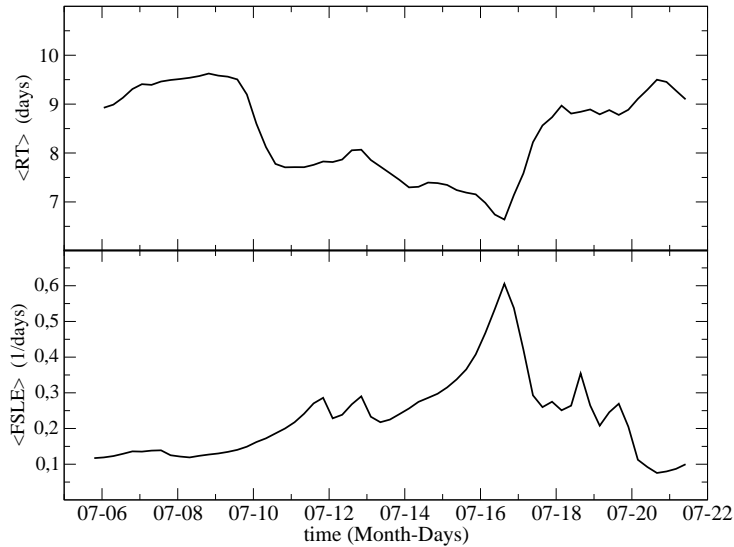


Figure 5.10: Time series throughout July of (top) spatial average of residence times and (bottom) spatial average of FSLE computed for the bottom layer.

close to the ocean. The correlation of RT values with FSLE lines is weaker than in the upper layer, but still we see that the relatively lower values of RT in the western part of the Bay at that particular day appear bounded by backwards FSLE lines, indicating a temporal escape route of particles in that region towards the southwest. The spatial distribution of the time average of RT plotted in Fig. 5.9 b) shows that highest average values of RT are concentrated in the northwestern region of the Bay. Fig. 5.3 c) displays high values of FSLE located precisely in the same region where the RT qualitatively change to high values. This suggests the presence of persistent barriers that separate this southeastern region from the rest in this bottom layer. The formation of these persistent LCSs is, probably, produced by the gradient of the bathymetry (see Fig. 5.1).

The time evolution of the spatial average of RT and FSLE are plotted in top and bottom panel of Fig. 5.10 respectively. Contrarily to the surface, in the bottom layer the diurnal fluctuations in the time series of RT disappear, showing that the flow at this depth is not directly influenced by breeze. The RT values are larger than in the surface, and therefore the interchange between the ocean and

5.6. CONCLUSIONS

the Bay is less intense at bottom layers. This is a consequence of the smoothness of the flow produced by the absence of the wind forcing at deepest levels. In average, there is a negative relation between stirring and residence times: when the flow is more dispersive the particles transit during less time over the Bay, so that maxima of RT correspond to minima of FSLE and vice-versa.

5.6

Conclusions

Properties of coastal transport in the Bay of Palma, which is a small semi-enclosed region of the Island of Mallorca, were studied in a Lagrangian framework, by using a realistic model velocity data at high resolution. We have applied two Lagrangian methods (FSLEs and RT) to analyze the small scales of this coastal currents. LCSs have been detected as ridges of FSLE, and virtual experiments with particle trajectories have shown that these structures really act as barriers, organizing the coastal flow. Global and average aspects of the transport in different seasonal months show that, in the period studied, in autumn there are more interaction between the Bay and the open ocean than in summer. One explanation is that during July the flow conditions restrict motion of the coastal marine surface to the zonal direction, preventing the flow to enter or scape toward the open ocean. The transport of particles at the deepest layer, strongly influenced by the bottom topography, is less active than in the surface. Regions with different values of RT are separated by ridges of FSLE, proving the fact that FSLE separate regions of qualitatively different dynamics also in small coastal regions. Thus, we think that these Lagrangian quantities can be used as key variables determining the dynamics and health of other bays or estuaries, particularly in relation with human activities. The dynamical point of view provided by the analysis of the FSLE is a valuable tool to extract information about transport, mixing and residence time embedded in the Eulerian time dependent velocity fields obtained from numerical models or High Frequency Radar systems. Future improvements include the adaptation of these methods to three-dimensional spaces and capture three-dimensional effects, such as upwelling and downwelling in coastal areas, and analyzing longer periods of time.

Appendix: Mixing rise in coastal areas induced by waves

We analyze the influence of waves on the modification of the LCS in the coastal area of the Bay of Palma. To accomplish it, we compute the FSLE from an ocean circulation model with realistic winds in two different situations: with and without gradients of the radiation stress tensor, to model the presence/absence of surface gravity waves. Besides, the results are compared with available data from a set of eight lagrangian drifters.

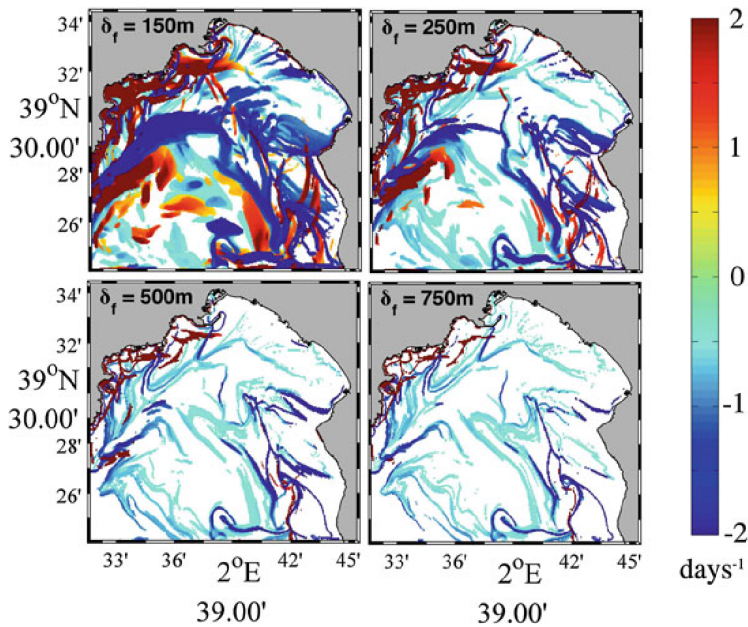


Figure 5.11: FSLEs for final separation of $\delta_f = 150m$ ($\delta_f/\delta_0 \approx 2$), $\delta_f = 250m$ ($\delta_f/\delta_0 \approx 3.3$), $\delta_f = 500m$ ($\delta_f/\delta_0 \approx 6.7$) and $\delta_f = 750m$ ($\delta_f/\delta_0 \approx 10$) November 23, 2009 at 18:00h. Just for plotting, we have considered positive the values of λ^+ and negative the ones for λ^- .

The study has been performed in the area defined in the box of Fig 5.1. Velocity data were obtained from the Regional Ocean Model System (ROMS) described in Section 5.2.

5.7. APPENDIX: MIXING RISE IN COASTAL AREAS INDUCED BY WAVES

We used velocity data from the third nested domain covering the study area which has a grid resolution of $dx = dy = 75m$ with 348×260 nodes and 10 vertical levels. The study was done from November 10th to November 24th, 2009. During this period two different simulations were performed by forcing the ocean model with realistic wind fields and described in Section 5.2 (hereafter set I), and forcing the model with the same wind fields plus the additional gradients of the radiation stress tensor (set II).

For set II, the effects of waves are included in the three domains by adding the gradient of the radiation stresses which describe the excess of momentum flux caused by surface waves (Longuet-Higgins and Stewart, 1964). These terms have been added to the horizontal momentum equations at the free surface in order to properly represent the effect of the phase averaged waves in the mean flow (Warner JC, 2008). The radiation stresses were obtained in the same domains of the circulation model by integrating WAM model, a third generation spectral wave model specifically designed for global and shelf sea applications (Komen and Janssen, 1994).

Although the wave model is not appropriate for very shallow waters since typical physical processes at those areas, such as diffraction, triad-wave interactions or depth-induced wave breaking are not considered, the model provides for typical wavelengths the correct wave field for depths higher than 10m. Stresses were updated into the ROMS model every three hours being internally interpolated between two consecutive values.

Additionally, on November 19th eight drifting buoys were deployed in the area of study for three days. The buoys were specifically designed for coastal studies and they provide the position through GPS positioning transmitting via GSM every 5min.

From the velocity fields obtained in sets I and II we obtain the FSLEs using the Eq. 5.3 where δ_0 coincides with the grid size for the velocity (75m). Through this appendix we will represent FSLE computed backwards in time as λ^- whereas FSLE computed forward in time as λ^+ .

We have performed simulations with the circulation model for the considered period. The baroclinic time step for the model is set to 15s and we store the surface velocity fields every 5min. For both sets I and II the wind forcing and waves are interpolated every 5min from the original 3 h-resolution fields. Additionally to compute the FSLE, four sets of virtual particles are launched in the domain. Particles were advected using a first order Euler algorithm which integrates in time the velocity data from the numerical model.

CHAPTER 5. COASTAL LAGRANGIAN TRANSPORT

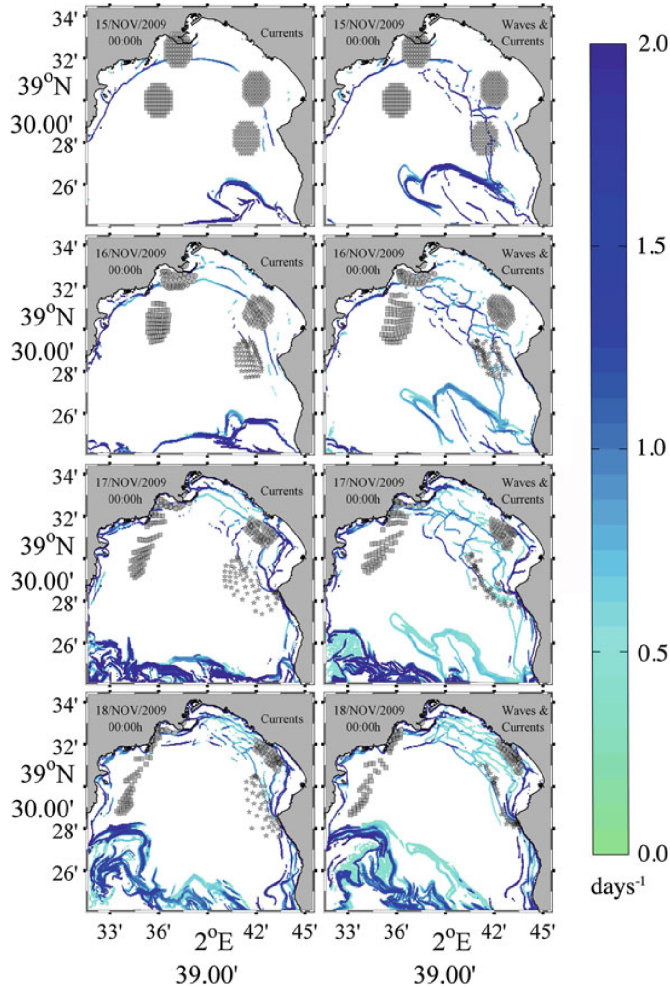


Figure 5.12: Daily snapshots of λ^- starting on November 15th (mild wind conditions), computed for only currents (left panel) and with waves and currents (right panel) . Virtual particles at four different areas are marked by *circles, diamonds, squares and stars*.

Firstly, we try to estimate the optimal δ_f . For this we performed for a given day (November 23rd, 2009 at 18.00h) simulations with set I and different values of

5.7. APPENDIX: MIXING RISE IN COASTAL AREAS INDUCED BY WAVES

$\delta_f = 150m$, $\delta_f = 250m$, $\delta_f = 500m$ and $\delta_f = 750m$ (see Figure 5.11) where the maximum values of the FSLEs are displayed.

Their typical filamentous structures that approximate the LCS are already clear and well defined with $\delta_f = 500m$ (Figure 5.11,c) which correspond roughly with the separation between six mesh points. To reduce computational costs we take this value to proceed with further analysis. In the following the LCS are computed only for the backwards in time dynamics (λ^-).

The influence of waves in the stirring of the surface layer area is assessed by analysing the LCS during two periods, 15th-18th and 21st-24th November, with different wave conditions. Starting on November 15th relatively mild wave conditions were present in the area. For this period, we compute the λ^- for both set I (Figure 5.12, left panel) and set II (Figure 5.12, right panel). LCS are shown for November 15th to November 18th at 00.00h. Not surprisingly the structure of the LCS displays a similar pattern for both sets of data. A barrier parallel to the coast appears and it is present during all the period separating two areas in the shallow zone. Shallow areas are characterized by stronger mixing as seen by the complex pattern of the LCS. Spatially averaged values of λ^- for currents are 0.09, 0.13, 0.29 and 0.21 days⁻¹ for November 15th, 16th, 17th and 18th, respectively, corresponding to mixing times of approximately 21, 14.6, 6.54, and 9 days.

For the same period these values including waves and currents (set II) are 0.13, 0.13, 0.28 and 0.23 days⁻¹ (mixing times of 14.6, 14.6, 6.77 and 8.24, days).

The general performance of LCS in describing the flow is usually assessed by using virtual neutrally buoyant Lagrangian particles (Shadden et al., 2009). In Fig. 5.12 we also represent the positions of 296 virtual particles at four different locations for November 15th-18th for the two sets. As expected, similar paths are followed by the particles deployed under current conditions (Fig. 5.12, left), and the particles deployed under waves and currents (Fig. 5.12, right) that are attracted in both cases on the LCS.

A different situation is presented for November 21st to November 24th. During this period, significant wave height (H_s) measured at deep waters reached 1m. The effect of waves is to increase mixing and therefore to modify the transport at the surface. The LCS for this period are displayed each day at 00.00h in Fig. 5.13 for set I (left) and for set II (right). Mean values of the wind stress imposed in set I during this period is 0.1N/m². For set II, mean values of stresses (wind plus radiation from waves) increased up to 0.25N/m². The barrier that was located near the coast during the analyzed mild wave condition of November 15th-18th has now moved onshore appearing new areas of strong mixing in the middle of the Bay and new LCS are present for both set I and set II with larger values of

CHAPTER 5. COASTAL LAGRANGIAN TRANSPORT

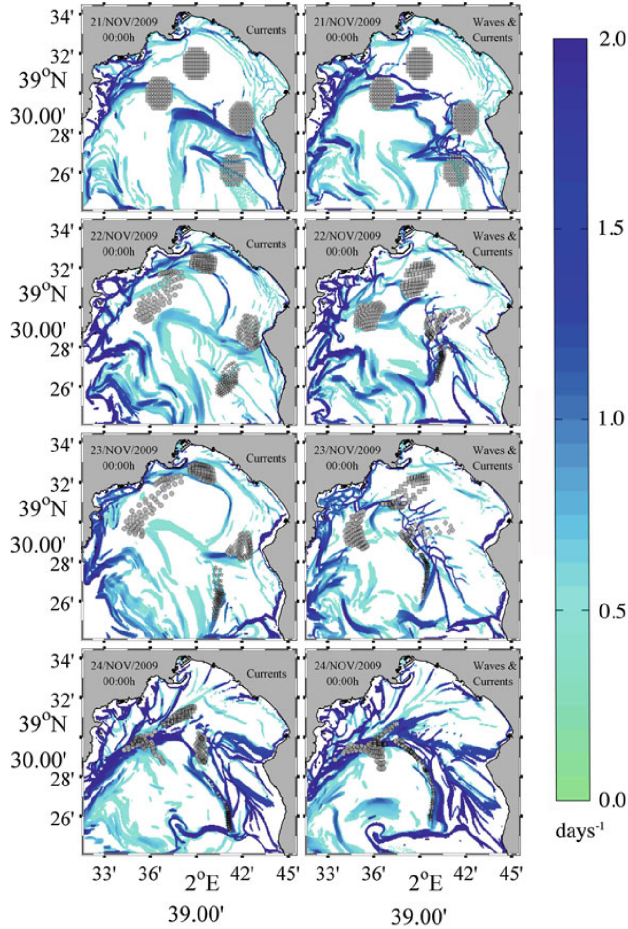


Figure 5.13: Daily snapshots of λ^- starting on November 21st (strong wind conditions), computed for only currents (left panel) and with waves and currents (right panel). Virtual particles at four different areas are marked by circles, diamonds, squares and stars.

λ^- in set II. Contrarily to the previous situation, the LCS from set I and the LCS from set II provide different patterns.

In general, the effect of waves is to increase the number of LCS, or rather to make them more convoluted. The spatially averaged values of λ^- for set I are -0.35 ,

5.7. APPENDIX: MIXING RISE IN COASTAL AREAS INDUCED BY WAVES

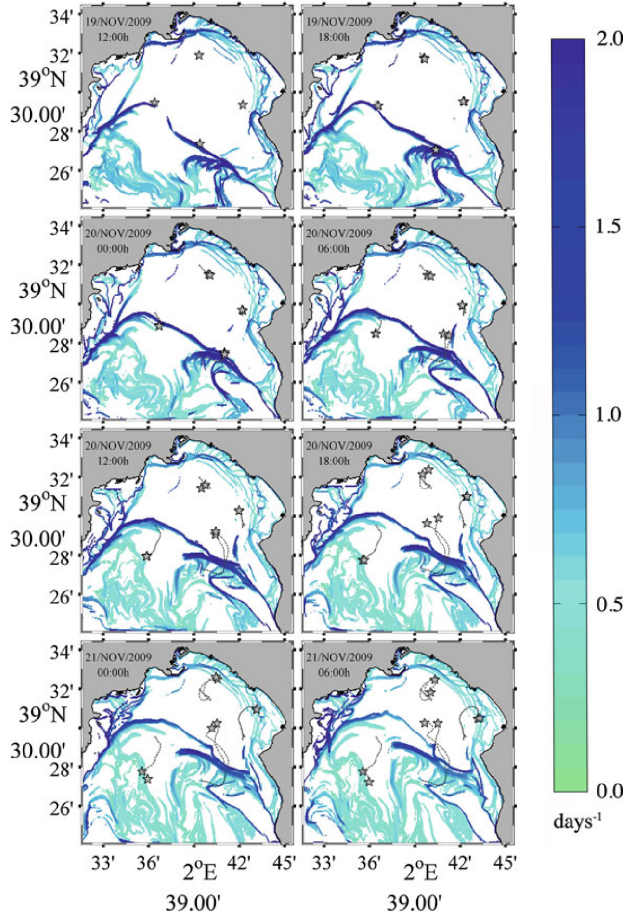


Figure 5.14: Six hour snapshot of λ^- computed for only currents (set I), and trajectories of Lagrangian drifters.

-0.45 , -0.37 and -0.59 days^{-1} (mixing times of 5.4, 4.2, 5.1 and 3.2, days) for currents at November 21st, 22nd, 23rd and 24th respectively. For the same days the spatially averaged values of λ^- for the coupling of waves and currents are respectively -0.41 , -0.49 , -0.42 and -0.64 days^{-1} (mixing times of 4.6, 3.9, 4.5 and 2.9 days). Again, we deployed 296 virtual particles in four different areas selected so as to be initially at different sides of any LCS. On November 22nd the particles of set I launched in the south-eastern part of the Bay hardly moved,

CHAPTER 5. COASTAL LAGRANGIAN TRANSPORT

being the centroid located at the same position than 24h before. Contrarily, in set II, Lagrangian particles deployed on the eastern part of the Bay (diamonds and stars) are well mixed, and they start to allocate along the LCS that is being generated in the north-south direction (second row of Fig. 5.13). One day later, on November 23rd, differences become more evident. The two groups of particles originally deployed on the eastern side, moved to the center of the Bay. The same snapshot for set I shows a very different situation, where the two groups evolve in a different way attracted by two weaker LCS. On the evening of November 23rd wave heights decrease. Both LCS fields on November 24th are very similar (Fig. 5.13, bottom column). Obviously, due to the history of the dynamics, particles are disposed over different lines of attraction. Besides, particles deployed initially at different areas are totally mixed in set II (bottom row in Fig. 5.13).

To further explore the role of the waves on the mixing in coastal areas coastal areas, four pairs of Lagrangian drifters were deployed on November 19th at 12.00h. The position of the drifters are displayed, every 6h, together with the computed LCS for sets I and II in Figs. 5.14 and 5.15 respectively. In these figures the trajectory of the buoys is also shown. During the first 18h H_s was below 0.3m and this is reflected in the pattern of the LCS. During this period, there is a clear separation between two areas of the Bay, with the deeper part more diffusive than the shallower one since currents for this conditions are mainly driven by the shelf slope dynamics. Drifters in the shallow part travel short distances indicating large residence times of surface waters. These buoys are located on a small diffusive zone for both set I (Fig. 5.14) and set II (Fig. 5.15). We want to recall at this point that since LCS are material surfaces, particles can not travel across them. This fact is violated in set I where a drifter crosses the ridge of the λ^- that divides the Bay on the 20th (second row of Fig. 5.14). More realistically, this LCS does not exist for set II (second row of Fig. 5.15), giving a natural pathway for the drifter. In the rest of the snapshots one also sees that the Lagrangian drifters follow more clearly the LCS from λ^- provided by set II. To quantify this fact, we compute the mean value of the FSLE in trajectories following by drifters in set I, which is near to 0.50 days⁻¹ while for set II, the same value is above 0.90 days⁻¹, i.e., drifters follow the LCS computed by set II in a better way than LCS computed in absence of waves.

We have shown that a proper characterization of currents using coupled models of waves and currents is necessary to obtain the correct patterns of LCS which describe the dynamics of the area. The analyzed situation suggests that the effects of waves is to increase coastal mixing up to 10-20% with respect to the mixing induced by only-wind driven currents.

5.7. APPENDIX: MIXING RISE IN COASTAL AREAS INDUCED BY WAVES

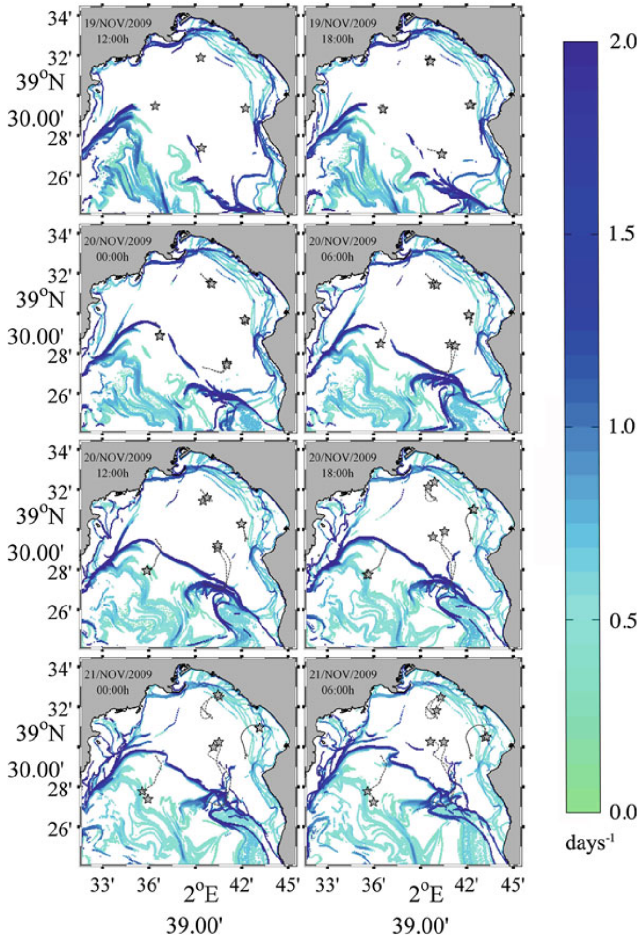


Figure 5.15: Six hour snapshot of λ^- computed for currents and waves (set II), and trajectories of Lagrangian drifters.

Effect of transport on plankton dynamics in the Benguela upwelling region

Recent studies, both based on remote sensed data and coupled models, showed a reduction of biological productivity due to vigorous horizontal stirring in upwelling areas. In order to better understand this phenomenon, we have considered a system of oceanic flow in the Benguela area coupled with a simple biogeochemical model of Nutrient-Phyto-Zooplankton (NPZ) type. For the flow three different surface velocity fields are considered: one derived from satellite altimetry data, and the other two from a regional numerical model at two different spatial resolutions. We computed horizontal particle dispersion in terms of Lyapunov Exponents, and analyzed their correlations with phytoplankton concentrations. Our modelling approach confirms that in the south Benguela there is a reduction of biological activity when stirring is increased. Two-dimensional offshore advection and north-south differences in the growth rate of phytoplankton seem to be the dominant processes involved. In the northern area, other factors not taken into account in our simulation are influencing the ecosystem. We provide explanations for these results in the context of studies performed in other Eastern Boundary upwelling areas.

Introduction

Marine ecosystems of the Eastern Boundary Upwelling zones are well known for their major contribution to the world ocean productivity. They are characterized by wind-driven upwelling along the coast of cold nutrient-rich waters that supports elevated plankton and pelagic fish production (Mackas et al., 2006). Variability is introduced by strong advection along the shore, physical forcings by local and large scales winds, and high sub- and mesoscale activities over the continental shelf and beyond, linking the coastal domain with the open ocean.

The Benguela Upwelling System (BUS) is one of the four major Eastern Boundary Upwelling Systems (EBUS) of the world. The coastal area of the Benguela ecosystem extends from southern Angola (around 17°S) along the west coast of Namibia and South Africa (36°S). It is surrounded by two warm temperate boundary currents, the Angola Current in the north, and the Agulhas Current in the south. The BUS can itself be subdivided into two subdomains by the powerful Luderitz upwelling cell (Hutchings et al., 2009). Most of the biogeochemical activity occurs within the upwelling front and the coast, although it can be extended further offshore toward the open ocean by the numerous filamental structures developing offshore (Monteiro, 2009). In the BUS, as in the other major upwelling areas, high mesoscale activity due to eddies and filaments impacts strongly marine planktonic ecosystem over the continental shelf and beyond (Brink and Cowles, 1991; Martin, 2003; Sandulescu et al., 2008; Rossi et al., 2009).

The purpose of this study is to analyze the impact of horizontal stirring on phytoplankton dynamics in the BUS within an idealized two dimensional modelling framework. Based on satellite data of the ocean surface, Rossi et al. (2008, 2009) recently suggested that mesoscale activity has a negative effect on chlorophyll standing stocks in the four EBUS. This was obtained by correlating remote sensed chlorophyll data with a Lagrangian measurement of lateral stirring in the surface ocean (see Methods section below). This result was unexpected since mesoscale physical structures, particularly mesoscale eddies, has been related to higher planktonic production and stocks in the open ocean (McGillicuddy et al., 2007) as well as off a major EBUS (Correa-Ramirez et al., 2007). A more recent and thorough study performed by Gruber et al. (2011) in the California and the Canary current systems extended the initial results from Rossi et al. (2008, 2009). Based on satellite derived estimates of net Primary Production, of upwelling strength and of Eddy Kinetic Energy (EKE) as a measure the intensity of mesoscale activity, they confirmed the suppressive effect of mesoscale structures on biological

6.1. INTRODUCTION

production in upwelling areas. Investigating the mechanism behind this observation based on 3D eddy resolving coupled models, Gruber et al. (2011) showed that mesoscale eddies tend to export offshore and downward a certain pool of nutrients not being effectively used by the biology in the coastal areas. This process they called "nutrients leakage" is also having a negative feedback effect by diminishing the pool of deep nutrients available in the surface waters being re-upwelled continuously.

In our work, we focused on the Benguela area, being the most contrasting area of all EBUS in terms of stirring intensity (Rossi et al., 2009). Although the mechanisms studied by Gruber et al. (2011) seem to involve 3D dynamics, the initial observation of this suppressive effect was essentially based on two-dimensional (2D) datasets (Rossi et al., 2008). In this work we use 2D numerical analysis in a semi-realistic framework to better understand the effect of 2D horizontal advection on biological dynamics, apart from the complex 3D bio-physical processes. The choice of this simple horizontal numerical approach is indeed supported by other theoretical 2D studies that also displayed a negative correlation between stirring and biomass (Tél et al., 2005; McKiver and Neufeld, 2009; Neufeld and Hernández-García, 2009). Meanwhile, since biological productivity in upwelling areas rely on the (wind-driven) vertical uplift of nutrients, we introduced in our model a nutrient source term with an intensity and spatial distribution corresponding to the upwelling characteristics. Instead of the commonly used EKE, which is an Eulerian diagnostic tool, we used here a Lagrangian measurement of mesoscale stirring that has been demonstrated as a powerful tool to study patchy chlorophyll distributions influenced by dynamical structures at mesoscale, such as upwelling filaments (Calil and Richards, 2010). To consider velocity fields with different characteristics and to test the effect of the spatial resolution, different flow fields are used, one derived from satellite and two produced by numerical simulations at two different spatial resolutions. Our modelled chlorophyll-a is compared with observed distributions of chlorophyll-a (a metric for phytoplankton) obtained from the SeaWiFS satellite sensor.

This Chapter is organized as follows. Sec. 6.2 is a brief description of the different datasets used in this study. Sec. 6.3 depicts the methodology, which includes the computation of the finite-size Lyapunov exponents, and the numerical 'plankton-flow' 2D coupled model. Then, our results are analyzed and discussed in context of the existing bibliography in Sec. 6.4. Finally in Sec. 6.6, we summed-up our main findings.

Satellite and simulated data

We used three different 2-dimensional surface velocity datasets of the Benguela area. Two are obtained from the numerical model ROMS (Regional Ocean Model System), and the other one from a combined satellite product.

6.2.1 Surface velocity fields derived from regional simulations

ROMS is a free surface, hydrostatic, primitive equation model, and the run used here was eddy resolving but climatologically forced (Gutknecht et al., 2011). At each grid point, linear horizontal resolution is the same in both the longitudinal, ϕ , and latitudinal, θ , directions, which leads to angular resolutions $\Delta\phi = \Delta_0$ and $\Delta\theta = \Delta\phi \cos \theta$. The numerical model was run onto 2 different grids: a coarse one at spatial resolution of $\Delta_0 = 1/4^\circ$, and a finer one at $\Delta_0 = 1/12^\circ$ of spatial resolution. In the following we label the data set from the coarser resolution as *ROMS1/4*, and the finer one as *ROMS1/12*. In both of them, vertical resolution is variable with 30 layers in total, while only data from the surface upper layer are used. Since the flows are obtained from climatological forcings, they would represent a mean annual cycle of the typical surface currents of the Benguela region.

6.2.2 Surface velocity field derived from satellite

A velocity field derived from satellite observations is compared to the simulated fields describe previously. It consists of surface currents computed from a combination of wind-driven Ekman currents, at 15 m depth, derived from Quikscat wind estimates, and geostrophic currents calculated using time-variable Sea Surface Heights (SSH) obtained from satellite (Sudre and Morrow, 2008). These SSH were calculated from mapped altimetric sea level anomalies combined with a mean dynamic topography. This velocity field, labeled as *Satellite1/4*, covers a period from June 2002 to June 2005 with a spatial resolution of $\Delta_0 = 1/4^\circ$ in both longitudinal and latitudinal directions.

6.2.3 Ocean color as a proxy for phytoplankton biomass

To validate simulated biological fields we used a three-year-long time series, from January 2002 to January 2005, of ocean color data. Phytoplankton pigment

concentration (chlorophyll-a) is obtained from monthly SeaWiFS (Sea viewing Wide Field-of-view Sensor) products, generated by the NASA Goddard Earth Science (GES)/Distributed Active Archive Center (DAAC). Gridded global data were used with a resolution of approximately 9 by 9 km.

6.3

Methodology

6.3.1 Finite-Size Lyapunov Exponents (FSLEs)

FSLEs (Artale et al., 1997; Aurell et al., 1997; Boffetta et al., 2001) provides a measure of dispersion, and thus of stirring and mixing, as a function of the spatial resolution. This Lagrangian tool allows one to isolate the different regimes corresponding to different length scales of the oceanic flows, as well as to identify Lagrangian Coherent Structures (LCSs) present in the data (d’Ovidio et al., 2004). FSLE are computed from τ , the time required for two particles of fluid (one of them placed at \mathbf{x}) to separate from an initial (at time t) distance of δ_0 to a final distance of δ_f , as

$$\lambda(\mathbf{x}, t, \delta_0, \delta_f) = \frac{1}{\tau} \log \frac{\delta_f}{\delta_0}. \quad (6.1)$$

It is natural to choose the initial points \mathbf{x} on the nodes of a grid with lattice spacing coincident with the initial separation of fluid particles δ_0 . Then, values of λ are obtained in a grid with lattice separation δ_0 . In most of this work the resolution of the FSLE field, δ_0 , is chosen equal to the resolution of the velocity field, Δ_0 . Other choices of parameter are possible and δ_0 can take any value, even much smaller than the resolution of the velocity field (Hernández-Carrasco et al., 2011). This opens many possibilities that will not be fully explored in this work (see also Fig. 6.3 and 6.5.1). We also investigate the response of the coupled biophysical system to variable resolution of the velocity field, using similar parameters for the FSLEs’ computation (see Hernández-Carrasco et al. (2011) for further details about the sensitivity of the FSLEs to the choice of parameters).

The field of FSLEs thus depends on the choice of two length scales: the initial, δ_0 and the final δ_f separations. As in previous works (d’Ovidio et al., 2004, 2009; Hernández-Carrasco et al., 2011) we will focus on transport processes at mesoscale, so that δ_f is taken as about 110 km, or 1° , which is the order of the size of mesoscale eddies at mid latitudes. To compute λ we need to know the trajectories of the particles, which gives the Lagrangian character to this quantity. The equations of motion that describe the horizontal evolution of particle trajectories

CHAPTER 6. EFFECT OF STIRRING ON PLANKTON DYNAMICS

in longitudinal and latitudinal spherical coordinates, $\mathbf{x} = (\phi, \lambda)$, are:

$$\frac{d\phi}{dt} = \frac{u(\phi, \theta, t)}{R \cos \theta}, \quad (6.2)$$

$$\frac{d\theta}{dt} = \frac{v(\phi, \theta, t)}{R}, \quad (6.3)$$

where u and v represent the eastwards and northwards components of the surface velocity field, and R is the radius of the Earth (6400 km).

The ridges of the FSLE field can be used to define the Lagrangian Coherent Structures (LCSs) (Haller and Yuan, 2000; d'Ovidio et al., 2004, 2009; Tew Kai et al., 2009; Hernández-Carrasco et al., 2011), which are useful to characterize the flow from the Lagrangian point of view (Joseph and Legras, 2002; Koh and Legras, 2002). In fact, since we are only interested in the ridges with large values of FSLE, the ones which significantly affect stirring, LCSs can be obtained as the regions with high values of FSLE, which have a line-like shape. We will compute FSLEs integrating backwards-in-time the particle trajectories, since attracting LCSs associated to this (the unstable manifolds) have a direct physical interpretation (Joseph and Legras, 2002; d'Ovidio et al., 2004, 2009). Tracers, such as temperature and chlorophyll-*a*, spread along the attracting LCSs, thus creating their typical filamental structure (Lehan et al., 2007; Calil and Richards, 2010).

6.3.2 The Biological model

The plankton model is similar to the one used in previous studies by Oschlies and Garçon (1998, 1999) and Sandulescu et al. (2007, 2008). It describes the interaction of a three-level trophic chain in the mixed layer of the ocean, including phytoplankton P , zoo-plankton Z and dissolved inorganic nutrient N , whose concentrations evolve in time according to the following equations:

$$\frac{dN}{dt} = F_N = \Phi_N - \beta \frac{N}{\kappa_N + N} P + \mu_N \left((1 - \gamma) \frac{\alpha \eta P^2}{\alpha + \eta P^2} Z + \mu_P P + \mu_Z Z^2 \right), \quad (6.4)$$

$$\frac{dP}{dt} = F_P = \beta \frac{N}{\kappa_N + N} P - \frac{\alpha \eta P^2}{\alpha + \eta P^2} Z - \mu_P P, \quad (6.5)$$

$$\frac{dZ}{dt} = F_Z = \gamma \frac{\alpha \eta P^2}{\alpha + \eta P^2} Z - \mu_Z Z^2, \quad (6.6)$$

where the dynamics of the nutrients, Eq. (6.4), is determined by nutrient supply due to the vertical mixing Φ_N , its uptake by phytoplankton (2^{nd} term) and its re-

6.3. METHODOLOGY

cycling by bacteria from sinking particles (3^{rd} term). Vertical mixing which brings subsurface nutrients into the mixed surface layer of the ocean is parameterized in our coupled model (see below), since the hydrodynamical part considers only horizontal 2D transport. Terms in Eq. (6.5) stand for phytoplankton growth by consuming N , the grazing by zooplankton, and phytoplankton natural mortality. The last equation, Eq. (6.6), represents zooplankton growth by consuming phytoplankton minus zooplankton quadratic mortality.

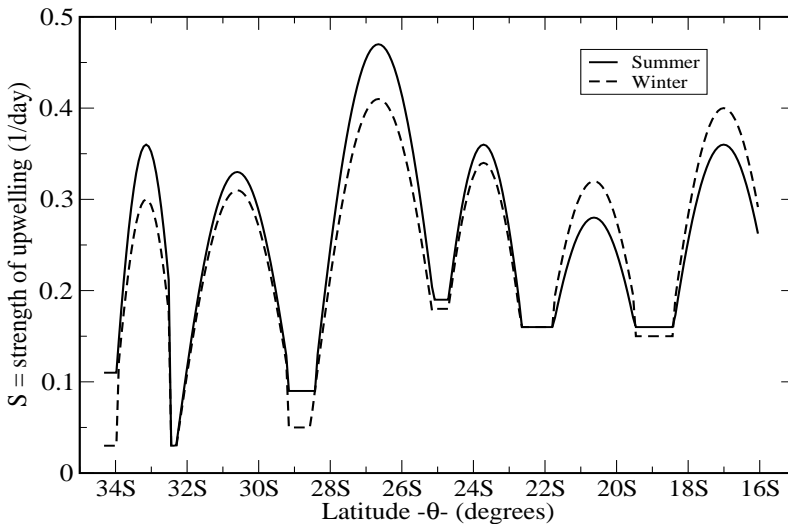


Figure 6.1: Shape and values of the strength (S) of the upwelling cells used in the simulations for winter and summer seasons (following Veitch et al. (2009)).

An important term of the model is the parameterization of the vertical uplift of nutrients due to coastal upwelling. Assuming constant nutrient concentration N_0 below the mixed layer, this term reads:

$$\Phi_N = S(\mathbf{x}, t)(N_0 - N), \quad (6.7)$$

where the temporally and spatially dependent (on the two dimensional location \mathbf{x}) function S determines the strength and the horizontal spatial distribution

CHAPTER 6. EFFECT OF STIRRING ON PLANKTON DYNAMICS

of vertical mixing in the model, thus specifying the strength of the coastal upwelling. Thus, the function S represents the vertical movement due to coastal upwelling in our 2D model. Upwelling intensity along the coast is characterized by a number of coastal cells of enhanced vertical Ekman driven transport that are associated with similar fluctuations of the alongshore wind (Demarcq et al., 2003; Veitch et al., 2009). Following these results, we defined our function S as being null over the whole domain except in a 0.5° wide coastal strip, varying in intensity depending on the latitude concerned (see Fig. 6.1). Six separate upwelling cells can be discerned in the figure, peaking at approximately 33°S , 31°S , 27.5°S , 24.5°S , 21.5°S , 17.5°S . These cells are named Cape Peninsula, Columbine+Namaqua, Luderitz, Walvis Bay, Namibia and Cunene, respectively, Luderitz being the strongest. For the temporal dependence, S switches between a summer and a winter parameterization displayed in Fig. 6.1.

When Φ_N is frozen to either its summer or its winter shape described in Fig. 6.1, the dynamical system given by Eqs. (6.4,6.5,6.6) evolves towards an equilibrium distribution for N , P and Z . The transient time to reach equilibrium is typically 60 days with the initial concentrations used (see Sec. 6.3.3). The parameters are set following a study by Pasquero et al. (2004) and are listed in Table 6.1.

Parameter	Symbol	Value
Phytoplankton growth rate	β	0.66 day^{-1}
Prey capture rate	η	$1.0 (\text{mmol N m}^{-3})^{-2} \text{ day}^{-1}$
Assimilation efficiency of Zooplankton	γ	0.75
Maximum grazing rate	a	2.0 day^{-1}
Half-saturation constant for N uptake	k_N	$0.5 \text{ mmol N m}^{-3}$
Inefficiency of remineralization	μ_N	0.2
Specific mortality rate	μ_P	0.03 day^{-1}
(Quadratic) mortality	μ_Z	$0.2 (\text{mmol N m}^{-3})^{-1} \text{ day}^{-1}$
Nutrient concentration bellow mixed layer	N_0	$8.0 \text{ mmol N m}^{-3}$

Table 6.1: List of parameters used in the biological model.

6.3.3 Coupling hydrodynamical and biological models in Benguela

The evolution of the simulated concentrations advected within a flow is determined by the coupling between the hydrodynamical and biological models, as described by an advection-reaction-diffusion system. The complete model is given by the following system of partial differential equations:

6.4. RESULTS AND DISCUSSION

$$\frac{\partial N}{\partial t} + \mathbf{v} \cdot \nabla N = F_N + D\nabla^2 N, \quad (6.8)$$

$$\frac{\partial P}{\partial t} + \mathbf{v} \cdot \nabla P = F_P + D\nabla^2 P, \quad (6.9)$$

$$\frac{\partial Z}{\partial t} + \mathbf{v} \cdot \nabla Z = F_Z + D\nabla^2 Z. \quad (6.10)$$

The biological model is the one described before by the functions F_N , F_P and F_Z . Horizontal advection is the 2D velocity field \mathbf{v} , which is obtained from satellite data or from the ROMS model. We add also an eddy diffusion term, via the ∇^2 operator, acting on N , P , and Z to incorporate the small-scale turbulence, which is not explicitly taken into account by the velocity fields used.

The eddy diffusion coefficient, D , is given by Okubo's formula (Okubo, 1971), $D(l) = 2.055 * 10^{-4} l^{1.15}$, where l is the value of the resolution, in meters, corresponding to the angular resolution $l = \Delta_0$. The formula gives the values $D=26.73 \text{ m}^2/\text{s}$ for *Satellite1/4* and *ROMS1/4*, and $D=7.4 \text{ m}^2/\text{s}$ for *ROMS1/12*.

The coupled system Eqs. (6.8),(6.9) and (6.10) is solved numerically by the semi-Lagrangian algorithm described in Sandulescu et al. (2007) and in A.4, combining Eulerian and Lagrangian schemes. The initial concentrations of the tracers were taken from Koné et al. (2005) and they are $N_0 = 1 \text{ mmolNm}^{-3}$, $P_0 = 0.1 \text{ mmolNm}^{-3}$, and $Z_0 = 0.06 \text{ mmolNm}^{-3}$. The inflow conditions at the boundaries are specified in the following way: at the eastern, western, and southern edges of the computation domain fluid parcels enter with very low concentrations ($N_L = 0.01N_0 \text{ mmolNm}^{-3}$, $P_L = 0.01P_0 \text{ mmolNm}^{-3}$, and $Z_L = 0.01Z_0 \text{ mmolNm}^{-3}$). Across the northern boundary, fluid parcels enter with higher concentrations ($N_H = 5 \text{ mmolNm}^{-3}$, $P_H = 0.1 \text{ mmolNm}^{-3}$, and $Z_H = 0.06 \text{ mmolNm}^{-3}$). Nitrate concentrations are derived from CARS climatology (Condie and Dunn, 2006), while P and Z concentrations are taken from Koné et al. (2005). The integration time step is $dt = 6$ hours.

6.4

Results and discussion

In this section we first compute the FSLEs on the velocity fields to quantify the horizontal stirring activity over the area. Then we analyze the simulations of the coupled biological-hydrodynamic model. Finally we investigate the relationship between horizontal stirring activity and biological productivity.

6.4.1 Validation of our simple 2D idealized setting using satellite data

Horizontal stirring

We compute the FSLE with an initial separation of particles equal to the spatial resolution of each velocity field ($\delta_0 = 1/4^\circ$ for *Satellite1/4* and *ROMS1/4*, and $\delta_0 = 1/12^\circ$ for *ROMS1/12*), an a final distance of $\delta_f = 1^\circ$ to focus on transport processes by mesoscale structures at mid latitudes. The areas of more intense horizontal stirring due to mesoscale activity can be identified by large values of temporal averages of backward FSLEs (see Figure 6.2). There are visible differences between the results from the different velocity fields, specially in the small scale patterns, but a quantitative comparison in terms of the spatial correlation can be considered as relatively good: for instance, correlation coefficient R^2 between FSLEs map from *Satellite1/4* and from *ROMS1/4* is 0.81. Correlation coefficients between *Satellite1/4* and *ROMS1/12* on one hand, and between *ROMS1/4* and *ROMS1/12* on the other hand, are lower (0.61 and 0.77 respectively) since the FSLE were computed on a different resolution. More details on the effect on the grid resolution when computing FSLEs can be found in Hernández-Carrasco et al. (2011). For all data sets high stirring values are observed in the southern region, while the northern area displays significantly lower values, consistent with Rossi et al. (2009). Note that the separation is well marked for *Satellite1/4* where high and low values of FSLE occur below and above a line at 27° approximately. In the case of the ROMS data sets, the stirring activity is more homogeneously distributed, although the north-south gradient is still present. We associate this latitudinal gradient with the injection of strong and numerous Agulhas rings into the south of the area from the Agulhas retroflection. Following Gruber et al. (2011) we compute the EKE, another proxy of the intensity of mesoscale activity. There are regions with distinct dynamical characteristics as the southern subsystem is characterized by larger EKE values than the northern area, in good agreement with the analysis arising from FSLEs (Fig. 6.2). Spatial correlations (not shown) indicate that EKE and FSLE patterns are well correlated using a non-linear fitting (power law). For instance, EKE and FSLE computed on the velocity field from *Satellite1/4* exhibit a R^2 of 0.86 for the non-linear fitting: $FSLE = 0.009 \cdot EKE^{0.49}$. This is in agreement with the initial results from Waugh et al. (2006); Waugh and Abraham (2008), for a related dispersion measurement, and confirmed the thorough investigation of the relationship between EKE and FSLE by Hernández-Carrasco et al. (2011).

To analyze the variability of horizontal mixing with latitude, we compute longitudinal averages of the plots in Fig. 6.2 for two different coastally-oriented

6.4. RESULTS AND DISCUSSION

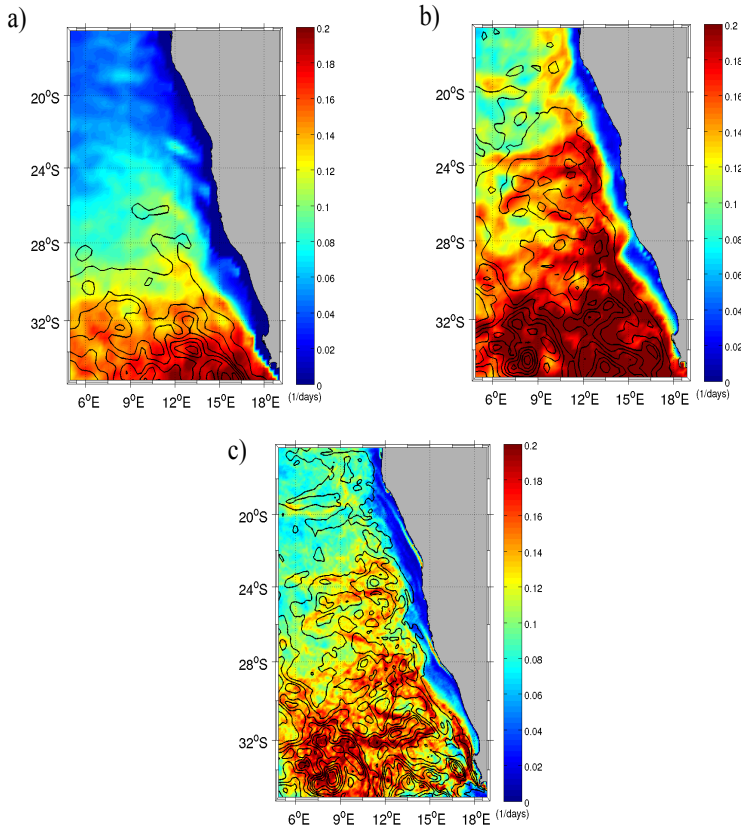


Figure 6.2: Spatial distribution of time average of weekly FSLE maps in the Benguela region. a) Three years average using data set *Satellite1/4*; b) one year average using *ROMS1/4*; c) one year average using *ROMS1/12*. The units of the colorbar are $1/days$. The black lines are contours of annual EKE. The separation between contour levels is $100cm^2/s^2$.

strips extended: a) from the coast to 3° offshore, and b) from 3° to 6° offshore (see Fig. 6.3). It allows analyzing separately subareas characterized by distinct bio-physical characteristics (see also Rossi et al. (2009)), the coastal upwelling (3° strip) with high plankton biomasses and moderated mesoscale activity, and the open ocean (from 3° to 6° offshore) with moderated plankton biomasses and high mesoscale activity. It is clear that horizontal stirring decreases with latitude. In

CHAPTER 6. EFFECT OF STIRRING ON PLANKTON DYNAMICS

Fig. 6.3 (a) we see that, for *Satellite1/4*, the values of FSLEs decay from 0.18 days^{-1} in the southern to 0.03 days^{-1} in the northern area, with similar significant decays for *ROMS1/4* and *ROMS1/12*. Specifically the North-South difference for *Satellite1/4*, *ROMS1/4* and *ROMS1/12* are of the order of 0.15 days^{-1} , 0.15 days^{-1} and 0.08 days^{-1} , respectively, confirming a lower latitudinal gradient for the case of *ROMS1/12*.

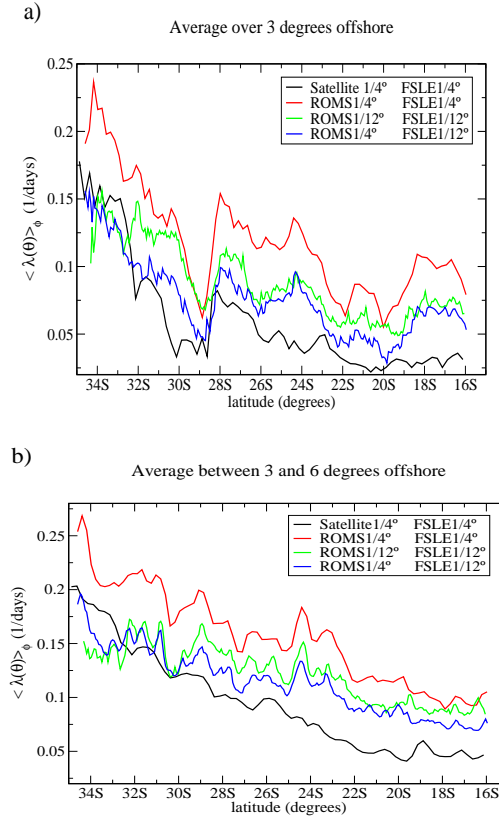


Figure 6.3: Zonal average over coastal bands of the FSLE time averages from Fig. 6.2 as a function of latitude. a) from the coast to 3 degrees offshore; b) between 3 and 6 degrees offshore.

Note that there are differences in the stirring values (FSLEs) depending on the type of data, their resolution, the averaging strip, and the grid size of FSLE computation. In general, considering velocities with the same resolution, the

6.4. RESULTS AND DISCUSSION

lower values correspond to *Satellite1/4* as compared to *ROMS1/4*. On average, values of stirring from *ROMS1/4* are larger than those from *ROMS1/12*, whereas we would expect the opposite considering the higher resolution of the latter simulation favoring small scales processes. However, this comparison is hampered by the known fact that spatial means of FSLE values are reduced when computing them in grids of higher resolution, because the largest values become increasingly concentrated in thinner lines, a consequence of their multifractal character (Hernández-Carrasco et al., 2011). When FSLEs are computed using velocity data from *ROMS1/12* and *ROMS1/4* but on the same FSLE grid with a fixed resolution of $1/12^\circ$, one finds smaller values of FSLEs for the coarser velocity field (*ROMS1/4*) (see green and blue lines in Fig. 6.3). The effect of reducing the velocity spatial resolution on the FSLE calculations is considered more systematically in 6.5.1. A general observation consistent between all datasets is that horizontal mixing is slightly less intense and more variable in the region of coastal upwelling (from the coast to 3° offshore) than within the transitional area with the open ocean ($3-6^\circ$ offshore). Note also that a low-stirring region is observed within the 3° width coastal strip from 28° to 30° S on all calculations. These observations confirm that the ROMS model is representing well the latitudinal variability of the stirring as measured from FSLE based on satellite data. These preliminary results indicate that Lyapunov exponents and methods could be used as a diagnostic to validate the representation of mesoscale activity in eddy-resolving oceanic models, as suggested recently by Titaud et al. (2011). Overall, the variability of stirring activity in the Benguela derived from the simulated flow fields is in good agreement with the satellite observations.

Simulated phytoplankton concentrations

Evolution of N , P and Z over space and time is obtained by integrating the systems described by Eqs. (6.8), (6.9) and (6.10). The biological model is coupled to the velocity field after the spin-up time needed to reach stability (60 days). Analysing the temporal average of simulated P (Fig. 6.4), we found that coastal regions with high P extend approximately, depending on latitude, between half a degree and two degrees offshore. It is comparable with the pattern obtained from the satellite-derived chlorophyll data (Fig.6.4 d)). The spatial correlation between averaged simulated and satellite chlorophyll is as follows: $R^2 = 0.85$ for *Satellite1/4* versus *SeaWIFS*; $R^2 = 0.89$ for *ROMS1/4* versus *SeaWIFS* and $R^2 = 0.85$ for *ROMS1/12* versus *SeaWIFS*. Despite the very simple setting of our model, including the parameterization of the coastal upwelling, the distribution of phytoplankton biomass is relatively well simulated in the Benguela area. Note however that our simulated chlorophyll values are about $\approx 3-4$ times lower than satellite data, as shown by the colorbar scale. Many biological and physical

CHAPTER 6. EFFECT OF STIRRING ON PLANKTON DYNAMICS

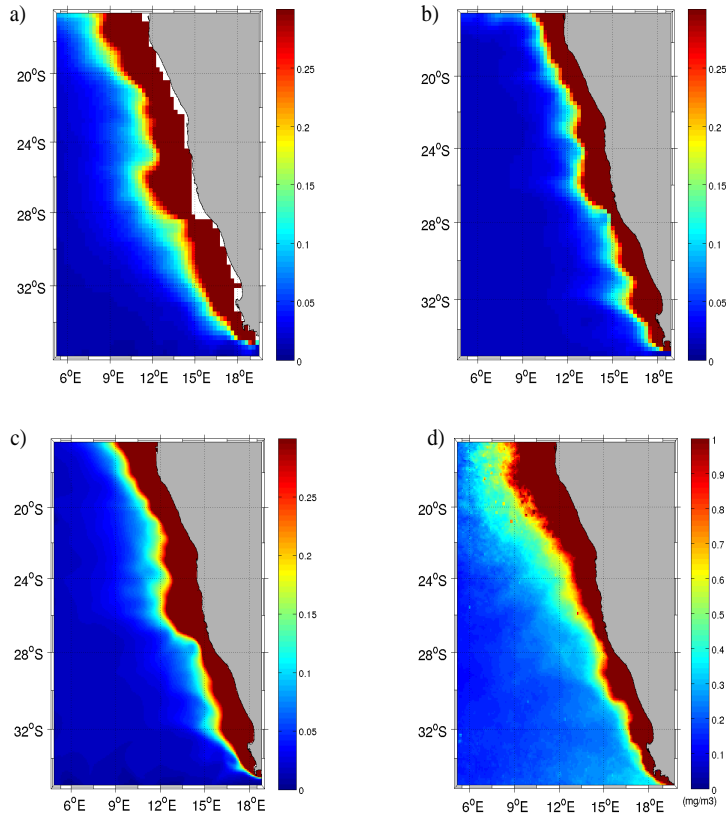


Figure 6.4: Spatial distribution of the time average of phytoplankton concentrations: a) Three years average using *Satellite1/4*, b) One year average from *ROMS1/4*, c) One year average from *ROMS1/12*, d) Three years average of monthly SeaWIFS data. The units of the colorbar are mg/m^3 .

factors not taken into account in this simple setting could be invoked to explain this offset. Another possible explanation is the low reliability of ocean color data in the optically complex coastal waters (Mélin et al., 2007).

We now examine the latitudinal distribution of P comparing the outputs of the numerical simulations versus the satellite chlorophyll-a over different coastally oriented strips (Fig.6.5). Simulated P concentrations are higher in the northern than in the southern area of Benguela, in good agreement with the chlorophyll-a

6.4. RESULTS AND DISCUSSION

data derived from satellite. A common feature is the minimum located just below the Luderitz upwelling cell (28°S), which may be related to the presence of a physical boundary, already studied and named the LUCORC barrier by Shannon et al. (2006) and Lett et al. (2007). The decrease of P concentration is clearly visible in the open ocean region of the *Satellite1/4* case (Fig. 6.5 b)). Correlations of zonal averages between simulated and satellite chlorophyll-a are poor when considering the whole area (R^2 ranging from 0.1 to 0.5). However, when considering each subsystem (northern and southern) independently, high correlation coefficients are found for the south Benguela (R^2 around 0.75), but not for the north. This indicates that our simple modelling approach is able to simulate the spatial patterns of chlorophyll in the south Benguela, but not properly in the northern part. In the north, other factors not considered here (such as the 3D flow, the varying shelf width, the external inputs of nutrients, realistic non-climatologic forcings, complex biogeochemical processes, etc...) seem to play an important role in determining the surface chlorophyll-a observed from space.

6.4.2 Relationship between phytoplankton and horizontal stirring

In Fig. 6.6 we show some snapshots of phytoplankton concentrations every 8 days during a 32 days period for *ROMS1/12*. Since both ROMS simulations were climatologically forced runs, the dates do not correspond to a specific year. The most relevant feature is the larger value of concentrations near the coast due to the injection of nutrients. Obviously the spatial distribution of P is strongly influenced by the submeso- and meso-scale structures such as filaments and eddies, especially in the southern subsystem. Differences are however observed between the three data sets. In particular, it seems that for *Satellite1/4* and *ROMS1/12* the concentrations extend further offshore than for *ROMS1/4* (not shown). In 6.5.1 we provide additional analysis of the effect of the velocity spatial resolution on phytoplankton evolution. We found that velocity data with different resolution produces similar phytoplankton patterns but larger absolute values of concentrations as the spatial resolution of the velocity field is refined (see Mahadevan and Archer (2000); Lévy et al. (2001)), supporting the need to compare different spatial resolutions.

Several studies (Lehan et al., 2007; d'Ovidio et al., 2009; Calil and Richards, 2010) have shown that transport of chlorophyll distributions in the marine surface is linked to the motion of local maxima or ridges of the FSLEs. This is also observed in our numerical setting when superimposing contours of high values of FSLE (locating the LCSs) on top of phytoplankton concentrations for *ROMS1/12* (see Fig. 6.6). In some regions P concentrations are constrained and stirred by lines of

CHAPTER 6. EFFECT OF STIRRING ON PLANKTON DYNAMICS

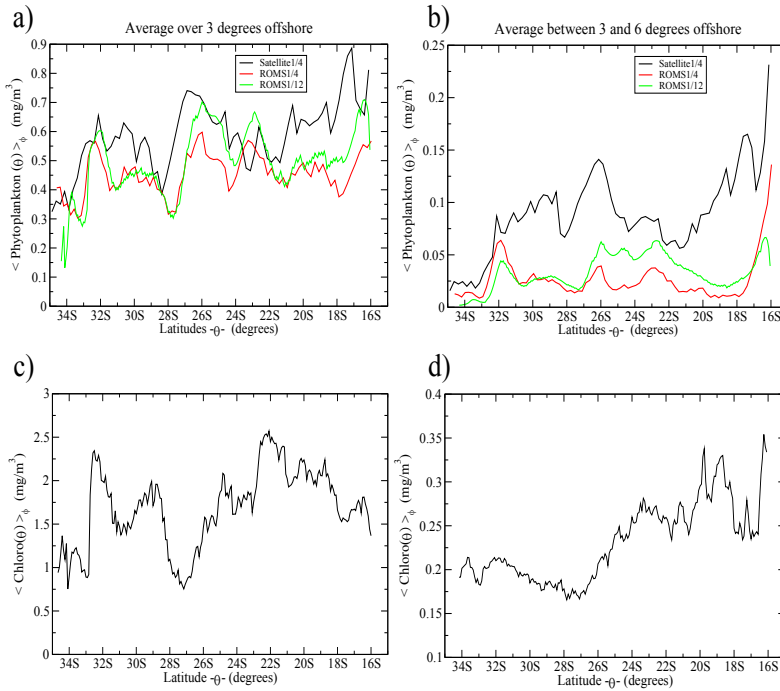


Figure 6.5: Zonal mean of simulated phytoplankton over a coastally oriented strip from the coast to 3 degrees (a) and from 3 degrees to 6 degrees offshore (b), plotted as a function of latitude. Zonal average of phytoplankton derived from satellite (SeaWIFS) over a coastal band from the coast to 3 degrees (c) and from 3 degrees to 6 degrees offshore (d).

FSLE. For instance, the elliptic eddy-like structure at 13°E , 32°S is characterized by high phytoplankton concentrations at its edge, but relatively low in its core. This reflects the fact that tracers, even active such as chlorophyll, still disperse along the LCSs.

From Fig. 6.5 it is clear that phytoplankton biomass has a general tendency to decrease with latitude, an opposite tendency to the one exhibited by stirring (as inferred from the FSLEs and EKE distributions in Figs. 6.2 and 6.3) for the three data sets. Moreover, note that the minimum of phytoplankton located just below the LUCORC barrier at 28°S (Fig. 6.5) coincides with a local maximum of stirring that might be responsible for this barrier (Fig. 6.3 a). Spatial mean and

6.4. RESULTS AND DISCUSSION

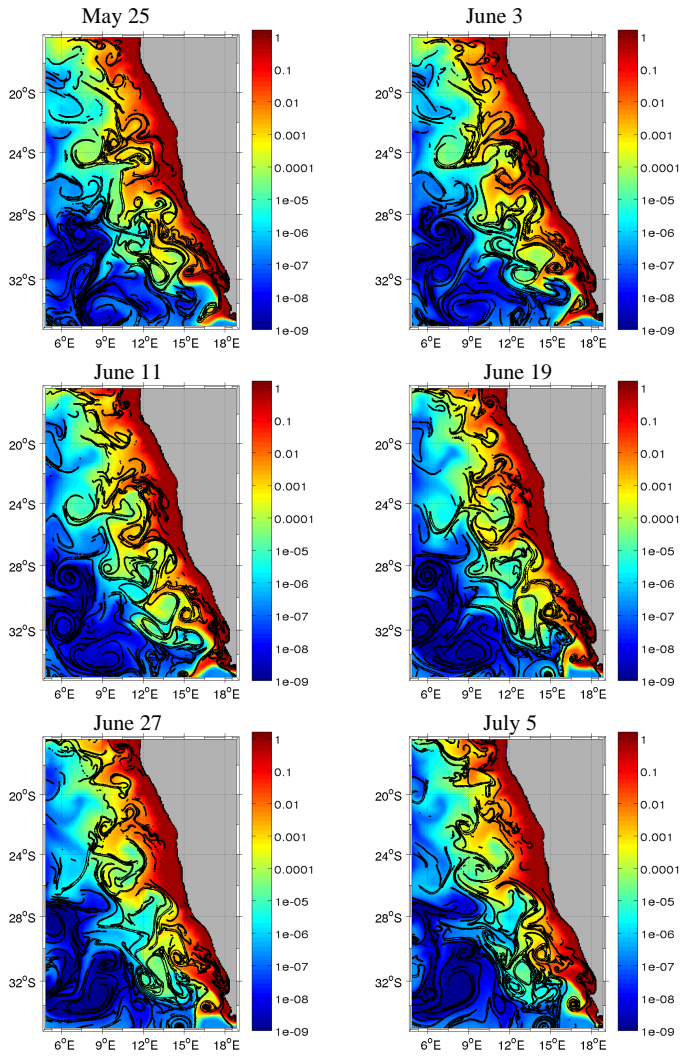


Figure 6.6: Snapshots every 8 days of large (top 30%) values of FSLE superimposed on P concentrations calculated from ROMS1/12 in mg/m^3 . Logarithmic scale for phytoplankton concentrations is used to improve the visualization of the structures

CHAPTER 6. EFFECT OF STIRRING ON PLANKTON DYNAMICS

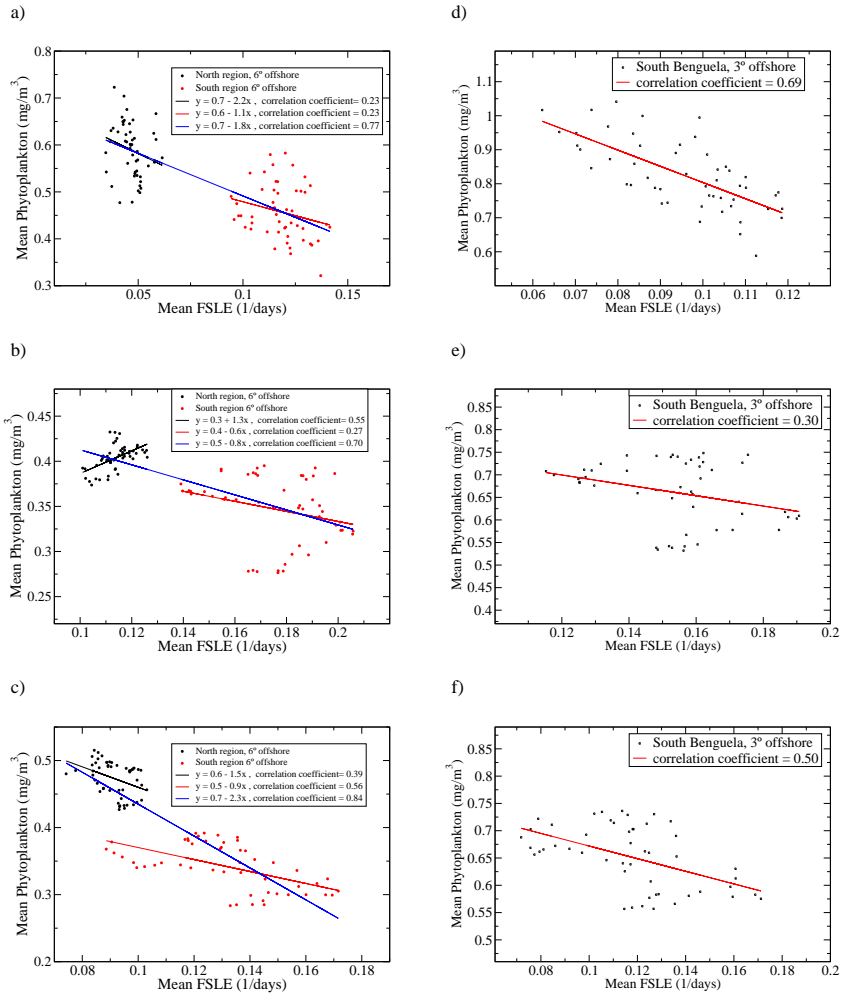


Figure 6.7: Weekly values of spatial averages of phytoplankton versus weekly values of spatial averages of FSLE, where the average are over the whole area (6° from the coast) and in North and South subareas of Benguela. a) *Satellite1/4*, b) *ROMS1/4* and c) *ROMS1/12*. Right column plots the average over 3° offshore in the south region: d) *Satellite1/4*, e) *ROMS1/4* and f) *ROMS1/12*

6.4. RESULTS AND DISCUSSION

latitudinal variations of FSLE and chlorophyll-a analyzed together suggest an inverse relationship between those two variables. The 2D vigorous stirring in the south and its associated offshore export seem sufficient to simulate reasonably well the latitudinal patterns of P . The numerous eddies released from the Agulhas system, moving north-westward in the south Benguela, might inhibit the development of P by exporting unused nutrients toward the open ocean. Although Gruber et al. (2011) invoked the offshore subduction of unused nutrients (3D effect), our results suggest that 2D offshore advection and intense horizontal mixing could solely affect negatively the phytoplankton growth in the southern Benguela.

To address the question of the negative effect of horizontal stirring on phytoplankton concentration in a more quantitative way we have examined the correlation between the spatial averages – over each subregion (North and South) and the whole area of study – of every weekly map of FSLE and the spatial average of the corresponding weekly map of simulated P , considering each of the three velocity fields (Fig.6.7). For all cases, a negative correlation between FSLEs and chlorophyll emerges. Thus, the higher the surface stirring/mixing, the lower the biomass concentration. The correlation coefficient taking into account the whole area is quite high for all the plots, $R^2=0.77$ for *Satellite1/4*, 0.70 for *ROMS1/4* and 0.84 for *ROMS1/12*, and the slopes (blue lines in Fig.6.7 have the following values: -1.8 for *Satellite1/4*, -0.8 for *ROMS1/4* and -2.3 for *ROMS1/12*. The strongest negative correlation appears to be produced by the setting with *ROMS1/12*. Note that, similarly to the results of Rossi et al. (2008, 2009) and Gruber et al. (2011), the negative slope is larger but less robust when considering the whole area rather than within every subregion. Moreover, if we average over the coastal strip (from coast to 3° offshore) and only in the south region (Fig.6.7 d),e),f)) we find high values of the correlation coefficient for the *Satellite1/4*, and *ROMS1/12* cases. The suppressive effect of stirring might be dominant only when stirring is intense, as in the south Benguela. Gruber et al. (2011) stated that the reduction of biomass due to eddies may extend beyond the regions of the most intense mesoscale activity, including the offshore areas that we do not simulate in this work.

In the following we perform further spatio-temporal analysis to better understand the mechanism behind this negative relationship.

CHAPTER 6. EFFECT OF STIRRING ON PLANKTON DYNAMICS

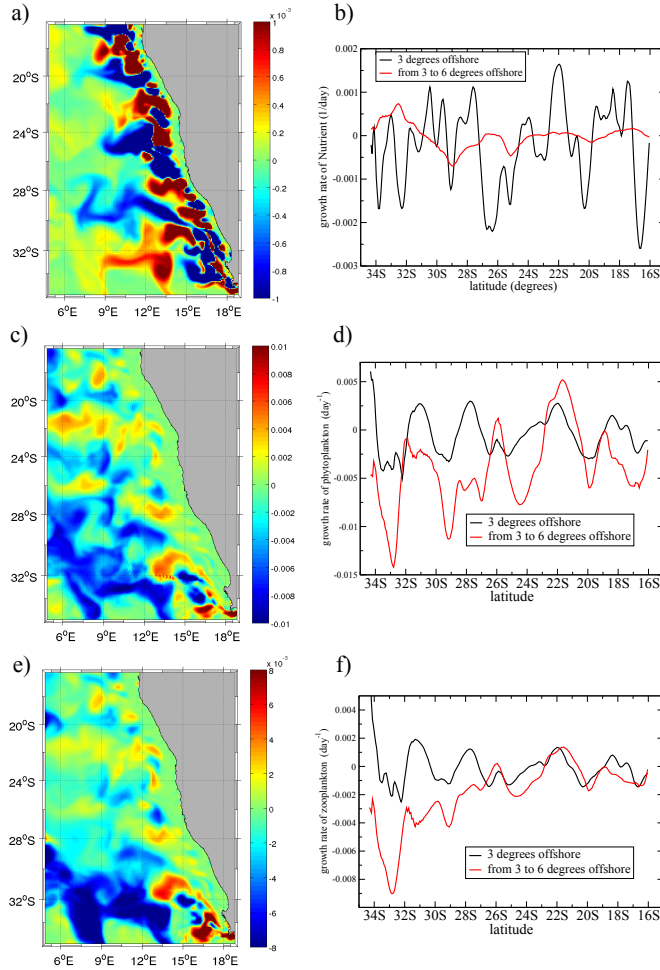


Figure 6.8: Spatial distribution of the annual average of the growth rate of nutrient (a), phytoplankton (c) and zooplankton (e) for *ROMS1/12* (the colorbar has units of day^{-1}). Zonal average of the annual growth rate of nutrient (b), phytoplankton (d) and zooplankton (f) as a function of the latitude and for different coastal bands.

6.4.3 Spatial analysis. What causes the variable biological responses within regions of distinct dynamical properties?

In the following, our analysis is focused on the setting using *ROMS1/12* as the previous results revealed that the negative correlation is more robust. However, similar results and conclusions can be obtained from the simulations using the two other velocity fields (not shown), attesting of the reliability of our approach (see correlation coefficients and slopes in Fig. 6.7).

An interesting quantity is the nutrient, phytoplankton and zooplankton per capita growth rates at fixed location $C^{-1}\partial C/\partial t$, where $C = C(\mathbf{x}, t)$ represents N , P and Z concentrations. In Fig. 6.8 a), c) and e) we plot the spatial distribution of their annual average. They reveal different regimes in each North and South subsystems, as well as from the coast to offshore. Particularly, there are large values (negative and positive) of growth rate of nutrients in the upwelling region, whereas the large negative values of growth rate of phytoplankton and zooplankton are located in the southern offshore region of Benguela. The spatial pattern between phytoplankton and zooplankton match well, but not with that of nutrient. In the right panels of Fig. 6.8 we show the corresponding spatial average over different coastal bands. In general, there are large fluctuations (particularly in nutrient and over the coastal region), though the most interesting feature is the general tendency to increase when latitude decreases, especially, between 3° and 6° offshore in the cases of P and Z (Fig. 6.8 d), f). This latitudinal gradient is not clear for nutrient (N) concentrations. Again, contrarily to the larger stirring activity in the southern area, the largest values of phytoplankton growth rate are obtained for the northern part. The mean values of the growth rate of P for each subsystem, North and South, are $-8 \cdot 10^{-4}$ and $-3 \cdot 10^{-3} \text{ day}^{-1}$, respectively. This confirms that nutrients and phytoplankton are being lost toward the open ocean by effect of horizontal stirring almost three times more in the south than in the north. It has to be compared with the stirring activity being about three times higher in the south than in the north (Fig. 6.3)

We next analyze the net horizontal transport of biological materials entrained by the flow. Gruber et al. (2011) suggested that offshore advection of plankton biomass enhanced by mesoscale structures could be one reason to explain the inverse relationship between biological activity and stirring intensity in upwelling areas. We have computed the zonal, J_{C_ϕ} , and meridional, J_{C_θ} , advective fluxes of N, P, Z (diffusive fluxes are smaller):

$$J_{C_\phi}(\mathbf{x}, t) = u(\mathbf{x}, t)C(\mathbf{x}, t), \quad (6.11)$$

$$J_{C_\theta}(\mathbf{x}, t) = v(\mathbf{x}, t)C(\mathbf{x}, t), \quad (6.12)$$

CHAPTER 6. EFFECT OF STIRRING ON PLANKTON DYNAMICS

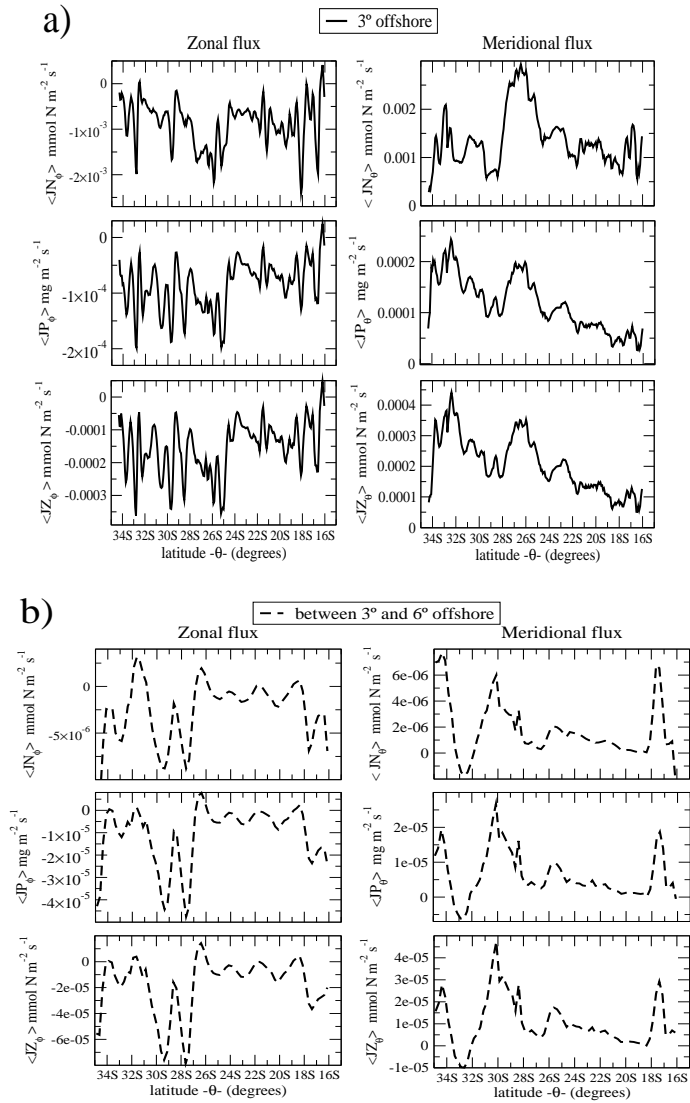


Figure 6.9: Zonal mean of zonal and meridional fluxes of N, P, Z concentrations for the *ROMS1/12* case, averaged from the coast to 3° offshore (a), and between 3° and 6° offshore (b).

6.4. RESULTS AND DISCUSSION

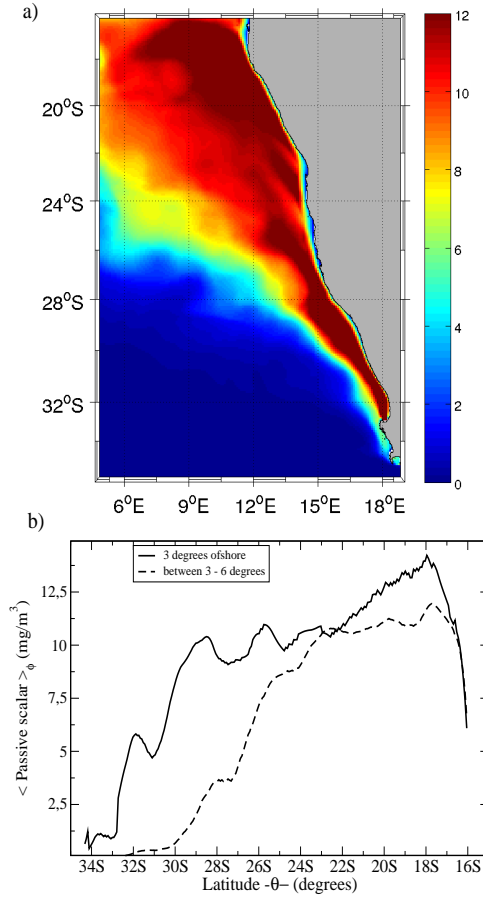


Figure 6.10: a) Spatial distribution of time average of the passive scalar concentration (see details at the end of subsection 6.4.3). b) Comparison of latitudinal profile of time averages of the passive scalar, as a function of latitude, for zonal average over different coastal bands.

where u and v are the zonal and meridional components of the velocity field respectively, and with C we denote the N, P and Z concentrations, all of them given at a specific point in the 2D-space and time (\mathbf{x}, t) . J_C is the flux of the concentration, C , i.e., JN_{ϕ} is the zonal flux of nutrients (eastward positive), and JP_{θ} is the meridional flux (northward positive) of phytoplankton, and so on. Annual averages of daily fluxes were computed, and then a zonal average as

CHAPTER 6. EFFECT OF STIRRING ON PLANKTON DYNAMICS

a function of the latitude was performed for the different coastal bands we are considering all along this Chapter. Fig. 6.9 shows these calculations for the velocity field from *ROMS1/12* (similar results for other data sets). Approximately the same behavior is observed for the fluxes of N , P and Z : Zonal fluxes are almost always negative, so that westward transport dominates, and meridional fluxes, are predominantly positive so that they are directed to the north. Comparing North and South in the 3° coastal band, it is observed that at high latitudes the zonal flux has larger negative values than low latitudes, and the meridional flux presents larger positive values at higher latitudes. In other words, the northwestward transport of biological material is more intense in the southern than in the northern regions, suggesting a higher ‘flushing rate’. In the work by Lachkar and Gruber (2011) the authors show that mesoscale processes reduce the efficiency with which the nutrients can be utilized by phytoplankton in terms of residence times. The longer residence times, i.e. the less mesoscale activity, favor accumulation of biomass. We suggest that regions with weak fluxes are associated with long residence times and high growth rate of phytoplankton. On the other hand, high mesoscale activity is favoring the northwestward advection which decreases the residence times, associated to lower growth rate of plankton.

A last spatial analysis was performed to clarify the role of the horizontal advection. For this, we have performed numerical simulations where no biological dynamics is considered. This amounts to solving Eq. (6.4) with $P = Z = 0$ and only lateral transport being added to this, so that N is a passive scalar with sources. In Fig. 6.10 we see the results (for the *ROMS1/12* case, but similar for the others). There is a very small tracer concentration in the southern domain, and the differences north-south are more pronounced than the case including the plankton dynamics (see Fig. 6.5). Thus, the main influence on the spatial distribution of biomasses is the horizontal transport.

6.4.4 Seasonal variability of the bio-physical coupled system

To better understand how this negative correlation emerges we next focus on the southern region of Benguela where the suppressive effect is stronger as well as being the region with the best correlation with the chlorophyll-a data from satellite.

We analyze the temporal evolution of total budgets of N , P and Z by computing the daily spatial average of the biological concentrations over the already mentioned coastal bands. In Figure 6.11 we display the temporal evolution through one year of the spatial averages of N , P and Z budgets and FSLEs for the *ROMS1/12*. We see that P and Z are tightly correlated in both coastal bands,

6.4. RESULTS AND DISCUSSION

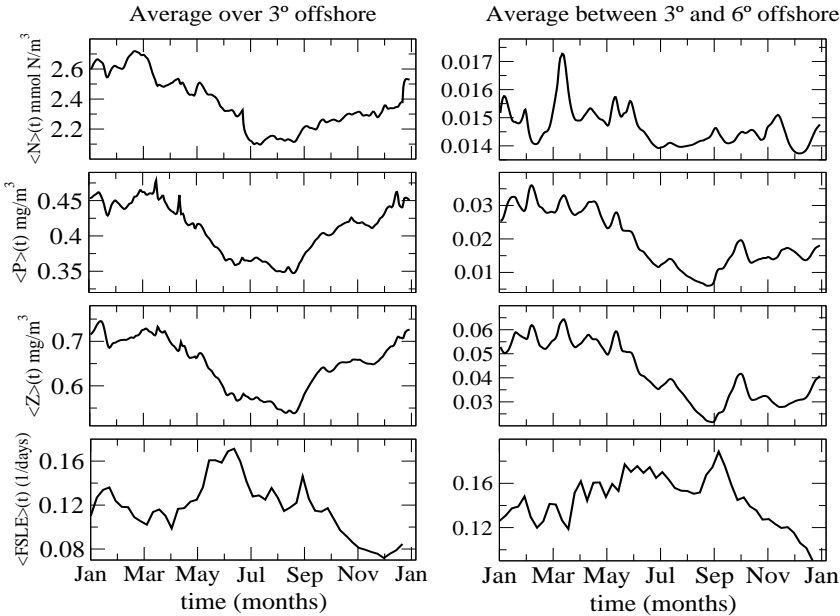


Figure 6.11: Temporal evolution of N, P, Z budgets for the *ROMS1/12* case, averaged for the southern region of Benguela and for different coastal strips. Bottom row correspond to the temporal evolution of horizontal stirring (Spatial average over the southern region of FSLEs) for *ROMS1/12*.

low P associated with low Z . However no clear correlation of N with P and Z is present in the open-ocean band.

Analysing the relationship between the biological budgets and FSLEs in the southern region, we observe that the seasonal increase in stirring (from January to June) corresponds to a decrease of P . This also illustrates the seasonal inhibiting effect that the stirring activity has on phytoplankton dynamics in winter time. Seemingly, the decrease of stirring intensity from September to January coincides with an increase in P . And this seasonal behavior is not induced by the seasonal variation of light (which is not considered in our model), nor by the temporal variability of the coastal upwelling cells (determined by function S) since when considering an homogeneous nutrient source without temporal variability, similar temporal evolution of the biological variables is observed (6.5.2).

CHAPTER 6. EFFECT OF STIRRING ON PLANKTON DYNAMICS

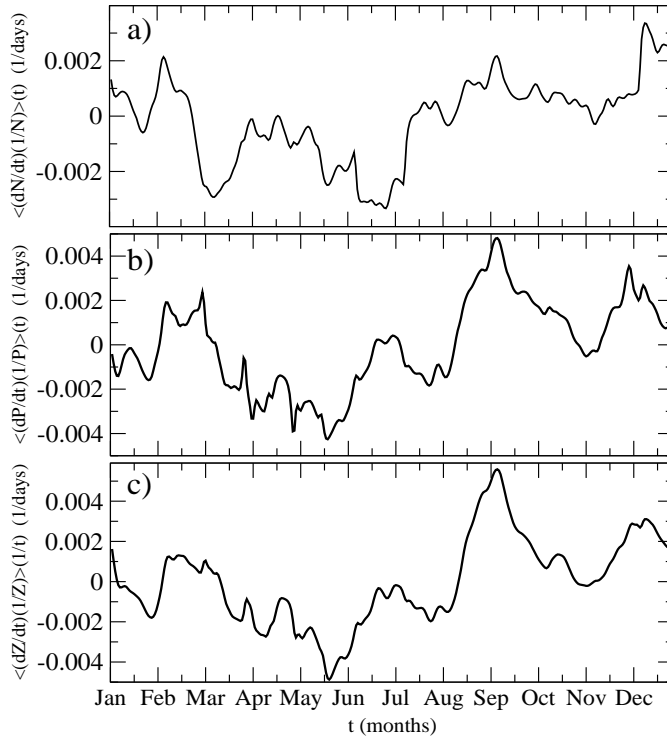


Figure 6.12: Time evolution of the spatial average in the south region of Benguela of the per capita growth rate of nutrient (a), phytoplankton (b) and zooplankton (c), for the *ROMS1/12* case.

Also, the evolution of spatial averages (over the coastal bands) of the per capita growth rate of N , P and Z , has been computed to test the mechanisms proposed by Gruber et al. (2011) (see Fig. 6.12 for the *ROMS1/12* simulation). The loss of N , P and Z is maximal in winter (maximum stirring). The seasonal response of the biological growth rates is again negatively correlated with mesoscale activity.

Sensitivity analysis

A number of numerical experiments were done to investigate the sensitivity of the coupled bio-physical model with respect to different variables.

6.5.1 Sensitivity with respect to different spatial resolution of the velocity field

In this experiment we used a velocity field from ROMS1/12 smoothed out towards a resolution $1/4^\circ$, and to be compared with ROMS1/4 and ROMS1/12 at their original spatial resolution. We coarse-grained the velocity field with a convolution kernel weighted with a local normalization factor, and keeping the original resolution for the data so that land points are equally well described as in the original data. The coarsening kernel with scale factor s , k_s , is defined as:

$$k_s(x, y) = e^{-\frac{(x^2+y^2)}{2s^2}}. \quad (6.13)$$

To avoid spurious energy dump at land points we have introduced a local normalization weight given by the convolution: $k_s(x, y) * M(x, y)$, where $M(x, y)$ is the sea mask. For points far from the land the weight is just the normalization of k_s , and for points surrounded by land the weight takes the contribution from sea points only. Thus v_s , the velocity field coarsened by a scale factor s , is obtained from the original velocity field v as:

$$v_s = \frac{k_s * v}{k_s * M}. \quad (6.14)$$

In Fig. 6.13 we compare two ROMS1/12 smoothed velocity fields at scales $s=3$ and $s=6$ (with an equivalent spatial resolution $1/4^\circ$ and $1/2^\circ$, respectively) with the original velocity field from ROMS1/12. It is clear that the circulation pattern is smoothed as s is increased. The FSLE computations using these smoothed velocity fields are shown in Fig 6.14. When the spatial resolution is reduced to $1/4^\circ$ the FSLEs and small-scale contributions decrease, but the main global features remain, as indicated in the study by Hernández-Carrasco et al. (2011). Further coarsening to $1/2^\circ$ smoothes most of the structures except the most intense ones.

The latitudinal variations of the zonal averages performed on the time averages of the FSLE maps plotted in Fig. 6.14 are compared in Fig.6.15. The mean FSLEs

CHAPTER 6. EFFECT OF STIRRING ON PLANKTON DYNAMICS

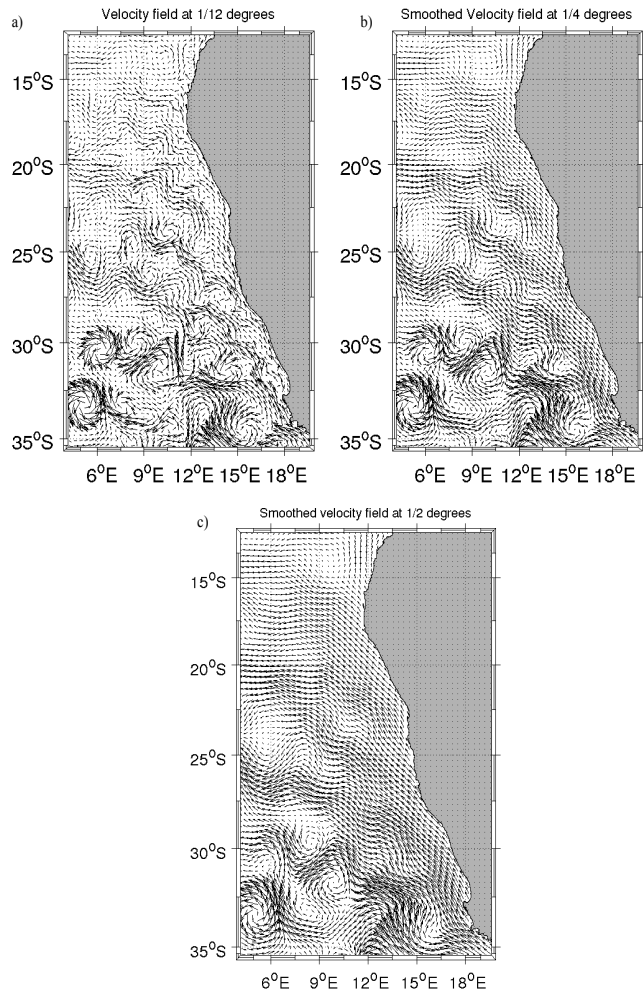


Figure 6.13: Vectors of a velocity field from *ROMS1/12*: a) at original resolution. b) smoothed by a scale factor of $s=3$, obtaining an equivalent spatial resolution of $1/4^\circ$, c) smoothed by a scale factor of $s=6$, obtaining an equivalent spatial resolution of $1/2^\circ$. The snapshots correspond to day 437 of the simulation.

6.5. SENSITIVITY ANALYSIS

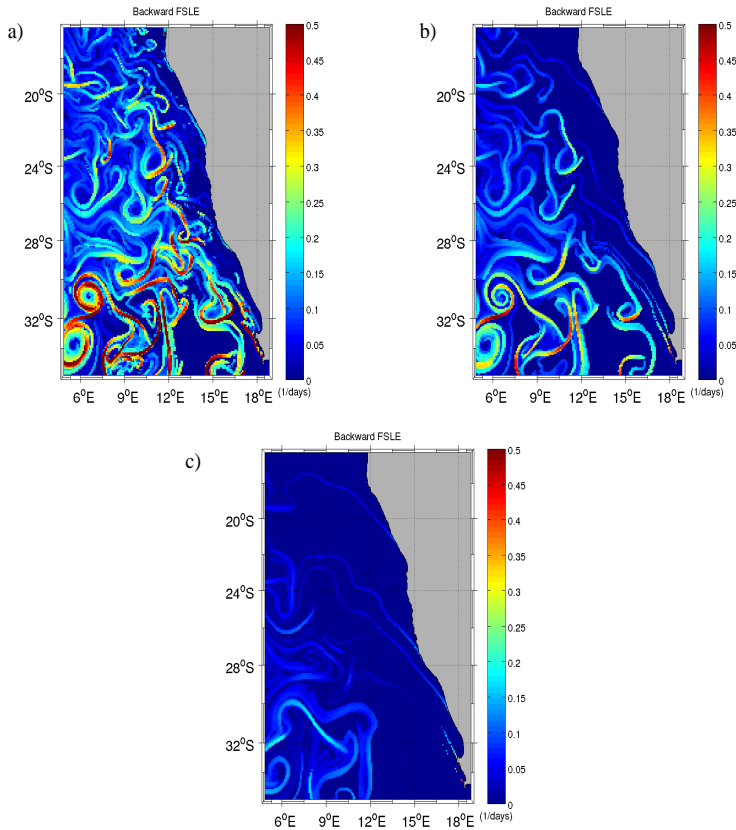


Figure 6.14: Snapshots of spatial distributions of FSLEs backward 437 days in time starting from day 437 of *ROMS1/12* at the same FSLE grid resolution of $1/12^\circ$, and using the velocity fields at different resolutions: a) at original resolution $1/12^\circ$. b) smoothed velocity field at equivalent $1/4^\circ$ and c) smoothed velocity field at equivalent $1/2^\circ$.

values strongly diminish when the velocity resolution is sufficiently smoothed out. This is due to the progressive elimination of mesoscale structures that are the main contributors to stirring processes. Also the latitudinal variability of stirring diminishes for the very smoothed velocity field (blue line in Fig. 6.15). Thus, latitudinal differences of stirring in the Benguela system are likely to be

CHAPTER 6. EFFECT OF STIRRING ON PLANKTON DYNAMICS

related to mesoscale structures (eddies, filaments, fronts, etc.) contained in the velocity fields.

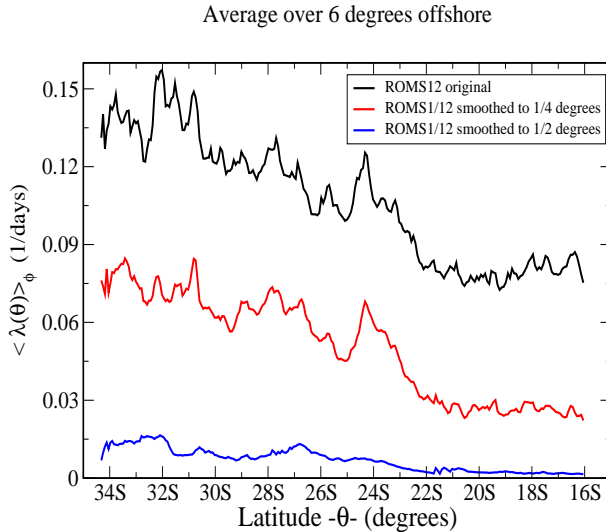


Figure 6.15: Latitudinal profile of the zonal mean values of annual averaged backward FSLEs (51 snapshots weekly separated) at the same FSLE grid resolution of $1/12^\circ$, and using different smoothed velocity fields.

We have also computed the phytoplankton using these smoothed velocity fields. Some instantaneous spatial distributions can be seen in Fig 6.16. The filaments of phytoplankton disappear in the very smoothed velocity field ($1/2^\circ$). The spatial distribution of the annual average of phytoplankton concentrations for the different velocity field shows, however, quite similar patterns (not shown).

In the time series of N , P and Z budgets for the coarser velocities one observes the same behavior as for the original velocity field (not shown).

6.5.2 Sensitivity with respect to different parameterization of the coastal upwelling of nutrients

In section 6.3.2 we mimicked coastal upwelling of nutrient via a source term in the nutrients equation which is determined by the function S , and was considered spatiotemporally variable. Here we explore the plankton dynamics using spatially and temporally homogeneous upwelling along the coast. S is fixed to

6.5. SENSITIVITY ANALYSIS

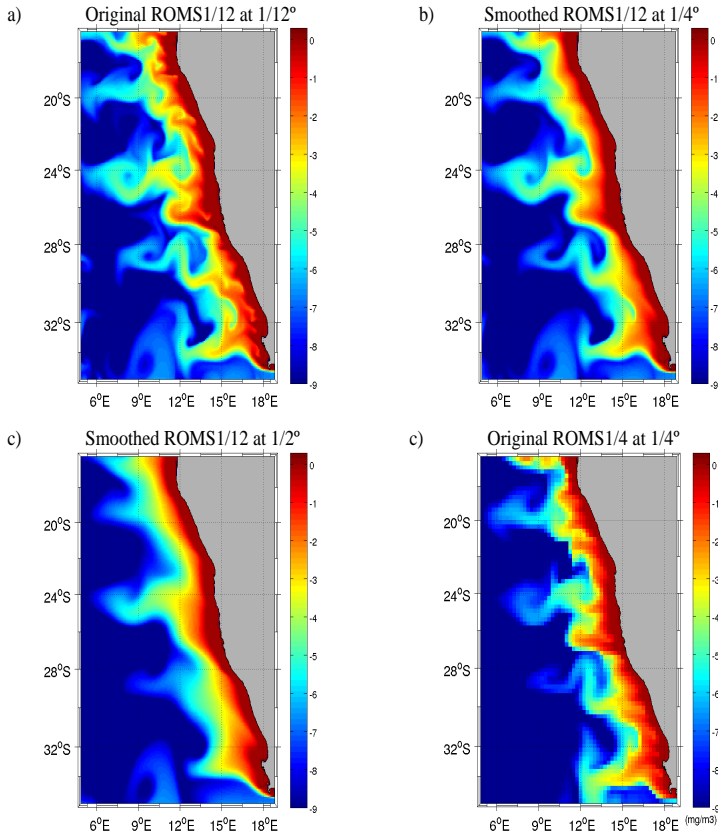


Figure 6.16: Snapshots of simulated phytoplankton field using different velocity fields: a) *ROMS1/12* at original resolution $1/12^\circ$, b) smoothed *ROMS1/12* velocity field at equivalent $1/4^\circ$, c) smoothed *ROMS1/12* velocity field at equivalent $1/2^\circ$, and d) *ROMS1/4* at original resolution $1/4^\circ$.

an average value $S = 0.1 \text{ day}^{-1}$ along the coast at any time. In Fig. 6.17 we show the annual average of P for the *ROMS1/12* (top panel), and the comparisons with the inhomogeneous case for the zonal mean (bottom panel). Therefore, this test suggests that the way we simulate vertical mixing along the coast has not a large effect on the 2D biological dynamics, which will be mainly determined by the interplay with horizontal advection.

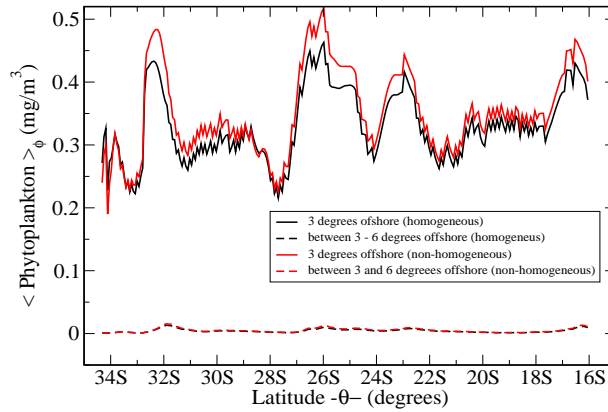


Figure 6.17: Comparison between zonal average over different coastal bands of annual time average of P , using homogeneous upwelling and the non-homogeneous upwelling cells described in Fig. 6.1.

6.6

Conclusions

We have studied the biological dynamics in the Benguela area by considering a simple biological NPZ model coupled with different velocity fields (satellite and model). Although in a simple framework, a reduction of phytoplankton concentrations in the coastal upwelling for increasing mesoscale activity has been successfully simulated. Horizontal stirring was estimated by computing the FSLEs and was correlated negatively with chlorophyll stocks. Similar results are found, though not presented in this manuscript, for the primary production, defined as the first term in F_P (Eq. 6.5), i.e. $PP = \beta \frac{N}{\kappa_N + N} P$. Some recent observational and modelling studies proposed the “nutrient leakage” as a mechanism to explain this negative correlation. Here we argue that Lagrangian Coherent Structures, mainly mesoscale eddies and filaments, transport a significant fraction of the recently upwelled nutrients nearshore toward the open ocean before being efficiently used by the pelagic food web. Although some studies dealt with 3D effect, we have shown that 2D advection processes seems to play an

6.6. CONCLUSIONS

important role in this suppressive effect. Our analysis suggest that the inhibiting effect of the mesoscale activity on the plankton occurs when the stirring reach high levels, as in the south Benguela. However, this effect is not dominant under certain levels of turbulence. We have also shown that the inhibiting effect of intense stirring is maximal during the winter months. It might indicate that planktonic ecosystems in oceanic regions with vigorous mesoscale dynamics can be, as a first approximation, easily modeled just by including a realistic flow field.

The fluxes of nutrients and organic matter reflect that transport is predominantly westward and northward. Biomass is transported towards open ocean or to the northern area. The small residence times of waters in the productive area will smooth out all the other neglected biological factors in interaction.

Our findings confirm the unexpected role that mesoscale activity has on biogeochemical dynamics in the productive coastal upwelling. Strong vertical velocities are known to be associated with these physical structures and they might have another direct effect by transporting downward rich nutrient waters below the euphotic zone. Further studies are needed such as 3D realistic modelling that take into account the strong vertical dynamics in upwelling regions to test the complete mechanisms involved.

General Conclusions

The objective of this thesis have been centered in the study of physical and biological processes in the ocean related to transport and mixing from the Lagrangian point of view. The study has been made with the idea of characterizing transport properties and coherent structures at different scales, from coastal to planetary scales. We have used several and complementary tools to assess the mechanisms occurring at these scales. Although we have chosen the FSLE as the baseline Lagrangian candidate. Lagrangian methods provide answers to problems which have a deep impact on risk management (e.g. control of pollutant dispersion) as well as on ecosystem analysis (e.g. tracking nutrient mixing and transport, identifying the role of horizontal mixing in primary productivity). They completely will give hints about dynamics processes in the ocean. The use of Lagrangian techniques for the assessment of the transport and mixing properties of the ocean has grown in importance in the latest years, with increasing efforts devoted to the implementation of appropriate techniques but few studies on the validity of the results when real data, affected by realistic constraints, have been addressed. Our study will serve to unify and interpret the analyses provided by Lagrangian methods when ocean data are processed.

Before to start applying FSLEs as a proxy of stirring and to uncover the flow geometry of marine flows, we studied some scale properties and robustness of FSLE in order to analyze their reliability. In Chapter 3, we have analyzed the sensibility of FSLE-based analyses for the diagnostic of Lagrangian properties of the ocean (most notably, horizontal mixing and dispersion). Our sensibility tests include the two most important effects when facing real data, namely dynamics of unsolved scales and of noise. Our results show that even if some dynamics are missed (because of lack of sampling or inaccuracy of any kind in the measurements) FSLEs results would still give an accurate picture of Lagrangian

CHAPTER 7. CONCLUSIONS

properties, valid for the solved scales. This does not mean that scale and/or noise leave FSLEs unaffected, but the way in which they modify this Lagrangian diagnostics can be properly accounted. Therefore, we can say that due to its robustness and scale invariance, the FSLE is a powerful Lagrangian technique to study mixing and transport properties of the Sea surface.

In Chapter 4, computations of FSLE at global scales show that the horizontal stirring is spatially non-uniform. We have shown that taking averages of FSLE we can analyze different temporal and spatial scales in order to classify the ocean in regions with different transport properties. We observed that level of stirring activity of the oceans tends to decay as the size of subtropical gyres increases, and that the areas with most intense horizontal stirring are located in the boundaries of oceans basins, particularly in the Western Boundary Currents. A latitudinal analysis shows that horizontal stirring tends to increase with latitude, probably related with the planetary vorticity and the effect of the strong winds at high latitudes or because of the barotropic instabilities. With regard to the time dependence of FSLE we observed that stirring shows different seasonal variability depending on the latitude. We studied the connection between Lagrangian FSLE and Eulerian EKE. We found two groups of oceanic regions with different Lagrangian-Eulerian relation, associated to different mesoscale activity. The existence of this two regimes implies that pair dispersion and stretching strength are larger in a class of ocean areas (represented by WBC) than in another (for instance EBC). This result can be relevant to understand global dispersion behavior of biogeochemical tracers and ocean biological activity.

In Chapter 5 we studied properties of coastal transport in the Bay of Palma, located in the Island of Mallorca, Spain. At these scales, the spatial distribution of FSLE and RT can be complex and time depending. We showed that the coastal LCSs, given by ridges of FSLE, act as barriers, organizing the coastal flow. We investigated global aspects of the transport by means of averages of FSLE and RT over different months. We found that in autumn there are more interaction between the Bay and the open ocean rather than in summer. One explanation is that the flow conditions produce a constant motion in the coastal marine surface in the zonal direction, producing high values of FSLE spatially distributed in the zonal direction and over all the Bay and preventing the flow to enter or scape toward the open ocean. The transport of particles at deepest layer, strongly influenced by the bottom topography, is less active than in the surface. We observed that LCSs separate regions with different transport properties in terms of times scales given by residence times spatially distributed on Synoptics Lagrangian maps. This proves the fact that LCSs are relevant in the flow dynamics of small coastal regions. Thus, we think that these Lagrangian quantities can be used as key variables determining the health of a Bay or an

estuary, particularly from human activities. Future improvements include a long period of data and the adaptation of this methods to three-dimensional spaces and capture three-dimensional effects.

Finally, in Chapter 6, based on an academic coupled modelling study, we investigated how plankton concentrations at the surface of Benguela area are controlled by the interplay between the physical mixing processes and the intrinsic biological dynamics. Our findings confirm the unexpected role that mesoscale activity has on biogeochemical dynamics in the productive coastal upwelling. In agreement with other previous studies, we found a reduction of phytoplankton concentrations in the south region of Benguela where the mesoscale activity is increased. Although some studies dealt with 3D effect, we showed that 2D advection processes seems to play an important role in this suppressive effect. LCSs, mainly mesoscale eddies and filaments, transport a significant fraction of nutrients nearshore toward the open ocean before being efficiently used by the pelagic food web. We found that the flux of nutrients and organic matter is westward and northward. This offshore transport induces small residence times of waters in the productive area, and thus, reducing the interaction between biological factors. Other mechanism can be the latitudinal difference of the growth rate of phytoplankton. We also showed that the inhibiting effect of intense stirring is maximal during the winter months.

To conclude, we have shown that the technique of the FSLEs is a robust and powerful tool to characterize both the horizontal stirring in the ocean surface at different scales and its impact on biological organisms.

Numerical algorithms

Fourth-order Runge-Kutta method

The Runge-Kutta algorithm is a method to solve first-order differential equations (DE). The generic problem in ordinary differential equations is thus reduced to the study of a set of N coupled *first-order* differential equations for the functions $x_i, i = 1, 2, \dots, N$, having the general form

$$\frac{dx_i(t)}{dt} = f_i(t, x_1, \dots, x_N), \quad i = 1, \dots, N \quad (\text{A.1})$$

where the functions f_i are known.

Runge-Kutta methods propagate a solution over an interval by combining the information from several Euler style steps (each involving one evaluation of f_i), and then using the information obtained to match a Taylor series expansion up to some higher order. The formula for the Euler method is

$$x_{n+1} = x_n + hf(t_n, x_n), \quad (\text{A.2})$$

which advances a solution from t_n to $t_{n+1} = t_n + h$. It advances the solution through an interval h , but uses derivative information only at the beginning of that interval.

The fourth-order Runge-Kutta method (Boyce and DiPrima, 1998; Press et al., 1996) requires four evaluations of the functions f_i per step h :

APPENDIX A. NUMERICAL ALGORITHMS

$$\begin{aligned}k_1 &= hf(t_n, x_n), \\k_2 &= hf\left(t_n + \frac{h}{2}, x_n + \frac{k_1}{2}\right), \\k_3 &= hf\left(t_n + \frac{h}{2}, x_n + \frac{k_2}{2}\right), \\k_4 &= hf(t_n + h, x_n + k_3), \\x_{n+1} &= x_n + \frac{k_1}{6} + \frac{k_2}{6} + \frac{k_3}{6} + \frac{k_4}{6} + O(h^5).\end{aligned}$$

A.2

Bilinear interpolation

We sometimes know the value of a function $f(x)$ at a set of points x_1, x_2, \dots, x_n , but we don't have an analytic expression for $f(x)$ that let us calculate its value at an arbitrary point.

In multidimensional interpolation, we seek an estimate $y(x_1, x_2, \dots, x_n)$ from an n -dimensional grid of tabulated values y and n one-dimensional vectors giving the tabulated values of each of the independent variables x_1, x_2, \dots, x_n .

In two dimensions (Press et al., 1996), we imagine that we are given a matrix of functional values $ya(j, k)$, where j varies from 1 to m , and k varies from 1 to n . We are also given an array $x1a$ of length m , and an array $x2a$ of length n . The relation of these input quantities to an underlying function $y(x_1, x_2)$ is

$$ya(j, k) = y(x1a(j), x2a(k)). \quad (\text{A.3})$$

We want to estimate, by interpolation, the function y at some untabulated point (x_1, x_2) .

An important concept is that of the grid square in which the point (x_1, x_2) falls, that is, the four tabulated points that surround the desired interior point. For convenience, we will number these points from 1 to 4, counterclockwise starting from the lower left. More precisely, if

$$\begin{aligned}x1a(j) &\leq x_1 \leq x1a(j+1), \\x2a(k) &\leq x_2 \leq x2a(k+1),\end{aligned}$$

defines j and k , then

A.3. HEUN'S ALGORITHM

$$\begin{aligned}y_1 &\equiv ya(j, k), \\y_2 &\equiv ya(j + 1, k), \\y_3 &\equiv ya(j + 1, k + 1), \\y_4 &\equiv ya(j, k + 1).\end{aligned}$$

The simplest interpolation in two dimensions is bilinear interpolation on the grid square. Its formulas are:

$$\begin{aligned}t &\equiv (x_1 - x1a(j))/(x1a(j + 1) - x1a(j)), \\u &\equiv (x_2 - x2a(k))/x2a(k + 1) - x2a(k),\end{aligned}$$

(so that t and u each lie between 0 and 1), and

$$y(x_1, x_2) = (1 - t)(1 - u)y_1 + t(1 - u)y_2 + tuy_3 + (1 - t)uy_4. \quad (\text{A.4})$$

A.3

Heun's algorithm

The Heun's algorithm is a method to solve stochastic differential equations (SDE) based on the order two Runge-Kutta method for ordinary differential equations (ODE). A generic SDE has the following expression for a dynamical variable $x(t)$:

$$\frac{dx(t)}{dt} = q(x, t) + g(x, t)\xi_w(t),$$

where $q(x, t)$ and $g(x, t)$ are functions, linear or non linear, and $\xi_w(t)$ is a white Gaussian noise, which properties are

$$\begin{aligned}\langle \xi_w \rangle &= 0, \\ \langle \xi_w(t)\xi_w(t') \rangle &= 2D\delta(t - t').\end{aligned}$$

A possible algorithm (San Miguel and Toral, 2000) to solve the SDE is

$$\begin{aligned}k &= hq(t, x(t)), \\l &= h^{1/2}u(t)g(t, x(t)), \\x(t + h) &= x(t) + \frac{h}{2} [q(t, x(t)) + q(t + h, x(t) + l + k)] + \\ &\quad + \frac{1}{2}h^{1/2}u(t) [g(t, x(t)) + g(t + h, x(t) + k + l)]\end{aligned}$$

where h is the temporal step and $u(t)$ is a independent set of random Gaussian numbers with zero mean and variance equal to one.

Semi-Lagrangian numerical algorithm

In the study of the plankton response to physical processes often is used advection-reaction-diffusion systems given by the Partial Differential Equation (PDE),

$$\frac{\partial C(\mathbf{x}, t)}{\partial t} + \mathbf{v}(\mathbf{x}, t) \cdot \nabla C(\mathbf{x}, t) = F_C(\mathbf{x}, t) + D\nabla^2 C(\mathbf{x}, t), \quad (\text{A.5})$$

where, in the context of this thesis, C is referred to the concentrations of Nutrients, N , Phytoplankton, P , and Zooplankton, Z (see Equations 6.8, 6.9, 6.10), \mathbf{v} is the velocity field and D is the diffusion coefficient. This PDE can be solved numerically by means of a semi-Lagrangian algorithm described in Sandulescu et al. (2007). The semi-Lagrangian algorithm accounts for the Lagrangian nature of the transport process but, at the same time, it allows to work on a fixed computational grid. In our case concentration fields of N , P and Z are represented on a grid, which size or number of grid points are given by the spatial resolution of the velocity field Δx . The integration scheme splits the computation into three steps corresponding to advection, reaction and diffusion which are performed sequentially in the following way:

1. **Advection:** We integrate the advection term, $\frac{dx}{dt} = \mathbf{v}(\mathbf{x}, t)$, of the PDE backwards in time, by using Runge-Kutta scheme (Appendix A.1) Thus, at each time t , every point of the grid \mathbf{x} is integrated for a time step dt backwards in time along the trajectory of a fluid parcel in the velocity field. This procedure yields the position from which a fluid parcel would have reached the chosen grid point. Typically this position is not located on a grid point but somewhere in between.
2. **Reaction:** Once the position of the fluid parcel in the past is found, we compute the values of the concentration fields of N , P and Z at this point at time $t - dt$ and take them as initial values for the reaction term ($dC/dt = F_C$) which is integrated forward in time for a time step dt , by using a Runge-Kutta scheme. Since the position of the fluid parcel, at time $t - dt$ is not on a grid point (where we have defined the concentrations) the concentration fields have to be evaluated by means of a bilinear interpolation (see Appendix A.2) using the nearest neighbor grid points.
3. **Diffusion:** Finally we perform a diffusion step at time t to integrate the diffusion term, $\frac{\partial C}{\partial t} = D\nabla^2 C$, which we do according to the Eulerian method. This method is composed by the forward Euler and central differences

A.4. SEMI-LAGRANGIAN NUMERICAL ALGORITHM

schemes. In a discretized time and space, we have the space-time grid

$$x_j = j\Delta x, \quad t_n = n\Delta t, \quad j = 0, \dots, N + 1, \quad n = 0, 1, \dots \quad (\text{A.6})$$

and we can approximate $C_j^n \approx C(t_n, x_j)$. Therefore,

$$C_j^{n+1} \approx C_j^n + D \frac{\Delta t}{(\Delta x)^2} (C_{j+1}^n - 2C_j^n + C_{j-1}^n) \quad (\text{A.7})$$

Note, that the reaction step induces already a numerical diffusion of the order $Dn \sim \Delta x^2/dt$ due to the interpolation. Therefore one has to make sure that the real diffusion, D , according to the Okubo estimate (Okubo, 1971) is larger than this numerical diffusion. The eddy diffusion coefficient, D , is given by Okubo's formula (Okubo, 1971), $D(l) = 2.055 * 10^{-4} l^{1.15}$, where l is the value of the resolution, in meters. Additionally the stability condition of the Eulerian diffusion step ($D\Delta t/\Delta x^2 < 1$ with Δt the diffusion time step) has to be fulfilled. Both conditions together require that the diffusion time step Δt is much smaller than dt . In our computations we have chosen $\Delta t = dt/10$.

List of publications

Publications related to this thesis:

- Hernández-Carrasco, I., C. López, A. Orfila, and E. Hernández-García 2013: Lagrangian transport in a microtidal coastal area: the Bay of Palma, Spain. *Submitted to Nonlinear Processes in Geophysics*.
- Hernández-Carrasco, I., V. Rossi, E. Hernández-García, V. Garçon and C. López, 2013: The reduction of plankton biomass induced by mesoscale stirring: a modelling study in the Benguela upwelling. *Under revision in Deep Sea Research Part I*,
- Hernández-Carrasco, I., C. López, E. Hernández-García, A. Turiel, 2012: Seasonal and regional characterization of horizontal stirring in the global ocean. *Journal of Geophysical Research.*, **117** C10007.
- Galan, A., A. Orfila, G. Simarro, I. Hernández-Carrasco, C. López, 2012: Wave mixing rise inferred from Lyapunov exponents. *Environ. Fluid Mech*, **12(3)** 291–300.
- Hernández-Carrasco, I., C. López, E. Hernández-García, A. Turiel, 2011: How reliable are finite-size Lyapunov exponents for the assessment of ocean dynamics?. *Ocean Modelling*, **36**, 208–218.

Publications in proceedings:

- Hernández-García, E.; Bettencourt, J.H.; Garçon, V.; Hernández-Carrasco, I.; López, C.; Rossi, V.; Sudre, J.; Tew Kai, E 2012: Biological impact of

LIST OF PUBLICATIONS

ocean transport: A finite-size Lyapunov characterization. Submitted to the proceedings of the *3rd Conference on Nonlinear Science and Complexity*, Ankara, July 2010 , Springer.

List of Tables

6.1	List of parameters used in the biological model.	122
-----	--	-----

List of Figures

1.1	Spatial and temporal scales in the ocean and associated processes (from Dickey (2003)).	2
1.2	Graphical representation of the heterogeneity of ocean scales. The plots are Sea Surface Temperature (SST) images from satellite. . .	3
1.3	A: Ocean chlorophyll concentrations of the coastal California from SeaWiFS (Sea-viewing Wide Field-of-view Sensor) with some typical physical features annotated. This map shows the complexity of the interactions between phytoplankton and physics in the surface ocean (from Kudela (2012)). B: Ocean color image of the ocean east of Tasmanian in December, 2004.	7
1.4	Schematic representation of the biological pump in the ocean, where the planktonic ecosystems in the upper ocean play a key role in the carbon cycle(from Lévy (2008)).	11
1.5	Global view of chlorophyll distribution from SeaWiFS sensor data generated by the NASA. The image corresponds to one year average. The blue color indicates poor chlorophyll concentrations (i.e. oligotrophic gyres), whereas green to red indicate high chlorophyll concentrations (i.e. eastern boundary upwelling systems, equatorial upwelling, high latitude spring bloom...).	13

LIST OF FIGURES

1.6	A schematic section of coastal upwelling systems and the eddy formation in the southern hemisphere. Equatorial trade winds are blowing almost all year along the coast, that create westward Ekman drift in the upper layer, and divergence in the coast, that is being compensated by upwelling of deep, cold and nutrient-rich waters. Picture from Williams (2011).	16
2.1	Pendulum setup	22
2.2	Pendulum phase portrait	23
2.3	Two points on either side of a separatrix will diverge from each other	25
2.4	a) Schematic depiction of FSLE in the multi-scale setting of the ocean. Hypothesis-I and -II correspond to non-local and local transport, respectively. Hypothesis-IIa shows a case if there is a significant spectral gap between the submesoscale and mesoscale coherent features inducing the relative dispersion (taken from Özgökmen et al. (2012)). b) Spatial average of FSLE ($\lambda(\delta)$) at different scales δ using velocity data sets of the south of Mallorca Sea from a realistic simulation ROMS at different high spatial resolution. The slopes of different regimes of relative dispersion correspond to ballistic, diffusive and Richardson are included in the plot.	30
2.5	Schematic representation of the evolution of particle pair trajectories initially located on the points of a grid.	35
3.1	Snapshot of the surface velocity field of the Balearic Sea corresponding to day 640 in the DieCAST simulation.	48
3.2	Snapshots of FSLEs backward in time starting from day 640 at different F-grid resolutions: a) $\delta_0 = 1/8^\circ$, b) $\delta_0 = 1/16^\circ$, c) $\delta_0 = 1/32^\circ$, d) $\delta_0 = 1/64^\circ$. In all of them we take $\delta_f = 1^\circ$. The values in the color bar have units of day^{-1}	50
3.3	Top: Comparison of the probability density functions $P(\delta_0, \Lambda)$ for the FSLEs at different resolutions. It is obtained from the temporal average (30 snapshots) of histograms. Dotted line is for $\delta_0 = 1/8^\circ$, dashed-dotted line $\delta_0 = 1/16^\circ$, dashed $\delta_0 = 1/32^\circ$, and solid line for $\delta_0 = 1/64^\circ$. Bottom: $D(\Lambda)$ for different values of δ_0 . Dotted for $\delta_0 = 1/8^\circ$, dashed-dotted line $\delta_0 = 1/16^\circ$, dashed $\delta_0 = 1/32^\circ$, and solid line line for $\delta_0 = 1/64^\circ$	53

LIST OF FIGURES

- 3.4 Snapshots of FSLEs backward in time starting from day 640 at different initial V-grid resolutions: a) $\Delta_0 = 1/8^\circ$, b) $\Delta_0 = 1/4^\circ$, c) $\Delta_0 = 1/2^\circ$. In all of them we take the same F-grid resolution of $\delta_0 = 1/8^\circ$, and $\delta_f = 1^\circ$. The color bar has units of day^{-1} 54
- 3.5 Relative error between the FSLE fields drawn in Fig. 3.4, at locations having a FSLE value larger than a threshold U . Dashed line is for ϵ between Fig. 3.4a) and Fig. 3.4c); solid line is between Fig. 3.4a) and Fig. 3.4b); and dotted line is the error between Fig. 3.4b) and Fig. 3.4c). In all of them the relative error decreases when the threshold increases. 55
- 3.6 Probability distributions (coded as grey levels) of FSLEs derived at a coarse velocity resolution (Λ_c , vertical axis) conditioned by a finer velocity grid (Λ_f , horizontal axis). The range of values of both axes run linearly from 0 to 0.5 day^{-1} . To obtain a statistics large enough, we have considered 30 FSLEs snapshots, starting from $t = 640$ up to $t = 1075$ days, in steps of 15 days. The brightest color (pure white) corresponds to the maximum probability at each column; the darkest color (pure black) corresponds to zero. *Left panel:* FLSEs derived from $1/4^\circ$ velocities conditioned by FSLEs at original $1/8^\circ$ velocities. *Right panel:* FSLEs from $1/2^\circ$ velocities conditioned by FSLEs from $1/4^\circ$ velocities. 56
- 3.7 Snapshots of FSLEs calculated backwards in time starting from day 600 at fixed spatial resolution ($\delta_0 = 1/64^\circ$), and at different α : a) $\alpha = 0$, b) $\alpha = 10$. In both of them we take $\delta_f = 1^\circ$. The color bar has units of day^{-1} . Initial conditions for which the separation δ_f has not been reached after 600 days are assigned a value $\Lambda = 0$ 57
- 3.8 Relative error $\langle \epsilon(t) \rangle$ of the FSLE fields for different perturbation intensity α in the velocity data. Solid line is for uncorrelated noise in space and time, dashed-dotted line is for uncorrelated noise in time and correlated in space, and dotted line is for uncorrelated noise in space and correlated in time. $\langle \epsilon(t) \rangle$ is obtained by averaging the RE in 100 snapshots (see Eq. (3.5)). The error bar is the statistical error of the temporal average $\langle \epsilon(t) \rangle$. Left: spatial resolution $\delta_0 = 1/8^\circ$. Right: spatial resolution $\delta_0 = 1/64^\circ$. In all calculations we take $\delta_f = 1^\circ$ 59

LIST OF FIGURES

- 3.9 Trajectories of five particles without diffusion (top) and with diffusion (bottom). The difference in the initial positions of all five particles is about 0.06° , and we use these initial conditions in both computations. The trajectories were computed for 50 days of integration. We used the eddy-diffusion $D_0 \sim 10m^2s^{-1}$ assigned by the Okubo formula to the resolution of the DieCAST model at Mediterranean latitudes. 61
- 3.10 FSLEs computed backwards from day 500 at the same spatial resolution ($\delta_0 = 1/64^\circ$), and for different eddy-diffusion values: a) $D = 0 m^2s^{-1}$ b) $D = 0.9 m^2s^{-1}$. We take $\delta_f = 1^\circ$. The color bar has units of day^{-1} . Initial conditions for which the separation δ_f has not been reached after 500 days are assigned a value $\Lambda = 0$ 62
- 3.11 Left: Relative error $\langle \epsilon(t) \rangle$ of the FSLE at the different values of D in the particle trajectories, with respect to the $D = 0$ case. Spatial resolution is $\delta_0 = 1/8^\circ$, and $\delta_f = 1^\circ$. $\langle \epsilon(t) \rangle$ is obtained by temporally averaging the relative errors in 100 snapshots. The (small) error bars indicate the statistical error in the $\langle \epsilon(t) \rangle$ average. Right: Dotted line is the RE $\langle \epsilon(t) \rangle$ of the FSLE at different spatial resolution δ_0 and at one assigned eddy-diffusion D for every spatial resolution in the particle trajectories with respect to the $D = 0$ case. Solid line is the RE $\langle \epsilon(t) \rangle$ of the FSLE at different spatial resolution δ_0 , and at the same eddy-diffusion $D_0 = 10m^2s^{-1}$ in the particle trajectories with respect to the $D = 0$ case. Dashed-dotted line is the RE of shuffled FSLE with respect to the original case ($D = 0$) at different spatial resolution. $\langle \epsilon(t) \rangle$ by temporally averaging the RE in 100 snapshots. The (small) error bar indicates the statistical error in the $\langle \epsilon(t) \rangle$ average. In all of them we take $\delta_f = 1^\circ$ 63
- 3.12 Comparison between probability density function for the FSLEs at different resolutions with different values of eddy-diffusion, and without diffusion. It is obtained from the temporal average (30 snapshots) of histograms. Solid line for $\delta_0 = 1/8^\circ$ with diffusion, dotted $\delta_0 = 1/8^\circ$ without diffusion, dashed $\delta_0 = 1/16^\circ$ without diffusion, dashed-dotted line for $\delta_0 = 1/64^\circ$ with diffusion, and circle-line for $\delta_0 = 1/64^\circ$ without diffusion. 64
- 3.13 **Top:** Velocity field coarsened by a scale factor $s = 2$, for a equivalent resolution $\Delta_0 = 1/4^\circ$. **Bottom:** Velocity field coarsened by a scale factor $s = 4$, for a equivalent resolution $\Delta_0 = 1/2^\circ$ 66

LIST OF FIGURES

4.1	Top: Snapshot of spatial distributions of FSLEs backward in time corresponding to November 11, 1990 of the OFES output. Resolution is $\delta_0 = 1/10^\circ$. Bottom: Zoom in the area of the box inside top figure (South Atlantic Ocean). Coherent structures and vortices can be clearly seen. The colorbar has units of day^{-1}	74
4.2	a) Time average of the FSLEs in the Global Ocean. Geographical regions of different stirring activity appear. The colorbar has units of day^{-1} . b) Spatial distribution of annual $EKE^{1/2}$ (cm/s). c) Time average of Relative Vorticity (ω) in the Global Ocean. The color bar has units of day^{-1} . In all the plots the averages are over the 52 weekly maps computed from November 1st, 1990 to October 31th, 1991.	75
4.3	Left column: Temporal evolution (from November 1st, 1990 to October 31th, 1991) of the horizontal stirring (Spatial average of FSLEs). Right column: PDFs of the FSLEs (histograms are built from the λ values contained at all locations of the 52 weekly maps computed for the second simulation output year). Top: for both hemispheres and for the whole ocean. Middle: for different oceanic regions. Bottom: for some main currents during one simulation year. In addition to the results from the second surface layer analyzed through the paper, panel a) shows also stirring intensity in a layer close to 100m depth.	76
4.4	Time average of the FSLEs in the Global Ocean for the each season. Spring: from March 22 to June 22. Summer: from June 22 to September 22. Autumn: from September 22 to December 22. Winter: from December 22 to March 22. The colorbar has units of day^{-1}	78
4.5	Standard deviation of weekly FSLE maps of one year. The colorbar has units of day^{-1}	79
4.6	Cross-ocean zonal average of the annual, relative Summer and relative Winter time average of FSLE maps from Fig 4.2a as a function of latitude (expressed as absolute degrees from Equator to make both hemispheres comparable). Top: Northern Hemisphere; bottom: Southern Hemisphere.	81

LIST OF FIGURES

4.7 Left: Lagrangian-Eulerian relations. Left: the conditional average $\bar{\lambda}_{EKE}$ as a function of its corresponding annually averaged (second year) \overline{EKE} for different regions and currents. We clearly observe two groups of relations FSLE-EKE. Right: same plot for the conditional average $\bar{\lambda}_\omega$ as a function of its corresponding annually averaged (second year) $\bar{\omega}$. Although we observe also the same two two groups of FSLE- ω relations, these functions are much noisier and region-dependent. 82

4.8 Scatter plots showing temporally averaged FSLE values at different spatial points in regions of Fig. 4.2a, and EKE values (as displayed in Fig. 4.2b) at the same points. The regions displayed here are eight of the main currents. Fittings of the type $y = cX^b$ are also displayed, where y is the temporal mean of FSLE and X is $EKE^{1/2}$. Note that this implies $\langle FSLE \rangle = c EKE^\alpha$ with $\alpha = b/2$. 84

5.1 Bathymetry contours (in meters) of the model domain. The black box indicates the Palma Bay and the inset graphics give the geographical location of Mallorca Island in the western Mediterranean Sea. 90

5.2 a) Time series throughout October of the zonal (top) and meridional (bottom) components of the velocity field every 6 hours (dashed-line) and daily averaged (solid line); b) the same that a) but for July. 94

5.3 Spatial distribution of the time average of 6-hourly FSLEs maps over different months and at different layers: a) October at surface layer, b) July at surface layer, c) July at bottom layer. 96

LIST OF FIGURES

5.4	Evolution of the locations of two sets of particles in the Palma Bay during a night of October, superimposed on the spatial distributions of high values of backward FSLEs. The colorbars specify FSLE values in days^{-1} . Zero FSLE values, displayed as white, are assigned to locations for which the particles do not attain the prescribed $\delta_f = 10\text{km}$ separation after 5-days integration. Note the highest values of FSLEs (green lines) act as a barrier practically dividing the Bay in two parts. The two sets of particles are deployed from both sides of the barrier. (a) Initial conditions of the particles on October 8 at 20:00 GMT, 2008.; (b) October 9 at 00:00 GMT, 2008 ; (c) October 9 at 04:00 GMT, 2008 ; (d) October 9 at 08:00 GMT, 2008. Particles marked by black dots were released in the right side (northeast) of the barrier while the particles marked with red were released on the left side of the barrier.	97
5.5	Average of 15 different subsequent estimations of $N(t)$, started at t_0 values separated 18 hours. $N(t)/N(t_0)$ is the proportion of particles remaining in Palma Bay at least for a lapse of time t after release at t_0 . Black and red lines are for surface layer in October and July respectively.	98
5.6	Lines are the locations of top values of FSLE (greater than 0.5 in October and greater 1.5 in July). Backward FSLE lines are colored in black and forward FSLEs in white. They are superimposed on spatial distributions of residence times in Palma Bay for different months. The colorbars give the residence times in days. a) and b) correspond to two different days in October, and c) and d) in July.	99
5.7	Spatial distributions of time averages of 60 snapshots of 6-hourly RT values collected over 15 days in Palma Bay for a) October and b) July. The colorbar units are <i>days</i>	100
5.8	a) Time series throughout October of the spatial average of residence times (top) and spatial average of FSLE (bottom) for the surface layer of Palma Bay. b) the same that a) but for July.	102
5.9	a) Snapshot of spatial distributions of residence times at the bottom layer in Palma Bay corresponding to July 17, 2009 at 18:00h (GMT). b) spatial distribution of time average of 60 snapshots of 6-hourly maps of RT collected over 15 days in July at the bottom layer.	103
		169

LIST OF FIGURES

5.10	Time series throughout July of (top) spatial average of residence times and (bottom) spatial average of FSLE computed for the bottom layer.	104
5.11	FSLEs for final separation of $\delta_f = 150m$ ($\delta_f/\delta_0 \approx 2$), $\delta_f = 250m$ ($\delta_f/\delta_0 \approx 3.3$), $\delta_f = 500m$ ($\delta_f/\delta_0 \approx 6.7$) and $\delta_f = 750m$ ($\delta_f/\delta_0 \approx 10$) November 23, 2009 at 18:00h. Just for plotting, we have considered positive the values of λ^+ and negative the ones for λ^-	106
5.12	Daily snapshots of λ^- starting on November 15 th (mild wind conditions), computed for only currents (left panel) and with waves and currents (right panel) . Virtual particles at four different areas are marked by <i>circles, diamonds, squares</i> and <i>stars</i>	108
5.13	Daily snapshots of λ^- starting on November 21 st (strong wind conditions), computed for only currents (left panel) and with waves and currents (right panel) . Virtual particles at four different areas are marked by <i>circles, diamonds, squares</i> and <i>stars</i>	110
5.14	Six hour snapshot of λ^- computed for only currents (set I), and trajectories of Lagrangian drifters.	111
5.15	Six hour snapshot of λ^- computed for currents and waves (set II), and trajectories of Lagrangian drifters.	113
6.1	Shape and values of the strength (S) of the upwelling cells used in the simulations for winter and summer seasons (following Veitch et al. (2009)).	121
6.2	Spatial distribution of time average of weekly FSLE maps in the Benguela region. a) Three years average using data set <i>Satellite1/4</i> ; b) one year average using <i>ROMS1/4</i> ; c) one year average using <i>ROMS1/12</i> . The units of the colorbar are $1/days$. The black lines are contours of annual EKE. The separation between contour levels is $100cm^2/s^2$	125
6.3	Zonal average over coastal bands of the FSLE time averages from Fig. 6.2 as a function of latitude. a) from the coast to 3 degrees offshore; b) between 3 and 6 degrees offshore.	126
6.4	Spatial distribution of the time average of phytoplankton concentrations: a) Three years average using <i>Satellite1/4</i> , b) One year average from <i>ROMS1/4</i> , c) One year average from <i>ROMS1/12</i> , d) Three years average of monthly SeaWIFS data. The units of the colorbar are mg/m^3	128

LIST OF FIGURES

6.5	Zonal mean of simulated phytoplankton over a coastally oriented strip from the coast to 3 degrees (a) and from 3 degrees to 6 degrees offshore (b), plotted as a function of latitude. Zonal average of phytoplankton derived from satellite (SeaWIFS) over a coastal band from the coast to 3 degrees (c) and from 3 degrees to 6 degrees offshore (d).	130
6.6	Snapshots every 8 days of large (top 30%) values of FSLE superimposed on P concentrations calculated from <i>ROMS1/12</i> in mg/m^3 . Logarithmic scale for phytoplankton concentrations is used to improve the visualization of the structures	131
6.7	Weekly values of spatial averages of phytoplankton versus weekly values of spatial averages of FSLE, where the average are over the whole area (6° from the coast) and in North and South subareas of Benguela. a) <i>Satellite1/4</i> , b) <i>ROMS1/4</i> and c) <i>ROMS1/12</i> . Right column plots the average over 3° offshore in the south region: d) <i>Satellite1/4</i> , e) <i>ROMS1/4</i> and f) <i>ROMS1/12</i>	132
6.8	Spatial distribution of the annual average of the growth rate of nutrient (a), phytoplankton (c) and zooplankton (e) for <i>ROMS1/12</i> (the colorbar has units of day^{-1}). Zonal average of the annual growth rate of nutrient (b), phytoplankton (d) and zooplankton (f) as a function of the latitude and for different coastal bands. . .	134
6.9	Zonal mean of zonal and meridional fluxes of N, P, Z concentrations for the <i>ROMS1/12</i> case, averaged from the coast to 3° offshore (a), and between 3° and 6° offshore (b).	136
6.10	a) Spatial distribution of time average of the passive scalar concentration (see details at the end of subsection 6.4.3). b) Comparison of latitudinal profile of time averages of the passive scalar, as a function of latitude, for zonal average over different coastal bands.	137
6.11	Temporal evolution of N, P, Z budgets for the <i>ROMS1/12</i> case, averaged for the southern region of Benguela and for different coastal strips. Botom row correspond to the temporal evolution of horizontal stirring (Spatial average over the southern region of FSLEs) for <i>ROMS1/12</i>	139
6.12	Time evolution of the spatial average in the south region of Benguela of the per capita growth rate of nutrient (a), phytoplankton (b) and zooplankton (c), for the <i>ROMS1/12</i> case.	140

LIST OF FIGURES

6.13	Vectors of a velocity field from <i>ROMS1/12</i> : a) at original resolution. b) smoothed by a scale factor of $s=3$, obtaining and equivalent spatial resolution of $1/4^\circ$, c) smoothed by a scale factor of $s=6$, obtaining and equivalent spatial resolution of $1/2^\circ$. The snapshots correspond to day 437 of the simulation.	142
6.14	Snapshots of spatial distributions of FSLEs backward 437 days in time starting from day 437 of <i>ROMS1/12</i> at the same FSLE grid resolution of $1/12^\circ$, and using the velocity fields at different resolutions: a) at original resolution $1/12^\circ$. b) smoothed velocity field at equivalent $1/4^\circ$ and c) smoothed velocity field at equivalent $1/2^\circ$	143
6.15	Latitudinal profile of the zonal mean values of annual averaged backward FSLEs (51 snapshots weekly separated) at the same FSLE grid resolution of $1/12^\circ$, and using different smoothed velocity fields.	144
6.16	Snapshots of simulated phytoplankton field using different velocity fields: a) <i>ROMS1/12</i> at original resolution $1/12^\circ$, b) smoothed <i>ROMS1/12</i> velocity field at equivalent $1/4^\circ$, c) smoothed <i>ROMS1/12</i> velocity field at equivalent $1/2^\circ$, and d) <i>ROMS1/4</i> at original resolution $1/4^\circ$	145
6.17	Comparison between zonal average over different coastal bands of annual time average of P , using homogeneous upwelling and the non-homogeneous upwelling cells described in Fig. 6.1. . . .	146

Bibliography

- Abraham, E., 1998: The generation of plankton patchiness by turbulent stirring. *Nature*, **391**, 577–580.
- Abraham, E., and M. Bowen, 2002: Chaotic stirring by a mesoscale surface-ocean flow. *Chaos*, **12**, 373–381.
- Abraham, E., C. Law, P. Boyd, S. Lavender, M. Maldonado, and A. Bowie, 2000: Importance of stirring in the development of an iron-fertilized phytoplankton bloom. *Nature*, **407**, 727.
- Aref, H., 1984: Stirring by chaotic advection. *J. Fluid Mech.*, **143**, 1–21.
- Aristegui, J., P. Tett, A. Hernandez-Guerra, G. Basterretxea, M. Montero, K. Wild, P. Sangra, S. Hernandez-Leon, M. Canton, and J. Garcia-Braun, 1997: The influence of island-generated eddies on chlorophyll distributions: a study of mesoscale variation around Gran Canaria. *Deep Sea Res I*, **44**, 71.
- Artale, V., G. Boffetta, A. Celani, M. Cencini, and A. Vulpiani, 1997: Dispersion of passive tracers in closed basins: Beyond the diffusion coefficient. *Phys. Fluids*, **9**, 3162–3171.
- Aurell, E., G. Boffetta, A. Crisanti, G. Paladin, and A. Vulpiani, 1997: Predictability in the large: an extension of the Lyapunov exponent. *J. Phys. A*, **30**, 1–26.
- Babiano, A., A. Provenzale, and A. Vulpiani, 1994: Chaotic Advection, Tracer Dynamics, and Turbulent Dispersion. *Proceedings of the NATO Advanced Research Workshop and EGS Topical Workshop on Chaotic Advection, Conference Centre Sereno di Gavo, Italy, 24-28 May 1993*, **76**.

BIBLIOGRAPHY

- Barabasi, A. L., and H. E. Stanley, 1995: *Fractal Concepts in Surface Growth*. Cambridge University Press.
- Barreira, L., and Y. Pesin, 2002: *Lyapunov Exponents and Smooth Ergodic Theory*. University Lecture Series, American Mathematical Society, Providence, R.I.
- Barton E. et al., 1998: The transition zone of the Canary Current upwelling region. *Progress in Oceanography*, **41**, 455–504.
- Beron-Vera, F., 2010: Mixing by low- and high-resolution surface geostrophic currents. *J. Geophys. Res.*, **115**, C10027.
- Beron-Vera, F., M. Olascoaga, and G. Goni, 2008: Oceanic mesoscale eddies as revealed by Lagrangian coherent structures. *Geophys. Res. Lett.*, **35**, L12603.
- Beron-Vera, F. J., M. J. Olascoaga, M. G. Brown, H. Koçak, and I. I. Rypina, 2010: Invariant-tori-like Lagrangian coherent structures in geophysical flows. *Chaos*, **20**(1), 017514.
- Bettencourt, J., C. López, and E. Hernández-García, 2012: Oceanic three-dimensional Lagrangian Coherent Structures: A study of a mesoscale eddy in the Benguela upwelling region. *Ocean Modell.*, **51**, 73–83.
- Boffetta, G., A. Celani, M. Cencini, G. Lacorata, and A. Vulpiani, 2000: Non-asymptotic properties of transport and mixing. *Chaos*, **10**, 50–60.
- Boffetta, G., G. Lacorata, G. Redaelli, and A. Vulpiani, 2001: Detecting barriers to transport: A review of different techniques. *Physica D*, **159**, 58–70.
- Boyce, W., and R. DiPrima, 1998: *Ecuaciones diferenciales y problemas con valores en la frontera*. Noruega Editores, Mexico.
- Bracco, A., J. H. LaCasce, and A. Provenzale, 2000: Velocity probability density functions for oceanic floats. *J. Phys. Oceanogr.*, **30**(3), 461–474.
- Brink, K., and T. Cowles, 1991: The Coastal Transition Zone Program. *J. Geophys. Res.*, **14**, 637–647.
- Buffoni, G., A. Cappelletti, and E. Cupini, 1996: Advection-diffusion processes and residence times in semi-enclosed marine basins. *Int. J. Numer. Methods Fluids*, **22**, 1–23.
- Buffoni, G., P. Falco, A. Griffa, and E. Zambianchi, 1997: Dispersion processes and residence times in a semi-enclosed basin with recirculating gyres: An application to the Tyrrhenian sea. *J. Geophys. Res.*, **102**, 18699–18713.

BIBLIOGRAPHY

- Calil, P., and K. Richards, 2010: Transient upwelling hot spots in the oligotrophic North Pacific. *J. Geophys. Res.*, **115**, C02003.
- Cencini, M., F. Cecconi, and A. Vulpiani, 2010: Chaos: From Simple Models to Complex Systems. *Series on Advances in Statistical Mechanics*, World Scientific,.
- Chelton, D., P. Gaube, M. Schlax, J. Early, and R. Samelson, 2011: The influence of Nonlinear Mesoscale Eddies on Near-Surface Oceanic Chlorophyll. *Science*, **334**, 328–332.
- Chelton, D., and M. Schlax, 1997: Global observations of oceanic Rossby waves. *Science*, **272**, 234–238.
- Chelton, D., M. Schlax, and R. Samelson, 2011: Global observation of nonlinear mesoscale eddies. *Prog. Oceanogr.*, **91**, 167–216.
- Condie, S., and J. R. Dunn, 2006: Seasonal characteristics of the surface mixed layer in the Australasian region: implications for primary production regimes and biogeography Marine and Freshwater Research. *Marine and Freshwater Research*, **57**, 1–22.
- Correa-Ramirez, M., S. Hormazabal, and G. Yuras, 2007: Mesoscale eddies and high chlorophyll concentrations off central Chile (29°S - 39°S). *Geophys. Res. Lett.*, **34**, L12604.
- Demarcq, H., R. Barlow, and F. Shillington, 2003: Climatology and variability of sea surface temperature and surface chlorophyll in the Benguela and Agulhas ecosystems as observed by satellite. *African Journal of Marine Science*, **25**, 363–372.
- Dickey, T., 2003: Emerging ocean observations for interdisciplinary data assimilation systems. *J. Marine Syst.*, **40-41**, 5–48.
- Dietrich, D., 1997: Application of a modified “a” grid ocean model having reduced numerical dispersion to the Gulf of Mexico circulation. *Dyn. Atmos. Oceans*, **27**, 201–217.
- d’Ovidio, F., V. Fernández, E. Hernández-García, and C. López, 2004: Mixing structures in the Mediterranean sea from Finite-Size Lyapunov Exponents. *Geophys. Res. Lett.*, **31**, L17203.
- d’Ovidio, F., J. Isern-Fontanet, C. López, E. Hernández-García, and E. García-Ladona, 2009: Comparison between Eulerian diagnostics and Finite-Size Lyapunov Exponents computed from Altimetry in the Algerian basin. *Deep-Sea Res. I*, **56**, 15–31.

BIBLIOGRAPHY

- d'Ovidio, F., S. Monte, S. Alvain, Y. Dandonneau, and M. Levy, 2010: Fluid dynamical niches of phytoplankton types. *Proc. Natl. Acad. Sci.*, **107**, 18366.
- d'Ovidio, F., E. Shuckburgh, and B. Legras, 2009: Local mixing events in the upper-troposphere and lower-stratosphere. Part I: detection with the Lyapunov diffusivity. *J. Atmos. Sci.*, **66**(12), 3678–3694.
- Early, J., R. Samelson, and D. Chelton, 2011: The Evolution and Propagation of Quasigeostrophic Ocean Eddies. *J. Phys. Oceanogr.*, **41**(8), 1535–1555.
- Falco, P., A. Griffa, and P. M. Poulain, 2000: Transport properties in the Adriatic Sea as deduced from drifter data. *J. Phys. Oceanogr.*, **30**(8), 2055–2071.
- Falconer, K., 1990: *Fractal Geometry: Mathematical Foundations and Applications*. John Wiley and sons, Chichester.
- Fernández, V., D. Dietrich, R. Haney, and J. Tintoré, 2005: Mesoscale, seasonal and interannual variability in the Mediterranean Sea using a numerical ocean model. *Progress in Oceanography*, **66**, 321–340.
- Fiorentino, L. A., M. J. Olascoaga, A. Reniers, Z. Feng, F. Beron-Vera, and J. H. MacMahan, 2012: Using Lagrangian Coherent Structures to understand coastal water quality. *Continental Shelf Research*, **47**, 145–149.
- Frisch, U., 1995: *Turbulence: The Legacy of A.N. Kolgomogorv*. Cambridge University Press.
- Galan, A., A. Orfila, G. Simarro, I. Hernández-Carrasco, and C. López, 2012: Wave mixing rise inferred from Lyapunov exponents. *Environmental Fluid Mechanics*, **12**(3), 291–300.
- Garçon, V., A. Oschlies, S. Doney, D. McGillicuddy, and J. Waniek, 2001: The role of mesoscale variability on plankton dynamics in the north Atlantic. *Deep Sea Research Part II*, **48**, 2199–2226.
- Garcia-Olivares, A., J. Isern-Fontanet, and E. Garcia-Ladona, 2007: Dispersion of passive tracers and finite-scale Lyapunov exponents in the Western Mediterranean Sea. *Deep Sea Research I*, **54**, 253–268.
- Gildor, H., E. Fredj, J. Steinbuck, and S. Monismith, 2009: Evidence for Submesoscale Barriers to Horizontal Mixing in the Ocean from Current Measurements and Aerial Photographs. *Journal of Physical Oceanography*, **39**, 1975–1983.
- Griffa, A., 1996: Applications of stochastic particle models to oceanographic problems. *Stochastic modelling in physical oceanography*, R. Adler, P. Muller, and B. Rozovskii, Eds., Birkhauser.

BIBLIOGRAPHY

- Gruber, N., H. Frenzel, S. Doney, P. Marchesiello, J. McWilliams, J. Moisan, J. Oram, G. Plattner, and K. Stolzenbach, 2006: Eddy-resolving simulation of plankton ecosystem dynamics in the California Current System. *Deep-Sea Research I*, **53**.
- Gruber, N., Z. Lachkar, H. Frenzel, P. Marchesiello, M. Münnich, J. McWilliams, T. Nagai, and G. Plattner, 2011: Eddy-induced reduction of biological production in eastern boundary upwelling systems. *Nature Geoscience*, **9**, 787–792.
- Gutknecht, E., I. Dadou, B. L. V. G. Cambon, J. Sudre, V. Garçon, E. Machu, T. Rixen, A. Kock, A. Flohr, A. Paulmier, and G. Lavik, 2011: Nitrogen transfers and air-sea N₂O fluxes in the upwelling off Namibia within the oxygen minimum zone: a 3-D model approach. *Biogeosciences Discuss*, **8**, 3537–3618.
- Haidvogel, D., J. Blanton, J. Kindle, and D. Lynch, 2000: Coastal Ocean Modeling: Processes and Real-Time Systems. *Oceanography*, **13(1)**, 35–46.
- Haidvogel, D. B., 1999: *Numerical Ocean Circulation Modeling*. Imperial College Press, London.
- Haller, G., 2000: Finding finite-time invariant manifolds in two-dimensional velocity fields. *Chaos*, **10(1)**, 99–108.
- Haller, G., 2001: Distinguished material surfaces and coherent structure in three-dimensional fluid flows. *Physica D*, **149**, 248–277.
- Haller, G., 2002: Lagrangian coherent structures from approximate velocity data. *Phys. Fluids*, **14**, 1851–1861.
- Haller, G., 2011: A variational theory of hyperbolic Lagrangian Coherent Structures. *Physica D*, **240(7)**, 574 – 598, Erratum and addendum: *Physica D* **241**, 439–441 (2012).
- Haller, G., and F. J. Beron-Vera, 2012: Geodesic theory of transport barriers in two-dimensional flows. *Physica D: Nonlinear Phenomena*, **241**, 1680 – 1702.
- Haller, G., and A. Poje, 1998: Finite time transport in aperiodic flows. *Physica D*, **119**, 352–380.
- Haller, G., and T. Sapsis, 2011: Lagrangian coherent structures and the smallest finite - time Lyapunov exponent. *Chaos*, **21(2)**, 023115.
- Haller, G., and G. Yuan, 2000: Lagrangian coherent structures and mixing in two-dimensional turbulence. *Physica D*, **147**, 352–370.

BIBLIOGRAPHY

- Halliwell, G., D. B. Olson, and G. Peng, 1994: Stability of the Sargasso Sea Subtropical Frontal Zone. *J. Phys. Oceanogr.*, **24**(6), 1166–1183.
- Halpern, D., 2000: *Satellites, Oceanography and Society*. Elsevier Sci., New York.
- Haza, A. C., T. M. Özgökmen, A. Griffa, A. Molcard, P.-M. Poulain, and G. Peggion, 2010: Transport properties in small-scale coastal flows: relative dispersion from VHF radar measurements in the Gulf of La Spezia. *Ocean Dynamics*, **60**, 861–882.
- Haza, A. C., A. C. Poje, T. M. Özgökmen, and P. Martin, 2008: Relative dispersion from a high-resolution coastal model of the Adriatic Sea. *Ocean Modell.*, **22**, 48–65.
- Hernández-Carrasco, I., C. López, E. H.-G. a, and A. Turiel, 2011: How reliable are finite-size Lyapunov exponents for the assessment of ocean dynamics? *Ocean Modelling*, **36**(3-4), 208 – 218.
- Hernández-García, E., and C. López, 2004: Sustained plankton blooms under open chaotic flows. *Ecol. Complex.*, **1**, 253–259.
- Hernández-García, E., C. López, and Z. Neufeld, 2002: Small-scale structure of nonlinearly interacting species advected by chaotic flows. *Chaos*, **12**, 470–480.
- Hernández-García, E., C. López, and Z. Neufeld, 2003: Filament bifurcations in a one-dimensional model of reacting excitable fluid flow. *Physica A*, **327**, 59–64.
- Hernández-García, E., C. López, and Z. Neufeld, 2003: Spatial Patterns in Chemically and Biologically Reacting Flows. *Chaos in Geophysical Flows*. OTTO Editore, Torino.
- Hua, B., and P. Klein, 1998: An exact criterion for the stirring properties of near-ly two-dimensional turbulence. *Physica D*, **113**, 98–110.
- Hua, B., J. McWilliams, and P. Klein, 1998: Lagrangian accelerations in geostrophic turbulence. *J. Fluid Mech.*, **366**, 87–108.
- Huhn, F., A. von Kameke, S. Allen-Perkins, P. Montero, A. Venancio, and V. Pérez-Muñuzuri, 2012: Horizontal Lagrangian transport in a tidal-driven estuary - Transport barriers attached to prominent coastal boundaries. *Continental Shelf Research.*, **39-40**, 1–13.
- Hutchings, L., C. van der Lingen, R. Shannon L.J. Crawford, H. Verheye, C. Bartholomae, A. van der Plas, D. Louw, A. Kreiner, M. Ostrowski, Q. Fidel, R. Barlow, T. Lamont, J. Coetzee, F. Shillington, J. Veitch, J. Currie, and

BIBLIOGRAPHY

- P. Monteiro, 2009: The Benguela Current: An ecosystem of four components. *Progress in Oceanography*, **83**, 15–32.
- Ide, K., D. Small, and S. Wiggins, 2002: Distinguished hyperbolic trajectories in time dependent fluid flows: analytical and computational approach for velocity fields defined as data sets. *Nonlin. Processes Geophys.*, **9**, 237–263.
- Isern-Fontanet, J., A. Turiel, E. Garcia-Ladona, and J. Font, 2007: Microcanonical Multifractal Formalism: application to the estimation of ocean surface velocities. *Journal of Geophysical Research*, **112**, C05024.
- Iudicone, D., G. Lacorata, V. Rupolo, R. Santoreli, and A. Vulpiani, 2002: Sensitivity of numerical tracer trajectories to uncertainties in OGCM velocity fields. *Ocean Modelling* 313–325.
- Joseph, B., and B. Legras, 2002: Relation between Kinematic Boundaries, Stirring, and Barriers for the Antarctic Polar Vortex. *J. Atm. Sci.*, **59**, 1198–1212.
- Klein, P., and G. Lapeyre, 2009: The oceanic vertical pump induced by mesoscale and submesoscale turbulence. *Annu. Rev. Mar. Sci.*, **1**, 351–375.
- Klein, P., A. Tréguier, and B. Hua, 1998: Three-dimensional stirring of thermal-haline fronts. *J. Mar. Res.*, **56**, 589–612.
- Koh, T.-Y., and B. Legras, 2002: Hyperbolic lines and the stratospheric polar vortex. *Chaos*, **12**(2), 382–394.
- Komen, G.J., L. C. M. D. K. H. S. H., and P. Janssen, 1994: *Dynamics and Modelling of Ocean Waves*. Cambridge University Press.
- Koné, V., E. Machu, P. Penven, V. Andersen, V. Garçon, P. Fréon, and H. Demarcq, 2005: Modeling the primary and secondary productions of the southern Benguela upwelling system: A comparative study through two biogeochemical models. *Global Biogeochem. Cycles*, **19**, GB4021.
- Kudela, R. F., 2012: Does horizontal mixing explain phytoplankton dynamics? *Proc. Natl. Acad. Sci.*, **107**, 18235.
- Lacasce, J., 2008: Statistics from Lagrangian observations. *Progress in oceanography*, **77**, 1–29.
- Lacasce, J., and C. Ohlmann, 2003: Relative dispersion at the surface of the Gulf of Mexico. *J. Mar. Res.*, **61**, 285–312.
- Lachkar, Z., and N. Gruber, 2011: What controls biological production in coastal upwelling systems? Insights from a comparative modeling study. *Biogeosciences*, **8**, 2961–2976.

BIBLIOGRAPHY

- Lacorata, G., E. Aurell, and A. Vulpiani, 2001: Drifter dispersion in the Adriatic Sea: Lagrangian data and chaotic model. *Ann. Geophysicae*, **19**, 121–129.
- Lai, Y., and T. Tel, 2011: *Transient Chaos: Complex Dynamics on Finite-Time Scales*. Springer.
- Lapeyre, G., 2002: Characterization of finite-time Lyapunov exponents and vectors in two-dimensional turbulence. *Chaos*, **12(3)**, 688–698.
- Lapeyre, G., and P. Klein, 2006: Dynamics of the upper oceanic layers in terms of surface quasigeostrophic theory. *Journal of Physical Oceanography*, **36**, 165–176.
- Lapeyre, G., P. Klein, and B. Hua, 1999: Does the tracer gradient vector align with strain eigenvectors in 2D turbulence? *Phys. Fluids*, **11(12)**, 3729–3737.
- Lathuiliere, C., M. Lévy, and V. Echevin, 2011: Impact of eddy-driven vertical fluxes on phytoplankton abundance in the euphotic layer. *Journal of Plankton Research*, **33**, 827–831.
- Legal, C., P. Klein, and A. Tréguier, 2007: Diagnosis of the Vertical Motions in a Mesoscale Stirring Region. *J. Phys. Oceanogr.*, **37**, 1413–1425.
- Lehan, Y., F. d’Ovidio, M. Lévy, and E. Heyfetz, 2007: Stirring of the Northeast Atlantic spring bloom: A Lagrangian analysis based on multisatellite data. *J. Geophys. Res.*, **112**, C08005.
- Lekien, F., C. Coulliette, A. J. Mariano, E. H. Ryan, L. K. Shay, G. Haller, and J. Marsden, 2005: Pollution release tied to invariant manifolds: A Case study for the coast of Florida. *Physica D.*, **210**, 1–20.
- Leong, C. W., and J. M. Ottino, 1989: Experiments on mixing due to chaotic advection in a cavity. *J. Fluid. Mech.*, **209**, 463.
- Lett, C., J. Veitch, C. van der Lingen, and L. Hutchings, 2007: Assessment of an environmental barrier to transport of ichthyoplankton from the southern to the northern Benguela ecosystems. *Marine Ecology Progress Series*, **347**, 247–259.
- Lévy, M., 2008: The Modulation of Biological Production by Ocean Mesoscale Turbulence. *Lect. Notes. Phys.*, **744**, 219–261.
- Lévy, M., R. Ferrari, P. Franks, A. P. Martin, and P. Riviere, 2012: Bringing physics to life at the submesoscale. *Geophys. Res. Lett.*, **39**, L14602.
- Lévy, M., P. Klein, and A. Tréguier, 2001: Impacts of submesoscale physics on phytoplankton production and subduction. *J. Mar. Res.*, **59**, 535–565.

BIBLIOGRAPHY

- Lipphardt, B., Jr., D. Small, A. Kirwan, Jr., S. Wiggins, K. Ide, C. Grosch, and J. Paduan, 2006: Synoptic Lagrangian maps: Application to surface transport in Monterey Bay. *Journal of Marine Research*, **64**, 221–247.
- Longuet-Higgins, M., and R. Stewart, 1964: Radiation stresses in water waves: a physical discussion with applications. *Deep Sea Res.*, **11**, 529–562.
- López, C., Z. Neufeld, E. Hernández-García, and P. Haynes, 2001: Chaotic advection of reacting substances: Plankton dynamics on a meandering jet. *Phys. Chem. Earth*, **B 26**, 313–317.
- Lyapunov, A., 1992: *The general Problem of the Stability of Motion*. Taylor and Francis, Washington. Translated from Russian to English by A. T. Fuller.
- Mackas, D., P. Strub, C. Thomas, and V. Montecino., 2006: Eastern ocean boundaries pan-regional view. *The Sea, vol 14a, The global Coastal Ocean: Interdisciplinary Regional Studies and Syntheses: Pan-Regional Syntheses and the Coast of North and South America and Asia*, A. Robinson and K. Brink, Eds. Harvard Univ. Press, chap. 2, Cambridge, Mass.
- Mahadevan, A., and D. Archer, 2000: Modeling the impact of fronts and mesoscale circulation on the nutrient supply and biogeochemistry of the upper ocean. *J. Geophys. Res.*, **105**, 1209–1225.
- Mancho, A., E. Hernández-García, D. Small, S. Wiggins, and V. Fernández, 2008: Lagrangian transport through an ocean front in the North-Western Mediterranean Sea. *J. Phys. Oceanogr.*, **38**, 1222–1237.
- Mancho, A. M., D. Small, and S. Wiggins, 2004: Computation of Hyperbolic and their Stable and Unstable Manifolds for Oceanographic Flows Represented as Data Sets. *Nonlin. Processes Geophys.*, **11**, 17–33.
- Mancho, A. M., D. Small, and S. Wiggins, 2006a: A Comparison of Methods for Interpolating Chaotic Flows from Discrete Velocity Data. *Computers & Fluids*, **35**, 416–428.
- Mancho, A. M., D. Small, and S. Wiggins, 2006b: A tutorial on dynamical systems concepts applied to Lagrangian transport in ocean flows defined as finite time data sets: theoretical and computational issues. *Physics Report*, **437**, 55–124.
- Mariano, A. J., A. Griffa, T. Ozgokmen, and E. Zambianchi, 2002: Lagrangian Analysis and Predictability of Coastal and Ocean Dynamics 2000. *Journal of Atmospheric and Oceanic Technology*, **19**, 1114.
- Martin, A., 2000: On filament width in oceanic plankton distributions. *J. Plank. Res.*, **22**, 597.

BIBLIOGRAPHY

- Martin, A., 2003: Phytoplankton patchiness: the role of lateral stirring and mixing. *Progress in Oceanography*, **57**, 125–174.
- Martin, A., K. Richards, A. Bracco, and A. Provenzale, 2002: Patchy productivity in the open ocean. *Global Biogeochemical Cycles*, **16**, 10.1029/2001GB001449.
- Masumoto, Y., 2010: Sharing the results of a high-resolution ocean general circulation model under a multi-discipline framework - a review of OFES activities. *Ocean Dynamics*, **60**, 633–652.
- Masumoto, Y., H. Sasaki, T. Kagimoto, N. Komori, A. Ishida, Y. Sasai, T. Miyama, T. Motoi, H. Mitsudera, K. Takahashi, and et al., 2004: A Fifty-Year Eddy-Resolving Simulation of the World Ocean - Preliminary Outcomes of OFES (OGCM for the Earth Simulator). *J. of the Earth Simulator*, **1**(April), 35–56.
- McGillicuddy, D., L. Anderson, N. Bates, T. Bibby, K. Buesseler, C. Carlson, C. Davis, C. Ewart, P. Falkowski, S. Goldthwait, D. Hansell, W. Jenkins, R. Johnson, V. Kosnyrev, J. Ledwell, Q. Li, D. Siegel, and D. Steinberg, 2007: Eddy/wind interactions stimulate extraordinary mid-ocean plankton blooms. *Science*, **316**, 1021–1026.
- McGillicuddy, D., A. Robinson, D. Siegel, H. Jannasch, R. Johnson, T. Dickey, J. McNeil, A. Michaels, and A. Knap, 1998: Influence of mesoscale eddies on new production in the Sargasso Sea. *Nature*, **394**, 263–265.
- McKiver, W., and Z. Neufeld, 2009: The influence of turbulent advection on a phytoplankton ecosystem with non-uniform carrying capacity. *Phys. Rev. E.*, **79**, 061902.
- McKiver, W., Z. Neufeld, and I. Scheuring, 2009: Plankton bloom controlled by horizontal stirring. *Nonlin. Processes Geophys.*, **16**, 623–630.
- McWilliams, J. C., 1985: Submesoscale, coherent vortices in the ocean. *Reviews of Geophysics*, **23**(2), 165–182.
- Mélin, F., G. Zibordi, and J. Berthon, 2007: Assessment of satellite ocean color products at a coastal site. *Remote Sensing Environ.*, **110**(2), 192.
- Mendoza, C., and A. M. Mancho, 2010: Hidden Geometry of Ocean Flows. *Phys. Rev. Lett.*, **105**, 501.
- Mendoza, C., and A. M. Mancho, 2012: The Lagrangian description of aperiodic flows: a case study of the Kuroshio Current. *Nonlinear Processes in Geophysics*, **19**(4), 449–472.

BIBLIOGRAPHY

- Molcard, A., A. Poje, and T. Özgökmen, 2006: Directed drifter launch strategies for Lagrangian data assimilation using hyperbolic trajectories. *Ocean Modelling*, **12**, 268–289.
- Monteiro, P., 2009: Carbon fluxes in the Benguela Upwelling system. *Carbon and Nutrient Fluxes in Continental Margins: A global Synthesis, Chap. 2*, K. Liu, L. Atkinson, R. Quiñones, and L. Talaue-McManus, Eds. Springer, Berlin.
- Morrow, R., A. Brut, and A. Chaigneau, 2003: Seasonal and interannual variations of the upper ocean energetics between Tasmania and Antarctica. *Deep-Sea Res. I*, **50**(3), 339–356.
- Neufeld, Z., 2012: Stirring effects in models of oceanic plankton populations. *Chaos*, **22**, 037102.
- Neufeld, Z., P. Haynes, V. Garçon, and J. Sudre, 2002: Ocean fertilization experiments may initiate a large scale phytoplankton bloom. *Geophys. Res. Lett.*, **29**, 10.1029/2001GL013677.
- Neufeld, Z., and E. Hernández-García, 2009: *Chemical and Biological Processes in Fluid Flows. A dynamical systems approach*. Imperial College, London.
- Neufeld, Z., C. López, and P. Haynes, 1999: Smooth-Filamental Transition of Active Tracer Fields Stirred by Chaotic Advection. *Phys. Rev. Lett.*, **82**, 2606.
- Neufeld, Z., C. López, E. Hernández-García, and T. Tél, 2000: The multifractal structure of chaotically advected chemical fields. *Phys. Rev. E.*, **61**, 3857.
- Ohlmann, J. C., J. H. LaCasce, L. Washburn, A. J. Mariano, and B. Emery, 2012: Relative dispersion observations and trajectory modeling in the Santa Barbara Channel. *J. Geophys. Res.*, **117**, C05040.
- Okubo, A., 1971: Oceanic diffusion diagrams. *Deep-Sea Res.*, **18**, 789.
- Oschlies, A., 2002a: Can eddies make ocean deserts blooms? *Global Biogeochem. Cycles*, **16**(4), 1106.
- Oschlies, A., 2002b: Nutrient supply to the surface waters of the North Atlantic: a model study. *J. Geophys. Res.*, **107**, 3046.
- Oschlies, A., and V. Garçon, 1998: Eddy-induced enhancement of primary productivity in a model of the North Atlantic Ocean. *Nature*, **394**, 266.
- Oschlies, A., and V. Garçon, 1999: An eddy-permitting coupled physical-biological model of the North-Atlantic, sensitivity to advection numerics and mixed layer physics. *Global Biogeochem. Cycles*, **13**, 135–160.

BIBLIOGRAPHY

- Oseledec, V., 1968: A multiplicative ergodic theorem: Lyapunov characteristic numbers for dynamical systems. *Trans. Moscow Math. Soc.*, **19**, 197–231.
- Ott, E., 1993: *Chaos in Dynamical Systems*. Cambridge Univ. Press, Cambridge (UK).
- Owen, R. W., 1981: Fronts and Eddies in the Sea: Mechanism, Interactions and Biological Effects. *Analysis of marine ecosystems*, A. R. Longhurst, Ed. Academic Press, London, 197–233.
- Özgökmen, T. M., A. C. Poje, P. F. Fischer, H. Childs, H. Krishnan, C. Garth, A. C. Haza, and E. Ryan, 2012: On multi-scale dispersion under the influence of surface mixed mixed layer instabilities and deep flows. *Ocean Modell.*, **56**, 16–30.
- Özgökmen, T. M., A. C. Poje, P. F. Fischer, and A. C. Haza, 2011: Large eddy simulations of mixed layer instabilities and sampling strategies. *Ocean Modell.*, **39**, 311–331.
- Pasquero, C., A. Babiano, and A. Provenzale, 2001: Parametrization of dispersion in two-dimensional turbulence. *J. Fluid Mech.*, **439**, 279–303.
- Pasquero, C., A. Bracco, and A. Provenzale, 2004: Coherent vortices, Lagrangian particles and the marine ecosystem. *Shallow Flows*, W. Uijttewaal and G. Jirka, Eds. Balkema, Leiden, 399–412.
- Pasquero, C., A. Bracco, and A. Provenzale, 2005: Impact of the spatiotemporal variability of the nutrient flux on primary productivity in the ocean. *J. Geophys. Res.*, **110**, C07005.
- Pasquero, C., A. Provenzale, and J. Weiss, 2002: Vortex statistics from Eulerian and Lagrangian Time Series. *Pys. Rev. Lett.*, **89**, 284501.
- Pattantyús-Ábrahám, M., T. Tél, T. Krámer, and J. Józsa, 2008: Mixing properties of a shallow basin due to wind-induced chaotic flow. *Advances in Water Resources*, **31**, 525–534.
- Peacock, T., and J. Dabiri, 2010: Introduction to Focus Issue: Lagrangian Coherent Structures. *Chaos*, **20**(1), 017501.
- Perruche, C., P. Rivière, P. Pondaven, and X. Carton, 2010: Phytoplankton competition and coexistence: Intrinsic ecosystem dynamics and impact of vertical mixing. *J. Mar. Syst.*, **81**, 99–111.

BIBLIOGRAPHY

- Poje, A. C., A. C. Haza, T. M. Özgökmen, M. G. Magaldi, and Z. D. Garraffo, 2010: Resolution dependent relative dispersion statistics in a hierarchy of ocean models. *Ocean Modelling*, **31**, 36–50.
- Press, W. H., S. A. Teukolsky, and W. T. Vetterling, 1996: *Numerical Recipes in Fortran90*. Oxford University Press, London.
- Provenzale, A., 1999: Transport by coherent barotropic vortices. *Annu. Rev. Fluid Mech.*, **31**, 55–93.
- Qiu, B., 1999: Seasonal Eddy Field Modulation of the North Pacific Subtropical Countercurrent: TOPEX/Poseidon Observations and Theory. *J. Phys. Oceanogr.*, **29**(10), 2471–2486.
- Qiu, B., and S. Chen, 2004: Seasonal Modulations in the Eddy Field of the South Pacific Ocean. *J. Phys. Oceanogr.*, **34**(7), 1515–1527.
- Ramis, C., and S. Alonso, 1988: Sea Breeze convergence line in Mallorca. A satellite observation. *Weather*, **43**, 288–293.
- Ramis, C., and R. Romero, 1995: A First Numerical Simulation of the Development and Structure of the Sea Breeze in the Island of Mallorca. *Ann. Geophys.*, **13**, 981–994.
- Rossi, V., C. López, E. Hernández-García, J. Sudre, V. Garçon, and Y. Morel, 2009: Surface mixing and biological activity in the four Eastern Boundary upwelling systems. *Nonlin. Processes Geophys.*, **16**, 557–568.
- Rossi, V., C. López, J. Sudre, E. Hernández-García, and V. Garçon, 2008: Comparative study of mixing and biological activity of the Benguela and Canary upwelling systems. *Geophys. Res. Lett.*, **35**, L11602.
- Rypina, I. I., F. J. Beron-Vera, M. G. Brown, H. Kocak, M. J. Olascoaga, and I. A. Udovydchenkov, 2006: On the Lagrangian Dynamics of Atmospheric Zonal Jets and the Permeability of the Stratospheric Polar Vortex. *J. Atm. Sci.*, **33149**, 3595.
- San Miguel, M., and R. Toral, 2000: *Stochastic Effects in Physical Systems, Instabilities and nonequilibrium structures*. Kluwer Academic Publisher, pp. 35-130.
- Sandulescu, M., E. Hernández-García, C. López, and U. Feudel, 2007: Plankton blooms in vortices: the role of biological and hydrodynamics timescales. *Nonlinear Process. Geophys.*, **14**, 443–454.

BIBLIOGRAPHY

- Sandulescu, M., C. López, E. Hernández-García, and U. Feudel, 2008: Biological activity in the wake of an island close to a coastal upwelling. *Ecological Complexity*, **5**, 228–237.
- Sasaki, H., Y. Sasai, M. Nonaka, Y. Masumoto, and S. Kawahara, 2006: An Eddy-Resolving Simulation of the Quasi-Global Ocean Driven by Satellite-Observed Wind Field – Preliminary Outcomes from Physical and Biological Fields. *J. Earth Simulator*, **6**, 35–49.
- Schneider, J., T. Tél, and Z. Neufeld, 2002: Dynamics of leaking Hamiltonian Systems. *Pys. Rev. E*, **66**, 066218.
- Schneider, J., V. Fernández, and E. Hernández-García, 2005: Leaking method approach to surface transport in the Mediterranean Sea from a numerical ocean model. *J. Mar. Syst.*, **57**, 111–126.
- Shadden, S. C., F. Lekien, and J. E. Marsden, 2005: Definition and properties of Lagrangian coherent structures from finite-time Lyapunov exponents in two-dimensional aperiodic flows. *Physica D*, **212**(3–4), 271 – 304.
- Shadden, S. C., F. Lekien, J. Paduan, F. Chavez, and J. E. Marsden, 2009: The correlation between surface drifters and coherent structures based on high-frequency radar data in Monterey Bay. *Deep Sea Res II. Top Stud Oceanogr*, **56**, 161–172.
- Shannon, L., G. Hempel, P. Malanotte-Rizzoli, C. Moloney, and J. Woods, 2006: *Benguela: Predicting a Large Marine Ecosystem*. Elsevier.
- Shchepetki, A., and J. C. McWilliams, 2005: The Regional Ocean Modeling System: A split-explicit, free-surface, topography following coordinates ocean model. *Ocean Modelling*, **9**, 347–404.
- Song, Y., and D. Haidvogel, 1994: A Semi-implicit Ocean Circulation Model Using a Generalized Topography-Following Coordinate System. *Journal of Computational Physics*, **115**(1), 228–244.
- Stammer, D., 1997: Global Characteristics of Ocean Variability Estimated from Regional TOPEX/Poseidon Altimeter Measurements. *J. Phys. Oceanogr.*, **27**(8), 1743–1769.
- Stewart, R. H., 2008: *Introduction to Physical Oceanography*. Texas and M University.
- Stommel, H., 1948: The westward intensification of wind-driven ocean currents. *Trans. Amer. Geophys. Union*, **29**(2), 202–206.

BIBLIOGRAPHY

- Sudre, J., and R. Morrow, 2008: Global surface currents: a high resolution product for investigating ocean dynamics. *Ocean Dyn.*, **58**(2), 101–118.
- Tél, T., A. de Moura, C. Grebogi, and G. Károlyi, 2005: Chemical and biological activity in open flows: A dynamical system approach. *Physics Reports*, **413**, 91–196.
- Tel, T., and M. Gruiz, 2006: *Chaotic Dynamics- An Introduction Based on Classical Mechanics*. Cambridge University Press, Cambridge.
- Tew Kai, E., V. Rossi, J. Sudre, H. Weimerskirch, C. López, E. Hernández-García, F. Marsac, and V. Garçon, 2009: Top marine predators track Lagrangian coherent structures. *Proc. Natl. Acad. Sci. U.S.A.*, **106**(20), 8245–8250.
- Titaud, O., J. M. Brankart, and J. Verron, 2011: On the use of Finite-Time Lyapunov Exponents and Vectors for direct assimilation of tracer images into ocean models. *Tellus A*, **63**, 1038–1051.
- Turiel, A., and A. del Pozo, 2002: Reconstructing images from their most singular fractal manifold. *IEEE Trans. on Im. Proc.*, **11**, 345–350.
- Turiel, A., C. Pérez-Vicente, and J. Grazzini, 2006: Numerical methods for the estimation of multifractal singularity spectra on sampled data: a comparative study. *Journal of Computational Physics*, **216**(1), 362–390.
- Turiel, A., H. Yahia, and C. Pérez-Vicente, 2008: Microcanonical Multifractal Formalism: a geometrical approach to multifractal systems. Part I: Singularity analysis. *Journal of Physics A*, **41**, 015501.
- Tzella, A., and P. H. Haynes, 2010: Smooth and filamental structures in chaotically advected chemical fields. *Phys. Rev. E*, **81**, 016322.
- Veitch, J., P. Penven, and F. Shillington, 2009: The Benguela: A laboratory for a comparative modeling studies. *Progress in Oceanography*, **83**(1-4), 296–302.
- Warner JC, Sherwood CR, S. R. H. C. A. H., 2008: Development of a three-dimensional regional, coupled wave, current, and sediment-transport model. *Comput Geosci*, **34**(10), 1284–1306.
- Waugh, D. W., and E. R. Abraham, 2008: Stirring in the global surface ocean. *Geophys. Res. Lett.*, **35**, L20605.
- Waugh, D. W., E. R. Abraham, and M. M. Bowen, 2006: Spatial Variations of Stirring in the Surface Ocean: A case of Study of the Tasman Sea. *J. Phys. Oceanogr.*, **36**, 526–542.

Wiggins, S., 1992: *Chaotic Transport in Dynamical Systems*. Springer-Verlag, New York.

Williams, R. G., 2011: Ocean eddies and plankton blooms. *Nature*, **4**, 739–740.

Zhai, X., R. J. Greatbatch, and J.-D. Kohlmann, 2008: On the seasonal variability of eddy kinetic energy in the Gulf Stream region. *Geophys. Res. Lett.*, **35**, L24609.

